NANO-STRUCTURED MATERIALS FOR ENERGY STORAGE APPLICATIONS

by

DONGXUE ZHAO

A DISSERTATION

Presented to the Faculty of the Graduate School of the

MISSOURI UNIVERSITY OF SCIENCE AND TECHNOLOGY

and

UNIVERSITY OF MISSOURI – ST. LOUIS

In Partial Fulfillment of the Requirements for the Degree

DOCTOR OF PHILOSOPHY

in

PHYSICS

2015

Approved by

Eric H. Majzoub, Advisor
Julia E. Medvedeva, Co-Advisor
Yew San Hor
Sonya Bahar
Phillip B. Fraundorf
Stephen M. Holmes

PUBLICATION DISSERTATION OPTION

Partial content of this dissertation has been prepared in publication format. Papers II, and III have been previously published in scientific journals. Paper IV has been previously presented at a conference meeting. Papers I has been formatted for publication in a scientific journal and is awaiting final review before submission. Although the formatting of these sections follows that of this dissertation, the text has not been changed from the original publications. Therefore, references cited in these papers appear at the end of each section. There is exception for figure and captions and they do not follow the general numbering format of this dissertation.

PAPERS:

Paper I, pages 74-85, "A Study of the Heat and Pressure Induced S105 Phase in $NaAlH_4$", D. Peaslee, G. Wang, D. Zhao, E. G. Sorte, S. Hayes, M. Conradi, B. Bowman, and E. H. Majzoub, *Awaiting Publication,* 2015.

Paper II, pages 86-107, "Effects of NaOH in Solid NaH: Solution/Segregation Phase Transition and Diffusion Acceleration", E. G. Sorte, E. H. Majzoub, T. E. Caleo, B. A. Hammann, G. Wang, D. Zhao, R. C. Bowman Jr. and M. S. Conradi, *J. Phys. Chem. C*, 2013, 117 (45), 23575-23581.

Paper III, pages 108-138, "Density Functional Theory of MH-MOH Solid Solubility (M= alkali) and Experiments in NaH-NaOH", G. Wang, C. L. Carr, D. Zhao, G. Sorte, M. S. Conradi, R. C. Bowman Jr. and E. H. Majzoub, *J. Phys. Chem. C*, 2015, 119 (15), 8062-8069.

Paper IV, pages 139-144, "Investigation of TiO_2 and Other Electrode Materials in Lithium-ion Batteries: Improving Capacity and Cycling Performance", A. M. McFarlane, D. Zhao and E. H. Majzoub, *The 22nd Annual Meeting of the NASA-Missouri Space Grant Consortium,* 2013.

ABSTRACT

Hydrogen is a non-polluting and efficient energy carrier. One barrier to utilizing hydrogen is a reliable, low-cost storage method. Metal hydrides possess good kinetics with low absorption/release temperatures, high hydrogen capacities and low cost. Compared with compressed gas and liquid hydrogen, metal hydrides have higher hydrogen storage density and much lower volume. Sodium aluminum hydride ($NaAlH_4$) is the prototypical example of a complex metal hydride with high hydrogen storage capacities (~ 5.5 wt.%) and acceptable reaction temperatures of around 100 ℃ when using catalyst.

On decomposition of these complex hydrides, such as $NaAlH_4$, one is left with monohydride NaH. The kinetics of diffusion in the monohydrides is important because reversibility hinges on mass transport and the formation of $[AlH_4]^-$ anions that must structurally coordinate with the alkali metal cation on hydrogen absorption. We implement in-situ X-ray diffraction and differential scanning calorimetry investigations of the NaH/NaOH system of a variety of molar ratios, and the results indicate a solid solution mixture of H^- and $[OH]^-$ that occurs across the phase diagram may play a large role in the mass transport necessary for hydrogen absorption and desorption in complex hydrides such as $NaAlH_4$.

Nanoporous frameworks for energy storage applications have attracted attention for batteries and supercapacitors. We prepare nanoporous ordered hard carbons (NPC) via a self-assembly method with block polymer templating. These NPC materials have large surface area (> 600 m^2/g), meso-pore structure, high pore volume (> 0.5 cc/g), and straightforward synthesis. The microstructure and pore size distribution is tunable, and

the resulting hard carbon is structurally robust and chemically stable for many applications. We discuss the synthesis and characterization of several NPC materials prepared for both hydrogen storage and battery applications.

Nano-sized TiO_2 is a superior material for lithium-ion batteries due to its high chemical stability, low cost, low volume change on lithiation (~ 3%), high energy density. It is also environmentally benign. We synthesize high purity (~ 100%) anatase TiO_2 nano-particles with controllable particle size from 9 to 38 nm and excellent electrochemical properties (> 220 mAh/g) using our efficient and reliable method. An optimum particle size range of 11 – 22 nm shows the best electrochemical properties with both high capacity and good recoverability after high C-rate cycling. We discuss the synthesis, characterization and electrochemical measurements of prepared anatase TiO_2 nano-particles for lithium-ion battery applications.

Diffusion in nanoparticle systems is of paramount importance for any intercalation material, including Li-ion and metal hydride batteries. We develop an extension of the galvanostatic intermittent titration technique (GITT) that utilizes the open cell potential of the relaxation portion of the GITT measurement. We present results for the lithium diffusion behavior in TiO_2 and SnO_2 nanoparticles and contrast the results, as these systems represent intercalation and conversion reactions, respectively.

ACKNOWLEDGMENTS

I would like to give special thanks to Dr. Eric H. Majzoub for the supervising and helping in my whole Ph.D. process. I have learned a lot from him including his teaching, patient directing and co-working with me, which is absolutely a valuable and significant part in my life. I enjoyed working with him.

I also would like to thank to all the group members including graduate students, postdoc research scholars and visiting scholars in Dr. Eric H. Majzoub's research group. They are: Dr. Xiangfeng Liu, Dr. Timothy Mason, Dr. David Peaslee, Dr. Hua Ning, Dr. Wenzheng Zhou, Dr. Mahesh Wickramasinghe, Dr. Kouji Sakaki, Mr. Patrick Sheehan, Mr. Gang Wang, Mr. Chris Carr, Mr. Mike Cowan, Mr. Henry Hamper, Mr. Marc Segales, Ms. Alyssa McFarlane, and Ms. Waruni Jayawardana. It was a nice journey of working them during my Ph.D. study and they have provided valuable suggestions and contributions to my work.

I appreciate the Physics Department provided me this great opportunity of Ph.D. study and financial support for the past 4 years.

Thanks to Dr. Bruce Wilking for navigating me through the whole graduate study in Physics Department. Also I appreciate all faculty and staff members of Physics Department who taught me and helped me.

I would like to thank my Ph.D. committee members both in University of Missouri – St. Louis and Missouri University of Science and Technology: Dr. Eric H. Majzoub, Dr. Julia Medvedeva, Dr. Yew San Hor, Dr. Sonya Bahar, Dr. Phillip Fraundorf, and Dr. Stephen Holmes. All of them provided useful suggestions to my work.

Last but not least, I would especially like to thank my parents for supporting and encouraging me all the time in my life. Thanks to my wife, she is always supporting me and helping me. Additionally, I want to thank my son, I have been feeling extremely happy since he came to the world.

TABLE OF CONTENTS

LIST OF ILLUSTRATIONS

PAPER III

PAPER IV

LIST OF TABLES

PAPER III

APPENDIX B.

1. INTRODUCTION

1.1. ENERGY STORAGE TECHNOLOGY FOR THE FUTURE

With the development of culture, industry, and our society, the energy problem becomes more and more important and it is the core problem in many countries. As a common sense, we cannot make the unconstrained consumption relying on fossil energies [1]. Therefore, we need a very reliable, efficient and economical energy storage system, which can convert the electrical energy from the large power grid systems into an energy storage unit and convert the stored energy back into electrical energy when needed [2-4]. With such electrical energy storage system, the electricity energy can be produced anytime regardless of the electricity demands and the production situations without energy loss caused by demands, and then we can use the electricity energy based on our real demands [5-6].

Actually, our human life has already significantly been improved by the energy storage systems in many aspects such as portable electronic device, compact power supply unit, pollution-free city buses, and electric cars [7-9]. There are many different storage methods for these energy storage systems. From high performance lithium-ion batteries to the solid hydrogen storage materials, the transportation industry and our daily life have benefited a lot from those new technologies. Furthermore, for some other renewable energy sources such as wind, solar and hydropower, it will be not easy or reliable to change the production rate based on real demands, which results in wasting of energy in the excess energy production case [10-13]. Hence, the energy storage system will solve these problems as the excess energy will be stored in system and released when needed. Especially for a large power grid system, we will have an optimized usage of energy with reliable, efficient and safe energy storage systems. Figure 1.1 shows a scheme of how energy storage systems incorporate into different power systems.

High capacity, low cost, and reliable lithium-ion battery units can play as a significant role in future energy storage technologies. Acting both as stationary and mobile energy storage units, lithium-ion batteries can be well used in different sections of a power system. Figure 1.2 represents how the stationary energy storage unit works. We

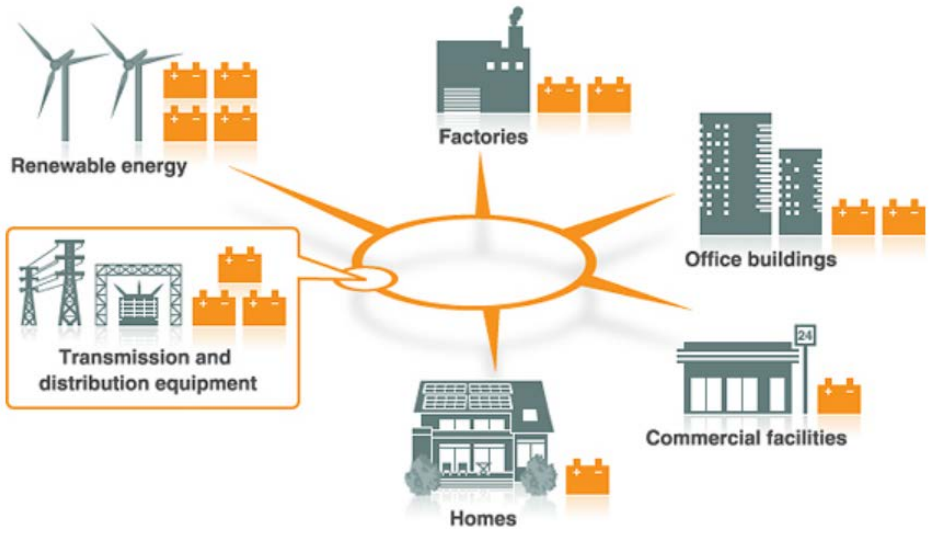

Figure 1.1. Energy storage systems incorporate into different power systems [14]

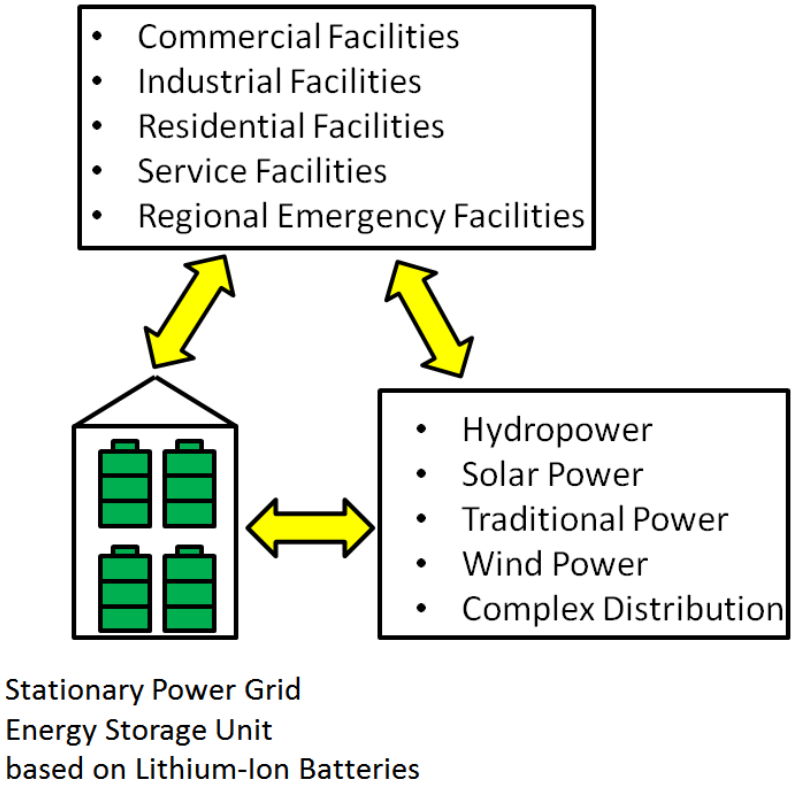

Figure 1.2. Stationary energy storage unit and the working scheme

can see the triangular relationship of the energy storage unit, power system, and consumption terminal. The energy storage unit would storage the excess energy generated by different power systems and release the energy when needed, which can make the whole cycling process “on-demand”. In spite of the peak period or the valley period of power generated from different energy sources, the energy storage system will definitely provide us an efficient way of using energy. The mobile energy storage unit makes the zero-emission vehicles available today as those vehicles just use the rechargeable battery pack as power supply. Nowadays the high performance lithium-ion battery is becoming a hotter topic, and commercial fully electric vehicles based on lithium-ion batteries such as Tesla cars [15] are available. Mobile energy storage units such as battery packs serve for different applications as shown in Figure 1.3.

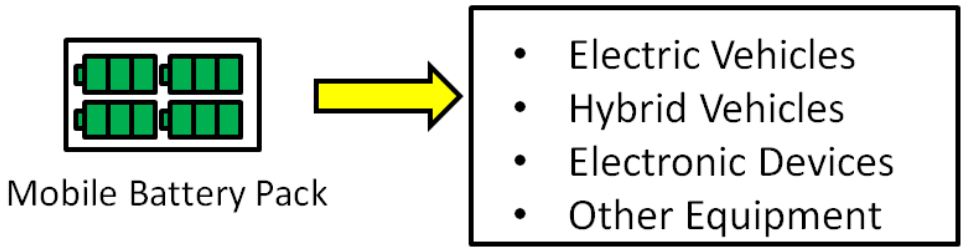

Figure 1.3. Mobile energy storage unit serves different applications

Hydrogen storage system is also a promising energy storage method. Hydrogen is the most common element on our earth, and hydrogen will never make pollution to the environment. In addition, hydrogen has calorific value as high as 3 times that of petrol and 5 times that of coal [16]. Currently there are already commercial hydrogen fuel cell vehicles available. In 2014, Japan’s leading vehicle company Toyota exhibited its first commercial hydrogen fuel cells vehicle called “Mirai” [17], and Mirai is now available in 2015. However, the hydrogen storage method for the Mirai car still uses an old technology – high pressure hydrogen tank, which may potentially be dangerous. The future hydrogen storage technology will be focused on solid hydrogen materials with low hydriding/dehydriding temperatures, which will be more efficient. Also, storing hydrogen in solid materials rather than in a high pressure tank would eliminate the potential safety hazard [18-20].

Further future energy storage information for lithium-ion batteries and hydrogen storage can be found on United States Department of Energy (DOE) Office of Electricity Delivery & Energy Reliability website [21] and Office of Energy Efficiency & Renewable Energy website [22].

1.2. HYDROGEN AS AN ENERGY CARRIER

With the development of culture, industry, and our society, the energy problem becomes more and more important and is entitled as the core problem by many countries. As a common sense, we cannot make the unconstrained consumption relying on the fossil energies [1, 16]. Therefore, we need a very reliable, efficient and economical energy storage system, which can convert the electrical energy from some clean and pollution-free energy carriers. Hydrogen as an energy carrier is a promising candidate for future energy solution [19, 20].

1.2.1. Production and Storage of Hydrogen. The easiest way to produce hydrogen is via electrolysis of water, which can be achieved in a reliable, low-cost way [23-25]. For instance, we have a huge amount of sea water on the earth we live, which can provide us a low cost and less quantity-restrained option to get hydrogen. Many efforts were invested to improve the hydrogen production process based on the electrolysis of water. A low cost and environmental friendly way is the TiO_2 photo catalytic water-splitting technology, and the early work was introduced in 1972 [25, 26]. However, the efficiency is still too low to be widely used for hydrogen production. Recently, by using Au/TiO_2 complex catalysts, high production rates and selectivities (>99.3%) can be achieved under the simulated solar light [27, 28], which is a breakthrough for this hydrogen production technology.

The hydrogen storage problem is a current key barrier of using hydrogen in an efficient and safe way. As we know that the easiest hydrogen storage way is just compress the hydrogen gas into a high pressure tank for instant use. However, the high pressure hydrogen gas is still too dangerous to be used [29], which inspires the research work on hydrogen storage in solid phase materials. Currently, there are two hot methods to store the hydrogen in solid state materials. One is that by using the high surface area metal organic frameworks (MOF) or mesoporous carbon [30-36], which have the

advantage of tunable pore size, so that the adsorption capacity of hydrogen can be tuned to meet different demands. The other method is chemically storing the hydrogen in complex metal hydrides such as $NaAlH_4$ and $LiBH_4$ [36-40], which generally has high theoretical hydrogen storage capacity. It is obvious that this method is much safer than the high pressure tank method, and the hydriding/rehydriding processes can be improved by doping catalysts in order to get lower chemical decomposition temperatures and faster reaction processes [39, 40]. However, either chemically storing the hydrogen or storing the hydrogen in mesoporous structured materials need to be improved both for cyclability and fast release rate.

1.2.2. Complex Metal Hydrides Hydrogen Storage Material. Generally, the complex metal hydrides have the chemical formula as $M_xM'_yH_n$, where M is the alkali metal cation, and M'_yH_n is a complex group such as AlH_4 or BH_4. For example $NaAlH_4$ and $LiBH_4$ are complex metal hydrides that can be used for hydrogen storage. Usually these complex metal hydrides have high hydrogen storage capacities. However, the hydrogen will be release in multiple steps rather than a single release process during the decomposition, which could make the reverse hydriding process complicated.

1.2.2.1 $LiBH_4$. Lithium borohydride has a high hydrogen storage capacity of 18.2 wt. % and has been considered as a good hydrogen storage material. There are at least two steps during the $LiBH_4$ decomposition. The first step will release hydrogen at around 370℃ and results in LiB at the same time. The LiB will decompose at above 600℃. There are two major disadvantages of LiB material for hydrogen storage. One is the high decomposition temperature [41], which will limit the accessible kinetics of releasing hydrogen. The other advantage is the possible toxic byproduct, which is diborane (B_2H_6), could make a potential dangerous factor during the release process of hydrogen [42, 43]. The $LiBH_4$ decomposition process is stated in following equations (1), (2) and (3).

$$LiBH_4 \longleftrightarrow LiH + B + \frac{3}{2}H_2 \quad (1)$$

$$LiH \longleftrightarrow Li + \frac{1}{2}H_2 \quad (2)$$

$$LiBH_4 \longleftrightarrow \frac{1}{2}B_2H_6 + LiH \quad (3)$$

1.2.2.2 $NaAlH_4$. Sodium aluminium hydride has a hydrogen storage capacity of 7.4 wt. % and has no toxic byproducts compare with $LiBH_4$. There are at least three steps during the decomposition. The kinetics and lower temperature have been improved either by doping catalysts [39, 40] or confining $NaAlH_4$ in highly ordered nanoporous carbons [44, 45]. Thus, $NaAlH_4$ is a promising hydrogen storage material. The $NaAlH_4$ decomposition process is stated in following equations (4), (5) and (6).

$$NaAlH_4 \longleftrightarrow \frac{1}{3} Na_3AlH_6 + \frac{2}{3} Al + H_2 \quad (4)$$

$$Na_3AlH_6 \longleftrightarrow 3NaH + Al + \frac{3}{2} H_2 \quad (5)$$

$$NaH \longleftrightarrow Na + \frac{1}{2} H_2 \quad (6)$$

1.3. NANO POROUS CARBONS FOR ENERGY STORAGE MATERIALS

Due to the highly ordered porous structure with high surface area and great electron conductivity, nano porous carbon is an excellent candidate for energy storage materials in many different aspects. Nano porous carbon can be used in lithium-ion batteries to increase chemical diffusion properties and enhance the electrode conductivity [46-48]. With the high surface area, nano porous carbon can also be used in super capacitors [49-50]. For example, the incorporation of metal oxides with nano porous carbon has greatly improved the electrochemical properties [51, 52]. Also, nano porous carbon shows excellent confinement property and can be used for hydrogen storage materials [36, 44].

1.3.1. General Introduction of Nano Porous Carbon. The nano porous carbon (NPC) usually has the pore size on the order of 1 ~ 20 nm and specific surface area range of 300 ~ 2000 m^2/g. The nano porous carbon in different surface areas and different pore sizes provides a good chance to fit with different application demands. Also the nano porous carbon has extremely strong structures and can serve as a hard template in many applications [53].

1.3.2. Synthesis of Nano Porous Carbon. There are many different ways to synthesize nano porous carbon, and generally, the two major synthesizing types are direct synthesis [54, 55] and synthesis by using hard templates [56]. Among various NPC synthesizing methods, in my research, I have selected the direct synthesis of FDU-15 type nano porous carbon based on organic-organic self-assembly method [55] due to the good reliability.

1.3.3. Nano Porous Carbon Coupling with Metal Oxides. Many materials have been investigated as electrode materials in super capacitors, including transition metal oxides, carbonaceous materials and conducting polymers. Each type of electrode material has its advantages and disadvantages. For example, metal oxides can provide higher energy density than conventional carbon materials and better cycling stability than polymer materials, but they have a key weakness of poor conductivity. On the other hand, carbon materials have high power density and long cycle life, nevertheless, the low specific capacitance greatly limits their further application. Therefore, it has inspired attempts to develop novel electrode materials via the coupling of the oxides and carbon materials in order to improve electrochemical performance.

Generally, small size can significantly enhance the utilization of active materials and shorten the transport path of ion and electron. Single-phased nano materials are still insufficient in performance because of their intrinsic weaker material properties in conductivity, cycling stability and mechanical stability in despite making them in the form of Nano materials. As a result, heterogeneous nanostructured materials with multi Nano components have been proposed. In this configuration, each component is tailored to meet different demands, e.g. high energy density, and high conductivity. The resulting materials exhibit synergistic properties by integrating the individual components, and greatly enhance the super capacitive performance. Among the various hybrid approaches,

the metal oxide-carbon combination has shown great potential. The metal oxide/carbon composites not only increase the utilization of the active materials, but also improve the electrical conductivity and mechanical strength of the composite materials.

1.3.3.1 Metal Oxide Coupling Methods. There are several different metal oxide and carbon incorporation methods for various applications. For metal oxide particles confined in the ordered nano porous carbons, generally there are 4 main coupling methods: ion-exchange method [57], impregnation method [58], sonochemical method [59], and direct synthesis method [52]. Another common coupling structure is metal oxide nanowires coated with nano porous carbons: a good example of this method is a novel Mn_3O_4/nano porous carbon hybrid nanowire [60]. In addition, there is a new type of nano porous carbon coupled with metal oxides structure called "hierarchical porous graphitic carbon (HPGC)-based structure" [61, 62]. The design of hierarchical porous structure is based on the different behaviors of electrolyte in pores with different sizes including macro-porous cores, mesoporous walls and micro-pores, which can result in high-performance electrode materials with short ion transport distance, low resistance, and large charge storage density. HPGC nanostructure is expected to combine with metal oxides as novel nano-composite materials for high electrochemical performance energy storage.

1.3.3.2 Different Nano-structured Porous Carbon with Metal Oxides. As discussed in **1.3.3.1**, there are several different coupling ways to incoporate the nano porous carbon and metal oxides. As a result, there are also many different nano-structured porous carbon with metal oxides. The first example is the crystalline TiO_2 embedded in the nano porous carbon frame [52], which has nano-sized TiO_2 crystals ranging from 2.6 ~ 9.7 nm, and the surface area of the nano porous carbon mains up to 639 m^2/g. This structure of TiO_2 nano crystals embedded in NPC provides great conductivity, high adsorption capacity and high energy density. Another example is the crystalline carbon-SnO_2 hollow sphere sturcture [63], in which the crystalline carbon hollow spheres were encapsulated with the 1 ~ 3 nm SnO_2 nano particles. This structure shows great promise for use in lithium-ion batteries. In addition, there is another method incorporating the metal oxides with nano porous carbon by doping the metal oxide particles into the nano porous channels of NPC. A good example is the novel structure in

which MnO_2 nano particles are confined in highly ordered mesoporous carbon [59]. The MnO_2 nano particles were doped into CMK-3 type nano porous carbons via a sonochemical method, and it provides a good electrochemical performance of more than 200 mAh/g reversible capacity. There are still many different NPC-metal oxide structures with improved energy storage properties, and this is a hot topic in the energy storage materials research.

1.4. LITHIUM-ION BATTERIES BASED ON METAL OXIDES

The lithium-ion batteries are more and more promising energy storage devices due to the advantages of high energy density, long life cycle, environment friendiness, good universality and no memory effect [64-67]. In the past decade there has been a lot of research works done on the carbonaceous materials for electrodes for the intrinsic advantage of good carbon conductivity [68-70]. However, the low energy density of carbonaceous materials limits the lithium-ion battery applications. The metal oxides provide high energy density but poor conductivity, so the combination of other metal oxides materials with carbon materials would improve lithium-ion battery performance.

1.4.1. Metal Oxides for Lithium-Ion Batteries. Some common metal oxides with high energy density for lithium-ion batteries such as SnO_2, TiO_2, MnO_2, etc. had shown good capacity results. However, combining these metal oxides with different structured carbons such as SnO_2 in carbon matrix [71] , TiO_2 in meso-porous carbon [52] , MnO_2 in porous carbon [72] , and SnO_2/carbon hollow spheres [63] ,etc., showed better properties both in energy density and cyclability.

1.4.2. TiO_2 for Lithium-Ion Batteries. Due to the high chemical stability, low cost, low volume change (~ 3%), high energy density and environmental friendiness, TiO_2 is a superior metal oxide material for lithium-ion batteries. TiO_2 has 4 common phases: Anatase, Rutile, Brookite, and TiO_2-B. Among these phases, anatase TiO_2 shows better Li^+ insertion property with $Li_{0.6}TiO_2$ [73-76], which results a better capacity. Although TiO_2-B has a higher insertion ratio of $Li_{1.01}TiO_2$-B [77, 78], due to the lower real experimental capacity and more complicated fabricating process, anatase TiO_2 becomes more and more interesting and has great potential for high performance lithium-ion batteries.

1.4.2.1 TiO_2 Incorporated with Nano Porous Carbon. The nano porous carbon has intrinsic good conductivity and the high surface area is excellent for charge transport and electrolyte penetration. In addition, the highly ordered porous channels can prevent agglomeration and degradation [79-81]. As discussed in **1.4.2**, TiO_2 is also a promising material for lithium-ion batteries, so that incorporating the TiO_2 nano crystals into nano porous carbon would significantly improve the electrochemical performance for lithium-ion batteries. Chang et al. [82] sucessfully synthesized nano crystalline TiO_2 embedded in the nano porous carbon by using the solvent evaporation-induced self-assembly (EISA) and in-situ TiO_2 crystallization at different calcination temperatures. The TiO_2 content in their method ranges from 50wt.% to 75wt.%, and these series materials shows high reversible capacity of above 500 mAh/g. However, in the synthesis process, they used $TiCl_4$ as the titanium source, where $TiCl_4$ is a dangerous toxic material. In my research work, I used the safe Ti (IV) isopropoxide as the titanium source and HCl as acid inhibitor, which is a safe process. The TiO_2 nano crystals are embedded in the nano porous carbon frame with particle size of about 8 nm.

1.4.2.2 Nano-sized TiO_2. Generally, nano structured active materials have significantly improved the lithium-ion batteries' properties including cyclability, specific capacity and retention [83]. As discussed above, anatase TiO_2 shows better Li^+ insertion property with a better capacity rating, so it is insteresting to investigate the anatase TiO_2 nano particles electrochemical property for lithium-ion batteries. Anatase TiO_2 nano particles have been previously synthesized using hydrolysis of Ti (IV) isopropoxide with a nitric acid inhibitor [84, 85] or triethylene glycol (TEG) [86], but those processes are

relatively complicated. For example, a long time peptization process is needed in the nitric acid inhibitor method, and a refluxing condenser is needed in the triethylene glycol (TEG) method.

I used a better anatase TiO_2 nano particle synthesis method with controllable particle size based on on hydrolysis of Ti (IV) isopropoxide by using a hydrochloric acid inhibitor, which apparently reduces the reaction temperature, avoids other chemical impurities, and produces phase pure anatase. This synthesis method shows a very controllable TiO_2 particle size range from 9 nm to 38 nm under different annealing temperatures with superior electrochemical properties.

1.5. LITHIUM DIFFUSION IN ELECTRODE ACTIVE MATERIALS

Lithium ion diffusion behavior plays an important role in the lithium insertion/de-insertion process in the electrode active materials. Lithium diffusion rate may afftect the rate of capacity and eletrochemical kinetics characteristic for lithium-ion batteries. It is newcessay to investigate the lithium difusion behavior and study the lithium diffusion cooefficient in the active materials.

I used Galvanostatic intermittent titration technique (GITT) to inverstigate the batteries based on synthesized anatase TiO_2 nano-particles in the size of 9 – 35nm. A newly developed lithium diffusion behavior model based on stretched exponential method was used for modelling the lithium diffusion and calculate the lithium diffusion coefficients by using the relaxation portions of GITT measurements of my samples. Also, I presented and compared the results for the lithium diffusion behavior in TiO_2 and SnO_2 nanoparticles, as these two different systems respectively represent intercalation and conversion reactions.

1.6. OUTLINE OF THE WORK

The work accomplished on complex metal hydride and metal hydride materials, nano porous carbon materials, and TiO_2 nano particle materials are outlined in the following sections.

Section 2 outlines the $NaAlH_4$ complex metal hydride prepared under different conditions and the properties were investigated by X-ray diffraction and differential

scanning calorimetry. The NaH/NaOH solubility was also investigated and analyzed by in-situ X-ray diffraction and differential scanning calorimetry.

Section 3 outlines the synthesis and characterization of nano porous carbon based on the FDU-15 type. Also, the ball mill effect before calcination and after calcination were investigated and analyzed.

Section 4 outlines the synthesis and characterization of TiO_2 nano crystals embedded into the nano porous carbon and the anatase TiO_2 nano particles with controllable particle size. For the TiO_2 nano particles, electrochemical characterization and lithium ion diffusion property were investigated.

Section 5 outlines the experimental investigation for TiO_2 and SnO_2 nano-particles by using galvanostatic intermittent titration technique (GITT). A newly developed lithium diffusion model based on stretched exponential method was used to compare the lithium diffusion behavior in two two different systems of lithium intercalation and conversion reactions, respectively.

Paper I presents the investigation of $NaAlH_4$ hydrogen storage material prepared under different environments especially the heat and pressure induced S105 phase, which showed improved property.

Paper II presents previous published work on the effect of NaOH in solid NaH. The phase transition and separation were investigated by in-situ X-ray diffraction and differential scanning calorimetry.

Paper III presents previous published work on the NaOH and NaH solid solubility with experimental investigation and compared with first-principle calculations by using density function theory.

Paper IV presents the previous conference research paper on TiO_2 nano crystals embedded into the nano porous carbon. The electrochemical properties were investigated and analyzed for the 65 wt. % TiO_2 content samples.

2. METAL HYDRIDES AND COMPLEX METAL HYDRIDES

2.1. INTRODUCTION

Complex anionic hydrides such as sodium aluminum hydride ($NaAlH_4$) are promising storage materials due to their high hydrogen storage capacities, and reasonable reaction temperatures (around 100 ℃ by using a catalyst). The first part of this section presents a study of the decomposition of highly pure bulk $NaAlH_4$ with a new phase created under a high hydrogen pressure around 200 bars and high temperature near 180 ℃. NMR studies have found a highly mobile Al-species (the “S105 phase”) in heat and pressure-treated $NaAlH_4$ [87, 88]. On decomposition of these complex hydrides, one is left with the alkali monohydride LiH, NaH, or KH. Reversibility hinges on mass transport and the formation of $[AlH_4]^-$ anions that must structurally coordinate with the alkali metal cation. Therefore the kinetics of diffusion in the monohydrides is important. Moreover, there is always contaminant oxygen present in even the most carefully prepared materials. Recent studies have found that OH^- in NaH improved the mobility of hydrogen in NaH, indicating that $[OH]^-$ may be a beneficial impurity that improves the kinetics of the rehydriding reaction [37]. The second part of this section presents an investigation the solubility of OH^- in alkali metal hydrides for Na using in situ X-ray diffraction (XRD) and differential scanning calorimetry (DSC).

2.2. INVESTIGATION OF SODIUM ALUMINIUM HYDRIDE

The $NaAlH_4$ structure was investigated by using “General Structure Analysis System” (GSAS) [89] software from the full pattern Rietveld refinement of X-ray diffraction data. The following reaction pathways were investigated by differential scanning calorimetry (DSC) and direct line-of-site mass spectrometry (DLOS-MS).

2.2.1. High Purity $NaAlH_4$ Preparation. High purity bulk $NaAlH_4$ crystals were synthesized via the evaporation crystallization method. Firstly, I added the commercial $NaAlH_4$ powders (Sigma-Aldrich) into tetrahydrofuran (THF) solution (Sigma-Aldrich) to make a saturated $NaAlH_4$ and THF solution. Then, during the evaporation process of the saturated solution, we can get some small crystallized $NaAlH_4$ seeds. Finally, the small crystallized $NaAlH_4$ seeds were added into the saturated solution again to make the small seeds to be grown to bulk crystals during the THF evaporation process. Thus I got the high purity bulk $NaAlH_4$ crystals. Then, two different types of treatments were implemented to these $NaAlH_4$ bulk crystals. One treatment is to heat the high purity $NaAlH_4$ just below the melting temperature under high H_2 pressure to get a sample without S105 phase, and this sample is labeled as N97. The other treatment is to heat the high purity $NaAlH_4$ just above the melting temperature under high H_2 pressure to get a sample with S105 phase, and this sample is labeled as N98.

2.2.2. X-Ray Diffraction Analysis. The powder X-ray diffraction (XRD) technique was used to get the diffraction pattern. The theoretical simulation of X-ray diffraction with accurate peak lines was done by a self-made X-ray diffraction simulation Matlab code for arbitrary materials (Appendix A). Then we fit the whole pattern profile by using Rietveld refinement Method. In this method, I fitted both apparatus' deviation and materials' structure coefficients. I_o is the observed intensity by XRD, and I_c is the calculated intensity during refinement. The criterion of the refinement goodness is determined by whole pattern residuals (R_p) with $R_p = \Sigma|I_o-I_c|/\Sigma I_o$, weighted residuals ($w_{Rp}$) with $w_{Rp} = (M_p/\Sigma w I_o^2)^{0.5}$ and $M_p = \Sigma w (I_o-I_c)^2$, and other calculated physical coefficients such as meaningful calculated particle sizes' range (calculated particle size given by Debye–Scherrer Equation: $D = 0.94\,\lambda/(\,FWHM\cos(\theta)\,)$. In these XRD experiments, the Cu-Kα (λ_1= 1.54056 Å and λ_2= 1.54439Å) radiation was used by Rigaku Ultima IV instrument. Detailed results are shown in Paper I.

2.2.3. Differential Scanning Calorimetry Analysis. The Differential Scanning Calorimetry (DSC) instrument was used to measure the experimental decomposition enthalpies for pure $NaAlH_4$, N97 and N98 as stated above. The small amount of sample (~1 mg) was put in the Hermetic-Aluminum pan, and then run the DSC with another empty reference sample. In addition, the Residual Gas Analyzer (RGA) instrument with mass spectrum was used to analyze the details of $NaAlH_4$ decomposition and the release of hydrogen. In order to better investigate and compare the decomposition pathways and hydrogen release processes of these samples, the DSC data compared with the RGA data for pure $NaAlH_4$, N97 and N98 at 1℃/minute, 4℃/minute, and 8℃/minute ramp rate are shown in Figure 2.1, Figure 2.2, and Figure 2.3.

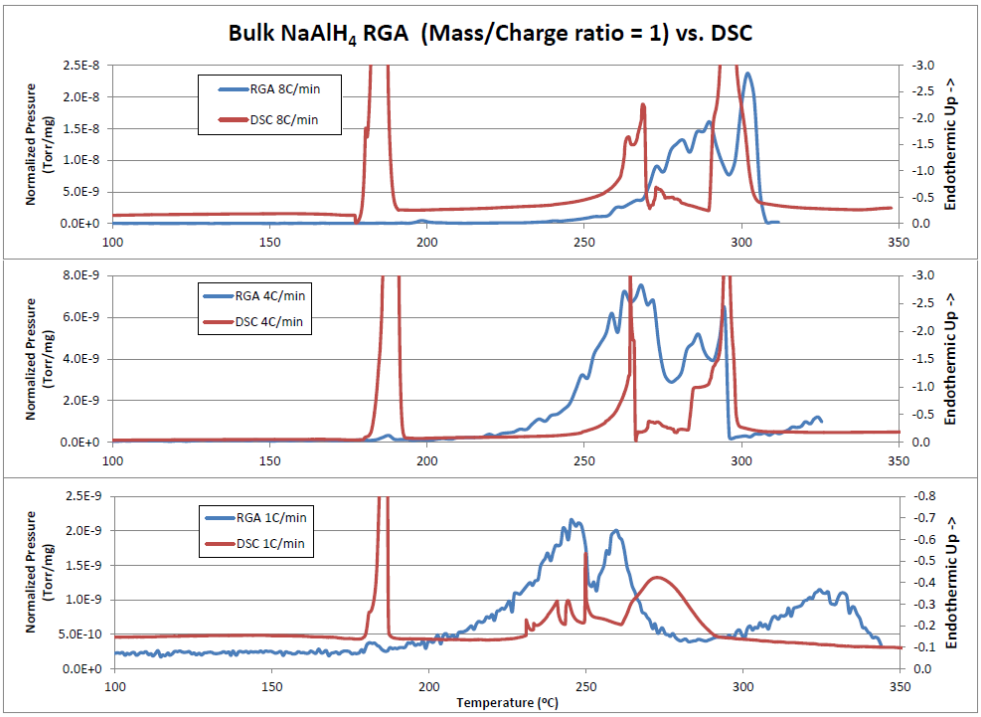

Figure 2.1. RGA and DSC plots for pure $NaAlH_4$ sample.

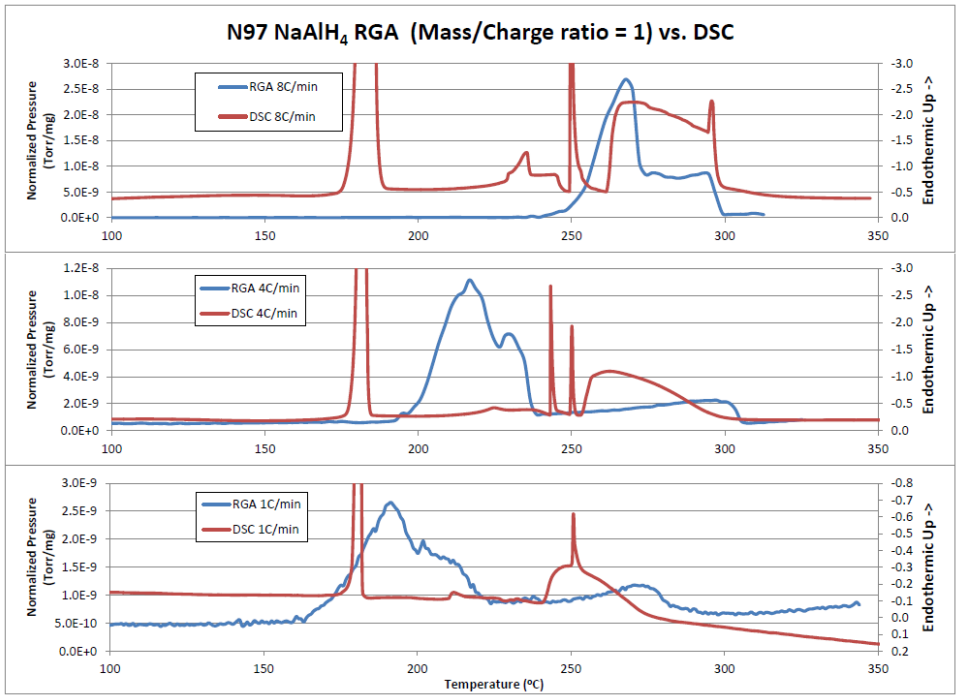

Figure 2.2. RGA and DSC plots for N97 $NaAlH_4$ sample.

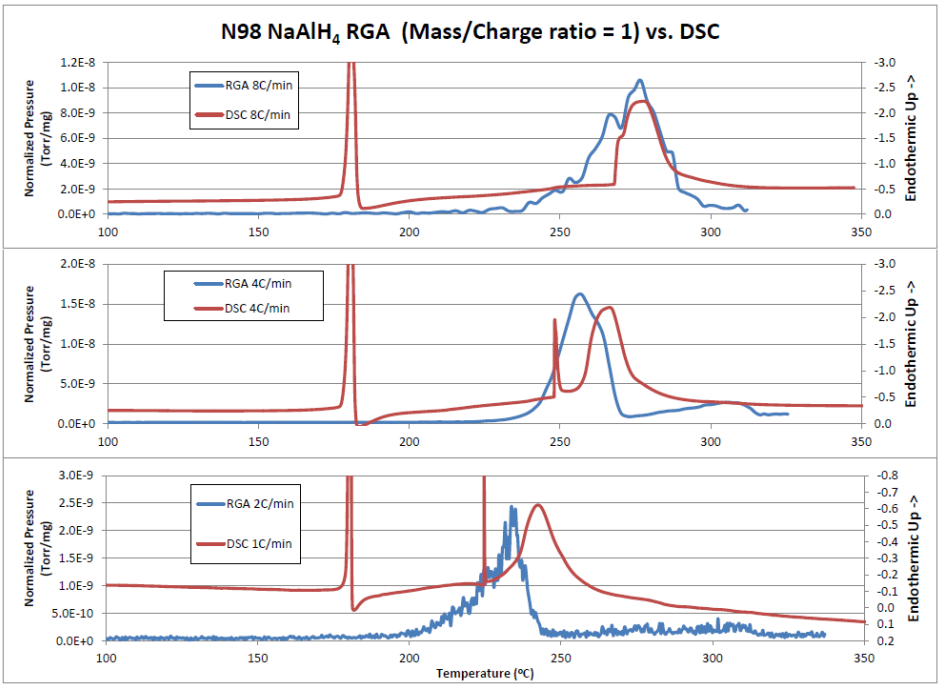

Figure 2.3. RGA and DSC plots for N98 $NaAlH_4$ sample.

The calculated enthalpies from differential scanning calorimetry (DSC) measurements at the heating ramp rate of 1℃/minute are shown in Table 2.1.

Table 2.1. Calculated enthalpies for different reaction processes from DSC measurements for pure $NaAlH_4$, N97 and N98 $NaAlH_4$.

	Reaction 1 & Reaction 2		Reaction 3	
	℃	kJ/mol H_2	℃	kJ/mol H_2
Bulk $NaAlH_4$	249	52.6	434	66.3
N97 $NaAlH_4$	250	36	402	86.5
N98 $NaAlH_4$	234	46.9	391	86.6

The DSC measurements plotted along with the RGA data and the results showed a strong correlation. The results of the DLOS-MS show that all 3 samples, bulk $NaAlH_4$, N97, and N98 $NaAlH_4$, decompose through the same reaction pathways, but we can clearly see that N97 and N98 $NaAlH_4$ decompose at a lower temperature than the bulk material. Additionally, N98 in the S105 phase shows a smaller temperature range for reaction 2 to complete.

2.3. INVESTIGATION OF SODIUM HYDRIDE/HYDROXIDE SOLUBILITY

The OH^- in NaH has been found to improve the hydrogen mobility in NaH in recent studies, indicating that $[OH]^-$ may be a beneficial impurity that improves the kinetics of the rehydriding reaction [37]. In this part, an investigation of the solubility of OH^- in alkali metal hydrides for Na using in situ X-ray diffraction (XRD) and differential scanning calorimetry (DSC) is shown.

2.3.1. Previous Study of Solubility in NaH/NaOH System. Figure 2.4 shows fusion diagram of a good solubility of Na-system done by Mikheeva et al. [90] in 1962. However, the details mechanism of the NaH-NaOH solid solution is still not fully understood yet. Figure 2.5 shows thermal analysis of NaOH done by Bleif et al. [91] in 1982, which illustrates the specific heat of NaOH.

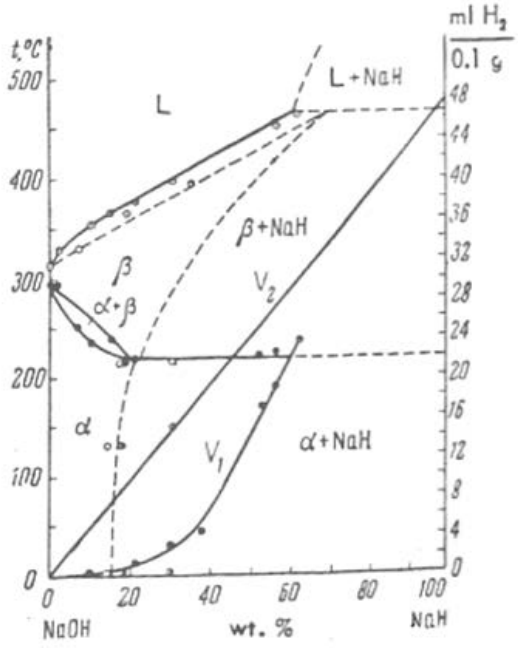

Figure 2.4. Fusion Diagram of NaH—NaOH system [90].

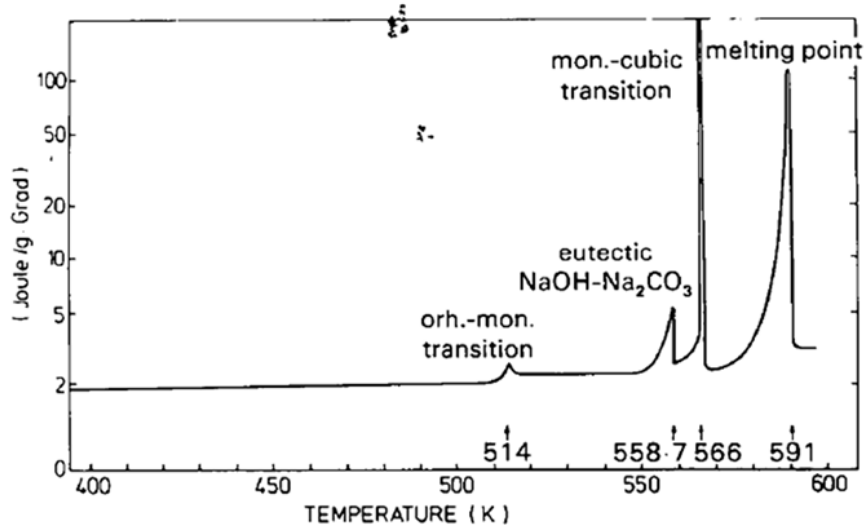

Figure 2.5. Temperature dependence of the specific heat of NaOH [91].

From Figure 2.5, we can clearly see that NaOH has several different phases at elevated temperatures. The NaOH space groups at different temperatures are shown in Table 2.2.

Table 2.2. NaOH phases at different temperatures.

Temperature (℃)	<240℃	240℃-292℃	292℃-318℃	>318℃
NaOH	Bmmb	P2_1/m	Fm3m	Melted

2.3.2. In Situ X-Ray Diffraction Analysis. In situ X-ray diffraction experiments of 40% NaH + 60% NaOH and 70% NaH + 30% NaOH in molar ratio were implemented to investigate the NaH/NaOH solubility in NaOH-rich conditions and NaH-rich conditions. The handling and processing of these two samples were in the argon gas-filled glovebox. All the samples were loaded on a rectangular stainless steel slide sealed with Kapton thin film on top in order to keep the sample isolated from air during the heating process.

The 40% NaH + 60% NaOH sample was heated to 240℃ first, and then the X-ray diffraction data were recorded during the cooling process in order to investigate the phase transition. The in situ XRD data are shown in Figure 2.6.

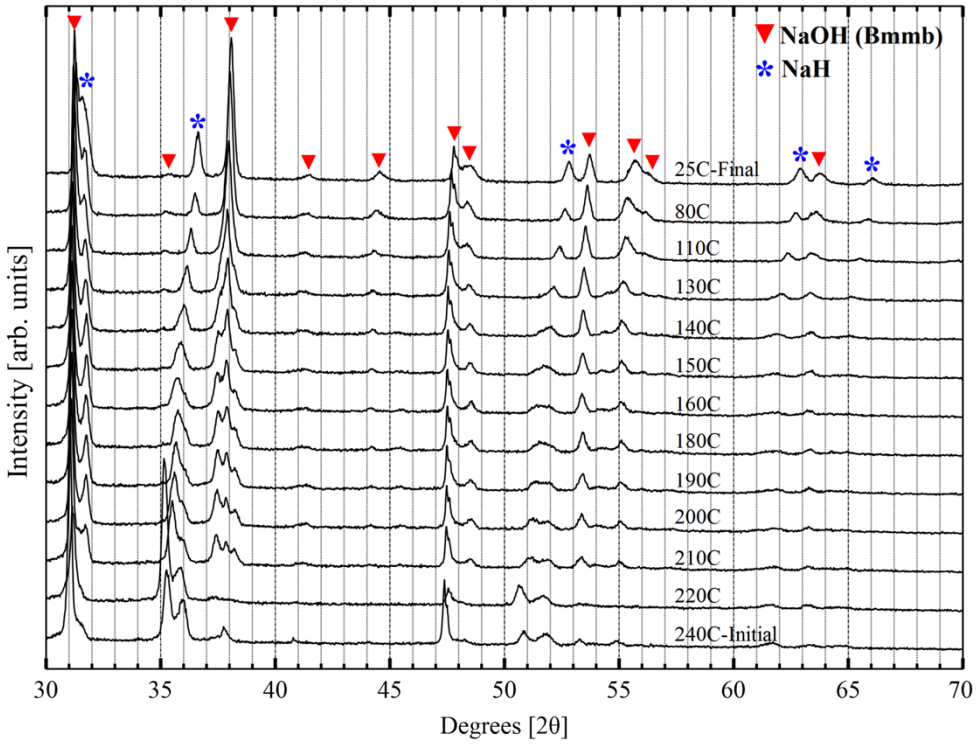

Figure 2.6. In-situ X-Ray Diffraction data of cooling process for 40% NaH + 60% NaOH. Vertical guidelines (dotted lines) are given to emphasize the peak shifts.

From Figure 2.6, we can see that XRD patterns in 210 °C down to 110 °C can be seen the peak changing process, especially for the “Tri-peaks” around 37°.There is a phase transition of NaOH from Bmmb phase to some unidentified phase which appears to be higher symmetry. There is clearly a complex phase transition during the cooling process from 210 °C down to 110 °C in this NaOH rich condition.

For 70% NaH + 30% NaOH mixture, the sample was heated from room temperature of 25°C to 240°C, and then cooled down back to 25 °C finally. The XRD dara were collected through the whole process at different temperature points. Figure 2.7 shows the XRD data in detail.

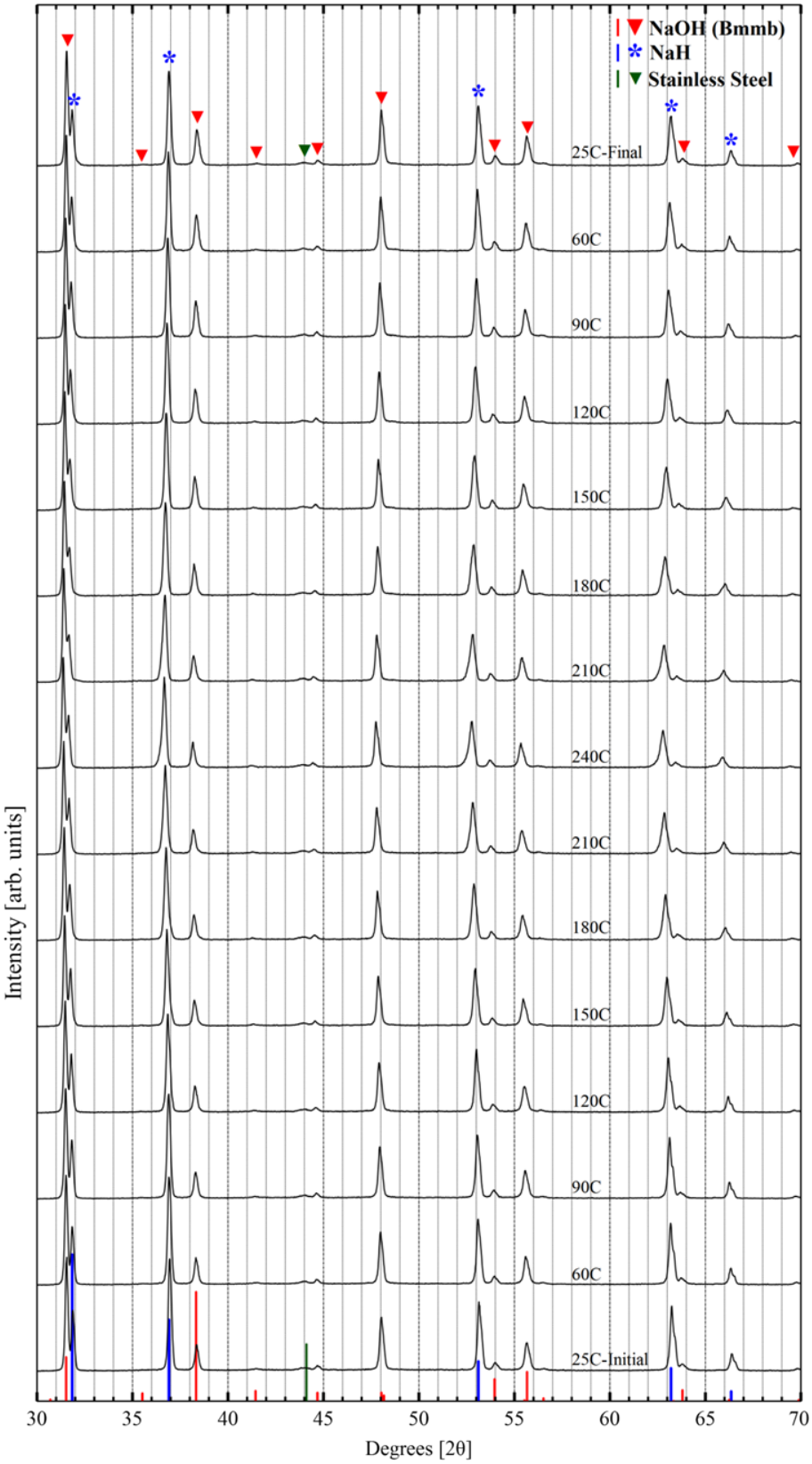

Figure 2.7. In-situ X-Ray Diffraction data of 70% NaH + 30% NaOH.

In this NaH rich sample, from the in-situ XRD pattern, there is a noticeable shoulder of NaH (2 2 0) peak around 53° at 240 °C, which indicates that there may exist multiple NaH phases of different lattice parameters. So that the phase transition is still complicated through all the heating and cooling process. But finally the intermediate phase separated back to NaH and NaOH single phase after cooled down back to room temperature. However, we cannot see the "Tri-peaks" as shown in the NaOH rich condition, so it is important to analyze the NaH lattice expansion process during the heating and cooling process. Figure 2.8 shows the NaH lattice parameters which were extracted from the in-situ XRD data by implementing full pattern Rietveld refinement using GSAS software [89].

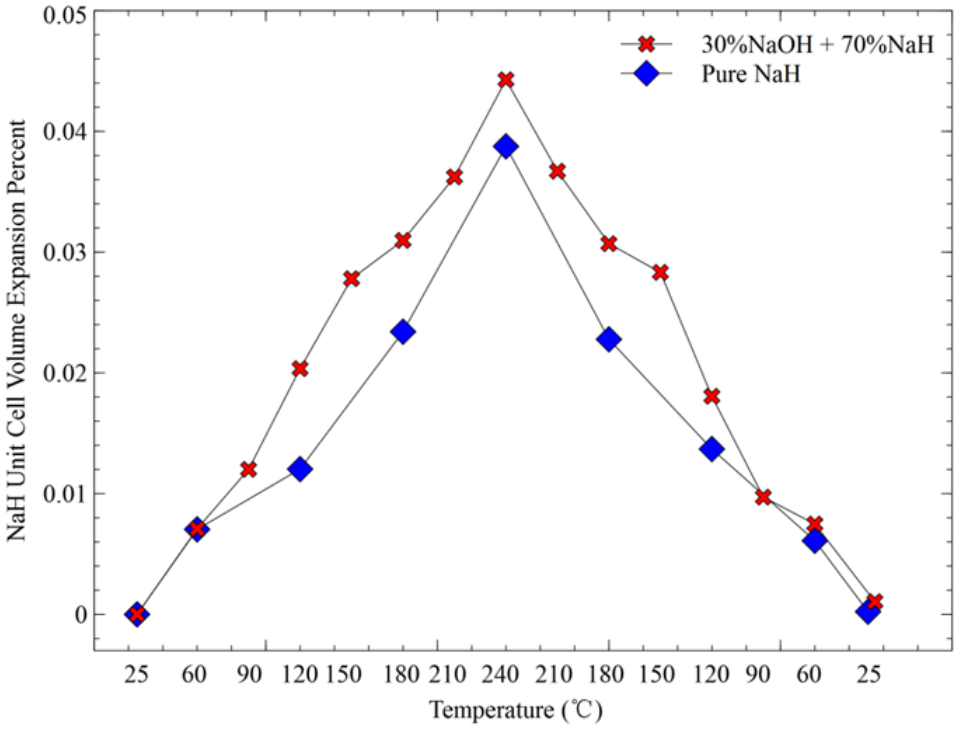

Figure 2.8. NaH unit cell volum expansion percent of pure NaH sample and 70% NaH + 30% NaOH sample. The NaH unit cell volume of 70% NaH + 30% NaOH sample expands more.

From the NaH unit cell lattice parameters expansion data, we can see that the the NaH in the NaH rich sample expanded more than that of the pure NaH sample. The coefficient of linear expansion for pure NaH and the NaH in 70% NaH + 30% NaOH

mixture sample were calculated as 59.33×10^{-6} /°C and it is in good agreement with that of the Kuznetsov's result: 60×10^{-6} /°C [92]. NaH in 70% NaH + 30% NaOH sample has a bigger lattice expansion, which may indicates the OH^- groups entered the NaH structure.

2.3.3. Differential Scanning Calorimetry Analysis. Differential Scanning Calorimetry (DSC) was performed on a TA Instruments Q2000 series analyzer. About 4 ~ 6 mg of sample was loaded in an aluminum hermatic pan with a sealed lid, and all handling and processing of materials were in an Argon filled glove box. The NaH/NaOH with different molar ratios of 100% NaOH, 15% NaH + 85% NaOH, 20% NaH + 80% NaOH, 25% NaH + 75% NaOH, 30% NaH + 70% NaOH, 35% NaH + 65% NaOH, and 40% NaH + 60% NaOH were investigated. The DSC scans for these samples were heated to 340 °C first, and then the DSC data were collected during the cooling processes for these samples. The DSC data for these samples are shown in Figure 2.9.

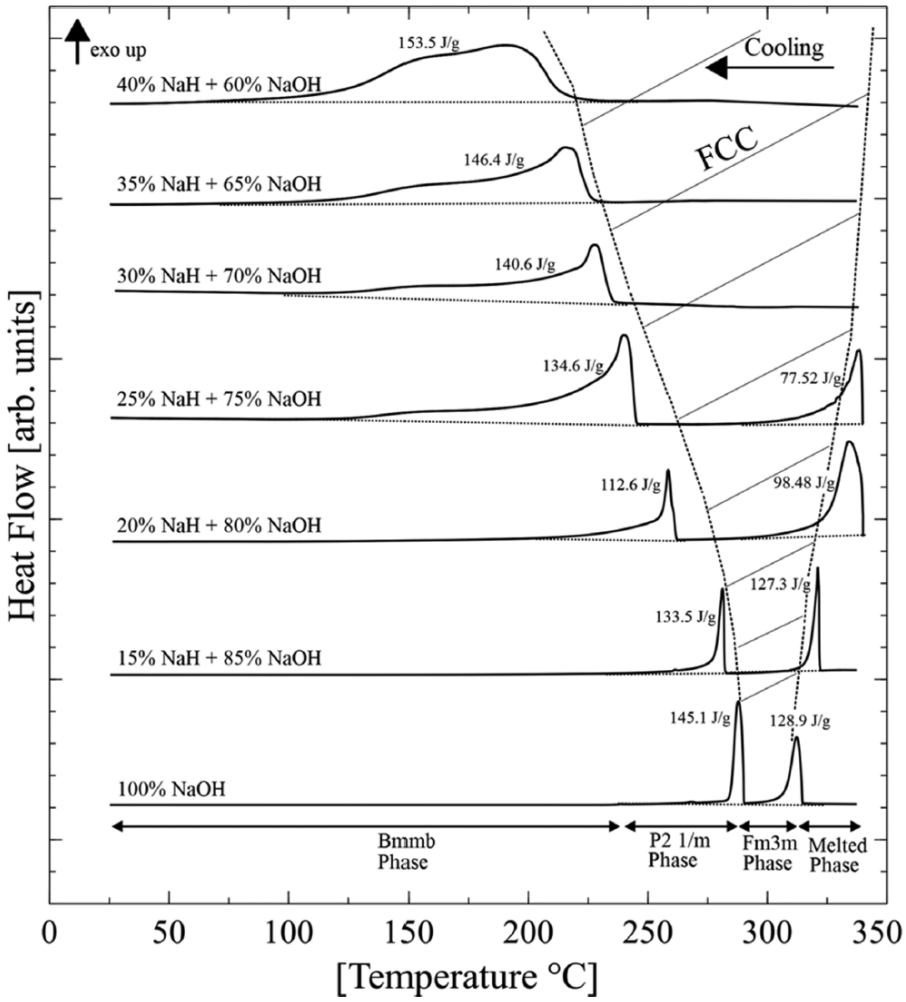

Figure 2.9. Differential Scanning Calorimetry (DSC) data of cooling scans. The dashed lines are guides for the eyes, serving as baselines.

With the increase of NaH ratio, the melting point of the mixture moves to higher temperature and goes beyond 340 °C from the 30% ratio of NaH and higher. The two phase transitions of NaOH moved to lower temperatures and merged together with the NaH/NaOH phase-separation process. For the 40% NaH + 60% NaOH composition, this process takes place over a wide temperature range from 240 °C to 60 °C.

In addition, the NaH rich condition was also investigated by DSC. 70% NaH and 30% NaOH sample was first heated from room temperature to 330 °C and then cooled down back to room temperature and then the heating and cooling process was cycled

from room temperature to 300 °C for more than two times. The 70% NaH and 30% NaOH sample DSC data are shown in Figure 2.10.

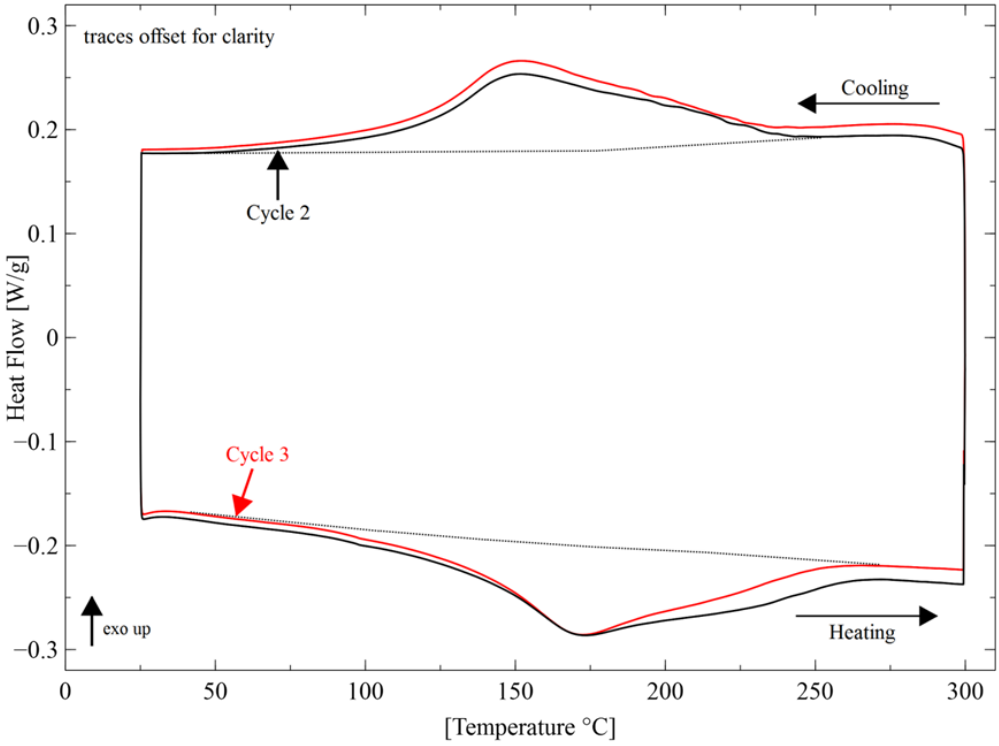

Figure 2.10. Differential Scanning Calorimetry (DSC) data of 70% NaH + 30% NaOH.

This is an interesting and reproducible process. Thermal activity both on heating and cooling appeared around 170 °C. The first cycle (not shown) was heated to 330 °C above NaOH melting point. The subsequent cycles below the melting temperature of NaOH show the reversible behavior. The dashed lines are the baselines. The two long phase transitions are shown both in heating and cooling processes, and it is highly reproducible, which indicates that the solid solution process of NaH/NaOH is a reversible one with complicated phase transitions.

2.4. FUTURE WORK

There are various metal hydrides and complex metal hydrides with great hydrogen storage potential. The future work should be focused on the materials that are

already researched and investigated extensively. The catalyst and doping impurity schemes should be a key direction to improve the hydrogen storage materials kinetic properties and cycling performances. Also, the same hydrogen storage materials treated under different physical or chemical environments should be investigated more than before because in real application the materials may be produced under different conditions.

2.5. CONCLUSIONS

The $NaAlH_4$ treated under different environments show changed reaction properties. Heat and pressure-treated $NaAlH_4$ in the S105 phase has been verified to melt and decompose into Na_3AlH_6 and hydrogen at a lower temperature than the as prepared bulk material, which indicate that the effect of pretreating $NaAlH_4$ with a high temperature and hydrogen pressure improves this material capability to store and release hydrogen at lower temperatures without catalysts.

The in-situ XRD and DSC investigations of the NaH/NaOH system indicates a solid solution mixture of H^- and $[OH]^-$ groups that occurs across the phase diagram. This reversible mixing appears to stabilize the NaOH Bmmb phase on the NaH-rich side of the psuedobinary NaH-NaOH phase diagram. The low temperature diffusion of species, as evidenced in the DSC data indicates that these solid solution phases may play a large role in the mass transport necessary for facile hydrogen absorption and desorption in complex hydrides such as sodium alanate ($NaAlH_4$).

3. HIGHLY ORDERED NANO POROUS CARBON

3.1. INTRODUCTION

Nano porous carbon (NPC) is a popular nano-sized material with high surface area, high pore volume, great adsorption properties and excellent intrinsic conductivity. Due to these advantages, nano porous carbon can be used in energy storage area for several applications including hydrogen storage, super capacitors and lithium-ion batteries [36, 44, 46-48]. In this section, I selected the FDU-15 type [55] nano porous carbon for research work. The synthesis method and characterization are included, also, the ball mill treatments and ball mill effects are investigated in this section. All detailed information records of fabricating different batches of nano porous carbon are shown in Appendix B.

3.2. SYNTHESIS METHODS

As discussed in Section 1, there are many ways to synthesize nano porous carbon with different characteristics. However, the FDU-15 type nano porous carbon is a commonly used one and the synthesis method is relatively easy and very reliable [55].

3.2.1. Regular Synthesis of FDU-15 Type Nanoporous Carbon. The FDU-15 type nano porous carbon with highly ordered hexagonal structure was prepared by using phenolic resins as carbon precursors and amphiphilic triblock copolymers as soft templates. The general synthesizing process was performed as follows: First, the phenolic resins were prepared using phenol and formaldehyde with NaOH as the catalyst and dissolved in ethanol after the removing the water by using vacuum pump; triblock copolymer pluronic F127 (Sigma-Aldrich) was then dissolved in ethanol and mixed with the above ethanol solution of phenolic resin, and the molar ratio of the chemicals is used as: phenol/formaldehyde/NaOH/F127 (1/2/0.1/0.012); the resulting mixture solution was then poured into petri dishes and dried after 24 hours evaporation of ethanol; the mixture was then dried under vacuum for another 24 hours; the mixture was baked at 200 ℃ in air for 2 hours, then the baked mixture was ground into fine powder with a coffee grinder; the ground polymer powder was calcinated in a programmable tubular furnace with flowing 2.5 % O_2/N_2 atmosphere at a flow rate of 105 cc/minute. The furnace was first heated to 350 ℃ with a rate of 1 ℃/min and kept at this temperature for 2 h to remove the triblock copolymer templates; finally it was heated to 800 ℃ with a rate of 1 ℃/minute and kept at this temperature for 1 hour to carbonize. The processing schemes with real experimental pictures are shown in Figure 3.1.

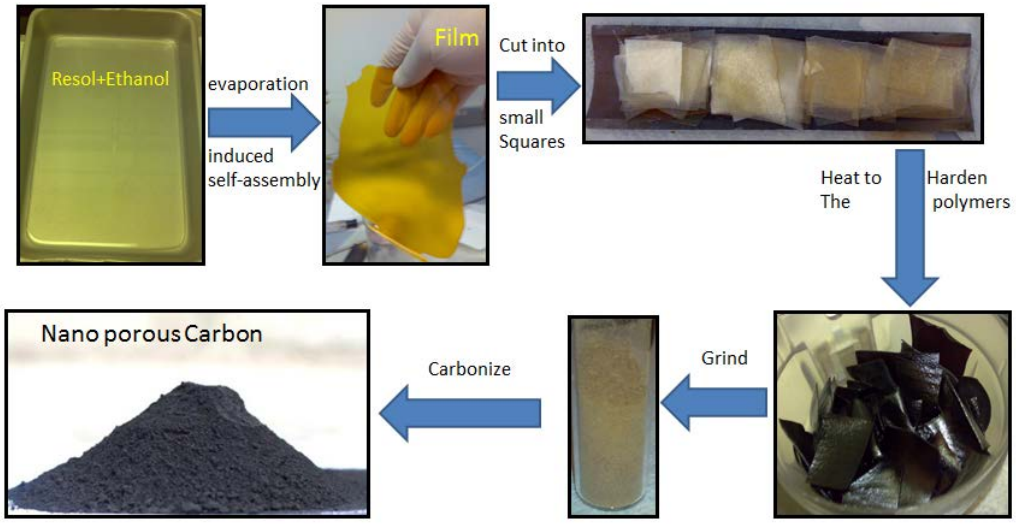

Figure 3.1. Regular FDU-15 type nano porous carbon synthesizing scheme.

3.2.2. Ball Mill Treatments. It is important to reduce the average particle size of the synthesized nano porous carbon in order to get the improved performance for different conditions. Generally, the particle size of nano porous carbon should be significantly reduced to avoid agglomerations and to improve the interfacial contact properties for lithium-ion batteries. In this section, ball mill treatments before and after the calcination of nano porous carbon were implemented. Before the final calcination process, the polymer powders were ball milled for 1, 2, 3, 4, and 5 minutes to get different final nano porous carbon particle sizes. As a comparison, another batch of nano porous carbon was ball milled for 5 minutes after the final calcination process. The ball mill treatments for polymer powders and nanoporous carbons were implemented via SPEX SamplePrep-8000M Mixer/Mill ball mill equipment.

3.3. CHARACTERIZATION OF NANOPOROUS CARBON

Usually, the Brunauer-Emmett-Teller (BET) method was used to characterize the specific surface areas (S_{BET}) using adsorption data in a relative pressure. The total pore volume of the nano porous carbon was estimated from the adsorbed amount at certain relative pressure based on the Barrett-Joyner-Halenda (BJH) calculation model. The nano porous carbon and the polymer powders morphologies were investigated with Scanning Electron Microscopy (SEM). The nano porous carbon inner channel structure was confirmed by Transmission Electron Microscopy (TEM).

3.3.1. BET/BJH Adsorption Analysis. Nitrogen adsorption isotherms were measured at 77 K by an SA3100 analyzer (Coulter). Before analysis, the sample of nanoporous carbon was outgassed for 1 hour at 300 °C under vacuum. The Brunauer-Emmett-Teller (BET) method was used to calculate the specific surface areas (SBET) using adsorption data in a relative pressure range of 0.05 - 0.2 bar. The total pore volume was estimated from the adsorbed amount at a relative pressure P/P_0 of 0.98 based on the Barrett-Joyner-Halenda (BJH) calculation model. Figure 3.2 shows the pore distribution plot with detailed pore size ranges of regular and un-ball milled FDU-15 type nano porous carbon.

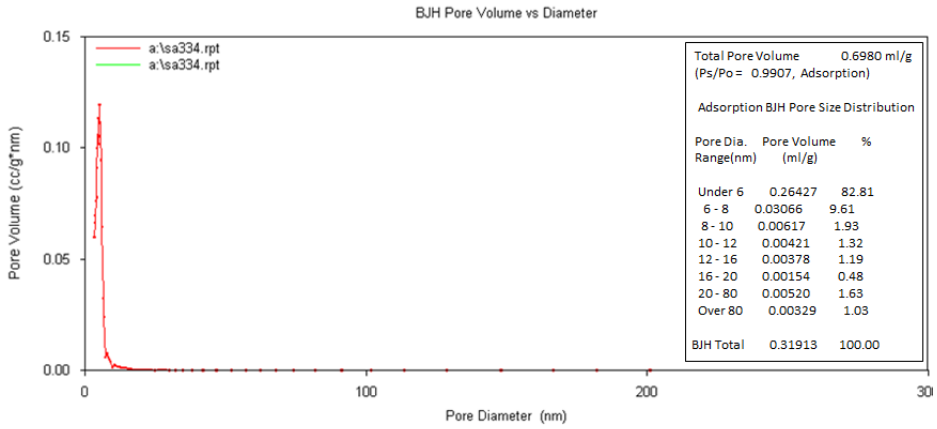

Figure 3.2. Pore distribution of regular and un-ball milled FDU-15 type nano porous carbon.

This regular FDU-15 type nano porous carbon has a high surface area of 992.63 m^2/g and a good pore volume of about 0.7 ml/g. From the detailed pore distribution statistical information in Figure 3.2, we can see that 94.35 % of the pores are under 10 nm, which means that most of the pores are very small and evenly under the 10 nm range. For most of the regular FDU-15 type nano porous carbon I had made, the surface area ranged from 900 ~ 1100 m^2/g, and the pore volume ranged from 0.65 ~ 0.7 ml/g.

It is also interesting to investigate the ball mill effect for the regular nano porous carbon, ball milled after/before calcination samples together. Figure 3.3 shows the BET/BJH results for these 3 samples.

BET Surface area: 1010.50 sq.m/g
Correlation Coefficient 0.99961
Total Pore Volume Report:
Total Pore Volume: 0.7094 ml/g
(Ps/Po = 0.9907, Adsorption)
Adsorption BJH Pore Size Distribution:

Pore Dia. Range (nm)	Pore Volume (ml/g)	%
Under 6	0.25530	79.65
6 - 8	0.04319	13.47
8 - 10	0.00505	1.58
10 - 12	0.00344	1.07
12 - 16	0.00348	1.09
16 - 20	0.00216	0.67
20 - 80	0.00538	1.68
Over 80	0.00254	0.79
BJH Total	0.32055	100.00

(a)

BET Surface area: 918.10 sq.m/g
Correlation Coefficient 0.99968
Total Pore Volume Report:
Total Pore Volume: 0.6747 ml/g
(Ps/Po = 0.9907, Adsorption)
Adsorption BJH Pore Size Distribution:

Pore Dia. Range (nm)	Pore Volume (ml/g)	%
Under 6	0.26016	78.87
6 - 8	0.04175	12.66
8 - 10	0.00597	1.81
10 - 12	0.00166	0.50
12 - 16	0.00241	0.73
16 - 20	0.00136	0.41
20 - 80	0.00859	2.60
Over 80	0.00796	2.41
BJH Total	0.32986	100.00

(b)

BET Surface area: 542.18 sq.m/g
Correlation Coefficient 0.99968
Total Pore Volume Report:
Total Pore Volume: 0.9226 ml/g
(Ps/Po = 0.9907, Adsorption)
Adsorption BJH Pore Size Distribution:

Pore Dia. Range (nm)	Pore Volume (ml/g)	%
Under 6	0.08197	11.16
6 - 8	0.01009	1.37
8 - 10	0.00278	0.38
10 - 12	0.00179	0.24
12 - 16	0.00193	0.26
16 - 20	0.00142	0.19
20 - 80	0.01557	2.12
Over 80	0.61876	84.26
BJH Total	0.73431	100.00

(c)

Figure 3.3. (a), regular un-ball milled NPC; (b), 5 minutes ball milled before final calcination; (c), 5 minutes ball milled after final calcination.

It is obvious that the un-ball milled carbon and the carbon of 5 minutes ball milled before, the BET surface area does not change much: meanwhile, both of the two samples' pore size distributions are good, about 80% of the pores are under 6 nm. So the inner structure of the cross-linked polymers does not collapse during the ball mill process. However, for the carbon of 5 minutes ball milled after, about 84% of the pores are over 80 nm, so this means the inner structure of the carbon collapsed during the ball mill process of the mesoporous carbon. So it is obvious that ball milling the polymer before final calcination can make the carbon to be smaller particles of the nano porous carbon.

3.3.2. TEM and SEM Analysis. The particle sizes of the ball milled polymers before final calcination were investigated by using Scanning Electron Microscope (SEM). The ball milled polymers before final calcination were labeled as BM0P (0 min ball milled), BM1P (1 min ball milled), BM2P (2 min ball milled), BM3P (3 min ball milled), BM4P (4 min ball milled) and BM5P (5 min ball milled). The SEM images combined with analysis via ImageJ software [93] of these polymer samples are shown in Figure 3.4.

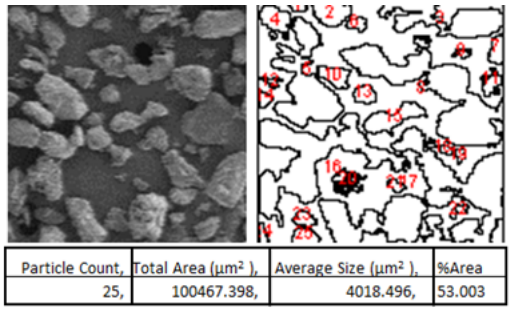

Particle Count,	Total Area (μm²),	Average Size (μm²),	%Area
25,	100467.398,	4018.496,	53.003

(a) 25X SEM of BM0P

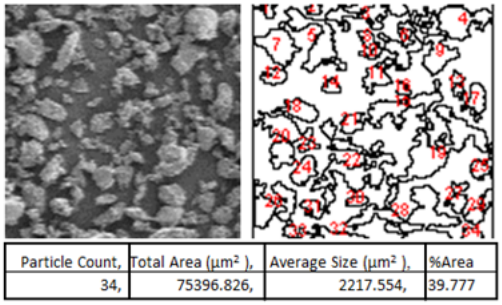

Particle Count,	Total Area (μm²),	Average Size (μm²),	%Area
34,	75396.826,	2217.554,	39.777

(b) 25X SEM of BM1P

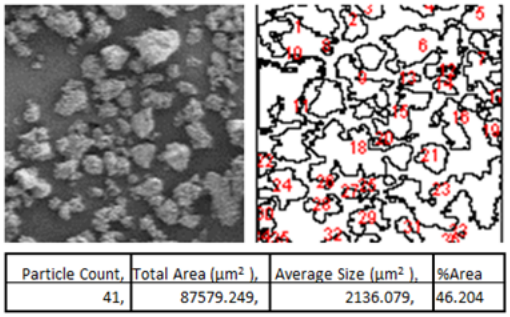

Particle Count,	Total Area (μm²),	Average Size (μm²),	%Area
41,	87579.249,	2136.079,	46.204

(c) 25X SEM of BM2P

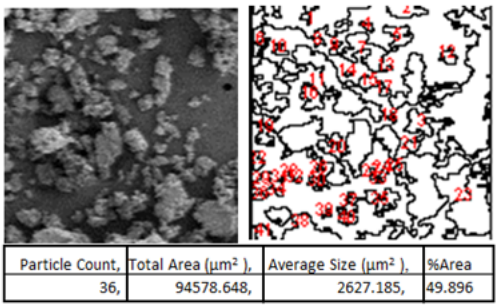

Particle Count,	Total Area (μm²),	Average Size (μm²),	%Area
36,	94578.648,	2627.185,	49.896

(d) 25X SEM of BM3P

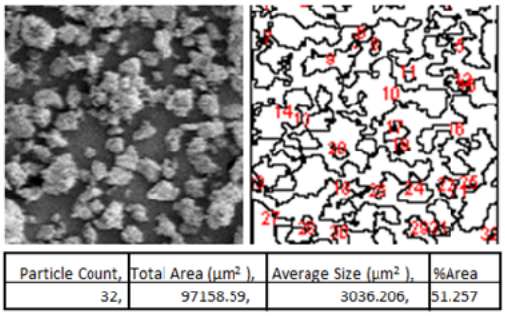

Particle Count,	Total Area (μm²),	Average Size (μm²),	%Area
32,	97158.59,	3036.206,	51.257

(e) 25X SEM of BM4P

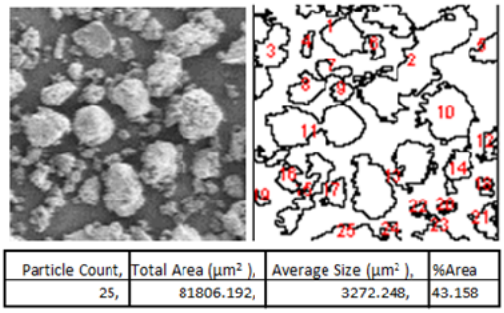

Particle Count,	Total Area (μm²),	Average Size (μm²),	%Area
25,	81806.192,	3272.248,	43.158

(f) 25X SEM of BM5P

Figure 3.4. (a), 25X SEM of BM0P processed using ImageJ; (b), 25X SEM of BM1P processed using ImageJ; (c), 25X SEM of BM2P processed using ImageJ; (d), 25X SEM of BM3P processed using ImageJ; (e), 25X SEM of BM4P processed using ImageJ; (f), 25X SEM of BM5P processed using ImageJ.

From Figure 3.4, it is easy to see that, with the increase of ball mill time from 0 to 5 minutes, the average particle size of polymers decreased first and then increased significantly from 3 minutes ball mill. I think the reason is that when you ball mill for a long time, at first, the particles will become smaller and smaller, then after the particles are reduced to a certain dimension, the balls in the ball mill machine will collide with the small particles and push the small particles together.

The un-ball milled and ball milled polymer powders before calcination: BM0P, BM1P, BM2P, BM3P, BM4P, and BM5P, were calcinated in a tubular furnace with flowing 2.5%O_2/N_2 atmosphere with flow rate of 105 cc/minute and heated to 350 ℃ with a rate of 1 ℃/min and kept at this temperature for 2 hours to remove the triblock copolymer templates. Finally they were heated to 800 ℃ with a rate of 1 ℃/min and kept at this temperature for 1 hour to carbonize. Then we got the final nano porous carbon with different particle sizes; these were labeled as BM0NPC, BM1NPC, BM2NPC, BM3NPC, BM4NPC, and BM5NPC. As a reference, a nano porous carbon sample made with the un-ball milled polymer powders was ball milled for 5 minutes and labeled as NPC-5BM for the pore structure analysis.

Figure 3.5 shows the scanning electron microscopy (SEM) images for nano porous carbon calcinated from the un-ball milled and ball milled polymer powders. It is clear that the nano porous carbon made with un-ball milled polymer powders

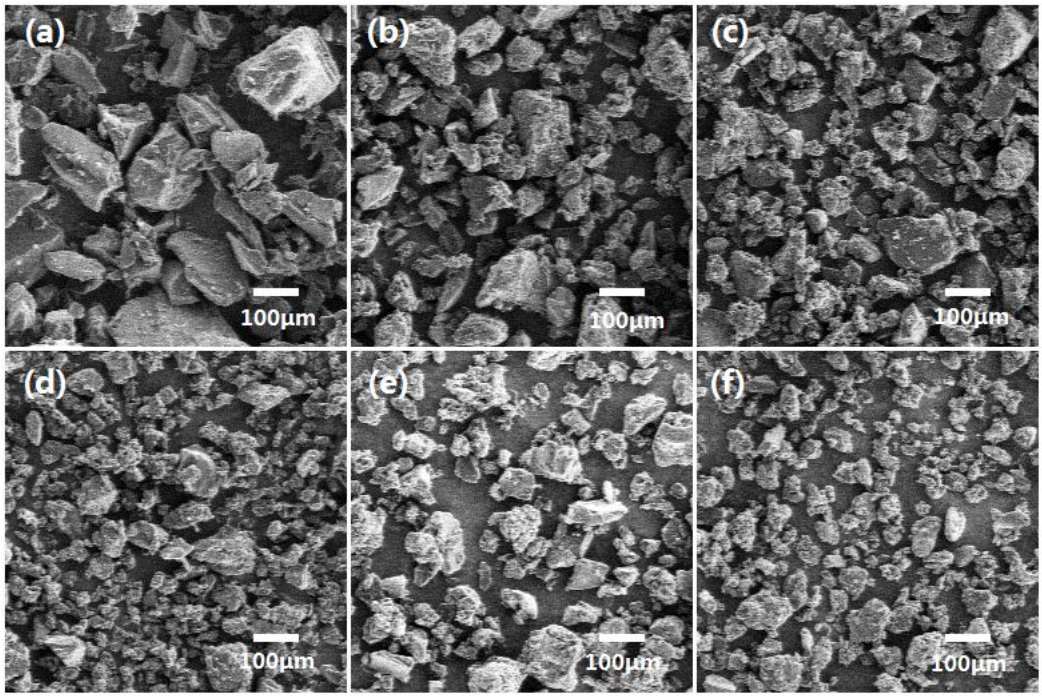

Figure 3.5. SEM images of nano porous carbon made with un-ball milled and ball milled polymer powders (a) without ball milling, (b) ball milled for 1 minute, (c) ball milled for 2 minutes, (d) ball milled for 3 minutes, (e) ball milled for 4 minutes, and (f) ball milled for 5 minutes.

has the biggest particle size with part of the particles apparently larger than 100 μm. With the increasing ball milling time from 1 minute to 5 minutes, the resulted nanoporous carbons' particle size decreased a lot, and the nanoporous carbon made with the 5 minutes ball milling of the polymer powders has the smallest particle size of about 15 - 25μm with homogeneous particle size distribution. Also, the nanoporous structures are not affected by the ball milling process of the polymer powders before calcination. The pore volume based on the Barrett-Joyner-Halenda (BJH) calculation and the specific surface area results based on the Brunauer-Emmett-Teller (BET) method are shown in Table 3.1 and Table 3.2 respectively.

Table 3.1. Pore volume measurements based on the Barrett-Joyner-Halenda (BJH) calculation model for nano porous carbon made with un-ball milled and ball milled polymer powders: (a) without ball milling, (b) ball milled for 1 minute, (c) ball milled for 2 minutes, (d) ball milled for 3 minutes, (e) ball milled for 4 minutes, and (f) ball milled for 5 minutes.

(a) Pore Dia. Range (nm)	Pore Volume (ml/g)	%
Under 6	0.19679	71.02
6 - 8	0.05404	19.50
8 - 10	0.01180	4.26
10 - 12	0.00532	1.92
12 - 16	0.00132	0.48
16 - 20	0.00138	0.50
20 - 80	0.00429	1.55
Over 80	0.00216	0.78
BJH Total	0.27710	100.00
90.52% pores under 8nm		

(b) Pore Dia. Range (nm)	Pore Volume (ml/g)	%
Under 6	0.17396	61.47
6 - 8	0.07061	24.95
8 - 10	0.02016	7.12
10 - 12	0.00820	2.90
12 - 16	0.00168	0.59
16 - 20	0.00115	0.40
20 - 80	0.00535	1.89
Over 80	0.00187	0.66
BJH Total	0.28298	100.00
86.42% pores under 8nm		

(c) Pore Dia. Range (nm)	Pore Volume (ml/g)	%
Under 6	0.16703	60.27
6 - 8	0.06747	24.35
8 - 10	0.01950	7.03
10 - 12	0.00612	2.21
12 - 16	0.00342	1.24
16 - 20	0.00125	0.45
20 - 80	0.00614	2.22
Over 80	0.00621	2.24
BJH Total	0.27715	100.00
84.62% pores under 8nm		

(d) Pore Dia. Range (nm)	Pore Volume (ml/g)	%
Under 6	0.17411	64.79
6 - 8	0.05669	21.09
8 - 10	0.01555	5.79
10 - 12	0.00543	2.02
12 - 16	0.00418	1.56
16 - 20	0.00093	0.35
20 - 80	0.00747	2.78
Over 80	0.00438	1.63
BJH Total	0.26874	100.00
85.88% pores under 8nm		

(e) Pore Dia. Range (nm)	Pore Volume (ml/g)	%
Under 6	0.19772	66.90
6 - 8	0.05686	19.24
8 - 10	0.01495	5.06
10 – 12	0.00621	2.10
12 - 16	0.00239	0.81
16 - 20	0.00206	0.70
20 - 80	0.00947	3.20
Over 80	0.00587	1.99
BJH Total	0.29553	100.00
86.14% pores under 8nm		

(f) Pore Dia. Range (nm)	Pore Volume (ml/g)	%
Under 6	0.18908	64.65
6 - 8	0.06001	20.52
8 - 10	0.01724	5.89
10 - 12	0.00609	2.08
12 - 16	0.00364	1.25
16 - 20	0.00233	0.80
20 - 80	0.00905	3.09
Over 80	0.00502	1.72
BJH Total	0.29245	100.00
85.17% pores under 8nm		

Table 3.2. Specific surface area measurements based on the Brunauer-Emmett-Teller (BET) method for nano porous carbon made with un-ball milled and ball milled polymer powders: (BM0NPC) without ball milling, (BM1NPC) ball milled for 1 minute, (BM2NPC) ball milled for 2 minutes, (BM3NPC) ball milled for 3 minutes, (BM4NPC) ball milled for 4 minutes, and (BM5NPC) ball milled for 5 minutes.

Nanoporous carbon samples	BM0NPC	BM1NPC	BM2NPC	BM3NPC	BM4NPC	BM5NPC
Specific BET surface area (m^2/g)	1010.50	812.69	787.37	894.57	1083.00	995.47

From Table 3.1 (a), the nanoporous carbon made with the un-ball milled polymer powders show a greatest ratio with 90.52 % of the pores in under 8 nm size range. For all other nanoporous carbon made with ball milled polymer powders, there are 84 % - 86 % of the pores are under 8nm size range. It is obvious that ball milling the polymer powders before calcination for carbon would not damage the nanoporous structure and most of the Nano-pores are under 10 nm, and the pore volume is ranged of about 0.27 - 0.29 cm^3/g. Table 3.2 shows the specific surface area results based on the Brunauer-Emmett-Teller (BET) method. Again, apparently, ball milling the polymer powders before calcination for carbon would not damage the nanoporous structure and the nanoporous carbons made by this method have high specific surface areas of about 800 - 1000 m^2/g.

However, the ball milling treatment would damage the nano-pore structure if the prepared nanoporous carbon is ball milled directly. A reference sample labeled as NPC-5BM made with the un-ball milled polymer powders was ball milled for 5 minutes was investigated for the pore structures. Table 3.3 shows the pore volume result that 84.26 % of the pores are over 80 nm, which indicated the nano-porous structure was damaged due to the ball milling treatment. And the specific surface area for this sample is 542.18 m^2/g, so this significantly reduced surface area agreed with the damaged nano-porous structure.

Table 3.3. Pore volume measurements based on the Barrett-Joyner-Halenda (BJH) calculation model for the nanoporous carbons made with un-ball milled polymer powders and then ball milled for 5 minutes.

Pore Dia. Range (nm)	Pore Volume (ml/g)	%
Under 6	0.08197	11.16
6 - 8	0.01009	1.37
8 - 10	0.00278	0.38
10 - 12	0.00179	0.24
12 - 16	0.00193	0.26
16 - 20	0.00142	0.19
20 - 80	0.01557	2.12
Over 80	0.61876	84.26
BJH Total	0.73431	100.00
84.26% pores over 80nm		

This work shows a good and easy ball milling method to reduce the nanoporous carbon particle size without damaging the nano-pore structure. For FDU-15 type nanoporous carbon, ball milling the polymer powders before calcination for carbon shows much better nano-pore structure property than those directly ball milled nanoporous carbons.

Also, the transmission electron microscopy (TEM) confirms the nano porous carbon's nano channel inner structure and TEM image for a regular FDU-15 type NPC is shown in Figure 3.6.

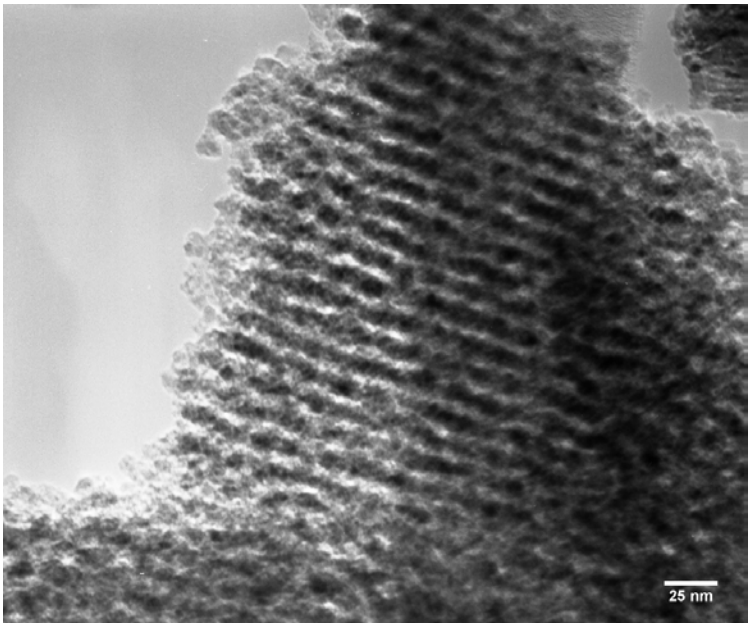

Figure 3.6. Transmission Electron Microscopy (TEM) of regular FDU-15 type NPC.

3.4. FUTURE WORK

There are plenty of possible points can be done to improve the nano porous carbon in order to get many other improved functions. In the processing technique, easy and reliable approaches should be focused in order to make the nano porous carbon available for scale-up production. Many factors such as chemical reaction restraints, gas flow/material contact, and calcination environments will affect the final quality and functions of the NPC, so a lot of work focused on those details should be done to optimize the NPC. Furthermore, modern characterization techniques should be developed to investigate the nano porous carbon at the atomic level especially in the synthesizing stages, and then the mechanism and principle of NPC in different morphologies will be well understood.

3.5. CONCLUSIONS

FDU-15 type nano porous carbon was used as an example and has been comprehensively investigated for ball mill effects on the pore structure, pore distribution and particle size for nanoporous carbon. We found an optimized process of ball milling the polymer powders just before calcination for final carbon products which resulted in nanoporous carbon with high pore volume, high surface area, and greatly reduced particle size ranged from 15 to 25 μm, which was confirmed by SEM and BET measurements.

.

4. TITANIUM DIOXIDE NANO-PARTICLES

4.1. INTRODUCTION

TiO_2 nano particles is a promising active material for lithium-ion batteries. In this section, two different types of TiO_2 nano particles are fabricated and investigated. The first type is the TiO_2 nano particles embedded into the nano porous carbon with mostly anatase phase and small amount of rutil phase, and more detailed work for electrochemical performance is shown in Paper IV. The second type is the anatase TiO_2 nano particles with controllable particle size synthesized by a new method based on the hydrolysis of Ti (IV) isopropoxide and post annealing. The second one shows great electrochemical properties and has potential for scale-up applications.

4.2. TITANIUM DIOXIDE EMBEDDED IN NANO POROUS CARBON

The TiO_2 nano crystals embedded in the nano porous carbon frames is based on the FDU-15 type NPC and fabricated by a modified method similar to the direct synthesis method with in-situ crystallization process [52, 82]. The titanium source used here is Ti (IV) isopropoxide and the final content of TiO_2 nano crystals is 65 wt. %.

4.2.1. Synthesis Process. 22.2g of Ti (IV) isopropoxide (Sigma-Aldrich) was dropped slowly in order to be mixed with 44.4 ml of deionized water, 55.5 ml ethanol (200 proof) and 30.5g HCl (Fisher A-144C-212 12mol/L concentration) with vigorous stiring until no precipitates can be seen. Then add 11g of 20 wt. % resol ethanolic solution synthesized using the method described in **3.2.1**. Separately, prepare 15g of F127 polymer dissolved into 150 ml of ethanol (200 proof) at 40℃. Then put the former two solution into this F127 ethanolic solution with vigorous stirring at room temperature for 1 hour until this mixture solution is red in color. Then the red solution is dried in air for at least 24 hours at room temperature and dried for another 24 hours in vacuum oven at 100℃. Then grind the dried materials by mortar and pestle and calcinate them in a tubular furnace under Argon flow at 600℃. Then theoretically, the final product will contain 65 wt. % TiO_2. The scheme of the processes is shown in Figure 4.1.

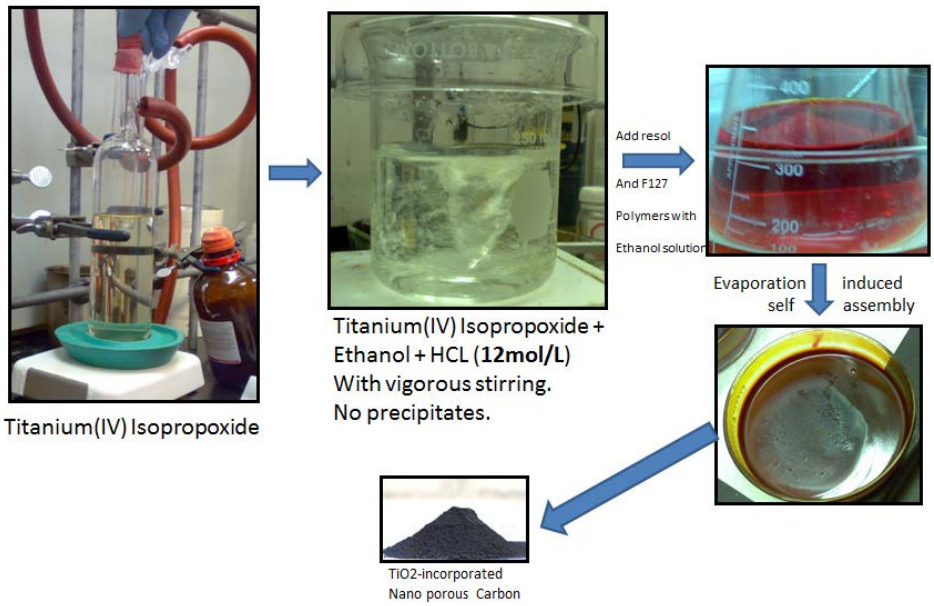

Figure 4.1. Process for synthesizing TiO_2 embedded into nano porous carbon.

4.2.2. X-Ray Diffraction Analysis. Powder X-ray diffraction was taken by Rigaku Ultima IV instrument. The 65 wt. % TiO_2 embedded into nano porous carbon XRD data with structure information is shown in Figure 4.2.

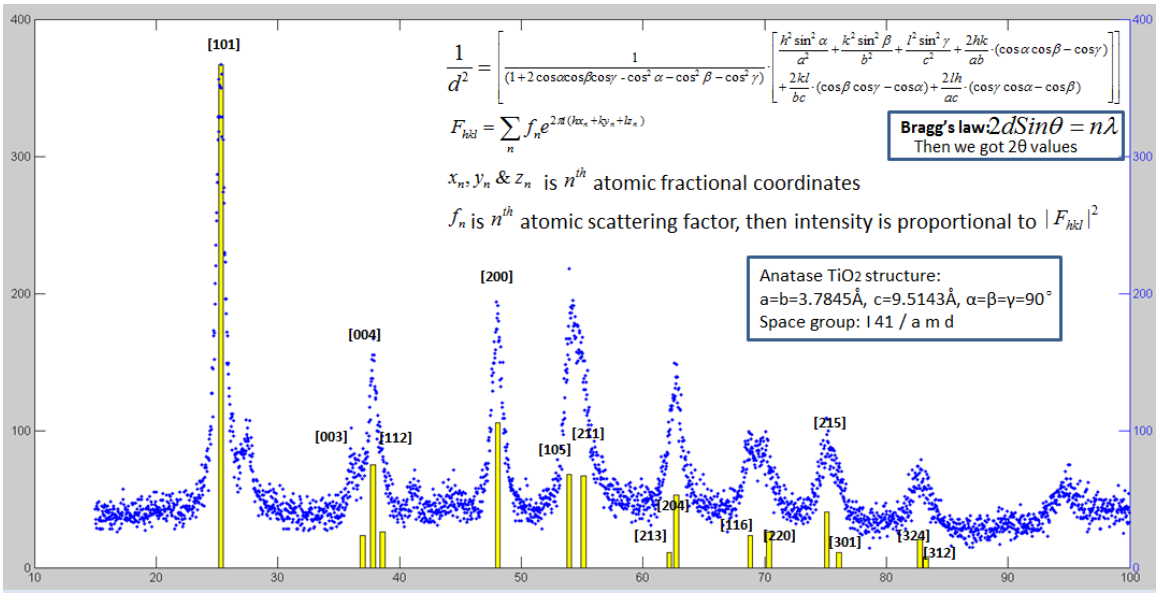

Figure 4.2. 65 wt. % TiO_2 embedded into nano porous carbon XRD data.

We can see clearly that most of the TiO_2 is in the anatase phase, shown with yellow color bars, in good agreement with the crystallization and phase transition temperatures of TiO_2. The anatase TiO_2 nano crystal particle size was calculated by using the Debye-Scherrer equation:

$$D = \frac{k\lambda}{\beta \cos\theta}$$

where D is the particle size in nm, λ is the Cu Kα radiation wavelength which is 0.15406nm, k is a constant set as 0.89, θ is the diffraction angle and β is the peak width at half maximum (FWHM) in radians. By using Fityk software [94], the XRD pattern can be fitted peak by peak using Pseudo-Voigt method. Part of this 65 wt. % TiO_2 embedded into nano porous carbon XRD data fitting with detailed calculated particle size information is shown in Figure 4.3. Calculated particle size of TiO_2 is around 7.1 ~ 8.7 nm. This is in the same order of magnitude with the BET test data.

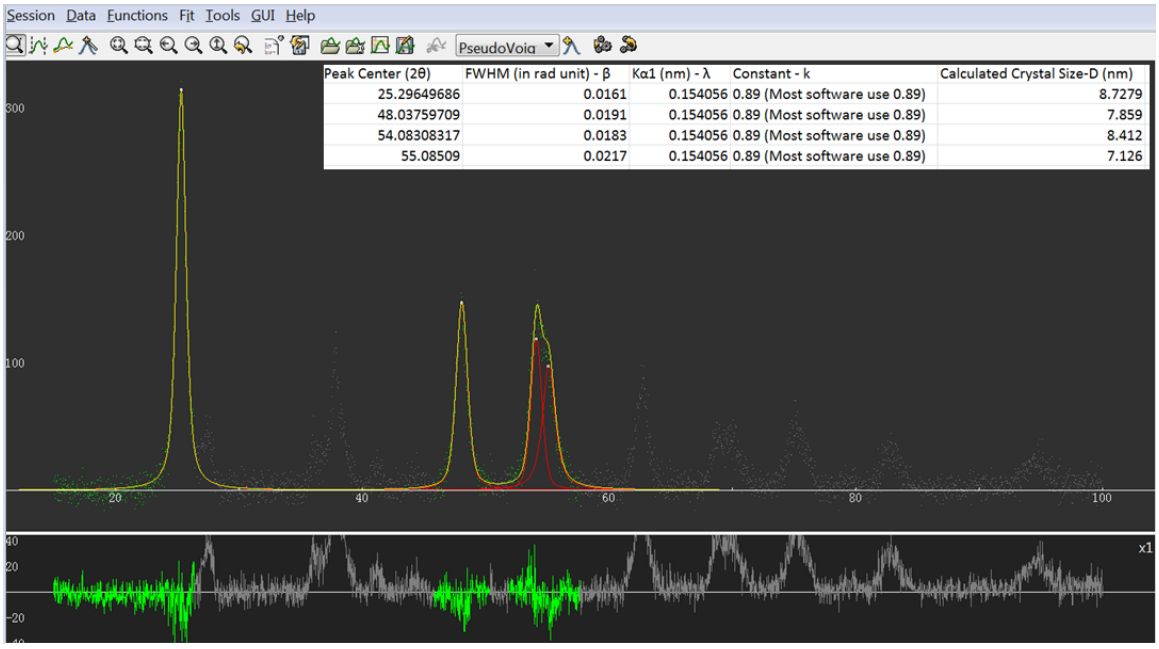

Figure 4.3. 65 wt. % TiO_2 embedded into nano porous carbon XRD data fitting based on Pseudo-Voigt method with detailed calculated particle size information.

4.2.3. SEM with EDS Analysis. Scanning electron microscopy (SEM) with energy dispersive spectroscopy (EDS) was impletemented by JEOL-6320F SEM with EDS spectroscopy instrument to investigate the 65 wt. % TiO_2 embedded into nano porous carbon sample. Figure 4.4 and Figure 4.5 show the SEM images of the sample at 25X magnification and 100X magnification respectively. Figure 4.6 shows the energy dispersive spectroscopy (EDS) element data, which confirmed the three elements of the sample: carbon, titanium, and oxygen.

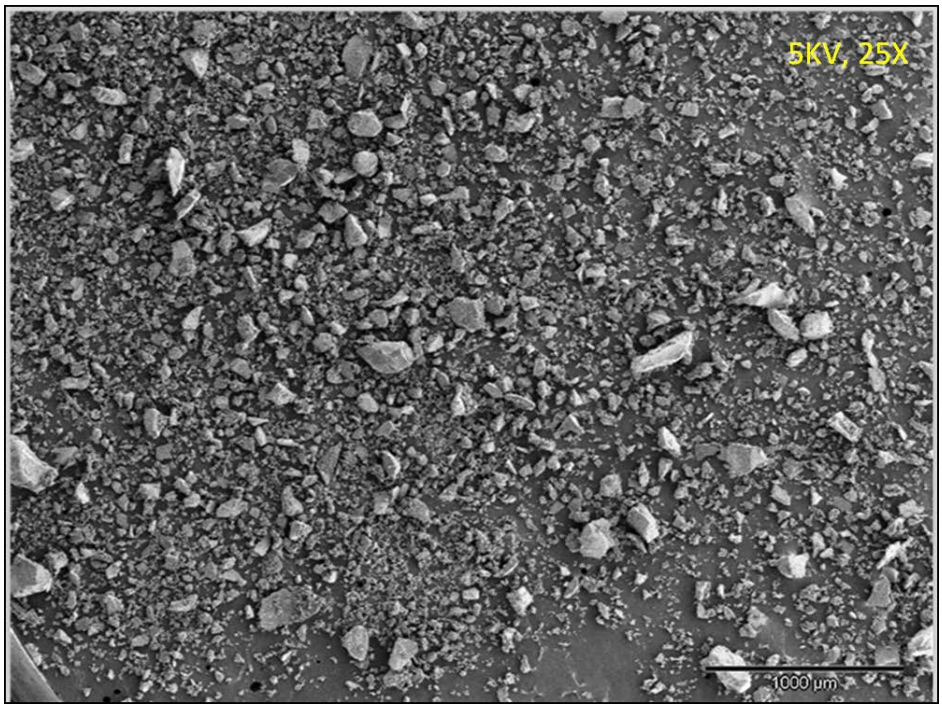

Figure 4.4. SEM image of 65 wt. % TiO_2 embedded into nano porous carbon with 25X magnification.

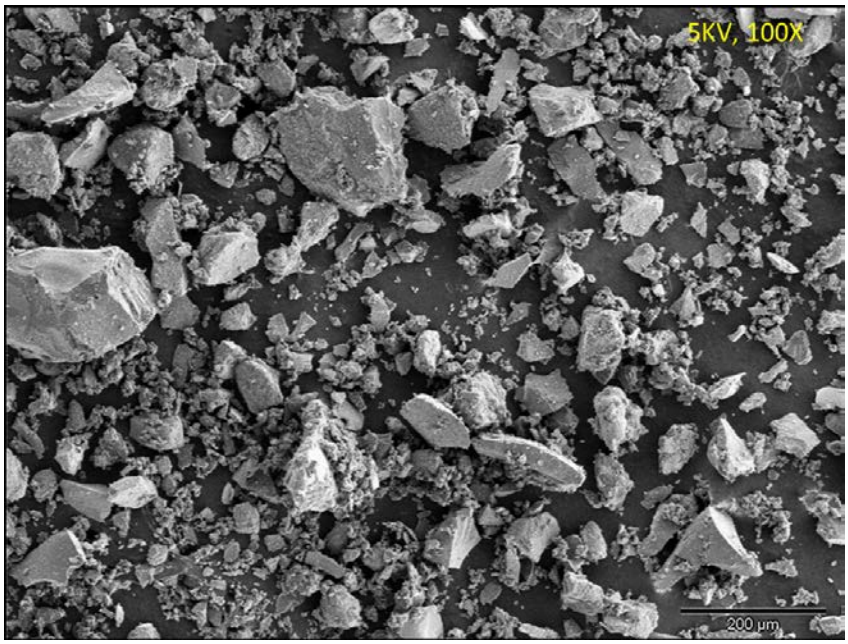

Figure 4.5. SEM image of 65 wt. % TiO_2 embedded into nano porous carbon, 100X magnification.

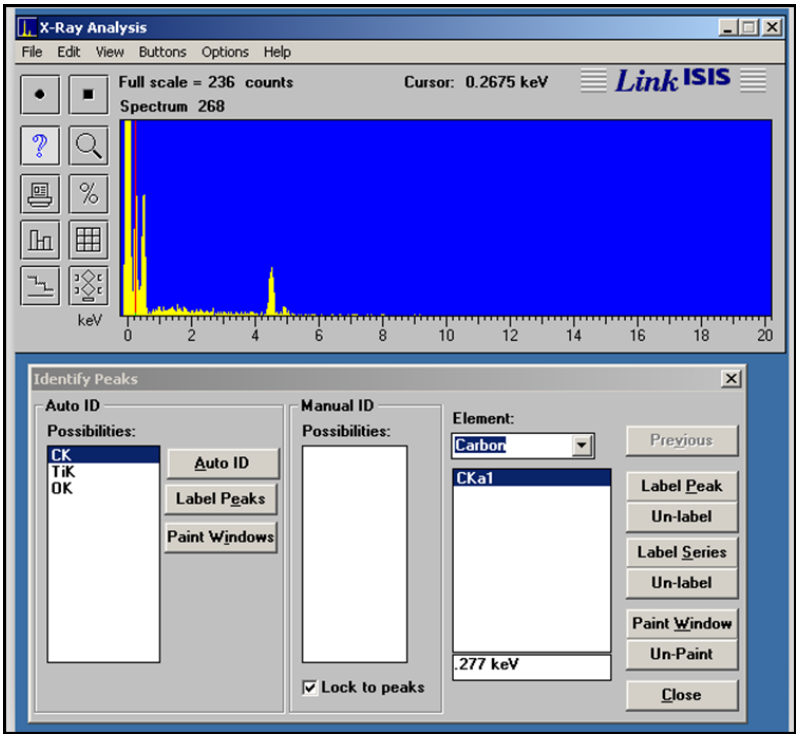

Figure 4.6. EDS spectrum (x-axis is in KeV) for 65 wt. % TiO_2 embedded into nano porous carbon.

In addition, the element ratio was investigated by using the energy dispersive spectroscopy (EDS) for selected areas in the SEM scanning range. Figure 4.7 shows the element atomic contents information from EDS spectroscopy for three different selected areas with two at 250X magnification and one at 1000X magnification.

Area1-250X:

Elmt	Spect. Type	Inten. Corrn.	Std Corrn.	Element %	Sigma %	Atomic %
C K	ED	1.020	1.46	9.28	0.23	39.49
O K	ED	0.346	0.77	14.06	0.42	44.89
Ti K	ED	0.917	1.00	14.65	0.16	15.62
Total				37.98		100.00

Area2-250X:

Elmt	Spect. Type	Inten. Corrn.	Std Corrn.	Element %	Sigma %	Atomic %
C K	ED	0.980	1.46	5.61	0.20	32.57
O K	ED	0.325	0.77	10.85	0.38	47.31
Ti K	ED	0.923	1.00	13.82	0.16	20.13
Total				30.27		100.00

Area3-1000X:

Elmt	Spect. Type	Inten. Corrn.	Std Corrn.	Element %	Sigma %	Atomic %
C K	ED	1.001	1.46	11.14	0.26	35.35
O K	ED	0.356	0.77	20.38	0.50	48.58
Ti K	ED	0.916	1.00	20.18	0.19	16.07
Total				51.71		100.00

Figure 4.7. Element contents information for 65 wt. % TiO_2 embedded into nano porous carbon from EDS spectroscopy for 3 selescted areas at 250X and 1000X magnification.

Assuming that one titanium atom combined with two oxygen atoms, and the calculation ignored the rest of the oxygen element, the calculated TiO_2 weight percent in the sample for these 3 selescted areas is as follows:

Area1-250X: TiO_2 wt. % = 72.50%

Area2-250X: TiO_2 wt. % = 80.42%

Area3-1000X: TiO_2 wt. % = 75.13%

Roughly the TiO_2 weight percent of this sample is 72% ~ 80%, while theoretically the TiO_2 wt.% should be 65%. One reason for this discrepancy is that it is difficult to control the loss of the carbon during the carbonization process. Also, the selected area may contain more excess element ratio that may affect the accuracy of real TiO_2 content. However, generally the result is good enough according the synthesis process with expected TiO_2 content range.

4.2.4. BET/BJH Analysis. BET/BJH measurements were taken by the Coulter SA-3100 equipment. Figure 4.8 shows the pore distribution with detailed information. From Figure 4.8, about 34% of the pores are under 20 nm. Also, the sample has a more than 200 m^2/g surafec area which maintained good adsorption property.

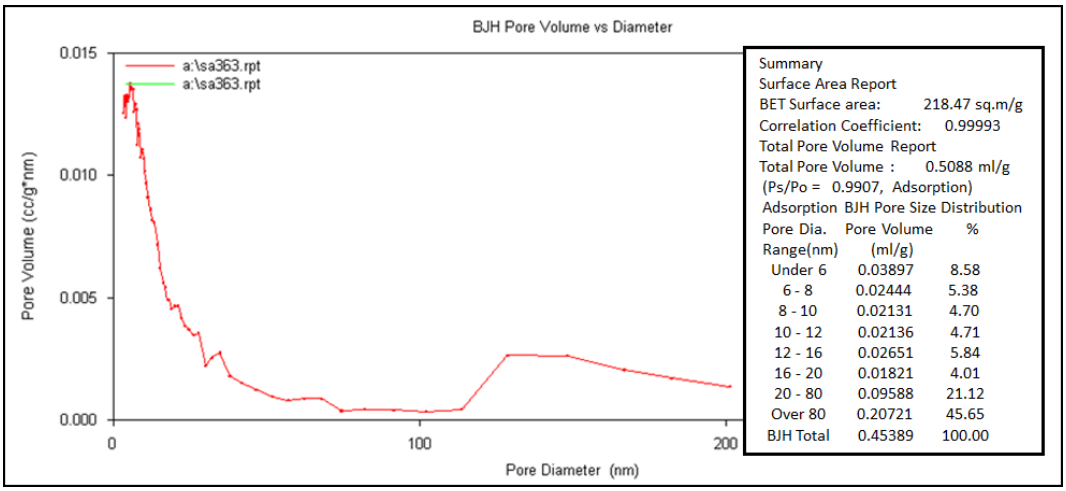

Figure 4.8. 65 wt. % TiO_2 embedded into nano porous carbon pore information.

4.3. TITANIUM DIOXIDE PARTICLES WITH CONTROLLABLE SIZES

The anatase TiO_2 nano particles with very controllable particle sizes were synthesized by a new method based on hydrolysis of Ti (IV) isopropoxide and post annealing treatments. The synthesis process, XRD for particle size analysis, TEM for morphology analysis, and electrochemical and galvanostatic intermittent titration technique (GITT) tests, are shown in this part.

4.3.1. TiO_2 Defects and Preparation Methods. Many properties of TiO_2 highly depend on the structural defects and dopants. Fundamental native defects such as titanium interstitial, oxygen interstitial, titanium vacancy and oxygen vacancy in anatase TiO_2: they have low formation energies and they can be formed inevitably [125]. Generally, the annealing process will reduce the TiO_2 crystal defects [123, 130] such as oxygen vacancies, which will result in donor states and change the conduction bands [124]. In real synthesizing process, it is very difficult to avoid heteroatoms or contaminations. Chlorine is a common contamination element during the TiO_2 synthesis, in the hydrolysis process: the chlorine can migrate to into the formed gel and replace the oxygen in the crystal cell of TiO_2 or exist in the crystal cell's interstitial sites [133]. Usually, the amorphous TiO_2 can absorb Cl^- anions much easier than that of anatase TiO_2 [127]. The chlorine will change local electronic structures, which may result in a change of bandgap [126, 133]. Therefore, the role of chlorine in TiO_2 crystal cells needs to be understood. In the sol-gel preparation process, the OH^- ions may also be absorbed onto the TiO_2 embryos [128] and on the surfaces by hydrogen bonds with nonequivalent surface hydroxyl groups [132]. Thus, those defects may play an important role to the electrochemical property of TiO_2.

Sol-gel method is commonly used to synthesize nano-scale TiO_2 particles. In sol-gel process, the solution will gradually transform to a gel-like system containing both both liquid and solid phases. The final product's size and shape will be dependent on temperature, precursor's concentration and pH level [84, 131, and 133]. In particular, the anatase TiO_2 particle size's uniformity is mainly governed by pH level [131]. My method is based on hydrolysis of titanium (IV) isopropoxide using hydrochloric acid as an inhibitor. In the sol-gel process, titanium alkoxides are polymerized and formed oxide network. Then the amorphous TiO_2 hydrous oxide will be formed and lead to TiO_2 precipitates. The hydrochloric acid will inhibit the agglomeration so that finally we will get the fine powders. Then the controllable crystal size is achieved by annealing in different temperatures.

4.3.2. Synthesis Process. Three different deionized water and hydrochloric acid solutions were prepared with different concentrations of H^+ for the hydrolysis process. First one: A 100 ml mixture of 50 ml 12 mol/L hydrochloric acid and 50ml deionized water. This solution has an H^+ concentration of 6 mol/L (pH = -0.78). Second one: A 200 ml mixture of 50 ml 12 mol/L hydrochloric acid and 150 ml deionized water. This solution has an H^+ concentration of 3 mol/L (pH = -0.48). Third one: A 250 ml mixture of 40 ml 12 mol/L hydrochloric acid and 210 ml deionized water. This solution has an H^+ concentration of 1.92 mol/L (pH = -0.28). The deionized water and hydrochloric acid solution was mixed well with vigorous stirring for 5 minutes with a stir bar. The precursor solution was a mixture of 15 ml ethanol (Decon: ethanol 200 proof) and 5 ml titanium (IV) isopropoxide (Sigma-Aldrich: ≥97.0%). The precursor mixture solution was slowly poured into the deionized water and hydrochloric acid solution followed by vigorous stirring at room temperature for 2 hours. Then the transparent liquid mixture was poured into petri dishes and evaporated the mixture at room temperature in air for 6 days. The white-yellow precipitates were washed with ethanol 3 times and then dried in air for 2 hours until the ethanol was evaporated. The precipitates were then dried in a vacuum oven at 100 ℃ for 4 hours and ground into fine powders using an agate mortar and pestle. Finally, I annealed the as-prepared powders in a tubular furnace (Lindberg tube furnace Model-54233) in air under elevated temperatures from 150 ℃ to 750 ℃ for 2 hours to obtain the desired particle sizes. The general scheme of the process is shown in Figure 4.9.

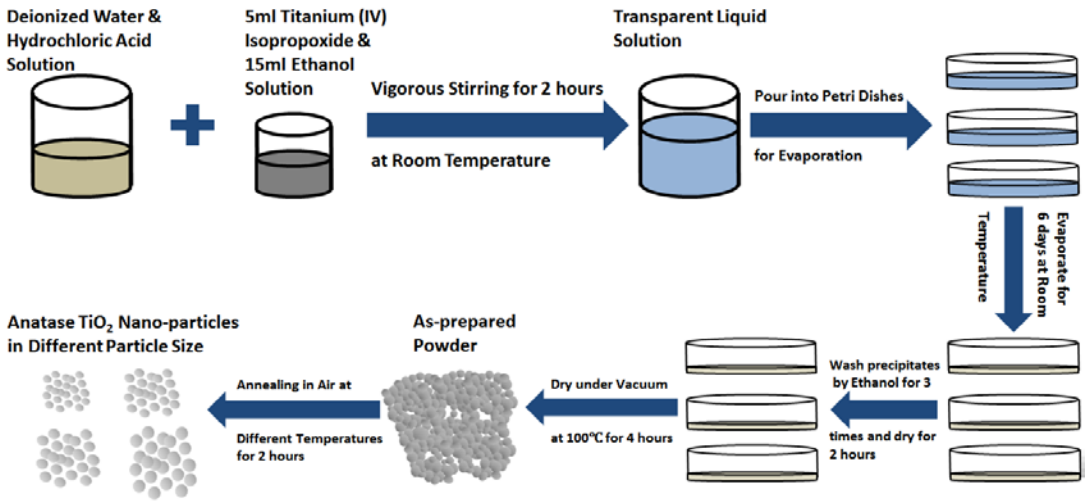

Figure 4.9. Synthesis of different sized anatase TiO_2 nano particles.

4.3.3. X-Ray Diffraction Analysis. The XRD spectra were taken for these TiO_2 nano particles prepared under 6 mol/L, 3 mol/L and 1.92 mol/L H^+ concentration environments. The average crystal size of the TiO_2 nano particles was calculated from the measured peak widths and the Debye-Scherrer equation [95] via the (101) peak for anatase TiO_2 and (110) peak for rutile TiO_2. XRD data peaks were fitted using the Fityk software package [94]. Figure 4.10 shows the shows the XRD patterns for the TiO_2 nano particles prepared under H^+ concentration of 6 mol/L (pH = -0.78) environment and annealed at elevated temperatures from 150 ℃ to 650 ℃. It is clear that annealing from 150 ℃ the TiO_2 has the anatase phase until the annealing temperature of 650 ℃. The broadened peaks become narrower with the increase of the annealing temperature. For TiO_2 nano particles prepared under an H^+ concentration of 6 mol/L, the particle size varies for different batches of samples. The details are shown in Table 4.1 and the particle size distribution varies by several nm for each temperature anneal under this synthesizing pH environment.

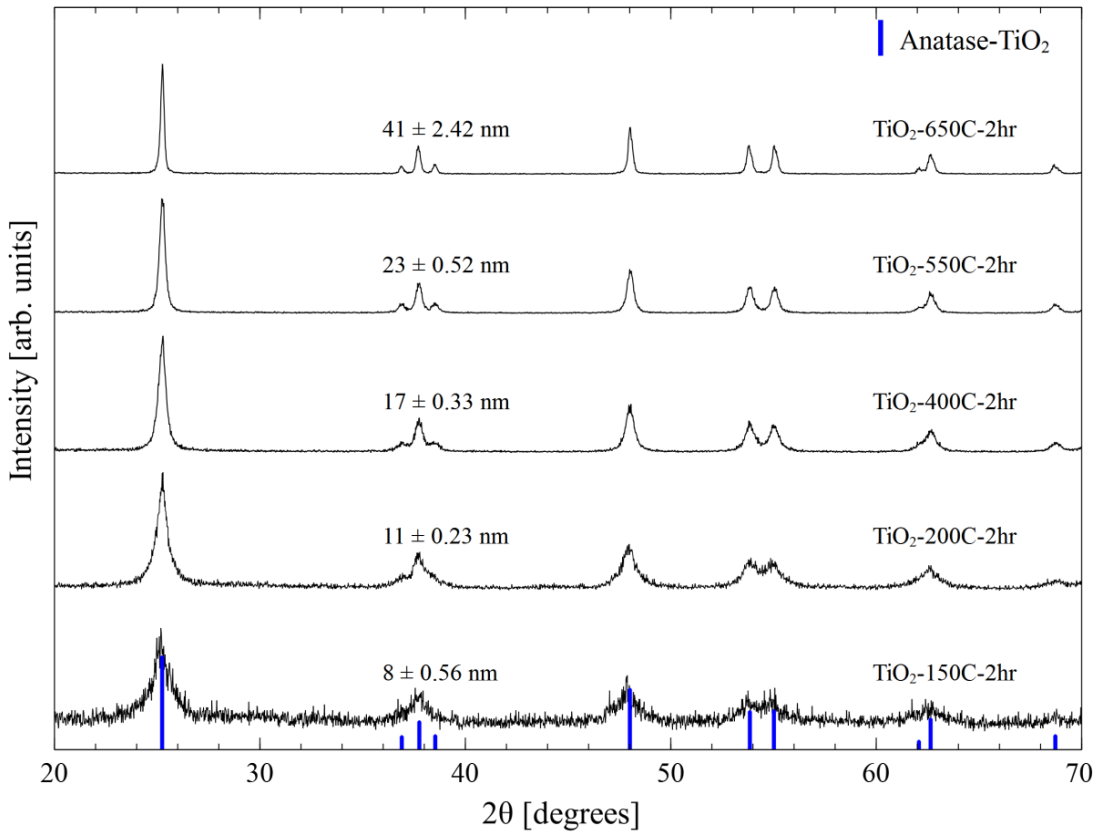

Figure 4.10. XRD patterns of TiO_2 nano particles prepared under H^+ concentration of 6 mol/L (pH = -0.78) environment and annealed at elevated temperatures from 150 ℃ to 650 ℃.

Table 4.1. Calculated particle size variation range of 3 different batches of TiO_2 nano particles prepared under H^+ concentration of 6 mol/L (pH= -0.78) environment and annealed at elevated temperatures from 150 ℃ to 650 ℃.

Annealing T(℃)	150	200	400	550	650
Average particle size (nm)	7.6~11.0	10.8~12.3	16.8~18.6	23.1~26.5	37.2~42.2

Figure 4.11 shows the XRD patterns for the TiO_2 nano particles prepared under H^+ concentration of 3 mol/L and annealed at temperatures from 250 ℃ to 750 ℃. In this experiment, the TiO_2 cannot be fully crystallized at temperatures below 225 ℃. It is clear that annealing temperatures from 250 ℃ to 650 ℃ produce anatase TiO_2. At 650 ℃ there

is a very small rutile peak that appears at about 27.3 degrees. The weight percent of rutile TiO_2 is roughly estimated from equation 1 as follows [85, 96]:

$$W_R = \frac{A_R}{0.884\,A_A + A_R} \tag{1}$$

where W_R is the rutile weight percent, A_A and A_R are integrated peak intensities for anatase (1 0 1) and rutile (1 1 0) from the XRD patterns. There is only about 1 wt.% of rutile phase when annealing at 650 ℃, and 17 wt.% when annealing at 750 ℃. For the TiO_2 nano particles prepared under an H^+ concentration of 3 mol/L the particle size distribution is highly repeatable and has very small particle size distribution (details are shown in Figure 4.11).

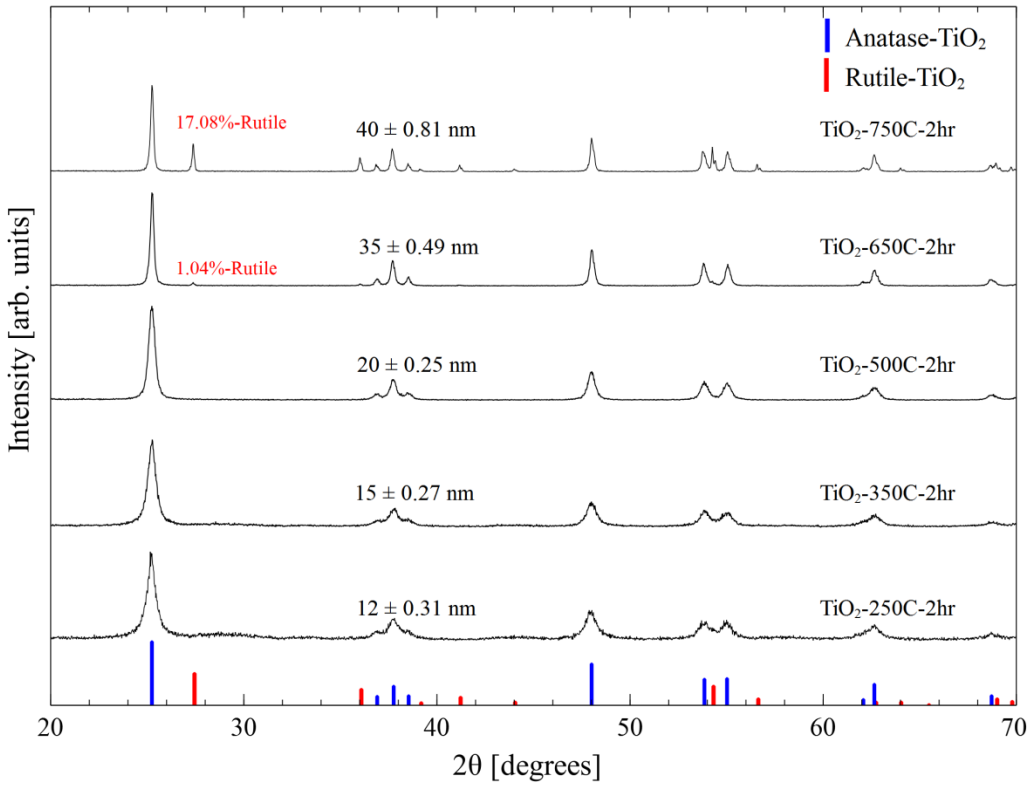

Figure 4.11. XRD patterns of TiO_2 nano particles prepared under H^+ concentration of 3 mol/L (pH = -0.48) environment and annealed at elevated temperatures from 250 ℃ to 750 ℃.

Figure 4.12 shows the XRD patterns for the nano particles prepared under an H^+ concentration of 1.92 mol/L and annealed at temperatures from 175 ℃ to 675 ℃. Interestingly, 660 ℃ is the critical temperature of the anatase to rutile phase transition for the TiO_2 nano particles prepared under an H^+ concentration of 1.92 mol/L (see Figure 4.13). In contrast, the anatase TiO_2 prepared via hydrolysis of titanium isopropoxide using a nitric acid inhibitor has the anatase to rutile phase transition temperature below 600 ℃ [84], and hydrolysis of titanium isopropoxide using triethylene glycol (TEG) has the anatase to rutile transition temperature between 700 ℃~800 ℃ [86].

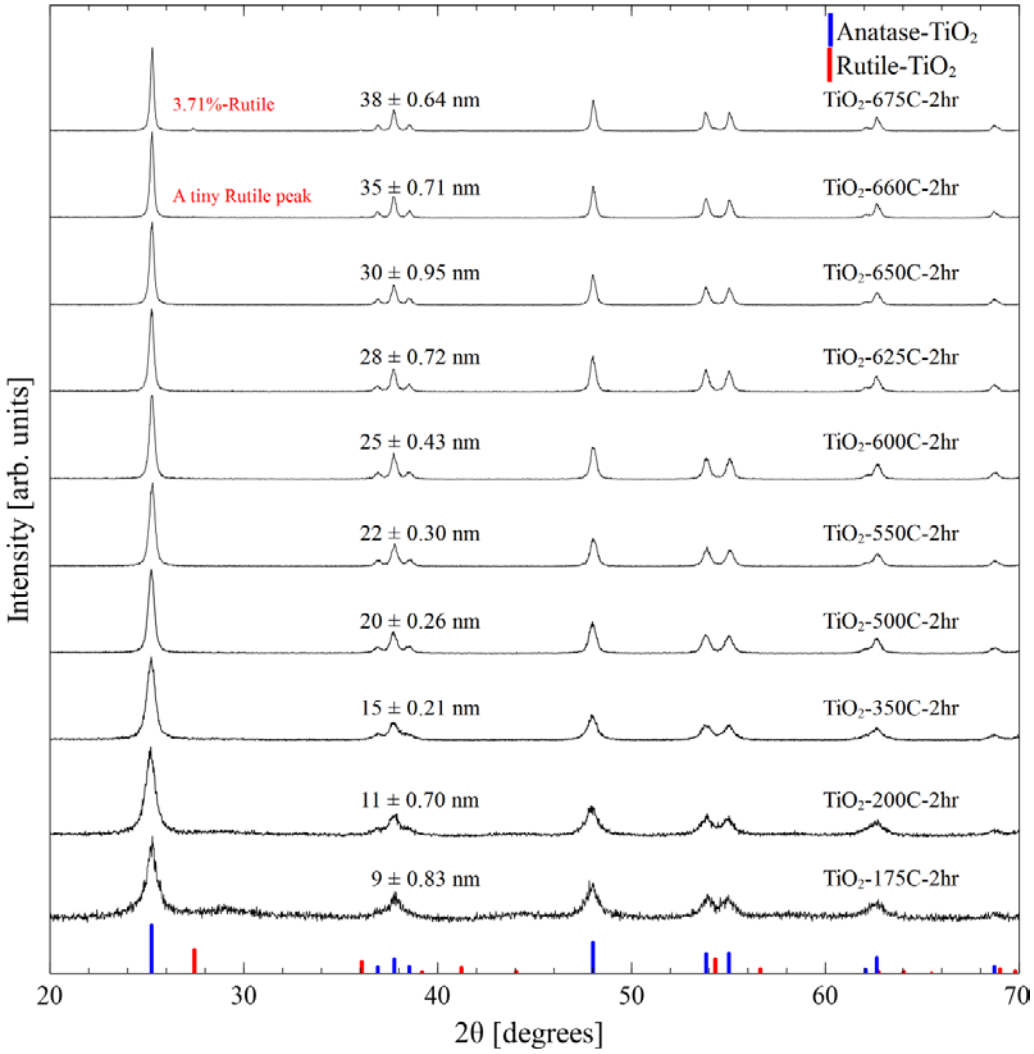

Figure 4.12. XRD patterns of TiO_2 nano particles prepared under H^+ concentration of 1.92 mol/L (pH = -0.28) environment and annealed at elevated temperatures from 175 ℃ to 675 ℃.

For the TiO_2 nano particles prepared under 3 mol/L H^+ concentration (pH = -0.48), there is already about 1wt.% of rutile phase at 650 ℃. Then evidently the pH environment has affected the phase transition temperature slightly. This may be due to nucleation events of the rutile phase in the nano particles being isolated from other nanoparticles and shifting the apparent transition temperature higher. Also the H^+ as 1.92 mol/L (pH = -0.28) samples resulted in a wider range of nano-particles size distribution of 9 ~ 38 nm with majority anatase TiO_2 phase (anatase weight percent is >95% in all cases).

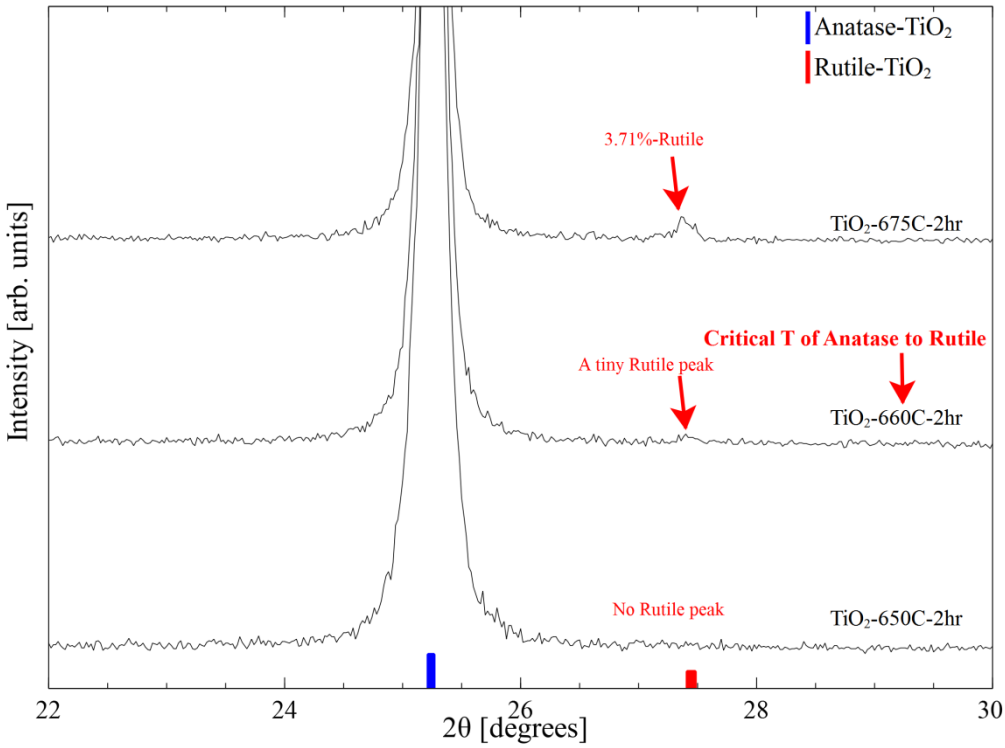

Figure 4.13. Detailed XRD spectra patterns of TiO_2 nano particles prepared under an H^+ concentration of 1.92 mol/L (pH = -0.28) and annealed at elevated temperatures from 650 ℃ to 675 ℃.

4.3.4. TEM Analysis. The particle morphology and size were investigated using a Philips EM430-ST transmission electron microscopy (TEM). Figure 4.14 shows the transmission electron microscopy (TEM) images of prepared TiO_2 crystallized nano particles in 3 different particle sizes of 15 nm, 25 nm, and 40 nm, and indicates a uniform size distribution.

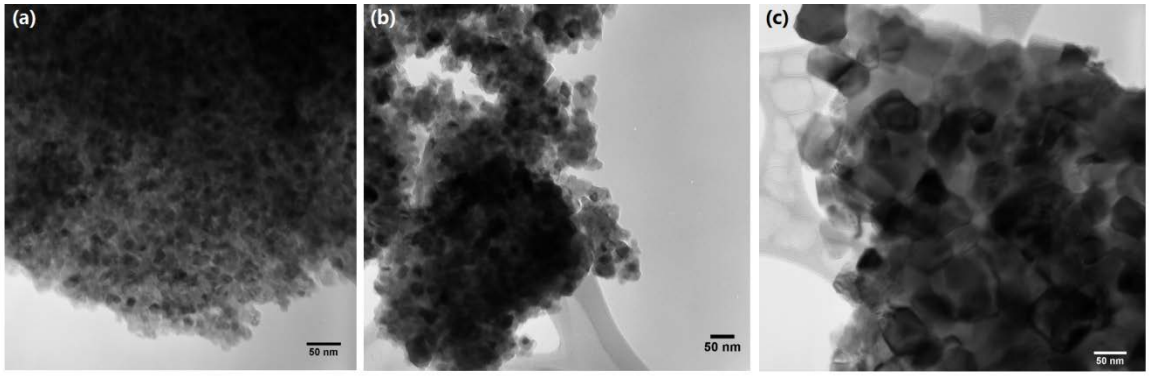

Figure 4.14. TEM images of (a) 15 nm anatase TiO_2 particles, (b) 25 nm anatase TiO_2 particles, and (c) 40 nm anatase TiO_2 particles. They are well dispersed and they have homogenous particle size distribution, which are in good agreement with XRD results.

4.3.5. Electrochemical Measurements and Analysis. The TiO_2 nano particle electrochemical properties were evaluated using lithium metal as the counter/reference electrode in a CR2032 coin cell. All handling and processing of materials was performed in an argon filled glove box with oxygen and water concentrations below 1 ppm. The TiO_2 nano particle powders were well mixed with carbon black (Vulcan-XC72R) and polyvinylidene fluoride (PVDF-301F) by mortar and pestle in a weight ratio of TiO_2-Carbon-PVDF = 8-1-1. The carbon black was dried under vacuum at 250 ℃ for 12 hours and the PVDF was dried under vacuum at 110℃ for 20 hours before the experiments. After the TiO_2, carbon black and PVDF were well mixed we added N-Methyl-2-pyrrolidone (NMP) drops and homogenized the slurry using a ratio of 0.8 ml NMP per 100 mg powder mixture. The electrodes were prepared by coating the slurry on a 0.1 mm thick copper foil. The electrodes were baked on a hotplate at 70 ℃ for 15 minutes, the temperature increased to 120 ℃ and baked for an additional 18 hours. When constructing the CR2032 positive cap, 2 drops of electrolyte (1 M solution of $LiPF_6$ in a solution of 1: 1 by weight DEC: EC) were added to make the electrode well saturated. Two layers of Celgard Li-ion Battery separator film, 25 μm for single layer, were added with another 4 drops of electrolyte. The coin cell was sealed with a hydraulic crimping machine (MTI: MSK-110) under a pressure of 50 kg/cm^2. The assembled coin cells rested for at least 3 hours prior to testing using a Maccor model-4300 constant current instrument. The different C-rate currents were estimated based on the TiO_2 theoretical capacity of 330 mAh/g [77, 97-99].

There are ten samples in different anatase phase particle sizes of 9, 11, 15, 20, 22, 25, 28, 30, 35, and 38 nm were investigated. The electrochemical properties under different C-rate currents are continuously tested as: C/3 for 25 cycles, 1C for 5 cycles, 5C for 5 cycles, 10C for 5 cycles, 20C for 5 cycles and finally C/3 for 5 cycles. Figure 4.15 shows the electrochemical properties under different C-rate currents for the 10 samples.

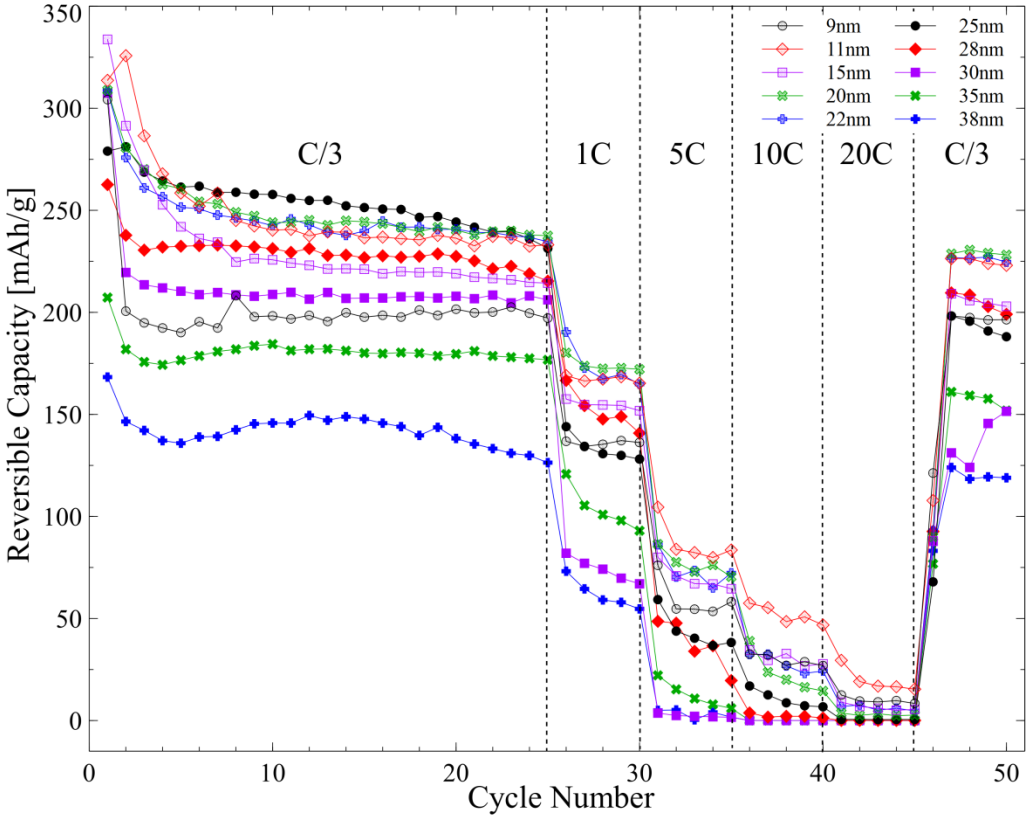

Figure 4.15. Reversible capacities at C/3, 1C, 5C, 10C, 20C, and 1/3C of prepared anatase TiO_2 nano particles with particle size of 9, 11, 15, 20, 22, 25, 28, 30, 35, and 38 nm.

The capacities of anatase particles of 11 - 30 nm can be stabilized above 200 mAh/g in the first 25 cycles under a rate of C/3. The 11, 20, 22, and 25 nm samples showed the best performance with stabilized capacities above 230 mAh/g during the first 25 cycles. It is interesting that there is a big difference in performance for 9 nm (annealed at 175 ℃) and 11 nm (annealed at 200 ℃) samples. This may be caused by the larger ratio of irreversible sites for Li-insertion in the non-ideal crystal lattice [86, 100-102], which is formed by the lower annealing temperature of 175 ℃. The 35 and 38 nm sized samples have much lower reversible capacities than all other samples during the first 25 cycles using a C/3 rate. Following the first 25 cycles, the testing C-rate currents increase up to 20C and finally back to C/3 to observe recovery trends. We can clearly see that the reversible capacities decrease with the increasing C-rate, and most of the sample's reversible capacities drop to below 20 mAh/g under a 20C rate. The 20C rate is very high

(3 minutes to full charge), which gives a low very reversible capacity. The particle size effects are dramatic. For example, 9, 15 and 30 nm samples have relatively similar reversible capacities during the first 25 cycles under C/3 current, and the reversible capacity of the 30 nm sample is larger than that for 9 nm. But under higher C-rate current, we can clearly see that the 30 nm sample reversible capacity is worse than that of 9 nm and 15 nm. Most importantly, in the final C/3 rate cycles, 9 nm and 15 nm samples are almost fully recovered, however, the 30 nm sample shows a much worse capacity recoverability (see Figure 4.16).

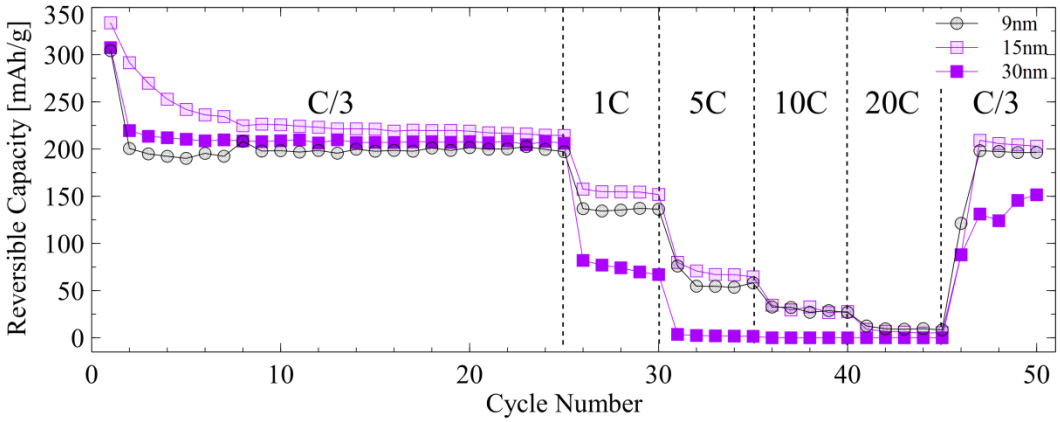

Figure 4.16. Reversible capacities at C/3, 1C, 5C, 10C, 20C, and C/3 of prepared anatase TiO2 nano-particles with particle size of 9, 15 and 30 nm.

Figure 4.17 shows the reversible capacities for the 10 samples at cycle#10, cycle#25 and cycle#50 under C/3 current. Cycle#50 is the final cycle after a series of high C-rate tests. For cycle#10, the two reversible capacity peak values are for 11 nm and 25 nm samples, and the two peak values are for 11 nm and 20 nm for cycle#25 and cycle#50. For particle sizes from 25 nm and above, the reversible capacity decreases essentially monotonically with the increasing particle size. It is interesting that reversible capacity for 15 nm is lower than that for 11 nm or 20 nm. So it seems that for anatase TiO_2 nano particles, 15 nm particle size results a local minimum reversible capacity value, further experiments are needed this particle size effect. We can see that the optimum particle size range for anatase TiO_2 nano-particles synthesized by our method is

11~22 nm with excellent reversible capacities that are above 200 mAh/g after several different high C-rate current tests.

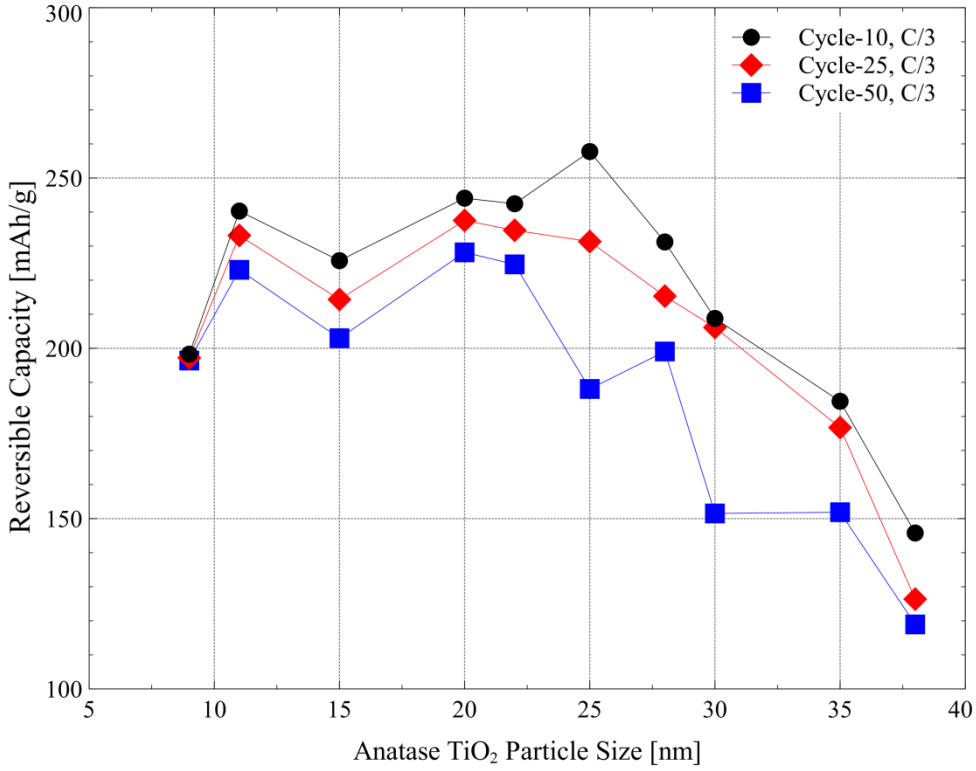

Figure 4.17. Reversible capacities at cycle#10, cycle#25 and cycle#50 under C/3 of prepared anatase TiO_2 nano particles with particle size of 9, 11, 15, 20, 22, 25, 28, 30, 35 and 38 nm. Cycle#50 is the final cycle after a series of high C-rate current tests.

Figure 4.18 shows the charge/discharge voltage profiles at cycle#5 under a C/3 rate for those samples. All the samples show plateau region around 1.75 - 1.78 V during the discharge process, and the charge process plateau regions are 1.90 - 1.95 V. The 38 nm sample shows the shortest plateau both in charge and discharge processes.

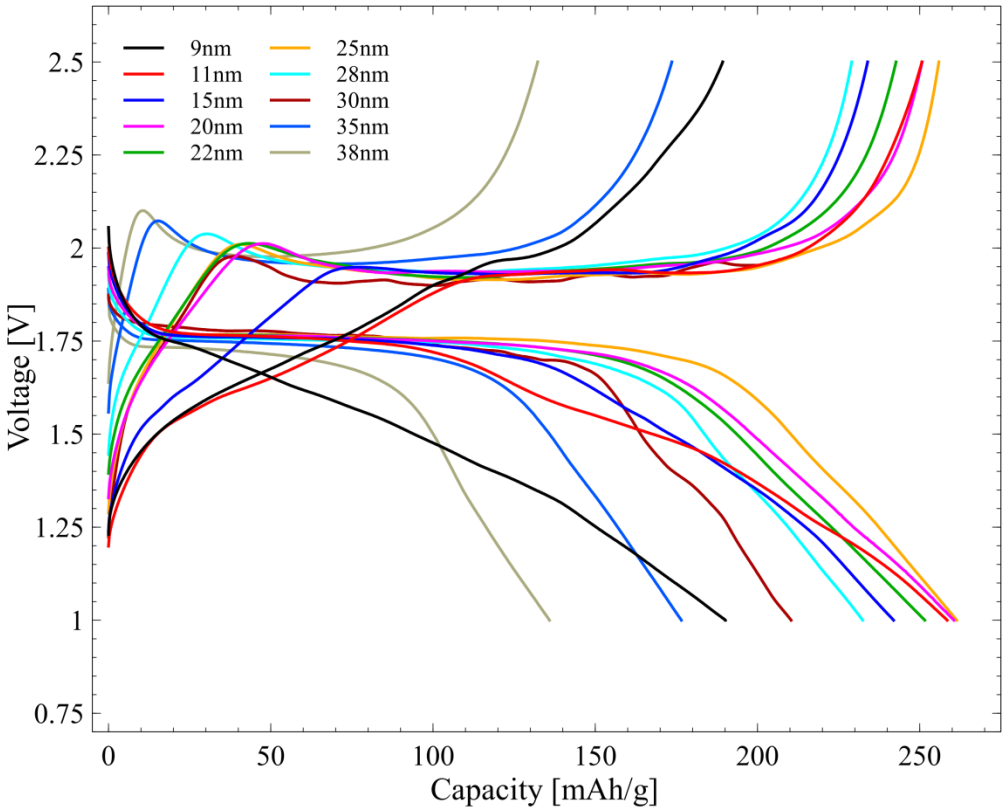

Figure 4.18. Charge/discharge voltage profiles at cycle#5 under C/3 of prepared anatase TiO_2 nano particles with particle size of 9, 11, 15, 20, 22, 25, 28, 30, 35 and 38 nm.

After the 50 cycles mentioned above, 9, 11, 15, 20, 22, 25, and 35 nm samples were investigated by a galvanostatic intermittent titration technique (GITT). All the batteries were discharged through 40 pulses and charged through another 40 pulses, each pulse lasts 15 minutes at a C/10 rate current for each battery, after each pulse, a following 2.5 hours open cell relax process was implemented. Figure 4.19 shows the GITT measurements for these samples. Detailed modeling and analysis for these GITT meaurements are shown in Section 5.

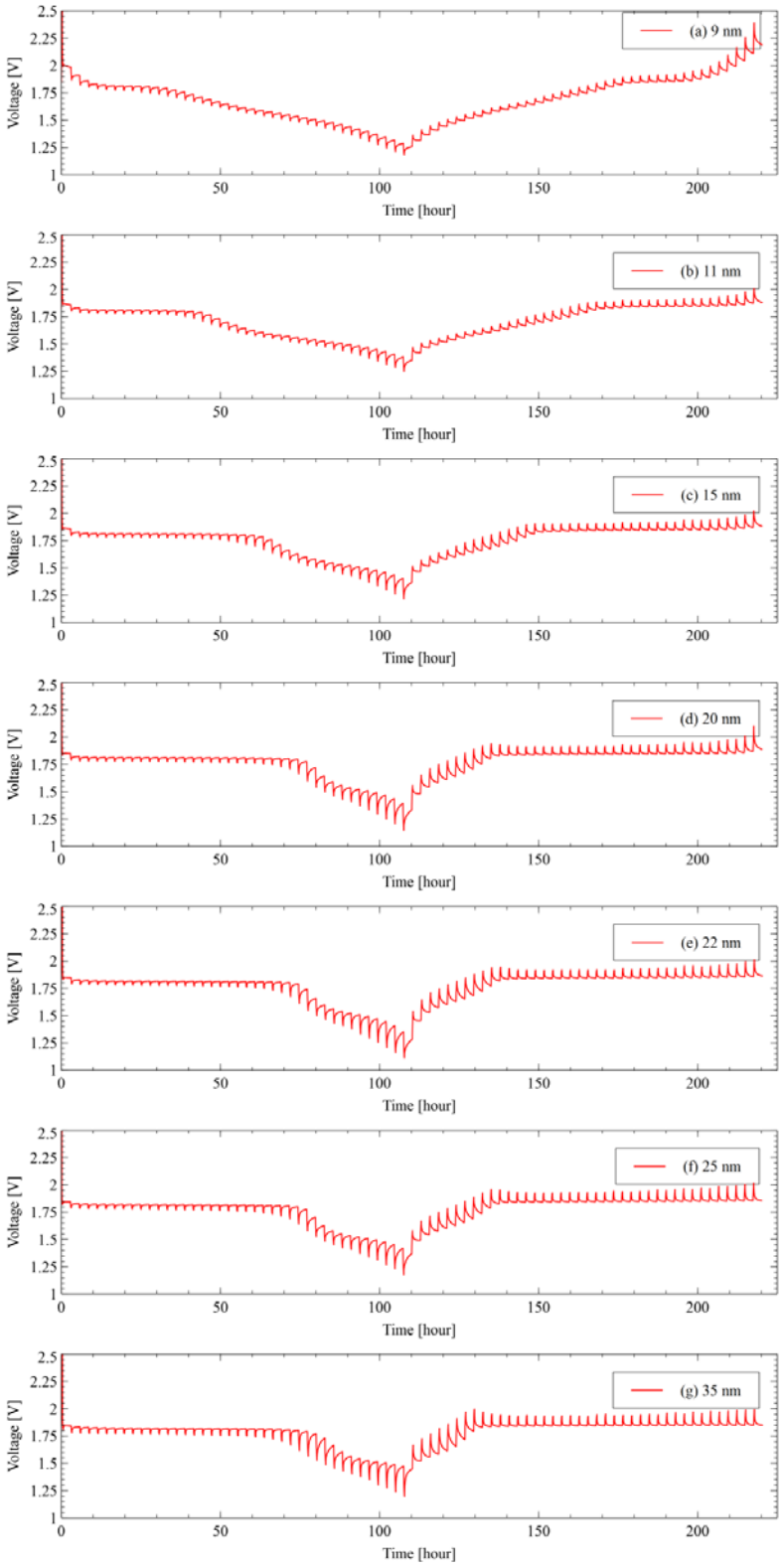

Figure 4.19. Galvanostatic intermittent titration technique (GITT) measurements for prepared anatase TiO_2 nano particles with particle size of (a) 9, (b) 11, (c) 15, (d) 20, (e) 22, (f) 25, and (g) 35 nm.

We can clearly see that during the GITT measurements, the plateau areas either in discharging process in the left part or the charging process in the right side for all the samples, 20 nm sample has longest plateau areas. The particle size effects do affect the diffusion properties of the batteries. More detailed modeling work and analysis are shown in **Section 5**.

4.4. FUTURE WORK

Future work for TiO_2 nano particles should be focused on the materials modeling research. From my work, it is obvious that the particle size would affect the electrochemical performance of the TiO_2 nano particles. However, in order to better understand the mechanisms of lithium ion diffusion behavior in different particle sizes and different temperature environments, more modeling and theoretical calculation work are needed.

4.5. CONCLUSIONS

Nano sized anatase TiO_2 is a promising material for lithium ion batteries. TiO_2 nano crystals can be doped into nano structured carbons such as nano porous carbon by direct synthesis and in-situ crystallization method. Also, TiO_2 nano particles with very controllable particle sizes can be synthesized by our newly developed method, which is an easy and reliable process and can be scaled up for larger quantity production. TiO_2 nano particles synthesized by our new method showed great electrochemical properties for lithium ion battery application and could serve as a potential large capacity lithium ion battery active materials. In addition, the particle size effects do affect the cycling, capacity and lithium ion chemical diffusion properties in lithium ion batteries.

5. LITHIUM DIFFUSION IN NANO-PARTICLES

5.1. INTRODUCTION

Lithium diffusion behavior plays an important role in the lithium intercalation or conversion processes in the active electrode materials. For lithium-ion batteries, the rate of capacity and eletrochemical kinetics characteristic may be affected and controlled by lithium diffusion. Investigation of the lithium difusion behavior and studying the lithium diffusion cooefficient in active materials become more and more important in lithium ion battery research. More broadly, diffusion in a nano-particle systems is of paramount importance for any intercalation material, including Li-ion and metal hydride batteries. Galvanostatic intermittent titration technique (GITT) was used to investigate lithium diffusion in synthesized anatase TiO_2 nano-particles of size 9 – 35nm. A new diffusion model based on the stretched exponential method proposed by Dr. Eric Majzoub was used to investigate and compare the lithium diffusion behavior in my synthesized TiO_2 nano-particles and commericial SnO_2 nano-particles, in order to compare the lithium duffusion behavior in lithium intercalation and conversion systems.

5.2. LITHIUM DIFFUSION MODEL

Galvanostatic intermittent titration technique (GITT) is a commonly used method for determining the lithium diffusion coefficient in the active electrode materials [107] and this theory was first introduced in 1977 by Huggins, et al. [108]. In the GITT technique, the lithium diffusion coefficient can be achieved by equation (1) shown as follows:

$$D = \frac{4}{\pi\tau}\left(\frac{m_B V_M}{M_B S}\right)^2 \left(\frac{\Delta E_s}{\Delta E_t}\right)^2 \qquad \left(\tau \ll \frac{L^2}{D}\right) \tag{1}$$

where D is the chemical diffusion coefficient (cm^2/s), τ is the constant current pulse time (s), m_B is the mass of insertion electrode material, V_M and M_B are molar volume and molar mass of the insertion electrode material respectively, S is the electrode electrochemical active area (cm^2), L is the diffusion length (cm), ΔE_s is the change of steady state voltage during a one-step GITT test, and ΔE_t is the total cell voltage change

during a constant current pulse τ of a one-step GITT test which neglects the IR drop. However, this theory is not always generally applicable for all materials [107, 109-111].

The newly developed lithium diffusion model is based on the stretched exponential method. For all of our cells, the discharging process refers to lithium insertion and the charging process refers to lithium de-insertion. The lithium diffusion equation during the relaxation process after the pulsed discharging is shown as equation (2), and the lithium diffusion equation during relax process after the pulsed charging is shown as equation (3). Figure 5.1 (a) and (b) also illustrate the pulsed discharging and charging processes respectively.

$$V = V_{max} - (V_{max} - V_0) e^{-(\frac{t-t_0}{\tau})^{\alpha}} \quad (2)$$

$$V = V_0 - (V_0 - V_{min}) [1 - e^{-\left(\frac{t-t_0}{\tau}\right)^{\alpha}}] \quad (3)$$

where for equation (2), which is during the relaxation process after one discharging pulse, V is the open cell voltage, V_{max} is the maximum voltage during the relaxation process, V_0 is the initial voltage just after the discharging pulse, t is the relaxation time, t_0 is the initial time point just after the discharging pulse, τ is the diffusion time constant which has the same unit as time t, and α is a structure related constant. For equation (3), which is during the relaxation process after one charging pulse, V is the open cell voltage, V_{min} is the minimum voltage during the relaxation process, V_0 is the initial voltage just after the charging pulse, t is the relaxation time, t_0 is the initial time point just after the charging pulse, τ is the diffusion time constant which has the same unit as time t, and α is a structure related constant. This model can be fit well to all the relaxation processes for all the samples. Figure 5.2 shows a good fit for one selected relaxation process after a discharging pulse and another selected relaxation process after a charging pulse of GITT measurement for a 25 nm anatase nano-particle sample. Xmgrace software package [112] was used for the fitting model to the data.

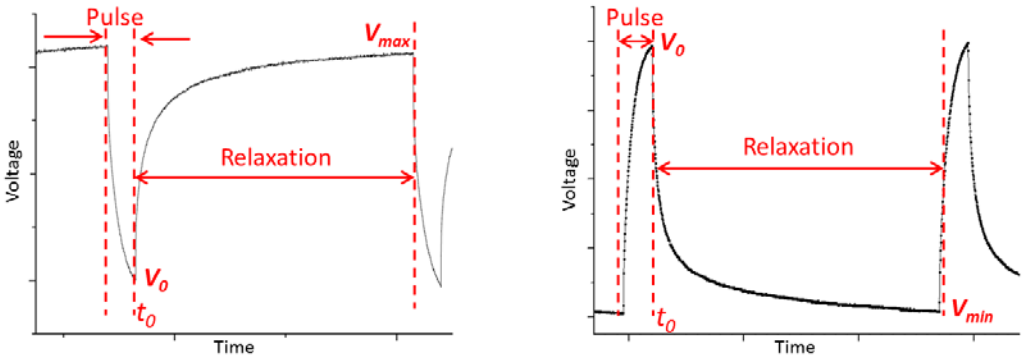

Figure 5.1. (a) Discharging pulse and a following open-cell relaxation process. (b) Charging pulse and a following open-cell relaxation process.

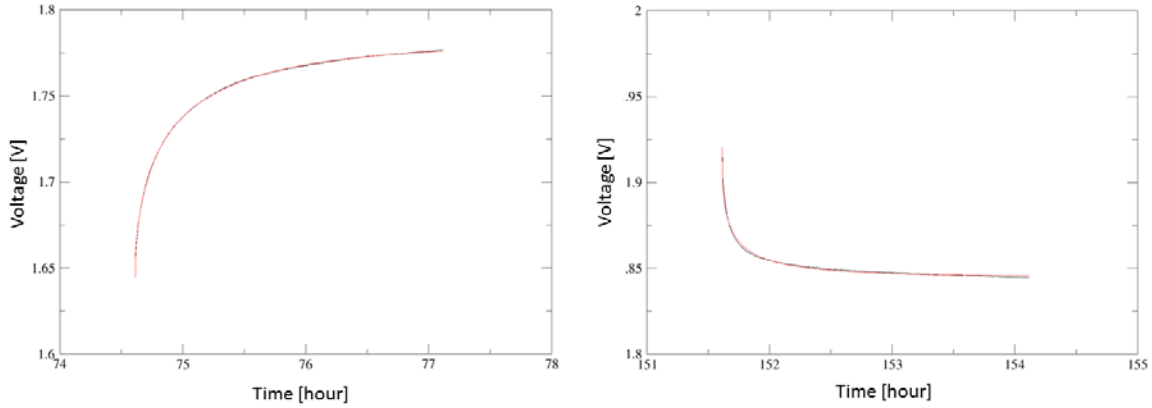

Figure 5.2. (a) Good fitting by our model for one selected open-cell relaxation process after a discharging pulse for 25nm sample. (b) Good fitting by our model for one selected open-cell relaxation process after a charging pulse for 25nm sample. Red lines are fitted lines based on our model, and black lines are the raw experimental data.

The lithium diffusion coefficient is calculated by equation (4).

$$D = \frac{L^2}{\tau} \qquad (4)$$

where D is the lithium diffusion coefficient with units of cm^2/s, L is the diameter of anatase TiO_2 nano-particles in cm unit, and τ is the diffusion time constant in seconds.

5.3. LITHIUM DIFFUSION IN TITANIUM DIOXIDE AND TIN DIOXIDE

The galvanostatic intermittent titration technique (GITT) measurements were implemented by Maccor model-4300 testing station. The GITT test has both insertion and de-insertion processes. Both in insertion process and de-insertion process, which refer to discharging process and charging process for these cells respectively, each single current pulse is in C/10 rated current and lasts for 0.25 hours and followed by a 2.5 hours' open-cell relax process. There are totally 40 pulse-relax sections both for insertion and de-insertion processes, which makes each battery theoretically fully discharged and then fully charged by these intermittent pulses. The TiO_2 samples were just synthesized anatse TiO_2 nano-particles by my newly developed method and the samples in 9 nm, 11 nm, 15 nm, 20 nm, 22 nm, 25 nm and 35 nm sizes were investigated. The SnO_2 nano-particles were purchased from US Research Nanomaterials, Inc. There are two different batches of the SnO_2 nano-particles, one batch is 35-55 nm in size and has 99.7% purity, and the other batch is 450 nm in size and has 99.9% purity.

5.3.1. Lithium Diffusion in TiO_2 Nano-particles. The lithium intercalates into the interstitial sites inside TiO_2 unit cells. The process is : xLi + $TiO_2 \leftrightarrow Li_xTiO_2$. The lithium diffusion model showed in **5.2** was used to fit the GITT measurement data. The fitted V_{max}/V_{min}, τ and α the samples are shown in Figure 5.3, Figure 5.4, and Figure 5.5 respectively. Calculated lithium diffusion coefficients D for these 7 anatse TiO_2 samples are shown in Figure 5.6. Note that in the x-axis, the normalized charge/discharge capacity ratio is used to show the capacity percent for each battery, and the maximum ratio for each battery is normalized to 100%.

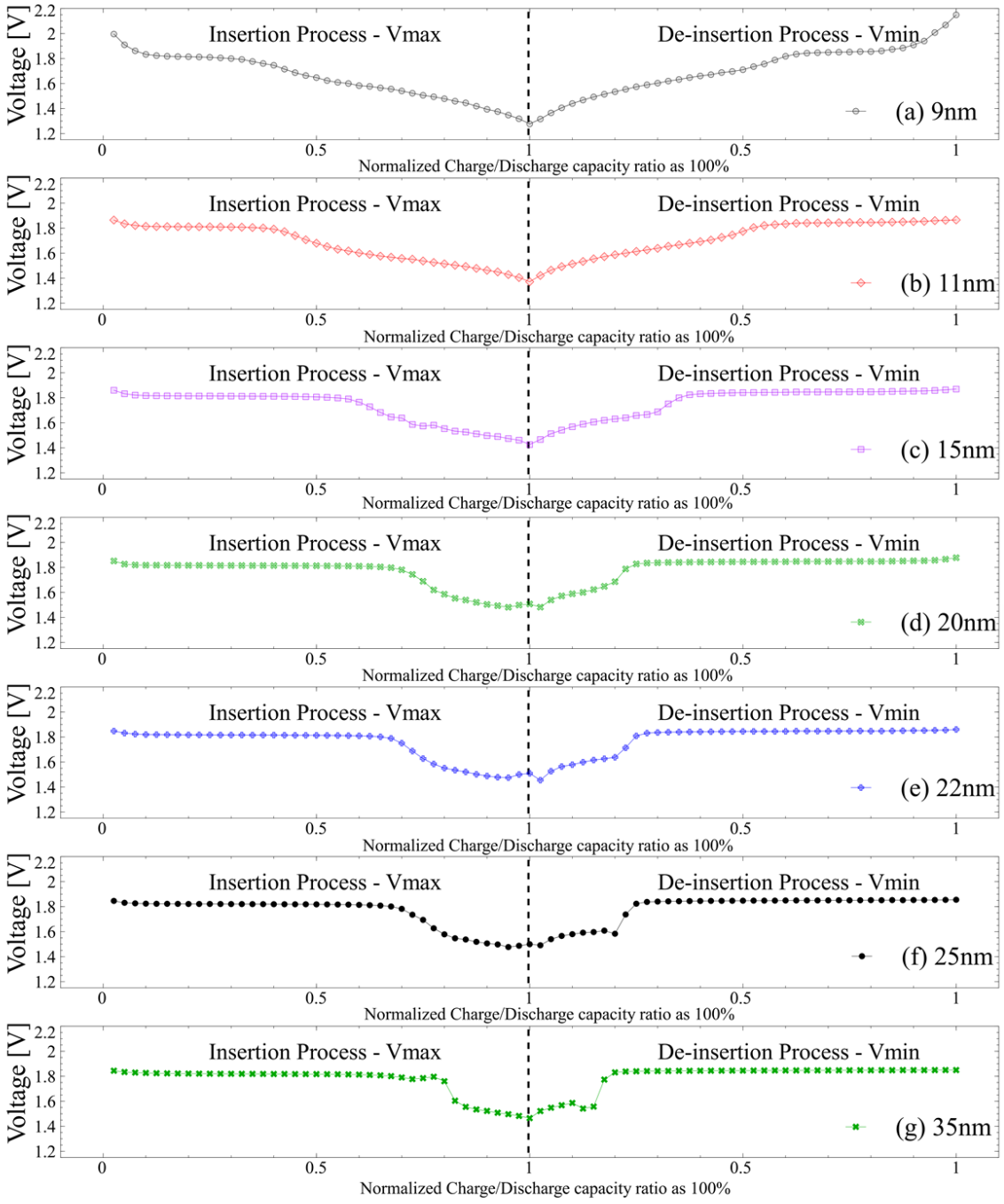

Figure 5.3. Fitted V_{max}/V_{min} from the GITT measurements for prepared anatase TiO_2 nano-particles with particle size of (a) 9, (b) 11, (c) 15, (d) 20, (e) 22, (f) 25, and (g) 35 nm. Left half of each panel shows lithium insertion process and right half shows lithium de-insertion process.

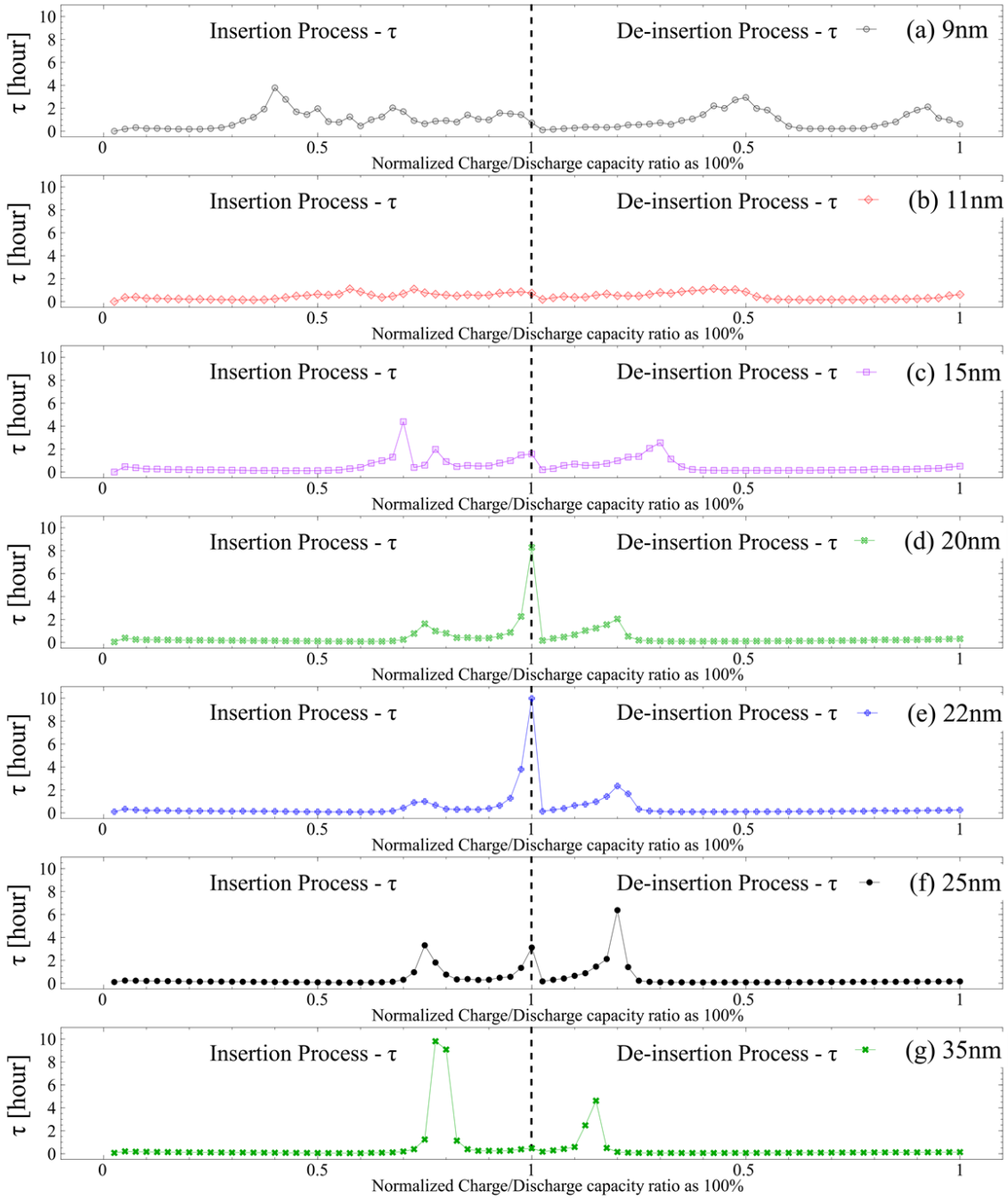

Figure 5.4. Fitted τ from the GITT measurements for prepared anatase TiO_2 nano-particles with particle size of (a) 9, (b) 11, (c) 15, (d) 20, (e) 22, (f) 25, and (g) 35 nm. Left half of each panel shows lithium insertion process and right half shows lithium de-insertion process.

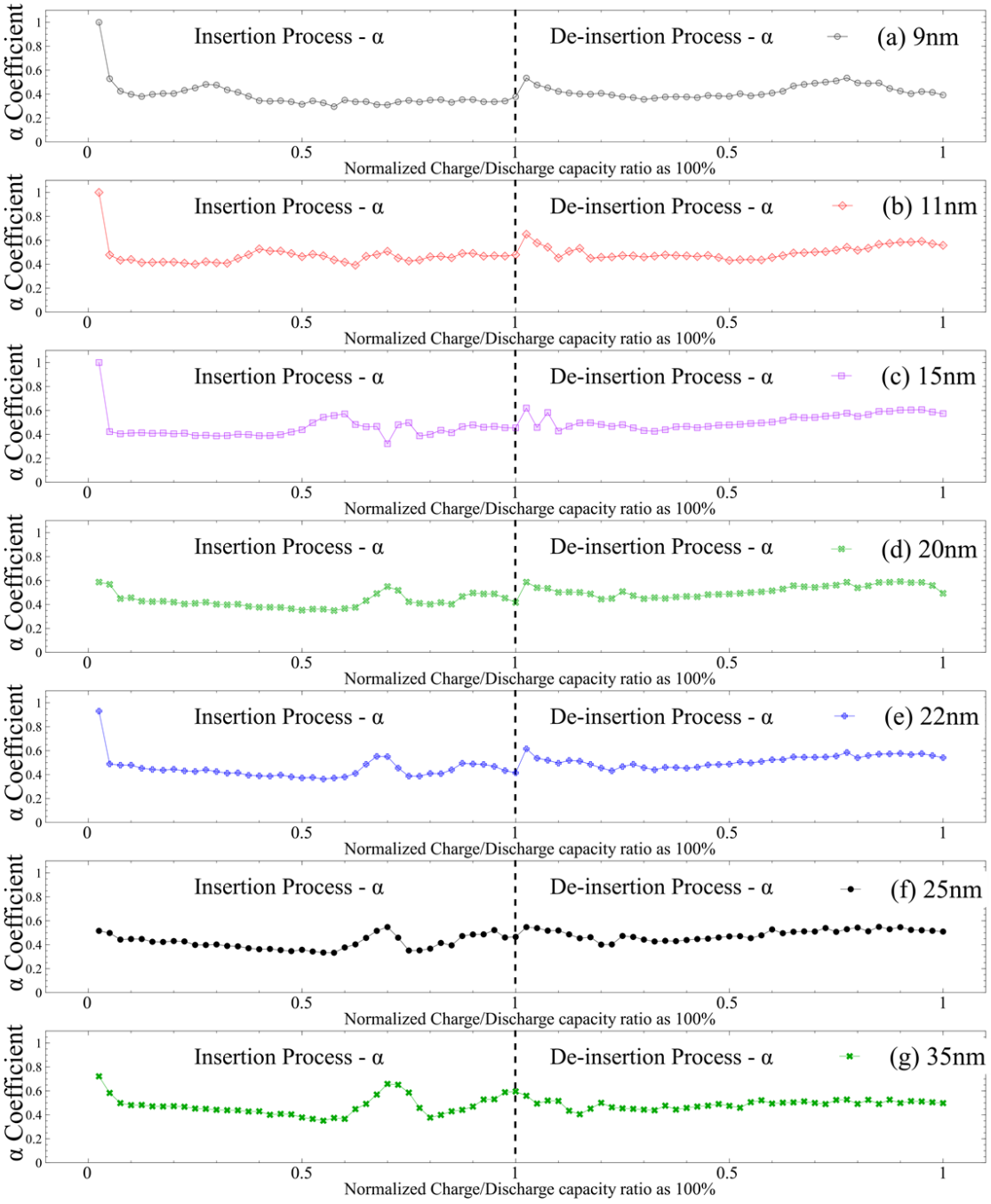

Figure 5.5. Fitted α coefficient from the GITT measurements for prepared anatase TiO_2 nano-particles with particle size of (a) 9, (b) 11, (c) 15, (d) 20, (e) 22, (f) 25, and (g) 35 nm. Left half of each panel shows lithium insertion process and right half shows lithium de-insertion process.

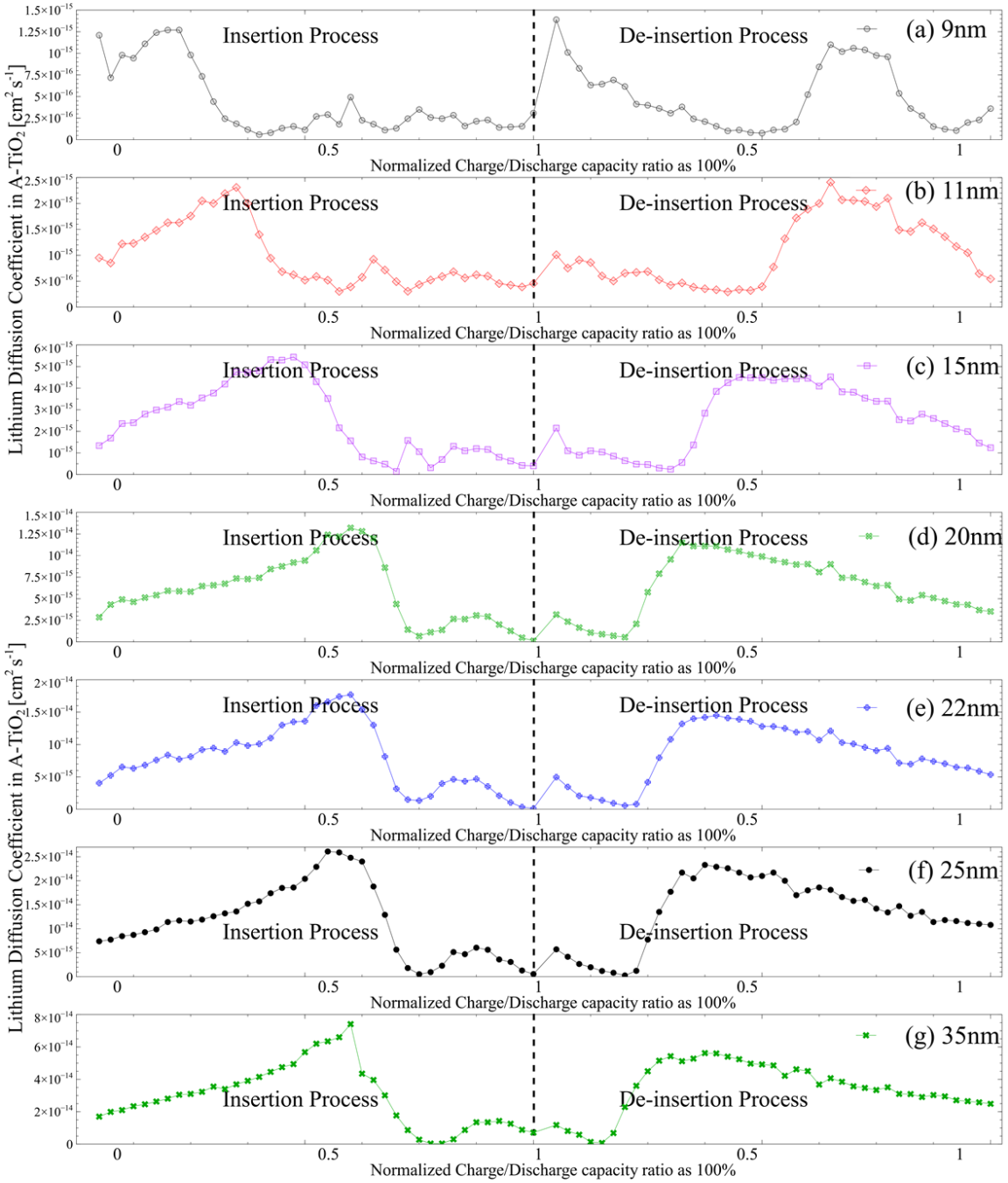

Figure 5.6. Calculated lithium diffusion coefficients for prepared anatase TiO_2 nano-particles with particle size of (a) 9, (b) 11, (c) 15, (d) 20, (e) 22, (f) 25, and (g) 35 nm. Left half of each panel shows lithium insertion process and right half shows lithium de-insertion process.

From Figures 5.3 to 5.6, we can see that the fitted V_{max}/V_{min} based on this stretched exponential model have plateau areas for each sample, and the particle sizes do affect the

plateau length, which give good agreement with the measurement GITT data in Figure 4.19. in Section 4. Generally the normalized plateau length increases as the particle size increases, and for 20 nm, the normalized plateau length reaches a local maximum; however, it is interesting that for 35 nm sample, the normalized plateau increases again. The diffusion time constant τ increases right after each V_{max}/V_{min} plateau area for all samples, which means that the diffusion behavior changed to a new condition after the charging or discharging plateaus saturated. Figure 5.5 shows the structure-related exponential constant α, which is roughly in the range of 0.35 ~ 0.60 for relaxed diffusion in insertion process and 0.45 - 0.60 for relaxed diffusion in de-insertion process. The exponential constant α is in a good agreement with previous studies by Ritger et al. [113, 114] in which the diffusion exponent was in the range of 0.43 - 0.85 for spherical structured samples. The calculated lithium diffusion coefficients are shown in Figure 5.6 and are in the range of 10^{-14} - 10^{-15} cm^2/s, which is in good agreement with the previous reported lithium diffusion coefficient range of 10^{-10} - 10^{-17} cm^2/s [115-120]. It is interesting that the lithium diffusion coefficient increased with increasing particle size. Also, the lithium diffusion coefficients increased during the plateau area in which the lithium ion concentration increased, and this is consistent with the work done by Wagemaker et al. [121] that because higher concentration of electrons will lead to stronger electronic screening of the neighboring occupied interstitial sites interaction so the activation energy for lithium titanate ($Li_{0.5}TiO_2$) is lower than for lithiated anatase ($Li_{0.03}TiO_2$).

5.3.2. Lithium Diffusion in SnO_2 Nano-particles. The lithium and SnO_2 have reactions: $8.4Li + SnO_2 \rightarrow 2Li_2O + Li_{4.4}Sn \leftrightarrow 2Li_2O + 4.4Li + Sn$, and the $8.4Li + SnO_2$ are two steps as: $4Li + SnO_2 \rightarrow 2Li_2O + Sn$; and $4.4Li + Sn \rightarrow Li_{4.4}Sn$ [122], which are two irreversible processes. This process is a more complex conversion process and it is different from the lithium intercalation in TiO_2. The formed multiphased Li-Sn alloy can have a huge volume change, even greater than 300% [122], which will significanly degrade the lithium-ion batteries cyclability. However, the lithium diffusion in this complex conversion process is of interest to have investigated and compared with that in the lithium intercalation system. In my research work, in the first insertion and de-

insertion cycle, the lithium diffusion behavior in SnO_2 nano-particles was investigated. Those two batches of commercial SnO_2 nano-particles were assembled into coin cells, and tested by GITT measurements and analyzed by the new model using exactly the same method as TiO_2 samples. The fitted V_{max}/V_{min}, τ and α are shown in Figure 5.7, Figure 5.8, and Figure 5.9 respectively. Calculated lithium diffusion coefficients D for these 2 SnO_2 samples are shown in Figure 5.10.

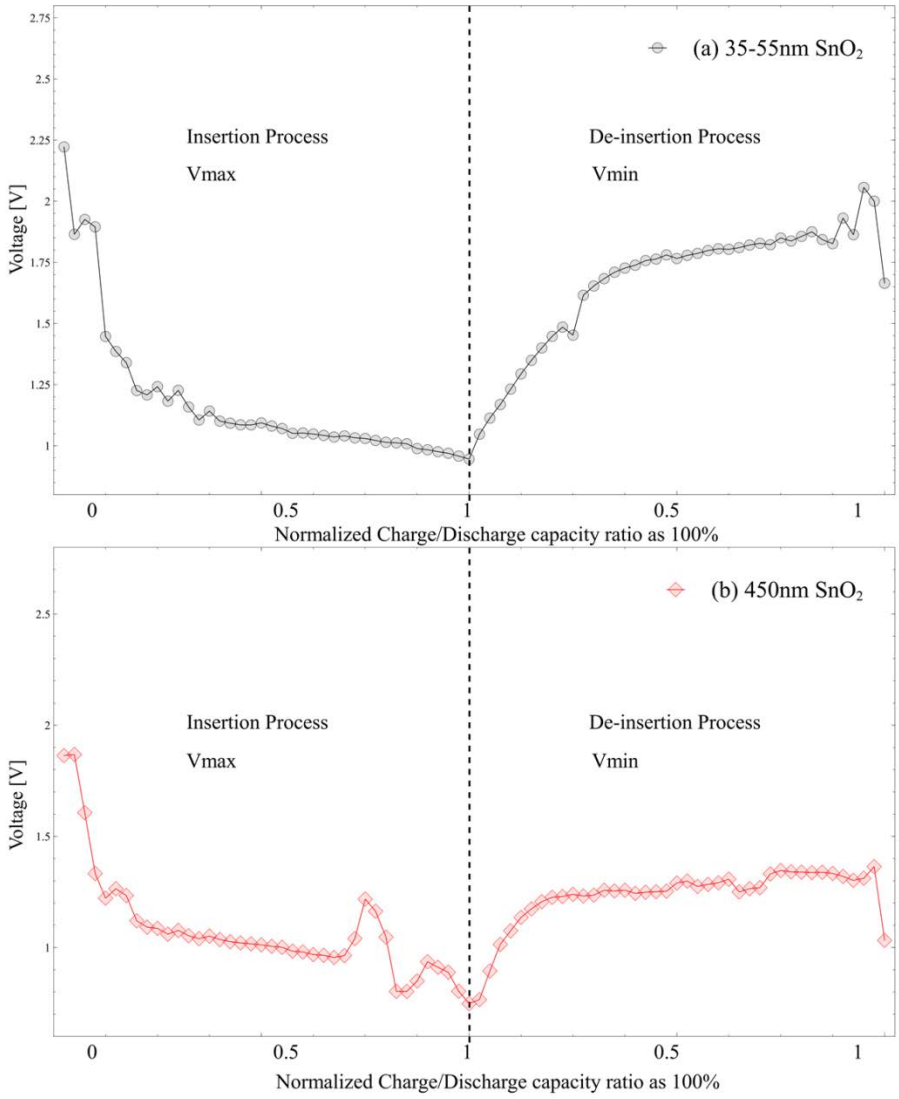

Figure 5.7. Fitted V_{max}/V_{min} from the GITT measurements for commercial SnO_2 nano-particles with particle size of (a) 35-55, and (b) 450 nm. Left half of each panel shows lithium insertion process and right half shows lithium de-insertion process.

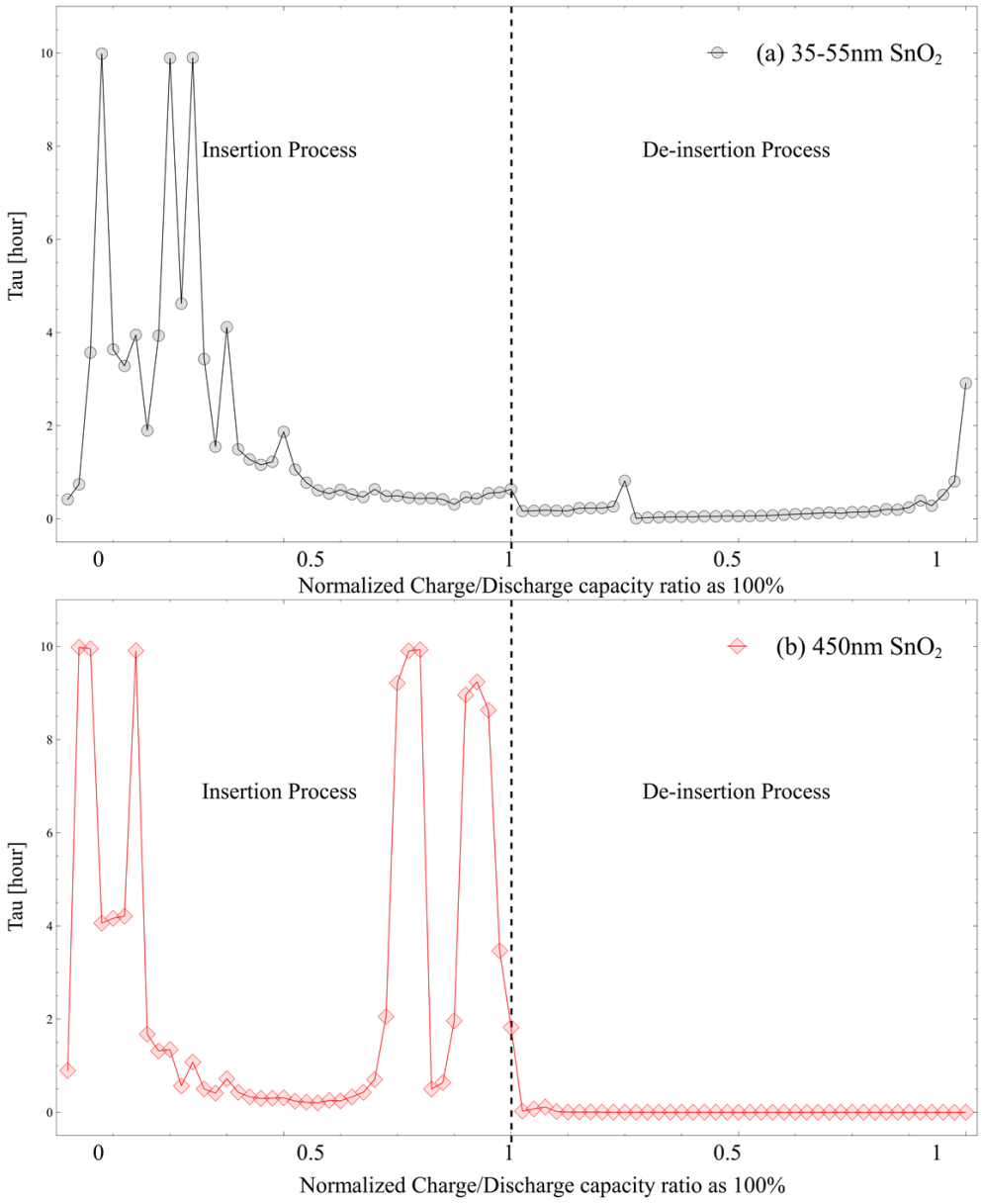

Figure 5.8. Fitted τ from the GITT measurements for commercial SnO_2 nano-particles with particle size of (a) 35-55, and (b) 450 nm. Left half of each panel shows lithium insertion process and right half shows lithium de-insertion process.

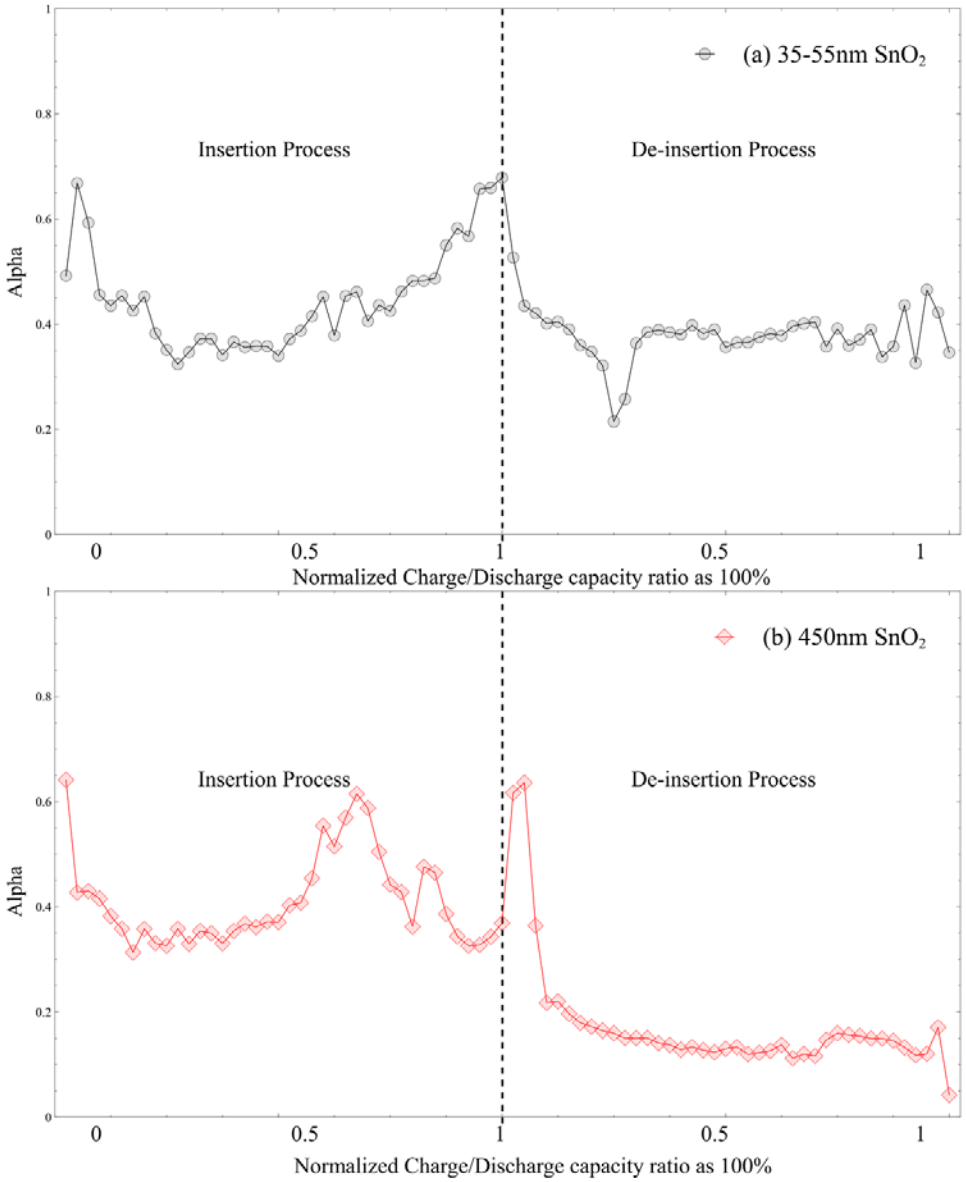

Figure 5.9. Fitted α coefficient from the GITT measurements for commercial SnO_2 nano-particles with particle size of (a) 35-55, and (b) 450 nm. Left half of each panel shows lithium insertion process and right half shows lithium de-insertion process.

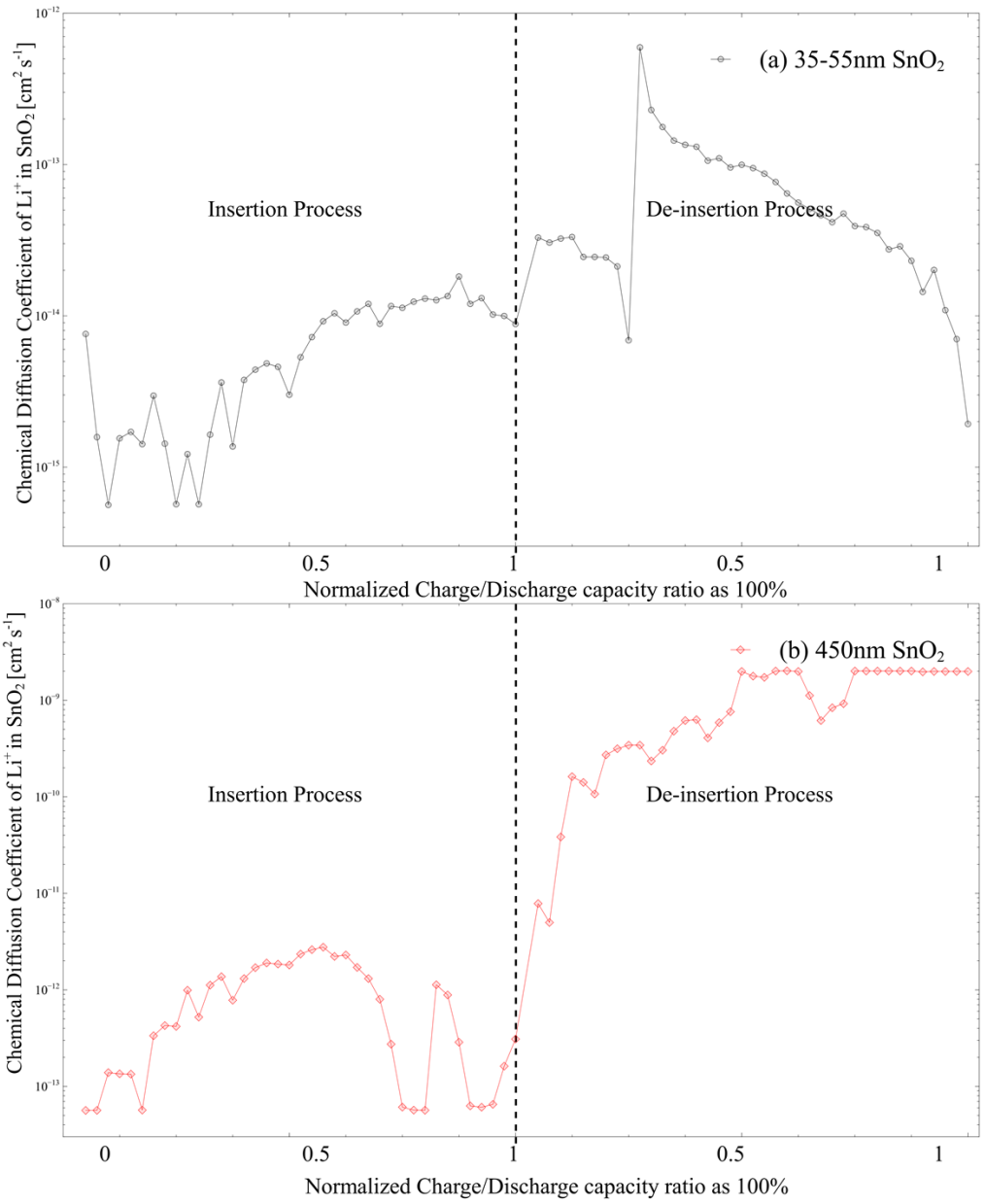

Figure 5.10. Calculated lithium diffusion coefficients for commercial SnO_2 nano-particles with particle size of (a) 35-55, and (b) 450 nm. Left half of each panel shows lithium insertion process and right half shows lithium de-insertion process.

From Figure 5.7, we can see that the fitted V_{max}/V_{min} based on this stretched exponential model do not have plateau areas for these two samples, which is because of the conversion process behavior. Based on the charge calculations of GITT measurements for these two samples, the atomic ratio for the 35 - 55 nm SnO_2 and

lithium is: $Li_{4.3858}SnO_2$ and $Li_{4.3859}SnO_2$ for the 450 nm sample. The atomic ratios of lithium and SnO_2 are similar for these two different sized samples. These two atomic ratios mean that the $4Li + SnO_2 \rightarrow 2Li_2O + Sn$ process had been completed, and the $4.4Li + Sn \rightarrow Li_{4.4}Sn$ process only partially completed. Figure 5.8 shows the fitted diffusion time constant τ and we can see that the diffusion time constant fluctuated during the insertion processes for both the samples, which show that the lithium conversion process is a more complex process than the lithium intercalation process. Figure 5.9 shows the fitted exponential constant α for these two samples, and α is in the range of 0.35 – 0.5, which is lower than that for TiO_2 nano-particles. The calculated lithium diffusion coefficients are shown in Figure 5.10 and is in the range of 10^{-14} - 10^{-15} cm^2/s for 35 – 55 nm SnO_2 and 10^{-12} - 10^{-13} cm^2/s for 450 nm SnO_2. The lithium diffusion coefficients increase as the particle size increases, which is the same behavior as shown in TiO_2 nano-particles.

5.4. FUTURE WORK

Future work for diffusion modeling should be broadened for more general diffusion systems such as metal hydrides and other complex systems. The more accurate diffusion model proposed, the better and more efficiently the model can be used in the study of complex systems. Also, the diffusion model should include some other factors that may affect the ions' or atoms' kinetic characteristics, for example, in the lithium-ion batteries active electrode materials, the electrolyte diffustion factor shouled be well considered and included in the whole lithium diffusion modelling work. Furthermore, the diffusion research work should integrate both theoretical and experimental parts, since as a lot of different diffusion systems may have huge differences in their diffusion behaviors. Combined with both theoretical and experimental work, we can explore the diffusion mysteries in a precise and efficient manner.

5.5. CONCLUSIONS

Based on the Galvanostatic intermittent titration technique (GITT) measurements, a new lithium diffusion model based on stretched exponential method was proposed by Dr. Eric Majzoub and demonstrated as a good lithium diffusion model. The lithium

diffusion coefficients for prepared anatase TiO_2 nano-particle batteries were calculated by using this new model, and the calculated lithium diffusion coefficients are in reasonable range and consistent with previous work done by others. The lithium diffusion behaviors for the TiO_2 and SnO_2 nano-particles derived from this new model show reasonable differences between the lithium intercalation and lithium conversion systems. This new model may be used further to investigate the lithium diffusion in other different nano-structured active materials.

PAPER

I. A Study of the Heat and Pressure-induced S105 Phase in $NaAlH_4$

David Peaslee[a], Gang Wang[a], Dongxue Zhao[a], Eric Sorte[b], Sophia Hayes[c], Mark Conradi[b], Bob Bowman[d], and Eric Majzoub[a]

[a]*Center for Nanoscience and Department of Physics and Astronomy, University of Missouri-St. Louis*

[b]*Department of Physics Washington University*

[c]*Department of Chemistry Washington University*

[d]*Oak Ridge National Laboratory*

INTRODUCTION

Hydrogen is an efficient and pollution-free energy carrier. The current barrier of entry for hydrogen in the energy market is a low cost and reliable storage method. Complex anionic hydrides such as sodium aluminum hydride ($NaAlH_4$) are promising storage materials due to their high hydrogen storage capacities (about 5-6 wt.%), and reasonable reaction temperatures (around 100 °C using a catalyst).

Here, we present a study of the decomposition of a high purity bulk $NaAlH_4$ (crystal structure shown in Figure 4.1) with a new phase created under a high hydrogen pressure (200 bar) and high temperature (near 180 °C). Recent NMR studies have found a highly mobile Al-species (the "S105 phase") in heat and pressure-treated $NaAlH_4$ [1, 2]. By studying the decomposition pathways with a high temperature direct line-of-sight mass spectrum residual gas analyzer (MS-RGA) approximation can be made on the decomposition energy and reaction rates of the bulk material.

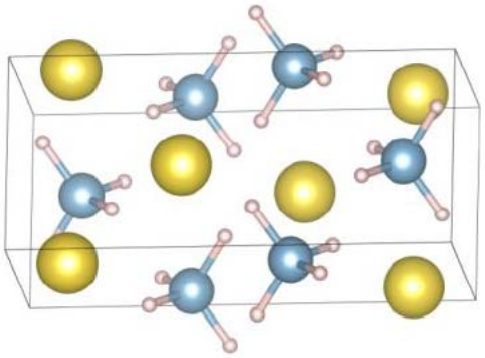

Figure 1. GSAS crystal structure representation of $NaAlH_4$ [3].

EXPERIMENTAL SECTION

Figure 2 shows how the high purity bulk $NaAlH_4$ crystals were synthesized using the evaporation crystallization method. Three samples have been created to determine some of the properties of this phase.

- Pure $NaAlH_4$: synthesized in our lab.
- N97 (no S105): Heated to just below melting temperature under high H_2 pressure.
- N98 (S105): Heated to just above melting temperature under high H_2 pressure.

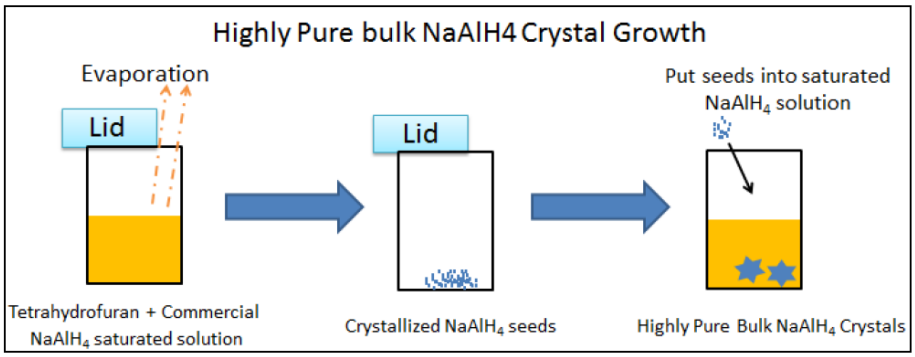

Figure 2. Preparation and crystal growth of high purity $NaAlH_4$.

Powder X-ray diffraction (XRD) was performed on a Rigaku Ultima IV X-ray diffraction (XRD) system with Cu Kα radiation. The XRD data is analyzed using the Rietveld refinement method. The refined pattern with optimized structure is shown in Figure 3. The criterion of the refinement fit is determined by whole pattern residuals (*Rp*) and weighted residuals (*wRp*).

$$Rp = \frac{\sum | I_0 - I_c |}{\sum I_0} \quad (1)$$

$$wRp = \frac{\sum w \cdot | I_0 - I_c |^2}{\sum w \cdot {I_0}^2} \quad (2)$$

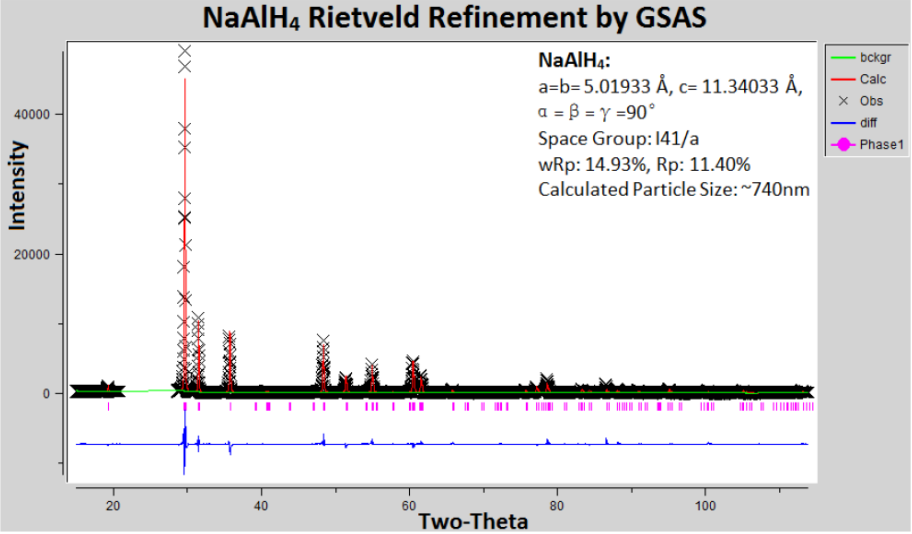

Figure 3. Rietveld Refined X-Ray Diffraction Pattern.

Here I_O is the XRD observed intensity, and I_C is the calculated intensity. The calculated particle sizes range is given by the Debye–Scherrer equation (3).

$$D = 0.94 \times \frac{\lambda}{FWHM \cdot \cos\theta} \quad (3)$$

We can clearly see that the pattern is well fitted with optimized structure constants by the whole pattern Rietveld refinement method. From Figure 3, *wRp* is 14.93, *Rp* is 11.40%, and the calculated coherence length is 740 nm.

RESULTS AND DISCUSSION

The First Principles Study of the Decomposition of $NaAlH_4$. $NaAlH_4$ decomposes by 3 steps:

$$NaAlH_4 \longleftrightarrow \frac{1}{3} Na_3AlH_6 + \frac{2}{3} Al + H_2 \text{ (Reaction 1)} \quad (4)$$

$$Na_3AlH_6 \longleftrightarrow 3NaH + Al + \frac{3}{2} H_2 \text{ (Reaction 2)} \quad (5)$$

$$NaH \longleftrightarrow Na + \frac{1}{2} H_2 \text{ (Reaction 3)} \quad (6)$$

Experimentally, the 3 decomposition steps occur in bulk material at 230, 265 and 660 °C [4]. By first-principles calculations of the thermodynamic free energy, at 1 atm of H_2 and ignoring kinetic barriers, they occur at -50.1, -19.15 and 591.85 °C.

Table 1. Theoretical and Experimental Enthalpies at 1 atm.

	ΔH [4]		ΔH (calc.)		ΔH (exp.)	
	℃	kJ/mol H_2	℃	kJ/mol H_2	℃	kJ/mol H_2
Reaction 1	230	25	-50	23	249.5	52.6
Reaction 2	265	39	-19	37		
Reaction 3	660	76	592	78	434.41	66.3

The melting temperature of $NaAlH_4$ was about 183 °C, and its experimental heat of fusion was 1.5 kJ/mol. The calculated enthalpy of the first two reactions are 64 kJ/mol H_2, which is greater than the experimental value of about 52.6 kJ/mol H_2. The difference

may be caused by the crystallization of Na_3AlH_6, from molten $NaAlH_4$, when the first decomposition proceeds to produce Na_3AlH_6, which has a melting temperature of 252 °C.

The reacting enthalpies are shown in Figure 4(a). They show the same trend as the experimental enthalpies show. They increase at the beginning, reach a peak and then decrease with the increase of temperature.

The phase diagram (pressure vs. temperature) has also been investigated as illustrated in Figure 4(b). The black, red and green boundaries clearly mark the edges of the three phase regions. In the first region, there is only $NaAlH_4$. In the second region, $NaAlH_4$ decomposes into Na_3AlH_6 and Al to release H_2. The temperature of the phase boundaries increases with the increase of H_2 pressure.

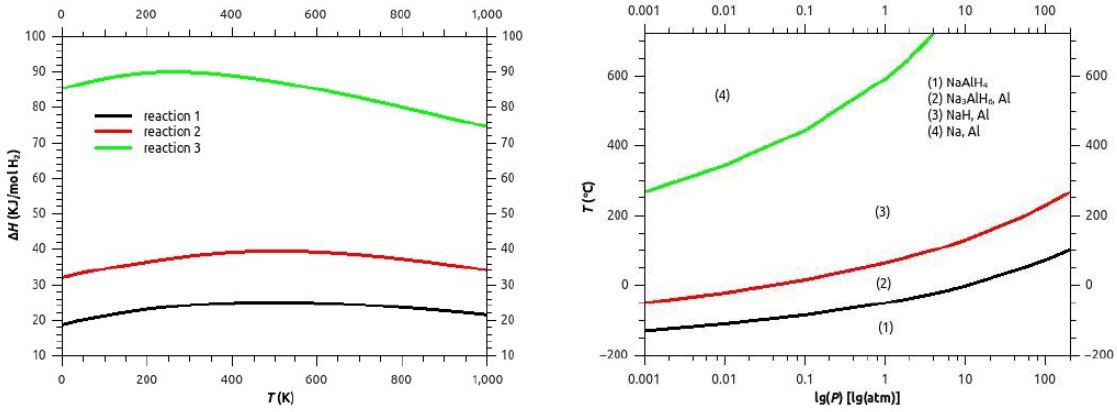

Figure 4 (Left) The calculated reaction enthalpies as a function of temperature.
Figure 4 (Right) The phase diagram of $NaAlH_4$.

Oxidized $NaAlH_4$ was also investigated using supercell first-principles calculations. $[AlH_4]^-$ was replaced with OH^- to inspect the solubility of NaOH in $NaAlH_4$, which can be determined by the difference of free energy between $(NaAlH_4)_{(1-x)}(NaOH)_x$ and $NaAlH_4$+NaOH by the equation:

$$\Delta F = F\left[(NaAlH_4)_{(1-x)}(NaOH)_x\right] - (1-x)\cdot F(NaAlH_4) - x\cdot F(NaOH) \qquad (7)$$

Figure 5(a) illustrates the calculated free energies of $(NaAlH_4)_{(1-x)}(NaOH)_x$. This clearly shows that the free energy increases with the increase of NaOH concentration up to the free energy of NaOH. The changes of free energies can be deduced from the data as shown in Figure 5(b). Within the temperature zone $0 < T < 1000$ K, the changes of the free energies gradually decrease, becoming favorable. The exception is for x=0.4375, which becomes favorable beyond 1000 K. This data clearly indicates that NaOH is soluble in $NaAlH_4$ over a wide composition range.

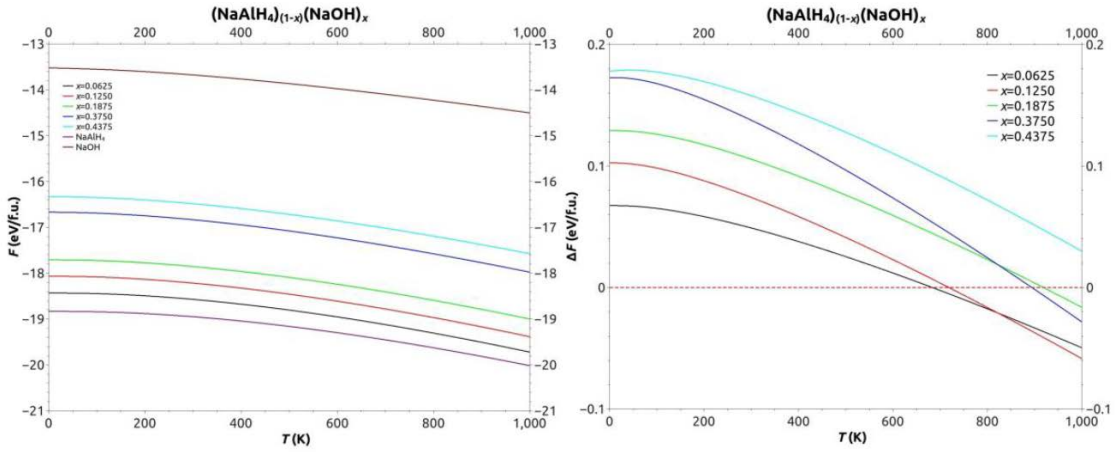

Figure 5 (Left) The free energies of $(NaAlH_4)_{(1-x)}(NaOH)_x$.
Figure 5 (Right) The changes of free energies. For a particular concentration x, OH^- is soluble when $\Delta F<0$. As x increases ΔF at 0 K also increases.

Figure 6(a) was derived from the changes of free energies of $(NaAlH_4)_{(1-x)}(NaOH)_x$ at the points ΔF just below 0, which illustrate the saturated concentrations of NaOH in $NaAlH_4$ at various temperatures. Furthermore, the solubility occurs above 650 K (400 °C). However, $NaAlH_4$ decomposes before this temperature, which implies that NaOH cannot dissolve into $NaAlH_4$ at 1 atm. The solubility might be observed at high H_2 overpressures where $NaAlH_4$ is prevented from decomposing. The solution enthalpies of $(NaAlH_4)_{(1-x)}(NaOH)_x$ have also been investigated.

Figure 6(b) shows the calculated enthalpies in a wide temperature range. The meaningful ones are above the temperatures at which solubility occurs. The figure shows that the reaction enthalpies increase with the increase of temperature, becoming more favorable.

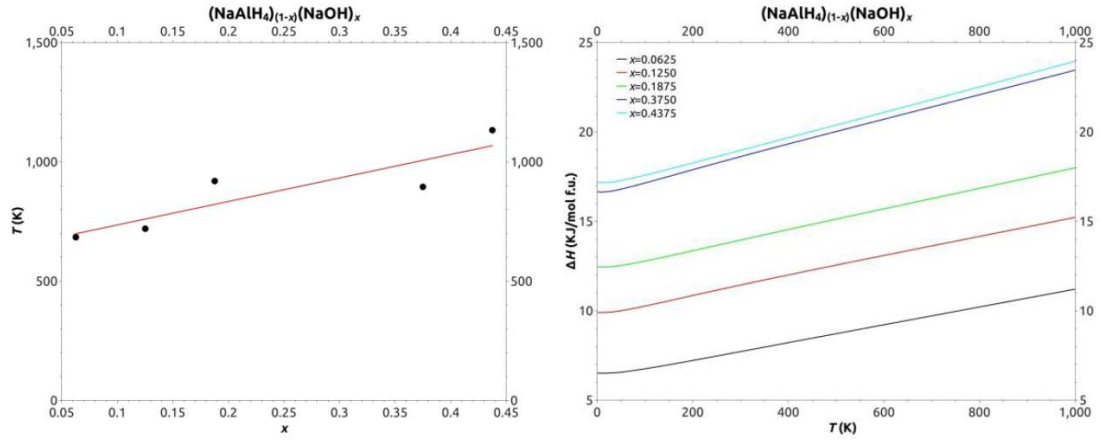

Figure 6 (Left) The solubility of NaOH into $NaAlH_4$ with temperature.
Figure 6 (Right) Molar solution enthalpies of $(NaAlH_4)_{(1-x)}(NaOH)_x$. As x increases the enthalpies also increase.

Experimental Evidence for the Reaction Pathways. Mass spectroscopy measurements during the decomposition of these materials reveal some important clues to their reaction pathways. Figure 7 outlines the decomposition of bulk $NaAlH_4$. Under ultra high vacuum, a mass spectrum residual gas analyzer (MS-RGA) detects that the bulk material melts at 180 °C, and begins to release H_2 at about 200 °C (blue/black boxes in Figure 8). This reaction reaches its peak rate at 245 °C, and in some cases, a second round of H_2 emission precedes the decomposition of Na_3AlH_6 (at 280 °C) into NaH, Al, and H_2 (yellow/grey boxes in Figure 8). In Figures 7 and 8, the mass (m/z) of 23 may represent the fracturing of NaH into the ions Na^+ and H^- implying that NaH is lost as a gas. Small amounts of other ions are detected in the MS-RGA, which indicate that other gases are present in the H_2 stream. These gasses may be forming from oxygen impurities in the sample.

We use a Differential Scanning Calorimetry (DSC) instrument to measure the experimental decomposition enthalpies for pure $NaAlH_4$, N97 and N98. The enthalpies for the materials heated at 1 °C/minute are listed in Table 2.

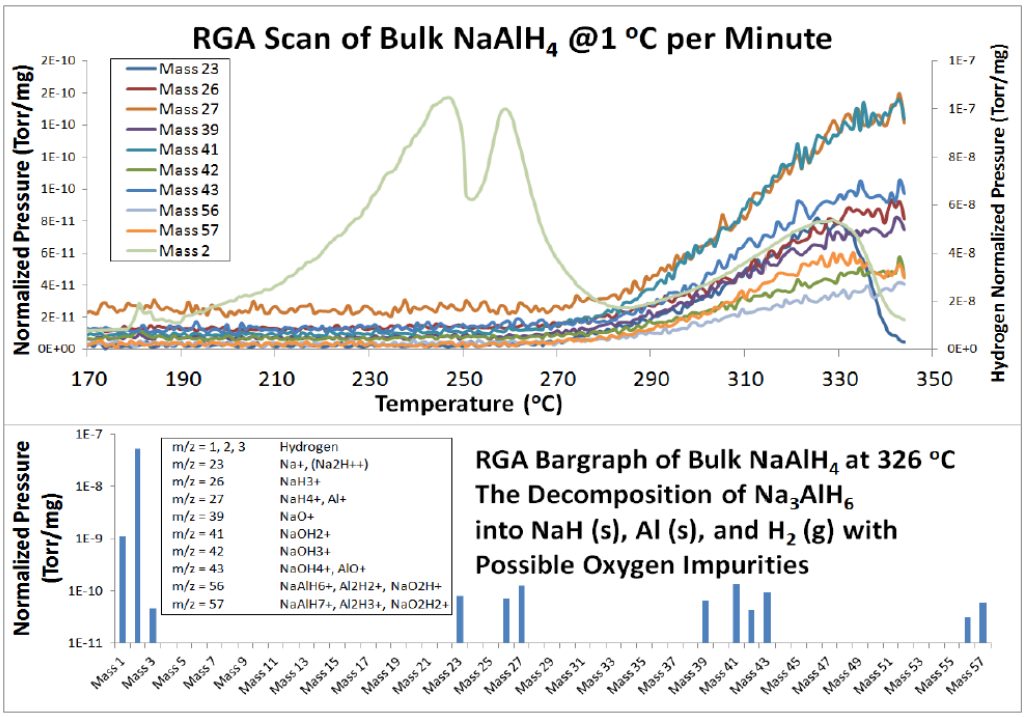

Figure 7. MS-RGA measurements of the thermal decomposition of $NaAlH_4$ showing increase in important masses during the second step of decomposition.

These DSC measurements are plotted along with the RGA data and most of the results have a strong correlation. The results of the MS-RGA show that all 3 samples decompose through the same reaction pathways, but N97 and N98 decompose at a lower temperature than the bulk material. Additionally, N98 in the S105 phase shows a smaller temperature range for reaction 2 to complete.

Table 2. DSC Experimentally Calculated Enthalpies.

	Bulk		N97		N98(S105 phase)	
	°C	J/g	°C	J/g	°C	J/g
Reaction 1	183	273	179	315	179	166
Reaction 2	250	487	250	333	234	434
Reaction 3	434	614	402	801	391	802

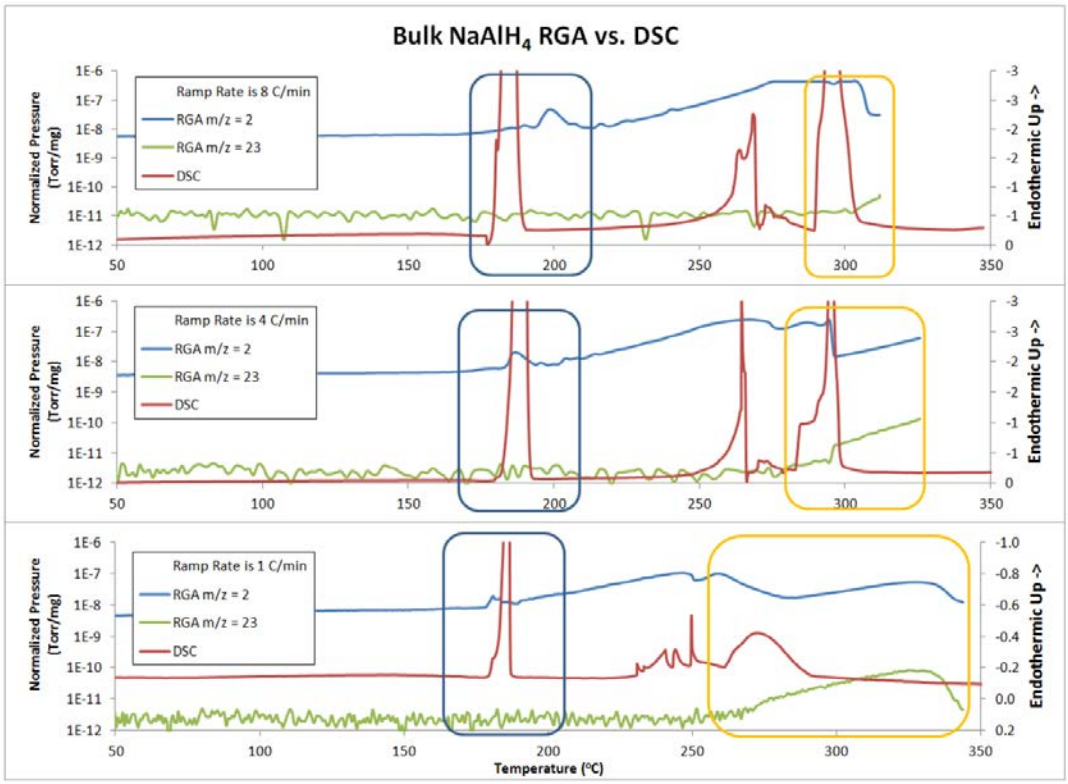

Figure 8.(a). MS-RGA measurements of the thermal decomposition at various ramp rates for bulk $NaAlH_4$. In figures (a)-(c): the top dark line represents the partial pressure of H_2, the bottom dark line represents DSC analysis, and the bottom grey line represents the partial pressure of NaH. Starting from the top chart, the ramp rates are 8, 4, and 1 °C/minute.

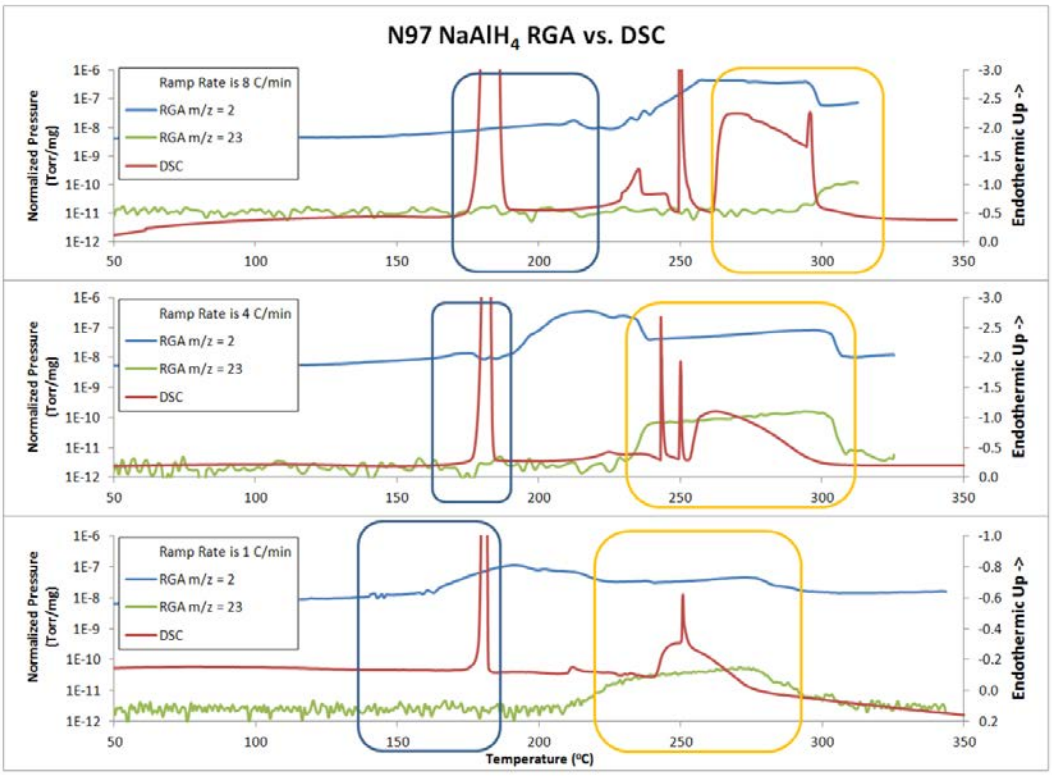

Figure 8.(b). MS-RGA measurements of the thermal decomposition at various ramp rates for high H_2 pressure N97.

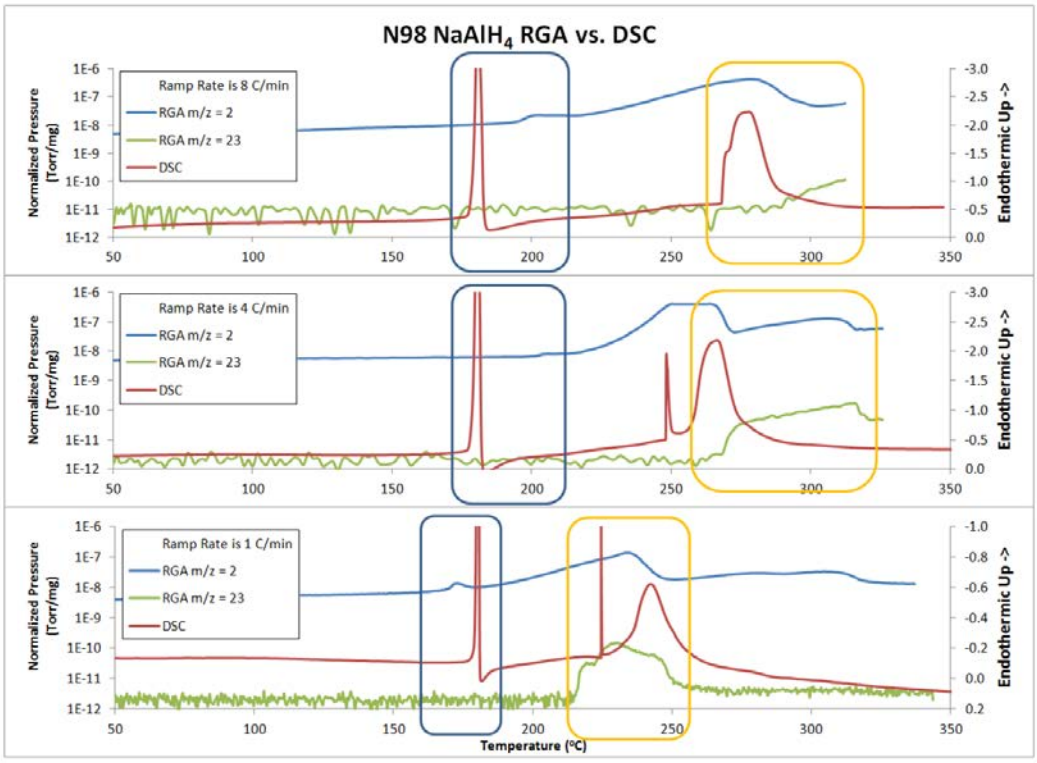

Figure 8.(c). MS-RGA measurements of the thermal decomposition at various ramp rates for the high temperature/pressure phase "S105" N98.

CONCLUSION

Heat and pressure-treated $NaAlH_4$ in the S105 phase has been shown to melt and decompose into Na_3AlH_6 and H_2 gas at a lower temperature than the as prepared bulk material. This would indicate that the effect of pretreating $NaAlH_4$ with a high temperature and H_2 pressure improves this material's ability to store and release H_2 gas at moderate temperatures without the use of catalysts.

ACKNOWLEDGEMENTS

The authors gratefully acknowledge support from DOE Basic Energy Sciences grant DE- FG02-05ER46256.

REFERENCES

[1] “Discovery of a New Al Species in Hydrogen Reactions of $NaAlH_4$” Ivancic, T. M.; Hwang, S-J.; Bowman, R. C., Jr.; Birkmire, D. S.; Jensen, C. M.; Udovic, T. J.; Conradi, M. S., *Phys. Chem. Lett*. 2010, 1, 2412- 2416.

[2] “Mobile Species in $NaAlH_4$” Eric Glenn Sorte, Robert C. Bowman, Eric H. Majzoub, Margriet H.W. Verkuijlen, Terrence J. Udovic, and Mark S. Conradi, *J. Phys. Chem. C*, Just Accepted DOI: 10.1021/ jp401134t.

[3] "General Structure Analysis System (GSAS)" A.C. Larson and R.B. Von Dreele, *Los Alamos National Laboratory Report* LAUR 86-748 (2000).

[4] “Metal-doped sodium aluminium hydrides as potential new hydrogen storage materials” B. Bogdanovic, R.A. Brand, A. Marjanovic, M. Schwicardi, J. Tolle, *J. Alloys and Compounds*, v302, 36, 2000.

II. Effects of NaOH in Solid NaH: Solution/Segregation Phase Transition and Diffusion Acceleration

Eric G. Sorte,[*,†] E. H. Majzoub,[‡] Tim Ellis-Caleo,[†] Blake A. Hammann,[§] Gang Wang,[‡] Dongxue Zhao,[‡] Robert C. Bowman, Jr.,[‖] and Mark S. Conradi [*,†,§]

[†]*Department of Physics, Washington University, One Brookings Drive, Saint Louis, Missouri 63130, United States*

[‡]*Center for Nanoscience and Department of Physics and Astronomy, University of Missouri St. Louis, One University Boulevard, St. Louis, Missouri 63121, United States*

[§]*Department of Chemistry, Washington University, One Brookings Drive, Saint Louis, Missouri 63130, United States*

[‖]*RCB Hydrides, LLC, 117 Miami Avenue, Franklin, Ohio 45005, United States*

ABSTRACT

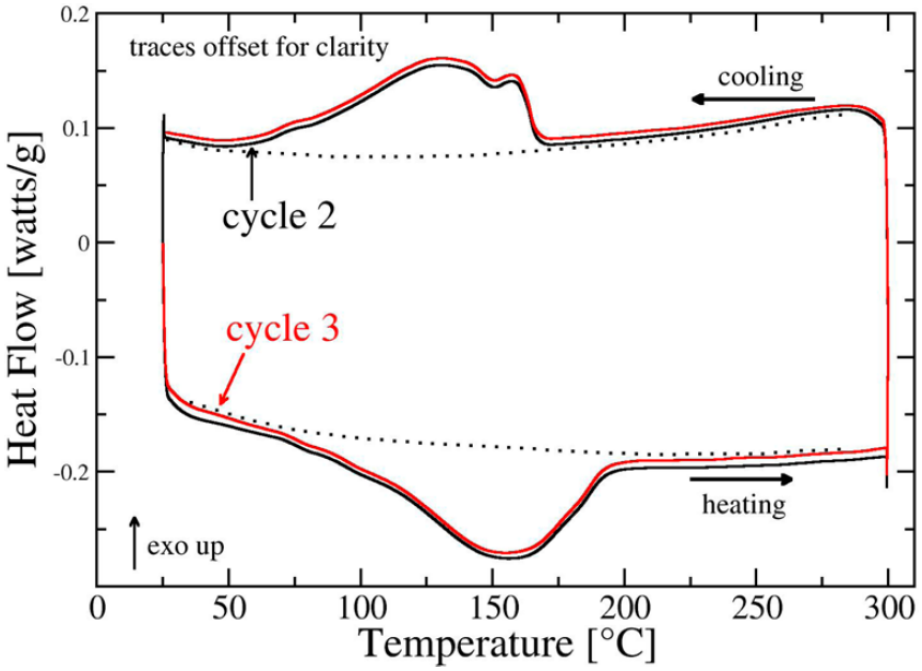

The presence of approximately 10 mol % NaOH mixed with NaH powder is shown to result in much more rapid hydrogen motion in the NaH above 150 °C, as indicated by the onset of hydrogen NMR line narrowing at this temperature. A similar result appears for air-exposed NaH due to the formation of hydroxide from atmospheric H_2O. The NMR line narrowing is too rapid, as a function of temperature, to be described by thermal activation; rather, it is suggestive of a phase transition. Indeed, differential scanning calorimetry finds, after an initial thermal cycle, a reversible thermal anomaly indicating a phase transition near 150 °C. Powder X-ray diffraction with an excess of NaOH displays a remarkable lattice expansion of the NaH in the temperature range of 100−240 °C where the (200), (220), and (311) reflections indicate a volume lattice expansion of up to 11%; the expansion is reversible upon cycling. The data thus point to a reversible phase transition in which NaOH enters the NaH structure above 150 °C and exits the NaH below that temperature. First-principles calculations using OH-substituted NaH supercells indicate significant solubility in the NaH lattice and find a transition temperature and enthalpy change that are in approximate agreement with differential scanning calorimetry (DSC) measurements, confirming the presence of a phase transition.

INTRODUCTION

The slow rate of hydrogen diffusion in many metal hydrides is often a limiting factor in whether the material can ultimately be useful as a means of practical hydrogen storage.[1–4] Diffusion of hydrogen in storage solids is crucial to the kinetics of dehydriding and rehydriding.[5] A well-known example of this is the "hydrogen-blockade" formed during hydriding of Mg: a thick layer of MgH_2 forms on the outside of Mg particles and, due to the slow diffusion of hydrogen through MgH_2, blocks further uptake and reaction of hydrogen.[6] As one of the simplest and most well-understood [7–9] light metal hydrides, NaH can provide a test case for many of the other hydrides of more practical interest. Moreover, $NaAlH_4$ (a viable hydrogen storage system) dehydrides to yield NaH, as well as Al and H_2 gas. Its rehydriding behavior is therefore dependent on the surface properties and impurity-induced changes of the NaH. Thus, the present results will be of interest to the larger hydrogen storage community. NMR has proven extremely useful in determining hydrogen diffusion rates in metal hydrides and for identifying strategies to enhance diffusion. [2,10–12] An earlier NMR study focused on the intrinsic, thermally activated hydrogen line narrowing of NaH. [13] While an investigation of the effects of NaOH in NaH was not the main focus of that work, it was noticed that one NaOH-containing sample showed substantially early hydrogen line narrowing (i.e., narrowing commencing at a lower temperature). This sample was estimated to contain 30 mol % NaOH on the basis of integrated X-ray diffraction (XRD) peak area and displayed ^{1}H NMR early line narrowing starting near 140 °C. A second NaOH-containing sample line narrowed in the 250−275 °C range, just as nominally pure NaH does. In that work,[13] this second sample was incorrectly estimated to contain 20 mol % NaOH; a reanalysis of the XRD data reveals that this sample had only 5 mol % NaOH. The normal hydrogen line-narrowing behavior of the second sample is therefore not unexpected. The surprising early line narrowing of the sample containing 30 mol % NaOH is the motivation for the current work. Here, we report the results of a thorough investigation of the effects of hydroxide additives on the hydrogen diffusion behavior of NaH, focusing on the effects of NaOH with NaH. We show new NMR line-shape measurements as a function of temperature as well as results from differential scanning calorimetry (DSC) and in situ

powder XRD. First principles calculations confirm the experimental results and provide a partial explanation of the behavior. Together, these data point to a solid−solid phase transition in NaH containing NaOH.

EXPERIMENTAL METHODS

NaH material was used as received from Sigma-Aldrich, with a stated purity of 95%. NaOH was also purchased from Sigma-Aldrich. One bottle of NaOH appeared to have absorbed some atmospheric water and is here termed wet NaOH; based on NMR measurements described below, we estimate our wet NaOH to have about 3.5 mol % H_2O. For some measurements, we dried NaOH at 150 °C under vacuum for 48 h to yield dry NaOH. All samples were handled in a glovebag with flowing pure N_2 gas (at WU) and in an argon atmosphere glovebox (at UMSL). Samples were flame-sealed into glass tubes for NMR measurements. Except when otherwise indicated, all samples were combined by hand-mixing the powders or grinding with a mortar and pestle for about 100 s in an inert atmosphere.

Hydrogen NMR lineshapes were obtained from a home-built spectrometer operating at 85.03 MHz (2.0 T). Free induction decays (FIDs) were corrected for the receiver blocking/probe ringing at early times and Fourier transformed.[14] Some ^{23}Na spectra were measured at 4.7 and 7.0 T (53.4 and 79.3 MHz). In all cases, care was taken to record fully relaxed signals (the proton spin lattice relaxation time T_1 in many of these samples is long). The temperature was controlled with a stream of heated, thermally regulated air flowing across the sample.

Differential scanning calorimetry (DSC) was performed on a Q2000 series analyzer (TA Instruments). About 6 mg of sample was loaded in an aluminum pan in an argon-filled glovebox and crimped with an aluminum hermetic lid. The sample was heated to a maximum of 300 °C; the typical heating and cooling rates were 5 °C/min. Hot stage (in situ) powder X-ray diffraction (XRD) was performed on a Rigaku Ultima IV diffractometer with an HT 1500 high-temperature attachment. XRD measurements used Cu Kα radiation, and the samples were held as thin, uniform layers of powder on a Pt slide and measured under dynamic vacuum. The temperature was measured with an R-type thermocouple in a temperature-controlled feedback loop. Air exposure of the

samples was unavoidable when loading into the Rigaku high-temperature attachment. As a result, we also performed some variable-temperature XRD measurements on a homemade XRD hot stage that permitted air/water exclusion from the sample. Samples were loaded in a glovebox on an aluminum XRD slide and sealed with Kapton tape (the adhesive is good to 260 °C according to the manufacturer's specifications). The slide was then loaded into the Rigaku diffractometer, and a 25 W Dale power resistor with a flat extruded aluminum case was attached to the bottom of the aluminum sample holder. The sample was heated by applying ac voltage to the power resistor through a variable autotransformer or through a temperature-regulating circuit. The temperature was measured and controlled with T-type thermocouples. Some XRD measurements at room temperature were also performed with samples sealed under a lowdensity polyethylene film (Saran wrap).

COMPUTATIONAL METHODS

First-principles calculations were performed using the planewave density functional theory (DFT) code VASP (Vienna Abinitio Simulation Package).[15,16] The generalized gradient functional of Perdew and Wang [17] was used to describe exchange-correlation of the electrons, and the projector augmented wave (PAW) method was used to describe the interaction between the valence electrons and ion cores.[18,19] The planewave cutoff energy was 600.0 eV for all calculations. Monkhorst−Pack meshes were used for k-point sampling of the Brillouin zone with a spacing of less than 0.05 $Å^{-1}$.[20]

Hydroxide-substituted crystal structures were generated by placing OH anions at random H locations in NaH supercells for a variety of OH/H ratios. These structures were relaxed using the conjugate gradient algorithm until the forces on the atoms were below 0.01 eV/Å and stresses were below 0.05 kbar. Finite-temperature thermodynamics were obtained from the crystal entropy in the harmonic approximation, using phonon frequencies calculated from the linear response capabilities in VASP5.

The phase diagram of the NaH/NaOH system was calculated by minimizing the Gibb's free energy as a function of temperature at constant pressure using the Grand Canonical Linear Programming method presented elsewhere.[21]

RESULTS AND DISCUSSION

NMR. The ^{1}H NMR linewidths as a function of temperature for several NaH samples appear in Figure 1. In essence, when the hydrogen nuclear spins begin to

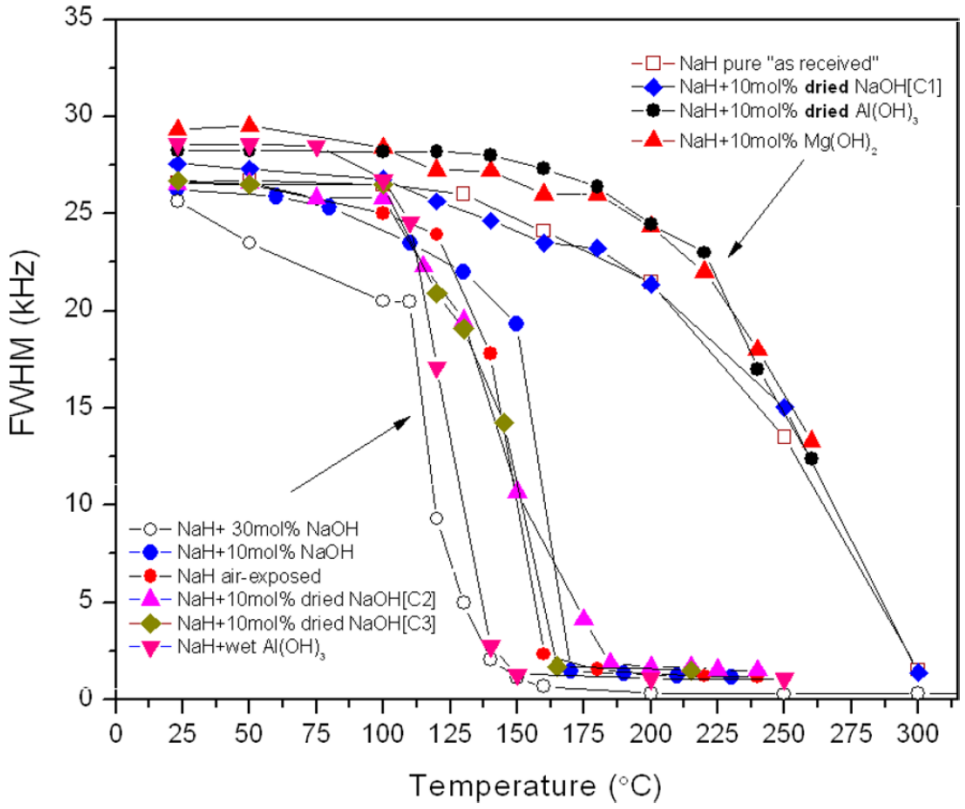

Figure 1. ^{1}H NMR linewidths of samples of NaH mixed with various additives. The plot indicates the full-width-at-half-maximum (fwhm) of the hydrogen resonance. Samples indicated in the top legend include pure NaH and NaH + dried hydroxides (C1 = temperature cycle 1). Samples indicated in the bottom legend include NaH + wet hydroxides, air-exposed NaH, and NaH + dried NaOH on the second and third temperature cycles (C2 and C3, respectively). The curves through the data are guides for the eyes.

translationally hop at a rate of 10^{5} s^{-1} or faster, the dipolar contributions to the hydrogen linewidth are time-averaged, resulting in a reduction in hydrogen NMR linewidth. Faster motion results in a narrower resonance line in this regime. The linewidth curves fall into two classes − those that narrow in the 250−275 °C range and those that narrow near 150

°C. The list of systems that narrow in the 250−275 °C range includes nominally pure NaH, NaH + dried NaOH on the first heating, NaH + dried $Al(OH)_3$, and NaH + $Mg(OH)_2$. All of the hydroxide additives are present in concentrations of approximately 10 mol %. Systems that narrow in the 150 °C range include NaH + wet (i.e., not specifically dried) NaOH in various concentrations, NaH + wet $Al(OH)_3$, air-exposed NaH, and the NaH + dried NaOH in subsequent heating cycles (indicated as [C2] and [C3] for temperature cycles 2 and 3 in Figure 1).

It is important to note that in all of the cases in Figure 1 the lineshapes showed uniform narrowing; that is, the entire resonance is narrowed. In Figure 2, the lineshapes

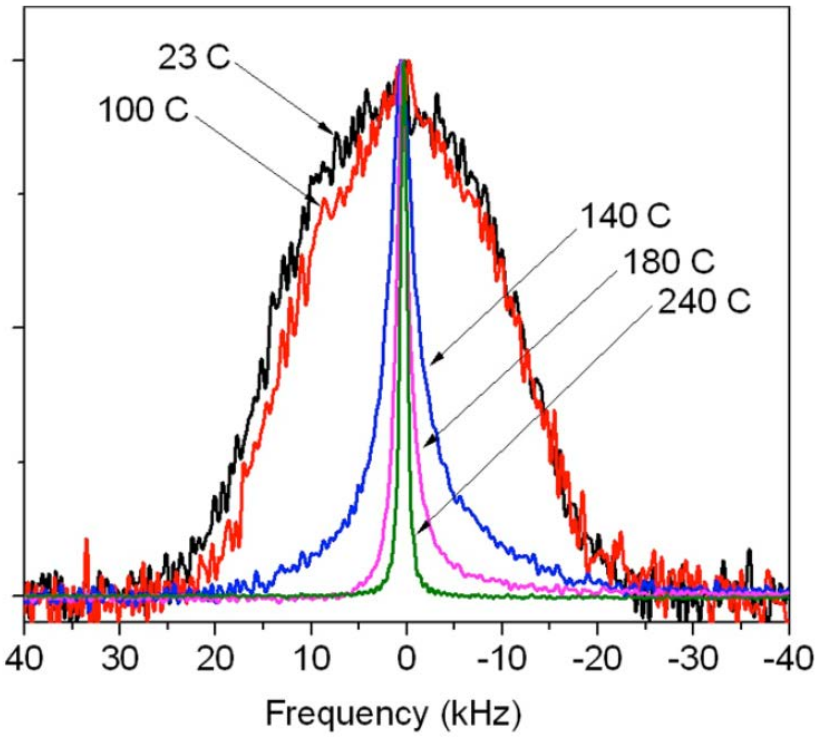

Figure 2. ^{1}H NMR of air-exposed NaH. The NaH was exposed to the air for 5 min prior to NMR measurements. All curves have been normalized to the room-temperature peak amplitude. Note the dramatic narrowing from 100 to 140 °C.

for air-exposed NaH are shown. This sample is representative of the group of samples whose resonances are seen to narrow around 150 °C in Figure 1. The uniform narrowing

observed here is in contrast to many reported systems, particularly ball-milled hydrides, which display a narrowed component superimposed on a broad resonance.[2,10,22] We also remark that NaH is the primary component in all the samples, so the hydrogen NMR signal is dominated by hydrogen from the NaH. For samples with smaller concentrations of NaOH, such as 1−5 mol % in hand-mixed powders, line narrowing was observed near 150 °C, but only for a portion of the hydrogen resonance. That is, for the samples with lower concentrations of NaOH, there was a broad signal (not narrowed) together with the narrowed component.

^{23}Na NMR was also performed on the samples above to investigate the effects of NaOH on the sodium motion. The previous study [13] of sodium hydride reported some cation motion in NaH with 30 mol % NaOH upon the second and third heating cycles at the highest temperatures. In the present study, where smaller amounts of NaOH were present, we saw no significant line narrowing of the ^{23}Na (beyond the narrowing expected from the hydrogen motion [13]), which would have indicated sodium motion in the samples (data not shown).

Thermal Activation Analysis. The hydrogen linewidths of the early narrowing samples in Figure 1 (example spectra for which are shown in Figure 2) are remarkably rapid functions of temperature. We tried fitting the thermal activation expression (Arrhenius, describing single particle, over-the-barrier motion) to the data using

$$\frac{1}{\tau} = \omega_0 \exp[-E/K_B T] \qquad (1)$$

Here τ is the jump time of hydrogen in NaH; ω_0 is the attempt frequency; E is the activation energy for hopping motion; and T is the absolute temperature. At the onset of narrowing, $1/\tau$ is nearly equal to the rigid lattice (unnarrowed) linewidth, about 10^5 s^{-1}. We set the attempt frequency to a typical vibrational frequency of 10^{13} s^{-1}. The activation energy is then chosen so that $1/\tau$ from eq 1 yields 10^5 s^{-1} at 150 °C; the result is E = 0.67 eV (E/k_B = 7800 K). However, as discussed below, this activation energy is too small to describe the strong temperature dependence of the narrowing.

In the regime of narrowing, the linewidth Δf varies reciprocally with the rate of motion [23−25]

$$\Delta f = \frac{1}{2\pi} M_2 \tau \qquad (2)$$

where M_2 is a mean-squared dipole−dipole interaction strength. Using the above-obtained estimate of activation energy E, the linewidth predicted from eq 2 falls approximately only half as rapidly with further temperature increase, compared to the data. A much larger value of E would describe the steep slope of the linewidths near 150 °C in Figure 1. However, this would require an unphysically large attempt frequency ω_0 to agree with the observed temperature (150 °C) of narrowing onset. Thus, a reasonable value of ω_0 and a value of E chosen to fit the temperature of the onset of narrowing cannot explain why the narrowing is such a strong function of temperature. As a comparison, for the samples that narrow in the 250−275 °C range, the variation of linewidth versus temperature is in accord with the activation energy (0.83 eV and E/k_B = 9600 K) similarly obtained. Indeed, the much steeper slope of the linewidth of the early narrowing samples, compared to those narrowing in the 250−275 °C range, is clearly evident in Figure 1. Thus, for the samples narrowing near 150 °C, the thermal activation calculations suggest that a more collective process, such as a phase transition, is involved in the rapid transition to complete motional narrowing. Measurements of linewidth on subsequent temperature cycles are reversible and repeatable, confirming that any phase transition is reversible.

Effects of Water. A perplexing aspect of the observed early narrowing is how a mixture of solid powders can interact at all since dry powder particles presumably touch only at asperities or protrusions. A more intimate and thorough contact would occur if there were small amounts of a liquid agent present. We performed hydrogen NMR on our wet NaOH powder without any added NaH to look for such a liquid. At and above 60 °C, a liquid signal is evident on top of the broad solid signal. According to published $NaOH{\cdot}H_2O$ phase diagrams, [26–28] a two-phase coexistence between pure NaOH solid and an NaOH-rich water-containing liquid occurs at and above 60 °C, which explains our observation of a liquid-like signal above 60 °C in the wet NaOH NMR. Below 60 °C the phase diagram predicts coexistence between NaOH solid and $NaOH{\cdot}H_2O$ monohydrate solid, and indeed only a solid signal is observed below that temperature in our wet

NaOH. According to the phase diagram, the relative amount of liquid in the two-phase coexistence above 60 °C increases with increasing H_2O content. From the relative intensities of the liquid and solid signals at 80 °C, we determined that the wet NaOH contained approximately 3.5 mol % water. We note that there was no liquid-like signal observed in specifically dried NaOH up to 250 °C.

In our NaH + wet NaOH mixed samples, we believe the absorbed water in the NaOH provides the medium to allow for the necessary contact between the NaH and NaOH powders. Similarly, in the NaH + wet $Al(OH)_3$ sample and the initially pure NaH sample that had been exposed to laboratory air for 5 min, we believe that residual water absorbed in the hygroscopic hydroxide or from the atmosphere reacts with the NaH to produce NaOH through

$$NaH + H_2O \rightarrow NaOH + H_2 \qquad (3)$$

Indeed, when the hydroxides were scrupulously dried prior to mixing with the NaH, the early line-narrowing effect vanished (see Figure 1) on the first heating. However, after heating beyond the 318 °C melting point of NaOH, subsequent heatings of the NaH + dry NaOH did show the onset of early line narrowing, indicating that the first thermal cycle caused a change in the NaH + dry NaOH mixture. Specifically, we propose that the molten NaOH partially dissolved into the NaH on the first heating, as discussed below, and exited the NaH as very small precipitates upon cooling. The resulting intimate NaH−NaOH contacts were effective on subsequent cycles for promoting rapid kinetics.

Effects of Other Additives. Beyond the systems in Figure 1, we examined many other systems, including NaH mixed with silica, alumina, NaBr, NaCl, NaF, and MgH_2. For hand-mixed samples of the above constituents, the effects on both the hydrogen and sodium linewidths were small. For ball-milled mixtures, even inert additives like SiO_2 resulted in a narrow component on top of a broad hydrogen resonance, similar to what has been reported for other ball-milled systems.[2,10,22] The effects of ball-milled impurities on NaH are not the subject of this work; by hand mixing our samples we avoided the complications of the narrow resonance component due to ball milling. We do note that ball milling our nominally pure dry NaH did not result in

any change in line narrowing of the main broad resonance compared to the initial NaH powder. It is possible that NaH does not ball mill to a small grain size in the absence of additives. For example, it has been noticed in LiH + LiOH that ball milling with additives leads to a much finer dispersal and mixing than does ball milling the compounds alone.[29] Also, some alanates ($NaAlH_4$ and $LiAlH_4$) are extremely difficult to refine by ball milling.[30]

Scanning Calorimetry. The strong temperature dependence of the line narrowing motivated us to use DSC on handmixed powders of NaH with wet NaOH. To enhance any effects, the concentration of NaOH was made to be 20 mol %, up from the 10 mol % used in many of the NMR samples. On first heating (not shown), there was a broad endothermic peak from 280 to 320 °C, which includes the melting of NaOH at 318 °C. Upon cooling, and on subsequent heating cycles, a prominent thermal anomaly was apparent near 150 °C, as presented in Figure 3. The heating (bottom) curves show an endothermic peak, and the cooling (top) curves show an exothermic peak, as would be expected for an equilibrium phase transition. Figure 3 presents data from the second and third heating cycles; clearly the data are reversible. The reversibility of this transition is a remarkable aspect of the NaOH−NaH system.

The enthalpy of the reaction calculated by integrating under the endothermic and exothermic peaks is roughly 50 J/g, i.e., 50 J per total grams, so 1360 J/mol. Thus, the

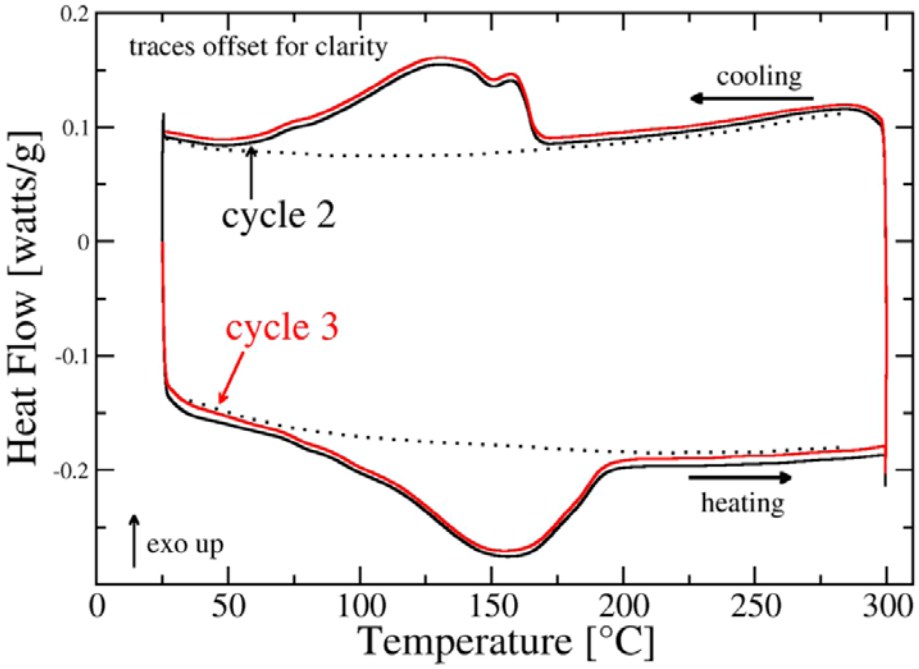

Figure 3. Differential scanning calorimetry (DSC) data for a 2:8 molar mixture of NaOH:NaH. The first cycle (not shown) is taken above the melting temperature of NaOH (318 °C). Subsequent cycles below the melting temperature of NaOH show the reversible behavior. The dashed lines are guides for the eyes, serving as baselines.

molar entropy change at the transition (taken as 150 °C) is 0.39R, where R is the gas constant. For an ideal solid solution of concentration *x*, the configurational entropy is

$$\Delta S = R\,[\,-x\,ln\,x - (1-x)\ln(1-x)\,] \qquad (4)$$

Using the present $x = 0.2$, we expect ΔS of about $0.5R$. The agreement with the measured value is as good as should be expected for such DSC data. In addition, the transition may not run to completion, and there may be short-range order in the solid solution, all of which would decrease the experimental entropy change.

The transition in NaH with NaOH resembles the behavior of KCl−NaCl, as studied by Barrett and Wallace.[31] There the miscibility gap between KCl and NaCl closes while still in the solid. At low temperatures, nearly pure KCl and NaCl are found, while a single-phase solid solution appears at high temperatures. Other systems such as NaCl−NaBr [32] and III−V pseudobinary semiconductor alloys [33] behave similarly.

X-ray Diffraction. In situ powder XRD was carried out to observe the NaH/NaOH mixtures during the heating process. We used a mixture of NaH + dried NaOH for this study. In situ XRD of physically mixed 2:8 ratio mixtures of NaOH:NaH from room temperature to 240 °C show a shifting of the NaH peaks, giving a thermal expansion of about 1.3% of the unit cell length, not significantly greater than our measurements of pure NaH at 1.15%. Our measurements of the thermal expansion of pure NaH were in reasonable agreement with those of Kuznetsov, with a linear expansion constant of $\alpha_L = 60 \times 10^{-6}$ °C. [34]

In an attempt to saturate the solubility limit of NaOH in NaH [35] and see the largest possible effect, we also used a mixture of approximately 80 mol % NaOH. The sample was exposed to an initial heat treatment of 330 °C for 1 h under 70 bar H_2, thus melting the NaOH. The sample was then cooled to room temperature and loaded into the hot-stage XRD. Figure 4 shows the initial XRD of the starting materials and relevant peak indices. The majority phase in this sample is NaOH, and the NaH (111) peak appears as a shoulder just below 32 degrees two-theta. The platinum peaks belong to the high-temperature sample holder. The in situ data are shown in

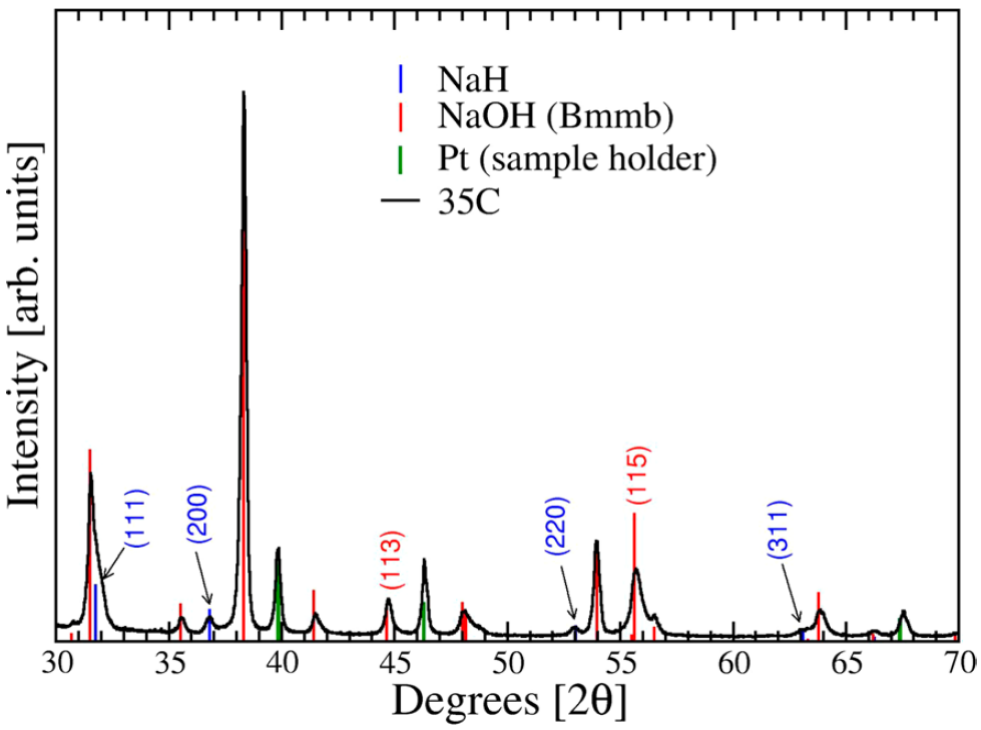

Figure 4. First XRD scan of the in situ data for premelted 80% NaOH with 20% NaH at 35 °C. Stick patterns are for NaH (blue), NaOH in spacegroup Bmmb (red), and platinum sample holder (green). The peak indexes (111), (200), (220), and (311) correspond to NaH.

Figure 5; the time progression begins at the bottom of the figure (T = 35 °C), proceeds upward as the sample is heated to

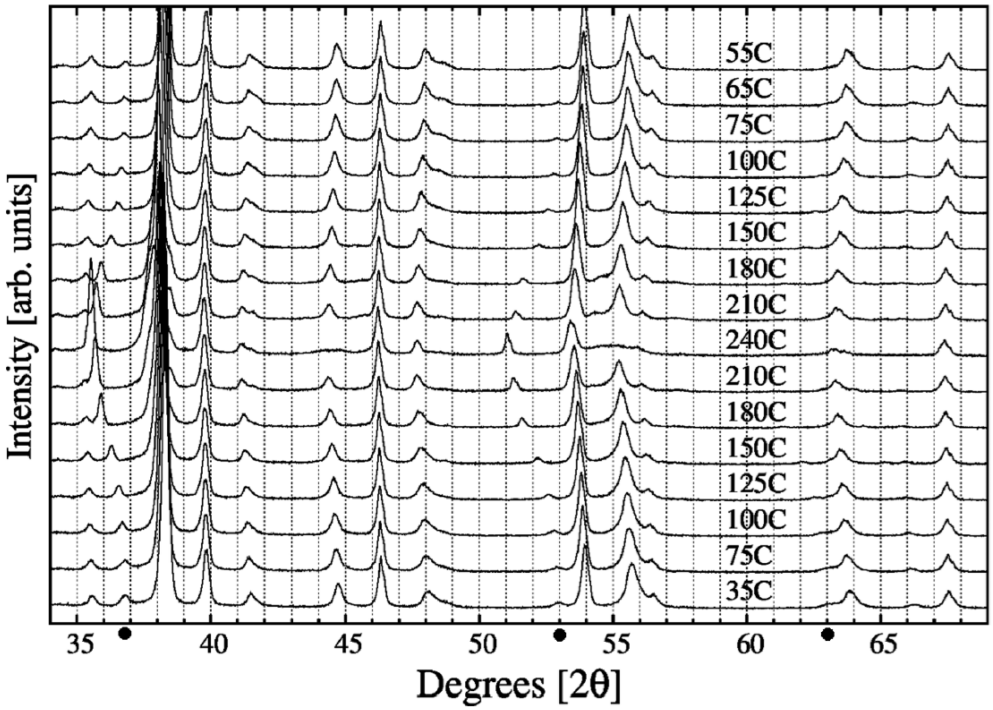

Figure 5. In situ XRD of 8:2 molar ratio of NaOH:NaH. Note the peak shifts of the NaH (200) at about 37° and (220) at about 53° (highlighted by black dots on the x-axis); the weak (311) at about 63° shifts similarly but is only evident with magnification. Refer to Figure 4 for identification of the peaks. Vertical guidelines (dotted lines) are given to emphasize the peak shifts.

240 °C, and ends at the top of the figure as the sample is cooled back to 55 °C.

The NaOH peaks present in Figure 5 shift slightly to lower angle as the temperature is increased and return to their roomtemperature positions as the sample is cooled. This shift corresponds to simple thermal expansion of the NaOH lattice with an increase in the cell volume from 131 $Å^3$ to about 134 $Å^3$, about 2% volumetrically (0.7% linear expansion). The NaH peaks, in contrast, show a more remarkable behavior. As the sample is heated to 240 °C, the NaH (200), (220), and (311) reflections (at 36.8°, 53.0°, and 63.1°, respectively, indicated by black dots in Figure 5) shift dramatically to lower angles, demonstrating an approximate 3.5% increase in lattice parameter, an approximately 11% increase in cell volume. As the sample cools, the reflections nearly return to their initial positions and intensities. The expansion suggests that some NaOH enters the NaH lattice on heating and exits upon cooling. At 240 °C, the NaH peaks sharpen and increase in intensity at the same time as several of the NaOH peaks (e.g., at

44.8°, 55.8°, and 64°) broaden and shrink. The loss of some NaOH peaks at 240 °C is likely related to the structural phase transition from Bmmb (orthorhombic) to $P2_1/m$ (monoclinic) that is reported to occur at 241 °C. [36,37]

In this picture, the effect of the first thermal cycle is to dissolve NaOH into the NaH and, upon cooling, to precipitate out the NaOH. The fine precipitates have larger contact area with the NaH and are small, both of which promote the kinetics in subsequent thermal cycles. The fine precipitates are involved in the DSC behavior on second and higher temperature cycles, as discussed above in connection with Figure 3.

For an fcc lattice (like NaH) with cube edge length *a*, the spacing *d* of the X-ray reflecting planes (specified by integers *h*, *k*, *l*) during a lattice expansion will obey the *d*-spacing formula

$$\frac{1}{d^2} = \frac{h^2+k^2+l^2}{a^2} \qquad (5)$$

The diffraction condition is given by

$$\frac{1}{d} = \frac{2\ \sin\theta}{\lambda} \qquad (6)$$

The NaH (200), (220), and (311) peaks appear to shift in accordance with the cubic *d*-spacing formula as temperature increases. Additionally, the shifted (220) peak appears to split at the highest temperatures, suggesting a small distortion in the fcc lattice. As the sample cools, the NaH returns to an fcc lattice parameter of 4.87 Å, the nominal value for pure NaH. [34] We note that NaOH has an fcc phase above 293 °C, [36] allowing NaOH to be compared to (fcc) NaH at the same temperature. For NaOH, the lattice parameter is 5.10 Å, [36] just 3% larger than the 4.95 Å of NaH, [34] all at 300 °C. The similar sizes imply that dissolution of NaOH into NaH is feasible.

We return to the question: why does the hydrogen in NaH diffuse so much faster (see Figures 1 and 2) once some NaOH has entered the NaH lattice? The increase in NaH lattice parameter even with the 20% NaOH material is barely larger than the thermal expansion for pure NaH (see above). Thus, lattice expansion does not explain the

increased rate of hydrogen motion. The OH dynamic orientational disorder may play a role [38] in the accelerated diffusion. In the end, the reason for enhanced motion of the hydrogen anions in NaH is not known.

First-Principles Calculations. The solubility of NaOH in NaH can be studied computationally by investigating the reaction

$$(1-x)\mathrm{NaH} + x\mathrm{NaOH} \rightarrow \mathrm{NaH}_{(1-x)}(\mathrm{OH})_x \qquad (7)$$

for $0 < x < 1$. The solid solution $NaH_{(1-x)}(OH)x$ is favorable when the free energy becomes less than the sum of the free energies of separated NaOH and NaH

$$\Delta F = F\left[NaH_{(1-x)}(OH)_x\right] - xF(NaOH) - (1-x)F(NaH) < 0 \qquad (8)$$

where F are molar free energies.

The free energy of a solid as a function of temperature can be evaluated by

Table 1. Total Energies (T = 0 K), Zero-Point Energy (ZPE), and Thermodynamic Data from First-Principles Calculations[a]

Compound	U_0 (eV/f.u.)	ZPE (eV/f.u.)	# f.u.	NaOH %	Conf. S (eV/K/cell)	Calc. S (298 K) (J/mol/K)	T_c (°C)	$\Delta H(T_c)$ (J/g)
NaOH	-13.766	0.364	32	-	-	60.78	-	-
NaH	-5.154	0.159	32	-	-	37.02	-	-
$Na_{32}H_{29}(OH)_3$	-190.200	5.651	1	9.38	0.00086	43.41	130	67
$Na_{32}H_{26}(OH)_6$	-215.709	6.290	1	18.75	0.00133	47.14	209	104

[a]The calculated critical temperatures indicate when the composite crystals become favorable. The enthalpy changes are given at the *calculated* critical temperatures.

$$F = U_0 + \sum_r \{\frac{\hbar\omega_r}{2} + k_B T(1-\exp[\frac{-\hbar\omega_r}{k_B T}])\} - TS_{conf} \qquad (9)$$

where U_0 is the electronic total energy (T = 0 K) of the structure from the geometric optimization via DFT; k_B is Boltzmann's constant; ω_r are the phonon frequencies of the crystal; and the first term in the sum is the zero-point energy (ZPE) representing the

atomic vibrations at T = 0 K. Sconf denotes the configurational entropy and is given by eq 4 for the pseudobinary compound $NaH_{(1-x)}(OH)_x$, considering the mixing between H and OH ions.

In the solid solubility calculations, the critical soluble temperature (T_c) is the temperature where the total free energy of a specific supercell becomes equal to that of the phase separated NaH and NaOH, i.e., where $\Delta F(T_c,x) = 0$, from eq 8. The enthalpy change at the critical temperature can be calculated by

$$\Delta H = T\Delta S = T[S(T,Na(OH)_x H_{(1-x)}) - xS(T,NaOH) - (1-x)S(T,NaH)] \quad (10)$$

Table 1 shows the calculated critical temperatures and enthalpy changes for the solid solution reactions. The appropriate supercell sizes were chosen to be large enough that the calculated entropies are close to the experimental values. The calculated critical temperatures indicate when the solid solution phase becomes favorable according to eq 8, and the enthalpy change is given at the calculated critical temperature. All calculations used a 2 × 2 × 2 density of k-space points.

The solution of NaOH in NaH was investigated by calculating the reaction free energies and enthalpies for reaction 7. In the calculations, NaOH in space group Bmmb was used since it is the stable phase in the experimental temperature range. The NaH/NaOH supercells were created by adding appropriate numbers of oxygen atoms in a 32 f.u. NaH supercell. Metropolis Monte Carlo Simulated Annealing (MMCSA) was used to distribute the OH positions uniformly in NaH by placing the OH as far apart in the supercell as possible (obeying periodic boundary conditions). The atomic coordinates and cell geometry of the generated structures were optimized using the DFT methods described above. The enthalpy changes for the solution transition were calculated for the critical temperature obtained from the Grand Canonical Linear Programming (i.e., ΔF = 0 in eq 8). Table 1 lists the calculated critical temperatures and the enthalpy changes of the solid solution of the NaOH in NaH at the critical temperatures. These temperatures in Table 1 are in reasonable accord with the experimental value of 150 °C from NMR at 10% NaOH content and from DSC at 20% NaOH. The enthalpies likewise show reasonable agreement, to within a factor of 2. The DFT calculations thus support the

interpretation of the NMR and DSC data, indicating a phase transition between segregated components and a solid solution.

CONCLUSIONS

Hydrogen NMR line narrowing of NaH hand mixed with NaOH occurs around 150 °C, approximately 100 °C cooler than for nominally pure NaH. Early hydrogen line narrowing is also obtained for NaH exposed to atmospheric moisture or moisture present in other compounds (i.e., wet $Al(OH)_3$) from the reaction

$$NaH + H_2O \rightarrow NaOH + H_2$$

The line narrowing is too strong a function of temperature to be represented by a physically reasonable Arrhenius dependence. Scanning calorimetry shows a reversible thermal anomaly near 150 °C for the system of mixed NaH and NaOH powders, after one thermal precycle. Powder XRD reveals a large and reversible lattice expansion of the NaH in the presence of excess NaOH beginning in the vicinity of 150 °C. DFT calculations show that the temperature for which $\Delta F = 0$ (the free energy of mixing) is comparable to our experimentally measured temperature.

Together, these data point to a reversible phase transition near 150 °C, with NaOH dissolving into solid NaH above the transition. Below this temperature, the NaOH is expelled from the NaH structure. The origins of the enhanced rate of hydrogen diffusion in NaH and the lower onset temperature of NMR line narrowing are not understood. However, the enhanced hydrogen diffusion observed here in sodium hydride samples containing hydroxide may be relevant for accelerating the hydrogen reaction kinetics of other hydrogen storage solids.

ACKNOWLEDGEMENTS

The authors gratefully acknowledge support from the US Department of Energy, Basic Energy Science, through grant DE-FG02-ER46256. TE-C acknowledges partial support from Washington University's Office of Undergraduate Research. We thank David Osborn in the Center for Nanoscience for assistance in collecting the in situ XRD

and DSC data. Special thanks are due to W. E. Buhro for alerting us to the work of Barrett and Wallace.

REFERENCES

(1) Jensen, T. R.; Andreasen, A.; Vegge, T.; Andreasen, J. W.; Stahl, K.; Pedersen, A. S.; Nielsen, M. M.; Molenbroek, A. M.; Besenbacher, F. Dehydrogenation Kinetics of Pure And Nickel-Doped Magnesium Hydride Investigated by in situ Time-Resolved Powder X-Ray Diffraction. *Int. J. Hydrogen Energy* **2006**, *31*, 2052−2062.

(2) Corey, R. L.; Ivancic, T. M.; Shane, D. T.; Carl, E. A.; Bowman, R. C., Jr.; von Colbe, J. M. B.; Dornheim, M.; Bormann, R.; Huot, J.; et al. Hydrogen Motion in Magnesium Hydride by NMR. *J. Phys. Chem. C* **2008**, *112*, 19784−19790.

(3) Gross, A. F.; Vajo, J. J.; Van Atta, S. L.; Olson, G. L. Enhanced Hydrogen Storage Kinetics of $LiBH_4$ in Nanoporous Carbon Scaffolds. *J. Phys. Chem. C* **2008**, *112*, 5651−5657.

(4) Stephens, R. D.; Gross, A. F.; Van Atta, S. L.; Vajo, J. J.; Pinkerton, F. E. The Kinetic Enhancement of Hydrogen Cycling in $NaAlH_4$ by Melt Infusion into Nanoporous Carbon Aerogel. *Nanotechnology* **2009**, *20* (204018), 1−6.

(5) Borgschulte, A.; Jain, A.; Ramirez-Cuesta, A. J.; Martelli, P.; Remhof, A.; Friedrichs, O.; Gremaud, R.; Züttel, A. Mobility and Dynamics in the Complex Hydrides $LiAlH_4$ and $LiBH_4$. *Faraday Discuss*. **2011**, *151*, 213−230.

(6) Stander, C. M. Z. Kinetics of Formation of Magnesium Hydride from Magnesium and Hydrogen. *Phys. Chem. N. F.* **1977**, *104*, 229−238.

(7) Hao, S.; Sholl, D. S. Role of Schottky Defects in Hydrogen and Metal Diffusion in NaH, MgH_2, and $NaMgH_3$. *J. Phys. Chem. Lett.* **2010**, *1*, 2968−2973.

(8) Singh, S.; Eijt, S. W. H. Hydrogen Vacancies Facilitate Hydrogen Transport Kinetics in Sodium Hydride Nanocrystallites. *Phys. Rev. B* **2008**, *78* (224110), 1−6.

(9) Gnanasekaran, T. Thermochemistry of Binary Na−NaH and Ternary Na−O−H Systems and the Kinetics of Reaction of Hydrogen/Water With Liquid Sodium −A Review. *J. Nucl. Mater.* **1999**, *274*, 252−272.

(10) Shane, D. T.; Corey, R. L.; McIntosh, C.; Rayhel, L. H.; Bowman, R. C., Jr.; Vajo, J. J.; Gross, A. F.; Conradi, M. S. LiBH4 in Carbon Aerogel Nanoscaffolds: An NMR Study of Atomic Motions. *J. Phys. Chem. C* **2010**, *114*, 4008−4014.

(11) Sorte, E. G.; Bowman, R. C., Jr.; Majzoub, E. H.; Verkuijlen, M. H. W.; Udovic, T. J.; Conradi, M. S. Mobile Species in $NaAlH_4$. *J. Phys. Chem. C* **2013**, *117*, 8105−8113.

(12) Skripov, A. V.; Cherepanov, Yu. G.; Aleksashin, B. A.; Rychkova, S. V.; Stepanov, A. P. Nuclear Magnetic Resonance Study of Deuterium Diffusion in $ZrCr_2D_x$. *J. Alloys Compd.* **1995**, *227*, 28−31.

(13) Sorte, E. G.; Corey, R. L.; Bowman, R. C., Jr.; Birkmire, D.; Zidan, R.; Conradi, M. S. NMR Studies of NaH. *J. Phys. Chem. C* **2012**, *116*, 18649−18654.

(14) Brady, S. K.; Conradi, M. S.; Majer, G.; Barnes, R. G. Proton Magnetic Resonance Spectra of YH_3 and LuH_3. *Phys. Rev. B* **2005**, *72* (214111), 1−4.

(15) Kresse, G.; Hafner, J. Ab initio Molecular Dynamics for Liquid Metals. *Phys. Rev. B* **1993**, *47*, 558.

(16) Kresse, G.; Furthmuller, J. Efficient iterative schemes for ab initio total-energy calculations using a plane-wave basis set. *Phys. Rev. B* **1996**, *54*, 11169−11186.

(17) Perdew, J. P. In Electronic Structure of Solids; Ziesche, P., Eschrig, H., Eds.; *Akademie Verlag: Berlin*, **1991**; Vol. *11*.

(18) Blochl, P. E. Projector Augmented-Wave Method. *Phys. Rev. B* **1994**, *50*, 17953−17979.

(19) Kresse, G.; Joubert, D. From Ultrasoft Pseudopotentials to the Projector Augmented-Wave Method. *Phys. Rev. B* **1999**, *59*, 1758−1775.

(20) Monkhorst, H. J.; Pack, J. D. Special Points for Brillouin-zone Integrations. *Phys. Rev. B* **1976**, *13*, 5188−5192.

(21) Akbarzadeh, A. R.; Ozolins, V.; Wolverton, C. First-Principles Determination of Multicomponent Hydride Phase Diagrams: Application to the Li-Mg-N-H System. *Adv. Mater.* **2007**, *19*, 3233−3239.

(22) Heitjans, P.; Wilkening, M. Ion Dynamics at Interfaces: Nuclear Magnetic Resonance Studies. *MRS Bull.* **2009**, *34*, 915−920.

(23) Anderson, P. W.; Weiss, P. R. Exchange Narrowing in Paramagnetic Resonance. *Rev. Mod. Phys.* **1953**, *25*, 269−276.

(24) Slichter, C. P. Principles of Magnetic Resonance; *Springer: New York*, **1980**.

(25) Abragam, A. The Principles of Nuclear Magnetism; *Oxford: London*, **1961**.

(26) Treptow, R. S. Phase Diagrams for Aqueous Systems. *J. Chem. Educ.* **1993**, *70*, 616−620.

(27) ORNL. Transphase cool storage test report. http://www.osti.gov/bridge/purl.cover.jsp?purl=/10112710/ (accessed Aug **2013**).

(28) JSIA. Safe handling of caustic soda. http://www.jsia.gr.jp/data/handling_01e.pdf (accessed Aug **2013**).

(29) Vajo, J. J.; Skeith, S. L.; Mertens, F.; Jorgensen, S. W. Hydrogen-Generating Solid-State Hydride/Hydroxide Reactions. *J. Alloys Compd.* **2005**, *390*, 55−61.

(30) Varin, R. A.; Czujko, T.; Wronski, Z. S. Nanomaterials for Solid State Hydrogen Storage; *Springer: New York*, **2008**.

(31) Barrett, W. T.; Wallace, W. E. Studies of NaCl-KCl Solid Solutions. I. Heats of Formation, Lattice Spacings, Densities, Schottky Defects and Mutual Solubilities. *J. Am. Chem. Soc.* **1954**, *76*, 366−369.

(32) Fineman, M. A.; Wallace, W. E. Heats of Formation and Some Derived Thermodynamic Properties of NaCl-NaBr Solid Solutions. *J. Am. Chem. Soc*. **1948**, *70*, 4165−4169.

(33) Wei, S.-H.; Ferreira, L. G.; Zunder, A. First-Principles Calculation of Temperature-Composition Phase Diagrams of Semiconductor Alloys. *Phys. Rev. B* **1989**, *41*, 8240−8269.

(34) Kuznetsov, V. G.; Shkrabkina, M. M. X-ray Diffraction Study of NaH and KH at Temperatures from 20 to 400 °C. *Zh. Struk. Khim*.**1962**, *3*, 553−558.

(35) Mikheeva, V. I.; Shkrabkina, M. M. Solid Solutions in the NaOH-NaH and KOH-KH Systems. *Russ. J. Inorg. Chem.* **1962**, *7*, 1251−1255.

(36) Bleif, H.-J.; Dachs, H. Crystalline Modifications and Structural Phase Transitions of NaOH and NaOD. *Acta. Cryst. A* **1982**, *38*, 470−476.

(37) Douglas, T. B.; Dever, J. L. Anhydrous Sodium Hydroxide: The Heat Content From 0° to 700° C, the Transition Temperature, and the Melting Point. *J. Res. Natl. Bur. Stand*. **1954**, *53*, 81−90.

(38) Sherwood, J. N. The Plastically Crystalline State; *Wiley & Sons: New York*, **1979**.

III. Density Functional Theory of MH–MOH Solid Solubility (M = Alkali) and Experiments in NaH–NaOH

Gang Wang,[†] C. L. Carr,[†] Dongxue Zhao,[†] E. G. Sorte,[‡,||] Tim Ellis-Caleo,[‡] M. S. Conradi,[‡] R. C. Bowman, Jr.,[§] and E. H. Majzoub[*,†]

[†]*Center for Nanoscience and Department of Physics and Astronomy, University of Missouri St. Louis, One University Boulevard, St. Louis, Missouri 63121, United States*

[‡]*Department of Physics, Washington University, One Brookings Drive, Saint Louis, Missouri 63130, United States*

[§]*RCB Hydrides, LLC, 117 Miami Avenue, Franklin, Ohio 45005, United States*

ABSTRACT

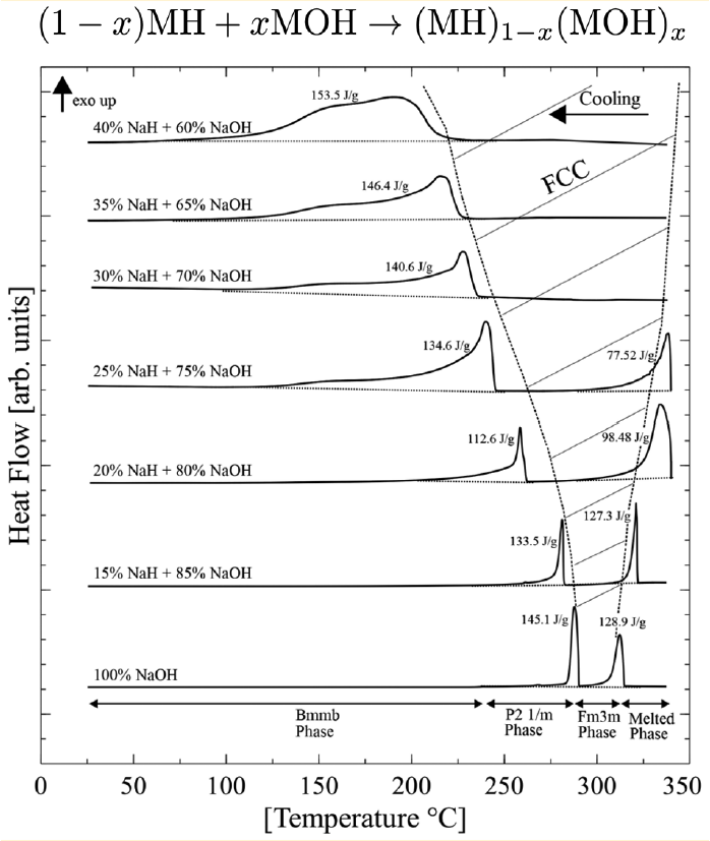

We present first-principles solubility calculations of $H^-/[OH]^-$ mixing in binary alkali metal hydrides MH and their corresponding hydroxides MOH, for M ={Li, Na, K, Rb, Cs}. Solid solubility in the MH−MOH system may play an important role in solid-phase reactions involving the MH system, including for example many aluminum-based complex hydrides of the alkali metals, such as $NaAlH_4$ and $LiAlH_4$. Our results indicate that the available cell volume for H^- and OH^- groups correlates strongly with mixing, and MOH is soluble in MH for M ={Na, K, and Rb} where available volumes for H^- and OH^- anions differ by less than about 15%, very similar to a Hume−Rothery type rule for intermetallics. The predicted mixing temperatures for the K and Rb systems are lower than for the Na system, in part because of the similarity in MH and MOH primitive cell volumes. Critical temperature diagrams for the formation of solid solution MH−MOH mixtures as a function of MOH concentration are calculated using a free energy minimization in the grand canonical ensemble. Differential scanning calorimetry and in situ X-ray diffraction measurements of the $NaH_{1-x}(OH)_x$ system are presented for a range

of compositions ($0.3 \leqslant x \leqslant 1.0$). As the temperature is raised, the polymorphic phase transitions present in NaOH occur concomitantly with H^-/OH^- mixing, eventually forming a single-phase cubic structure; the behavior is fully reversible on cooling. Finally, the formation of solid solution MH/MOH reduces the decomposition temperature of $NaH_{1-x}(OH)_x$ to lower temperatures than pure NaH while increasing the stability in the KH and RbH systems.

INTRODUCTION

Diffusion of hydrogen and the rapid mass transport of metal species are important for many complex anionic hydrogen storage materials. In particular, sodium aluminum hydride ($NaAlH_4$) decomposes in two steps, resulting in phase separated Na_3AlH_6 + Al, and NaH + Al, respectively. This system reversibly absorbs hydrogen with the addition of a few mol % of transition metal dopant.[1] While extensive theories of mass transport have been developed, [2,3] they do not consider the effect of impurities such as oxygen/hydroxide that are unavoidable in practical applications. The family of alkali metal alanates that are of interest in the hydrogen storage community also includes $LiAlH_4$, because of its large reversible hydrogen wt %, and $KAlH_4$, which is evidently reversible without the need for a catalyst.[4] Alanate reversibility could be influenced by residual oxygen contamination via faster diffusion and mass transport of M in an MH/MOH solid solution phase. Our results indicate that the similarity in cell volume available to H^- and OH^- anions in the MH and MOH lattices, respectively, strongly influences the onset of mixing and may provide a partial explanation of this behavior.

The objective of this work is to more fully understand the solid solution formation in alkali metals and alkali metal hydroxides that may be relevant for solid state reactions, including but not limited to metal hydrides. In previous work, we investigated mixing in the NaH/NaOH system, with a focus on the NaH-rich side of the pseudobinary NaH/NaOH phase diagram [5] and demonstrated that thermal activation alone was unable to account for ^{1}H NMR line narrowing with increasing temperature in a 10 mol % NaOH sample. Further, differential scanning calorimetry was indicative of a phase transition. This paper presents a comprehensive density functional theory (DFT) investigation of the enthalpy of mixing of MOH in MH where M ={Li, Na, K, Rb, and Cs}. We present these

results via the calculation of critical temperatures for the onset of mixing of MH and MOH, at *fixed* MH/MOH *ratios*, i.e., we calculate the onset of mixing for the reaction $(1 - x)\mathrm{MH} + x\mathrm{MOH} \rightarrow \mathrm{MH}_{1-x}(\mathrm{OH})_x$. We make no attempt to calculate the full pseudobinary phase diagram because of the difficulty introduced by the many soft modes that appear in structures containing OH^- groups, where the potential energy surface for OH^- rotations is relatively flat. Because we calculate the enthalpy of mixing at fixed concentration and ignore partially segregated possibilities, e.g., $y\mathrm{MH} + \mathrm{MH}_{1-z}(\mathrm{OH})_z$, our critical temperatures represent lower bounds for the onset of mixing.

In this work, we also present an experimental study of the NaH/NaOH pseudobinary phase diagram over a limited composition range and compare our findings with predictions obtained from the computational study and previous work. In the early studies by Mikheeva et al.,[6] the hydroxide-rich sides of the pseudobinary NaH/NaOH and KH/KOH phase diagrams were experimentally investigated. Their work demonstrated restricted regions of solid solution formation in the NaH/NaOH system. The authors determined there exists two regions of solid solution phases: the α phase solid solution consisting of H^- substitution on OH^- sites in orthorhombic (Bmmb) NaOH and the β phase solid solution consisting of H^- substitution on OH^- sites in fcc NaOH. The phase diagram shows the region of the α phase solution forms up to 27 and 32 mol % NaH at room temperature and 200 °C, respectively. The region of the β phase solution is shown to exist up to 36 and 75 mol % NaH at 240 and 450 °C respectively. Between the α and β regions there is a very small region that contains both α and β phase solid solutions. Outside these regions mixtures of α + NaH and β + NaH are present where the dividing line is at roughly 225 °C. There is no solubility shown for NaOH on the NaH-rich side of the phase diagram in the Mikheeva work.[6]

Because of its importance in hydrogen storage reactions, we study extensively the hydride-rich side of the phase diagrams, where our computational work shows that a solid solution can form for sample compositions containing less than 41 and 50 mol % hydroxide in the NaH/NaOH and KH/KOH systems, respectively. The extreme reactivity of KOH prevented us from collecting experimental data for this system, and we focused experimentally on the study of the NaH/NaOH system.

The manuscript is organized as follows. In the second section we introduce our computational methods and construction of the solid-solution supercells used in our DFT calculations. In the third section we discuss our experimental methods. The fourth section presents the main results obtained in this work.

COMPUTATIONAL METHODS

All density functional theory (DFT) calculations were performed using the Vienna ab initio simulation package (VASP).[7,8] Standard projector augmented wave (PAW) pseudopotentials were used along with the PW91[9,10] generalized gradient approximation (GGA) for the exchange correlation. The cutoff energy was 600 eV for all calculations with an electronic convergence criterion of 10^{-6} eV. Atomic coordinate and cell parameter relaxations were completed until the forces on the ions were less than 0.005 eV/Å. Frozen phonon calculations were performed in the harmonic approximation using the linear response capability in VASP 5, and the phonon frequencies were used to calculate finite temperature free energies.

Gas-phase energy of hydrogen was calculated by placing one H_2 molecule in a 20 × 20 × 20 $Å^3$ cell, using only the Γ point (k = 0). Cubic $Fm\bar{3}m$ 2 × 2 × 2 supercells of MH, M ={Li, Na, K, Rb, and Cs} were chosen to simulate the hydrides. Monkhorst−Pack grids were used for Brillouin zone integration. [11] Supercell sizes and the space groups of the crystal structures are listed in Table S1 (Supporting Information). K-point meshes are listed in Table S2. To improve the physical accuracy of the calculations, successively larger supercells were chosen to reproduce the experimentally measured entropies.

MH and MOH Crystal Structures and Construction of Supercells. Our DFT calculations of the solubility focused on the MH-rich side of the phase diagram; therefore, supercells of mixed MH/MOH were constructed by starting from a 2 × 2 × 2 supercell of cubic MH and substituting oxygen atoms in one of six octahedral positions around the hydrogen atoms, along the coordinate axes, to obtain a composition of $[MH_{1-x}(OH)_x]$. The initial O−H bond length was placed at 0.88 Å. The oxygen atom positions were randomized using a simulated annealing algorithm (SA).[12] The energy functional (cost function) used was the total electrostatic energy:

$$E = \sum_{i \neq j} \frac{e_i e_j}{r_{ij}} \quad (1)$$

where e_i and e_j are the reference charges of elements *i* and *j*. The idealized reference charges for M, H, and O were +1, +1, and −2, respectively, and r_{ij} is the distance between the elements *i* and *j*. For the purposes of this SA application, it is not important that the assigned atomic charges be correct. All randomized solid-solution structures were fully relaxed using the conjugate gradient algorithm in VASP. By use of periodic boundary conditions in the SA simulations, the Coulomb interaction was calculated within a radius of one unit cell dimension centered on every atom. Standard SA protocol compares the reference energies of an existing configuration (E_1) and a new configuration (E_2). All downhill moves are accepted, and uphill moves are accepted with a Boltzmann probability of $e^{-(E_2-E_1)/T}$ if $E_2 > E_1$, where T represents the annealing reference temperature.12 We used an exponential annealing schedule with $T_n = T_i e^{-[(1/N)ln(T_i/T_f)]n}$ where $T_i = 100$ was the initial temperature parameter and $T_f = 1 \times 10^{-3}$ was the final parameter. We used $N = 30$ temperature steps, where *n* refers to the *n*th step.

Solid-Solubility Calculations. The solubility of MOH in MH where M ={Li, Na, K, Rb, and Cs} can be studied by investigating the reaction

$$(1 - x)\mathrm{MH} + x\mathrm{MOH} \rightarrow \mathrm{MH}_{(1-x)}(\mathrm{OH})_x \quad (2)$$

where $0 < x < 1$. The compound $\mathrm{MH}_{(1-x)}(\mathrm{OH})_x$ is favorable when the free energy, *F*, of the compound is less than the sum of the free energies of MOH and MH:

$$\Delta F = F\,[\mathrm{MH}_{(1-x)}(\mathrm{OH})_x] - x\,F(\mathrm{MOH}) - (1-x)\,F(\mathrm{MH}) < 0 \quad (3)$$

The standard expression for the Helmholtz free energy of a solid as a function of temperature is given by

$$F = U_0 + \sum_r \left[\frac{1}{2}\hbar\omega_r + k_B T \ln\left(1 - e^{-\frac{\hbar\omega_r}{k_B T}}\right)\right] - TS_{conf.} \quad (4)$$

where U_0 is the electronic total energy of a crystal from the geometric optimization using DFT, k_B is Boltzmann's constant, ω_r values are the (harmonic) phonon frequencies derived via the linear response method in VASP, and $\sum_r (1/2)\hbar\omega_r$ is the zero point energy (ZPE) representing the atomic vibrations at absolute zero. S_{conf} denotes the configurational entropy. Random occupancy of a binary mixture was evaluated using the standard expression

$$S_{conf} = -Nk_B[x\ln(x) + (1-x)\ln(1-x)] \tag{5}$$

with $x = [OH^-]$ and $1 - x = [H^-]$, and N is the number of formula units.

In the solid solubility calculations, the critical soluble temperature (T_c) is obtained when $\Delta F(T_c,x) = 0$. As discussed above, we calculate T_c for the case of phase segregation into pure MH + MOH only. The enthalpy change at the critical temperature can be calculated from $dF = dH - TdS = 0$:

$$\Delta H = T\left[S\left(T, \mathrm{MH}_{(1-x)}(\mathrm{OH})_x\right) - xS(T,\mathrm{MOH}) - (1-x)S(T,\mathrm{MH})\right] \tag{6}$$

The formation of the solid solution is endothermic when $\Delta H > 0$.

We also include in our calculations the decomposition of the MH/MOH mixtures that results in the release of hydrogen gas. In these calculations, the Gibbs' free energy minimizations were performed using the grand canonical linear programming method (GCLP),[13] assuming a H_2 reservoir, to account for decomposition and hydrogen release at P = 1 bar H_2. The chemical potential of H_2 can be evaluated with the following expression.

$$\mu = U_0 + F_v(T) + F(T,p) \tag{7}$$

Here U_0 is the electronic energy of a hydrogen molecule evaluated by the first-principles calculations of a hydrogen molecule in a large volume-conserved cell. $F_v(T)$ is the

vibrational free energy. $F(T,p)$ contains the translational and rotational motions, along with the interactions between hydrogen molecules. The last term was taken from the experimental entropy of hydrogen under standard conditions.[14]

EXPERIMENTAL METHODS

NaH (95 wt %) was purchased from Sigma-Aldrich and used as received. NaOH (97 wt %) was purchased from Fisher Chemical and was dried at 300 °C under dynamic vacuum for 12 h in order to remove any remaining water. No hydrates were visible in X-ray diffraction or nuclear magnetic resonance measurements after drying.[5] All samples were prepared and handled in an Ar atmosphere glovebox with oxygen and H_2O levels below 1 ppm. All NaH/NaOH samples were hand mixed with mortar and pestle in our glovebox for approximately 5 min prior to calorimetry or X-ray diffraction measurements. All mixtures are given in molar percent.

Differential scanning calorimetry (DSC) was performed on a TA Instruments Q2000 series analyzer. About 6 mg of sample was loaded in an aluminum pan with a hermetically sealed lid in an Ar glovebox. The sample was heated from 25 °C to a maximum of 340 °C and then cooled to 25 °C at a rate of 5 °C/min using flowing nitrogen gas.

The in situ powder X-ray diffraction (XRD) was performed on a Rigaku Ultima IV diffractometer using the standard Bragg−Brentano scattering geometry and Cu K_α radiation. The NaH/NaOH samples were placed in a rectangular aluminum sample holder and sealed with thin adhesive Kapton tape during preparation in the glovebox. The Kapton tape provides an airtight seal up to about 300 °C. Powder samples were compacted in the sample holder for better thermal transfer than a loose powder would provide. The aluminum XRD sample holder was heated with a Dale 20 W power resistor fastened to the bottom surface. The sample temperature was maintained using an Omega Autotune controller, and the holder temperature was measured with type-K thermocouples. The samples were heated from room temperature up to 260 °C, and the XRD spectra were recorded in roughly 30−50 °C temperature intervals from 22 to 260 °C and again on cooling. For a few of the compositions, the samples were heated a second time to a temperature of 325 °C and cooled. XRD spectra were recorded at 325 °C and

again at room temperature. A range from 30° to 70° of 2θ was used for all scans. The step size was 0.02° 2θ, with a scanning speed of 1.5°/min.

Attempts were made to investigate the KH/KOH system, but strong reactivity of these samples with our Kapton tape and aluminum sample holders for XRD and DSC prevented the collection of reliable data. Further, it is generally observed that as one goes down the alkali metal group, the more reactive is the metal. Given the high reactivity of our KH/KOH samples with our sample holder materials, we did not attempt experiments with RbH/RbOH.

RESULTS AND DISCUSSION

Not surprisingly, crystal structures of the alkali hydrides and their hydroxides share many features. The structures of MH for M ={Li, Na, K, Rb, and Cs} all have the $Fm\bar{3}m$ space group.[15] The known structures of the hydroxides tend toward this cubic symmetry at high temperature presumably because of rapid rotation of the OH^- units except for LiOH that remains in *P*4/*nmm* up to 473 °C.[16] NaOH exhibits polymorphism starting with the low temperature structure in Bmmb until 241 °C. Between 241 and 295 °C, NaOH has the space group $P2_1/m$, and the structure above 295 °C is $Fm\bar{3}m$.[16] The low temperature structure of KOH is $P2_1/m$ until 244 °C at which point it transforms to $Fm\bar{3}m$.[16] The low temperature structure of RbOH is $Cmc2_1$ until −8 °C and is $P2_1/m$ from −8 to 235 °C. Above 235 °C, it is $Fm\bar{3}m$.[16] The structure of CsOH at temperatures below −39 °C is *Pmnb*, above which it becomes *Bmmb*, transforming to $Fm\bar{3}m$ above 225 °C.[16]

For the purpose of calculating the free energies and critical temperatures of mixing, we use the fully relaxed, ground-state structures obtained at T = 0 K. As mentioned above, DFT relaxation of literature structures for the alkali metal hydroxides often results in symmetry breaking due to the presence of soft modes. In nature, anharmonic effects at finite temperature likely stabilize these modes; recall our calculations treat phonon modes in the harmonic approximation. For example, DFT relaxation of the LiOH supercell using the literature structure in symmetry *P*4/*nmm* will break this symmetry, resulting in a structure with no symmetry (*P*1). Phonon vibrational frequencies calculated for supercells of the remaining hydroxides (NaOH, KOH, RbOH,

and CsOH) all contained imaginary modes. The method of mode following[17] was used to attain stable structures for all hydroxides. The resulting space groups are listed in Table S1. The differences in the DFT calculated total energies from these relaxations provide an estimated error of about ±80 °C for the calculated critical temperatures, T_c.

LiH/LiOH System. The LiH/LiOH system is uninteresting in that any mixture of LiH and LiOH is predicted via our GCLP calculations to decompose with the release of hydrogen gas before formation of a solid solution phase. The mixture of LiH and LiOH is predicted to release H2 through the reaction

$$\mathrm{LiH + LiOH \rightarrow Li_2O + H_2} \tag{8}$$

with an enthalpy change of −18.28 kJ/mol H_2 at T = 0 K. Forbidding the reaction in eq 8, the enthalpy of mixing was calculated for the composition $Li_{32}H_{31}OH$, even though the composite crystal is evidently unfavorable against H_2 formation. The solid solution would form at 708 °C with an enthalpy of 219 J/g (1.86 kJ/mol reaction), well above the predicted critical temperature for eq 8. Numerous experimental studies are consistent with these findings in that only the LiH, LiOH, Li_2O, and $LiOH·H_2O$ have been observed for this system under various conditions.[18−23]

NaH/NaOH System. The calculated cell volume of cubic NaH is 28.02 $Å^3$/f.u., and the cell volume of stable modefollowed *Bmmb* NaOH (in space group $Cmc2_1$) is 30.48 $Å^3$/f.u. Figure 1 shows the DFT-relaxed unit cell volume ratio of $MH_{(1-x)}(OH)_x$

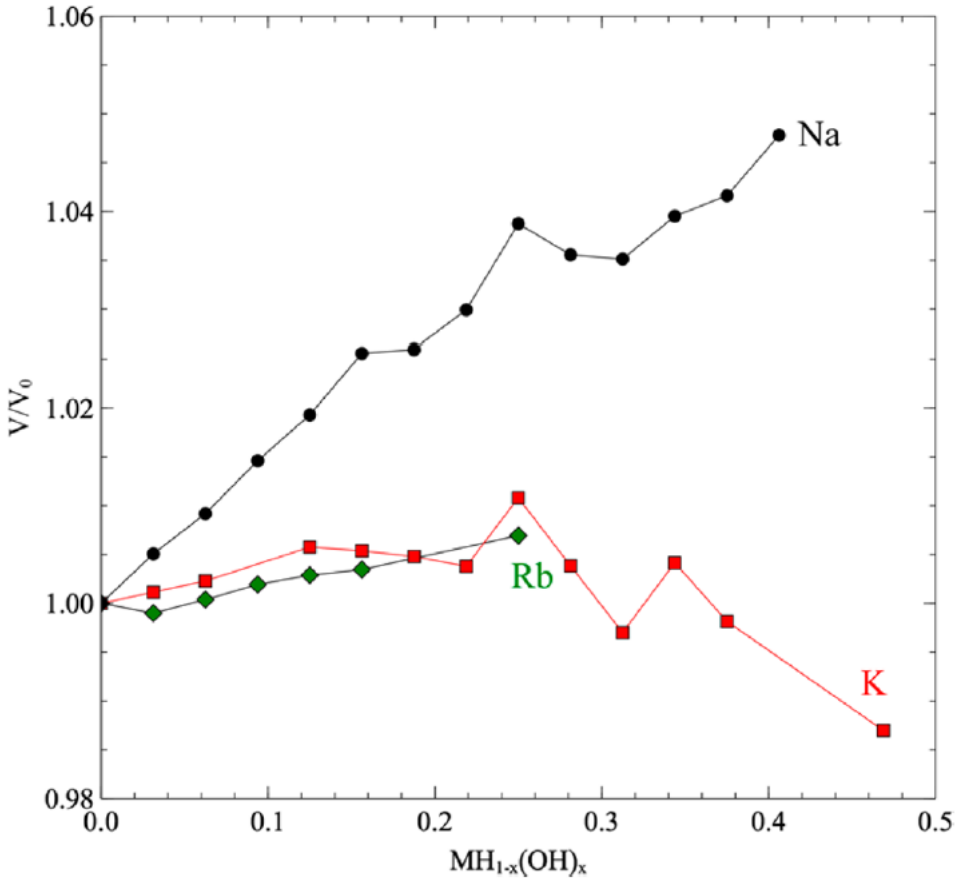

Figure 1. Relaxed crystal volume expansions as a function of MOH concentration; M = Na (black circle), K (red square), Rb (green diamond).

to MH for $0 \leqslant x \leqslant 1$. The black circles represent $NaH_{(1-x)}(OH)_x$. The volume increases with the increase of NaOH concentration (x) from NaH to NaOH. This is expected as the crystal shifts from NaH-like to NaOH-like and is consistent with the larger cell volume of pure NaOH.

Figure 2 shows the hydride rich side of the calculated critical temperature diagram for the NaH/NaOH system, which was not explored in Mikheeva's work. Below the green curve is where NaOH and NaH are phase separated. The green curve represents the calculated critical temperatures above which the solid solution is favorable:

$$(1-x)\mathrm{NaH} + x\mathrm{NaOH} \rightarrow \mathrm{NaH}_{(1-x)}(\mathrm{OH})_x \qquad (9)$$

Table S3 shows the critical temperature and enthalpy for eq 9 for different NaH/NaOH ratios. The data indicate that formation of the solution is endothermic above the critical temperature and also show that the critical temperature increases with the increase of hydroxide concentration x. The solution is predicted to be stable until x = 0.41, above which the two-phase mixture *decomposes before mixing* according to the following reaction.

$$NaH + NaOH \rightarrow Na_2O + H_2 \quad (10)$$

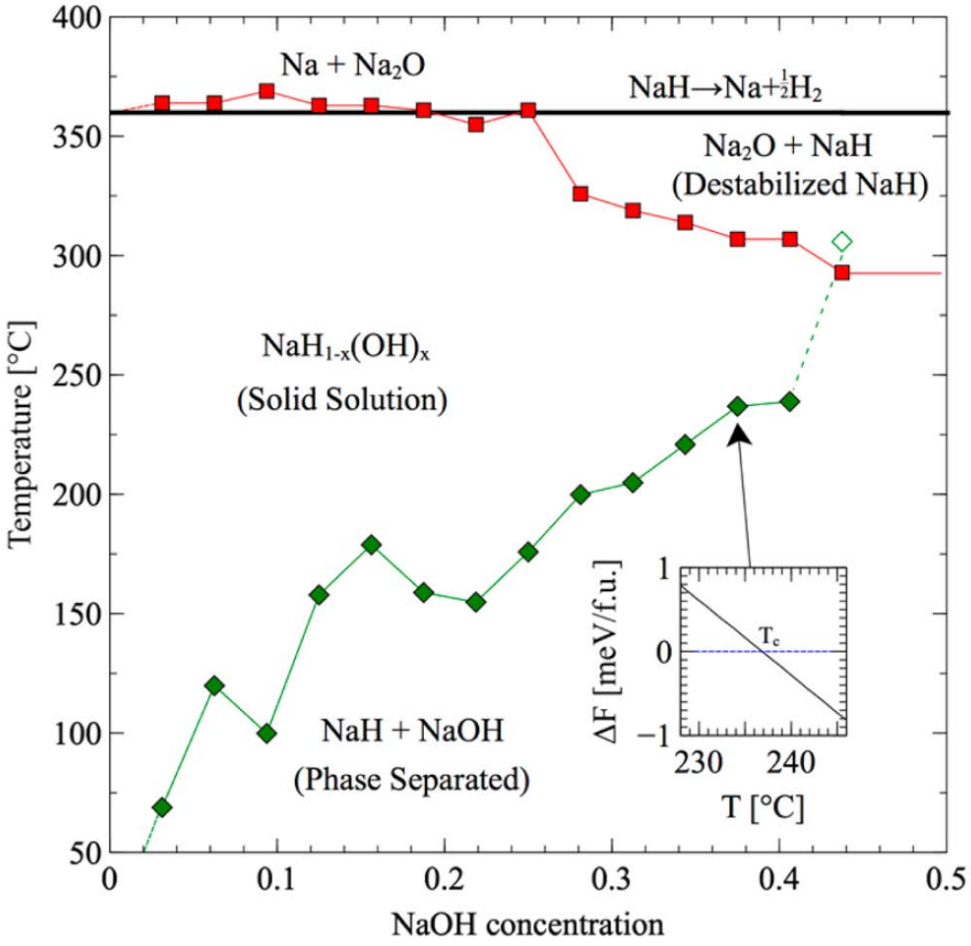

Figure 2. Critical temperatures for mixing and decompositions in the NaH/NaOH system: green, critical temperature; red, decomposition of solid solution; black, decomposition of NaH at P = 1 bar of H_2. Inset illustrates critical temperature.

This reaction is predicted to occur around 293 °C with an enthalpy of about 59 kJ/mol H_2 when $x > 0.41$. In Figure 2, the region between the green and red curves is where only the solid solution exists. The red curve represents the decomposition of the solid solution. At concentrations below about $x = 0.25$, the solid solution decomposes at essentially the same temperature as that of pure NaH, represented by the black line. At concentrations larger than $x = 0.25$, the decomposition temperature of the solid solution decreases, forming a new region containing Na_2O and NaH. This region extends above the red curve up to the black line that represents the decomposition of pure NaH. Solid solution decomposition occurs as

$$NaH_{(1-x)}(OH)_x \rightarrow (1-2x)NaH + xNa_2O + xH_2 \quad (11)$$

Reactions such as the mixing and decomposition shown in Figure 2 represent the free energy only and ignore kinetics. The free energy critical temperatures are a lower bound; if the reaction had no kinetic barrier, it would proceed as soon as thermodynamically feasible. In addition, the physical accuracy of DFT reaction enthalpies provides only rough estimates of the critical solution temperatures. As the decomposition curve (red in Figure 2) and the solid-solution/phase-segregation curve (green in Figure 2) approach each other at large OH^- concentrations, the actual physical behavior will be strongly influenced by the kinetic barriers. Our experiments show that the solid solution is evidently stable to higher temperatures at compositions $x > 0.44$ in contrast to our DFT calculations which show decomposition above $x = 0.44$, before formation of the solid solution.

Perhaps most interestingly, for concentrations above about $x = 0.25$, the solid solution has a lower temperature of decomposition and hydrogen desorption than does pure NaH as shown in Table S3. The DFT-calculated decomposition of pure NaH is around 360 °C with an enthalpy of 91 kJ/mol H_2:

$$2\ NaH \rightarrow 2\ Na + H_2 \quad (12)$$

NaOH-Rich Compositions. The NaOH-rich side of the critical temperature figure was investigated using an 8 formula unit cell in space group $P2_1/m$ for NaOH, for compositions $Na_8(OH)_7H$, $Na_8(OH)_6H_2$, and $Na_8(OH)_5H_3$. These cells were constructed by removing 1, 2, and 3 oxygen atoms from the $P2_1/m$ NaOH structure, since the mixing takes place at higher temperatures where NaOH is in the $P2_1/m$ space group. The mixed structures were optimized keeping the $P2_1/m$ symmetry and cell volume fixed but allowing the atomic coordinates to relax. The results (not shown) indicate that our selected mixed compounds $Na_8(OH)_7H$ and $Na_8(OH)_6H_2$ are favorable at and above −246 and −31 °C, respectively, but find that $Na_8(OH)_5H_3$ is unfavorable. This means that NaOH and NaH prefer to phase-separate at low temperature at a NaH content between 25 and 38 mol %, in agreement with Mikheeva et al.[6]. The enthalpy changes calculated at the experimentally observed temperatures (see DSC data) were calculated as 81 J/g at 275 °C for $Na_8(OH)_7H$ (12.5 mol % NaH) which is considerably lower than our 15 mol % NaH experimental value of 133.5 J/g determined from DSC. This is due to the experimental value being a combination of the solution enthalpy and the phase transition of NaOH from $Fm\bar{3}m$ to $P2_1/m$. However, we find an enthalpy of 142 J/g at 230 °C for $Na_8(OH)_6H_2$ in excellent agreement with our present DSC experimental value of 134.6 J/g for 25 mol % NaH (see below).

KH/KOH System. The red squares in Figure 1 show the DFT-relaxed unit cell volume expansion for $KH_{(1-x)}(OH)_x$, $0 \leqslant x \leqslant 1$. The calculated volume of cubic KH is 45.97 Å^3/f.u., while the volume of our stable KOH structure is 42.59 Å^3/f.u. The calculated volume of KOH in the experimental structure, space group $P2_1/m$, is 47.10 Å^3/f.u., and the calculated volume of KOH in the experimental structure in space group $Fm\bar{3}m$ is 46.23 Å^3/f.u. The volumes are similar; however, the volume of the mode-followed stable KOH structure is 7.3% smaller than the volume of KH. The calculated cell volumes in the solid solution phase hold roughly steady for KOH concentrations up to about 25 mol % and then begin to decrease.

Mixing in the potassium system is more favorable than in the sodium system, as the predicted temperatures for solution formation and the magnitude of the endothermic enthalpy changes are lower, as shown in Figure 3. The green curve represents the calculated critical temperature of solution formation, with the reaction

$$(1\text{-}x)\mathrm{KH} + x\mathrm{KOH} \rightarrow \mathrm{KH}_{(1\text{-}x)}(\mathrm{OH})_x \quad (13)$$

Table S4 contains the critical temperature of solution formation and their corresponding enthalpy changes as well as the decomposition temperature of the solid solution. Similar to the sodium system, the critical temperature increases as the concentration of KOH is increased. The calculated critical temperatures are quite low, ranging from below 0 °C up to 70 °C. However, because of a lack of kinetic barriers in our calculations, experimentally observed mixing may take place at higher temperatures. The black line represents the DFTcalculated decomposition temperature for pure KH with an enthalpy of 91 kJ/mol H_2.

$$2\mathrm{KH} \rightarrow 2\mathrm{K} + \mathrm{H}_2 \quad (14)$$

In contrast to the sodium system, upon mixing of KH/KOH, the solution is stable above the decomposition temperature of pure KH. The red curve is the predicted decomposition of the solution:

$$\mathrm{KH}_{(1\text{-}x)}(\mathrm{OH})_x \rightarrow (1\text{-}x)\mathrm{K} + x\mathrm{KOH} + \frac{(1-x)}{2}\mathrm{H}_2 \quad (15)$$

Evidently, KOH stabilizes KH in the entire range we investigated, and the stabilization is strengthened as the concentration of KOH increases.

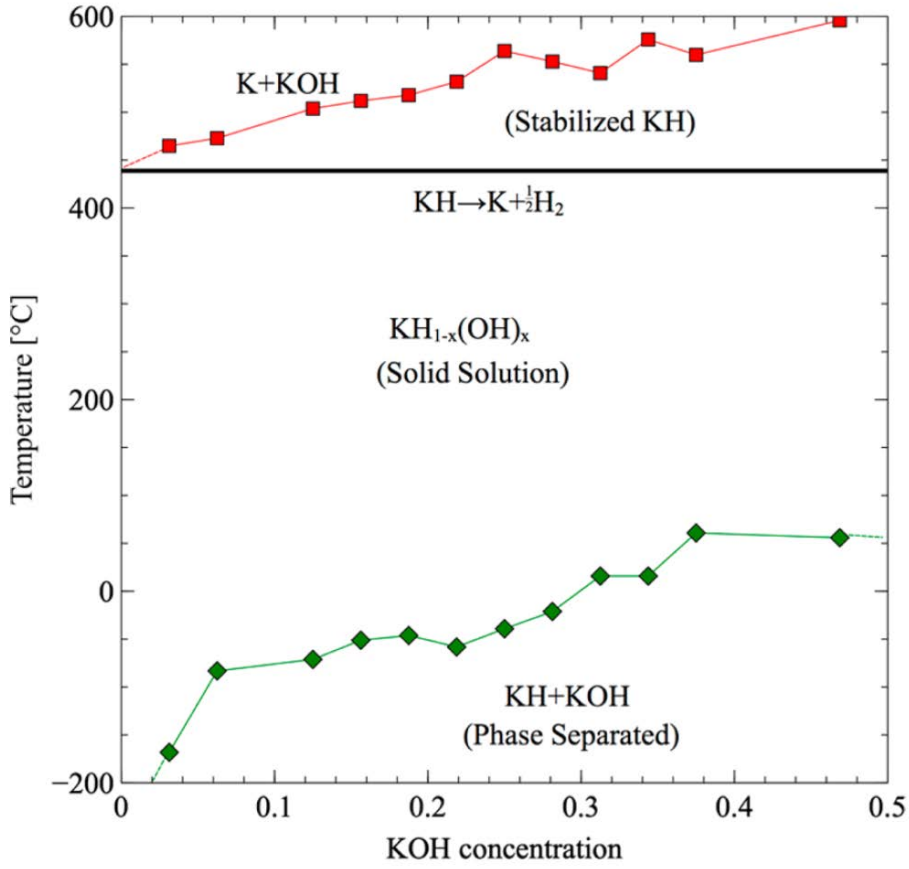

Figure 3. Critical temperatures for mixing and decompositions in the KH/KOH system: green, critical temperature; red, decomposition of solid solution; black, decomposition of KH at P = 1 bar of H_2.

RbH/RbOH System. The green diamonds in Figure 1 indicate the volume expansion of $RbH_{1-x}(OH)_x$ supercells as a function of OH^- concentration (x). The volume increases with the increase of RbOH concentration. Figure 4 shows the critical temperatures for mixing in the RbH/RbOH system, which is similar to KH/KOH system. The decomposition temperature of the solution is higher than the pure hydride decomposition temperature of 339 °C. Therefore, similar to the potassium system, formation of the solid solution phase stabilizes RbH to

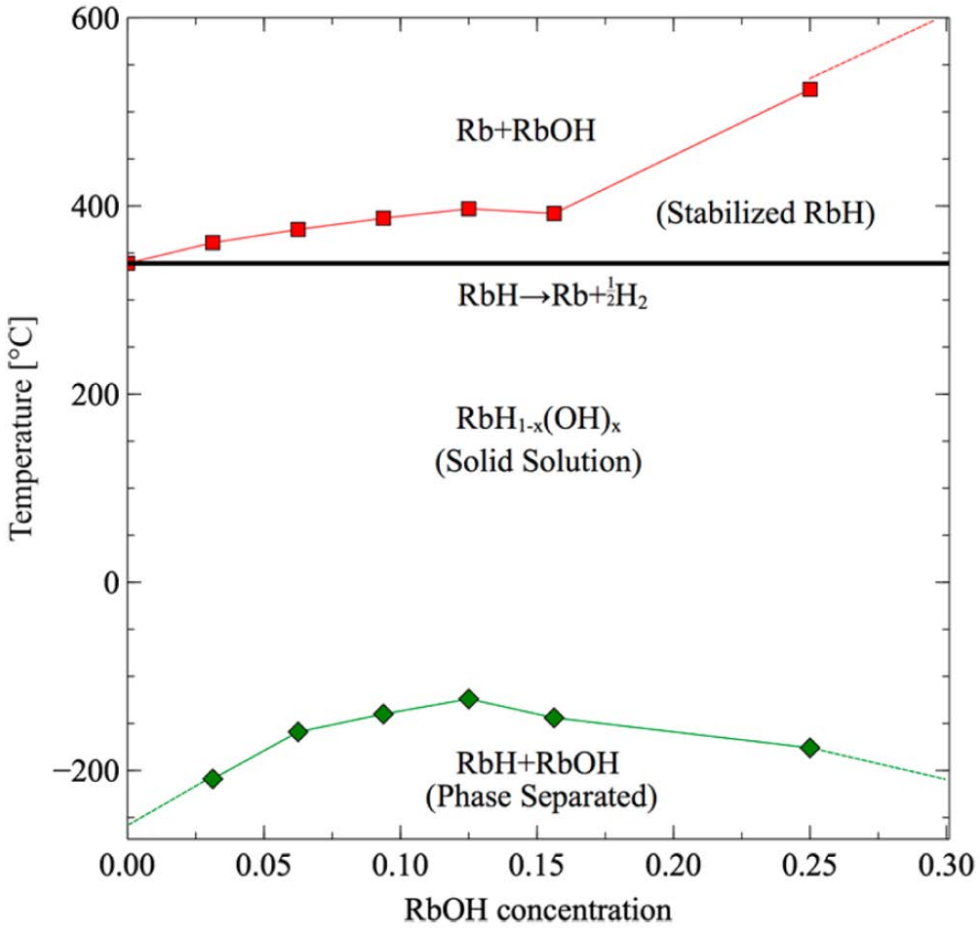

Figure 4. Critical temperatures for mixing and decompositions in the RbH/RbOH system: green, critical temperature; red, decomposition of solid solution; black, decomposition of RbH.

higher temperature. Table S5 contains the solid solution critical temperatures and the corresponding enthalpies as well as the decomposition of the solid solution. The critical temperature and enthalpy of mixing are very low, indicating that the solution is even more favorable than in the Na and K systems.

CsH/CsOH System. The cesium system, like lithium, does not indicate the formation of a solid solution phase. CsH decomposes before the mixture can form a solution:

$$2CsH \rightarrow 2\ Cs + H_2 \qquad (16)$$

The decomposition was predicted to occur at 423 °C, and it is an endothermic reaction, the enthalpy of which is 77 kJ/mol H_2.

Cell Volumes in the MH/MOH System. Table 1 shows the available anion volumes and cation radii for the alkali

Table 1. Available Anion Volumes for H^- and OH^- Determined from Standard Cation Radii in MH and MOH Systems[a]

metal	*r*[cation] (Å)	$V_{cal}[H^-]$ (Å^3)	$V_{cal}[OH^-]$ (Å^3)	ΔV_{cal} (%)
Li	0.68	14.79	27.14	83.50
Na	0.98	24.19	26.66	10.21
K	1.33	36.12	32.74	-9.36
Rb	1.48	35.92	35.53	-1.09
Cs	1.67	46.75	38.66	-17.30

[a]Cation radii were taken from Kittel.[24] V_{cal} is the calculated volume for the anions and is described in the text.

monohydrides or hydroxides. All the structures of hydrides are $Fm\bar{3}m$, and the structures of MOH (V_{cal}) are taken from the mode-followed structures of Bmmb MOH, which are *P*1 for LiOH, KOH, and CsOH, $CmC2_1$ for NaOH, and *Pc* for RbOH. The available anionic volumes were derived as $V_{cal} = V_{unitcell} - V_{cation}$, from our calculated volumes of the crystal minus the corresponding cation volume. Only a small portion of the resulting volume is physically available to the anion. However, it provides a reliable metric for the ability of the MH and MOH to form a solid solution phase. The table illustrates that the soluble systems (Na, K, and Rb) have similar H^- and OH^- available anionic volumes, while the insoluble systems (Li and Cs) have large differences in their respective available anionic volumes (see column ΔV_{cal}). These findings are somewhat analogous to the Hume−Rothery rules where valence and relative size determine metal−metal solid solution mixing tendencies.

DSC and in Situ XRD Results for the NaH/NaOH System. Differential scanning calorimetry (DSC) and in situ X-ray diffraction were used to investigate mixing in the NaH/NaOH system. Figure 5 shows DSC scans over a range of molar ratios of NaH/NaOH. These samples were first heated up to 340 °C, and the DSC data were collected during the cooling process. In agreement with Mikheeva's phase diagram, the melting point of the mixture moves to higher temperature with increasing NaH content. At the same time, the two phase transitions of NaOH move to lower temperature and merge together with the NaH/NaOH phase-separation process. For the 40 mol % NaH + 60 mol % NaOH composition, this process takes place over a wide temperature range from 240 to 60 °C. Calculated enthalpies on the NaOH-rich side of the phase diagram are in agreement with the DSC data as we indicated in the paragraph above on NaOH-rich compositions.

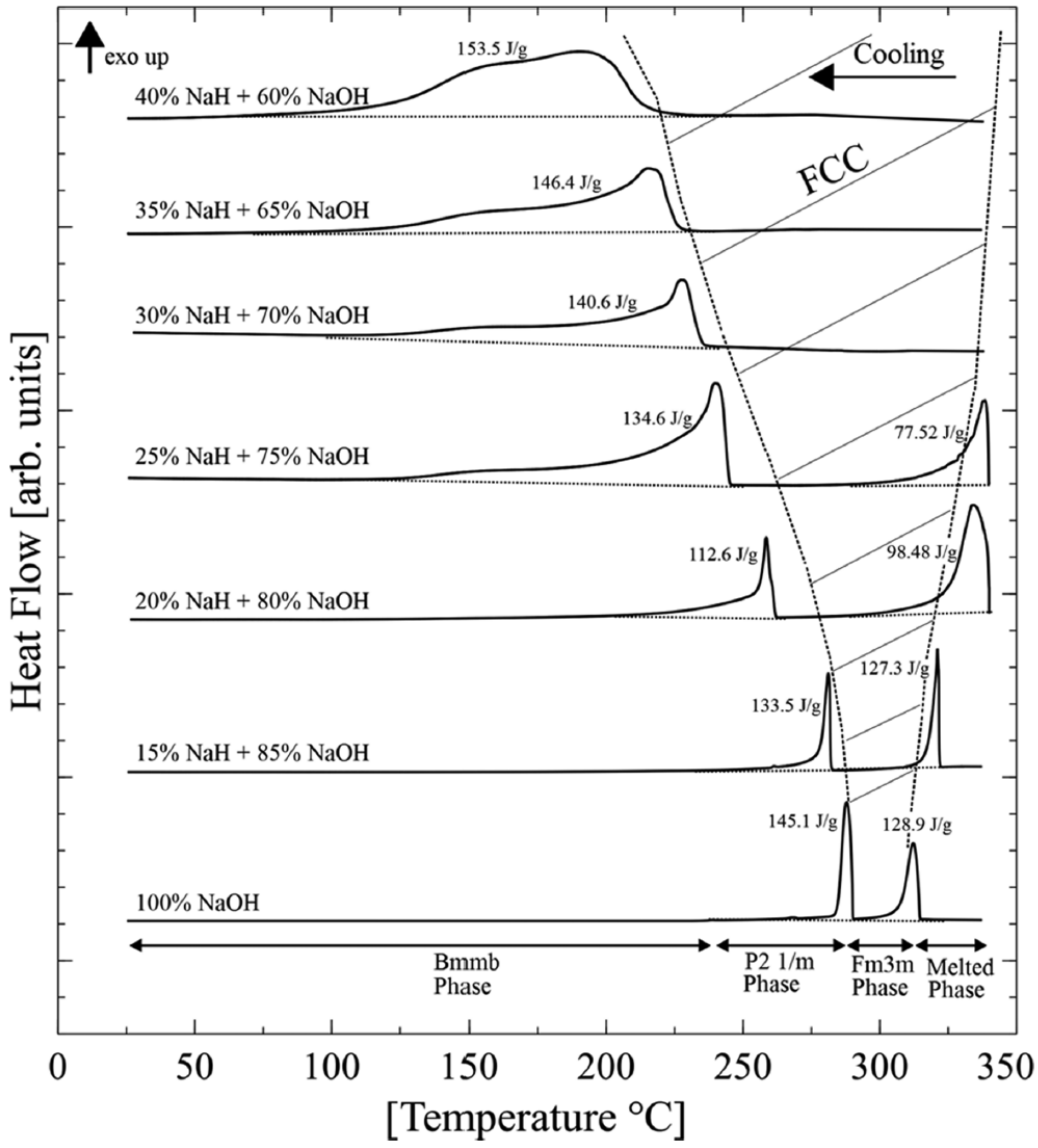

Figure 5. Differential scanning calorimetry (DSC) data of cooling scans. The horizontal dotted lines are guides for the eyes, serving as baselines. The hatched region indicates the approximate boundary of the cubic phase solid solution.

To investigate the dissolution and phase separation process, DSC was performed on a 70 mol % NaH + 30 mol % NaOH sample. The sample was first heated up to 330 °C in order to premelt the mixture. The data were recorded during sample heating up from 25 to 300 °C and then again upon cooling down to 25 °C at a ramp rate of 5 °C/min for multiple cycles. During the heating and cooling cycles, substantial, repeatable thermal activity occurred around 170 °C as presented in Figure 6. The heating (bottom) curves

show an endothermic peak, and the cooling (top) curves show an exothermic peak, which would be as expected for a reversible phase transition. The enthalpy of the reaction was calculated by integrating under the

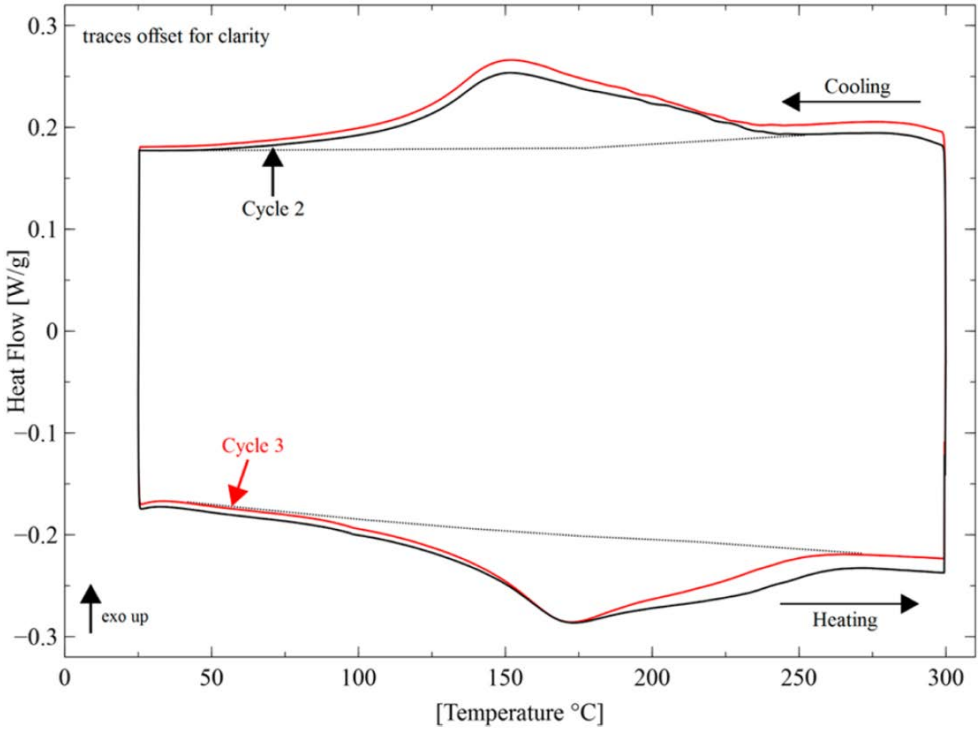

Figure 6. Differential scanning calorimetry (DSC) data for 70 mol % NaH + 30 mol % NaOH. The first cycle (not shown) was heated to 330 °C to premelt the mixture. The subsequent cycles below the melting temperature of NaOH show the reversible behavior. The dotted “baselines” are a guide for the eyes.

endothermic or exothermic peaks and was roughly 70 J/g at this composition.

In situ X-ray diffraction was performed on multiple NaH/NaOH samples of differing compositions to experimentally investigate the mixing process in the NaH/NaOH system. Figure 7 shows the heating and cooling process of a 40 mol %

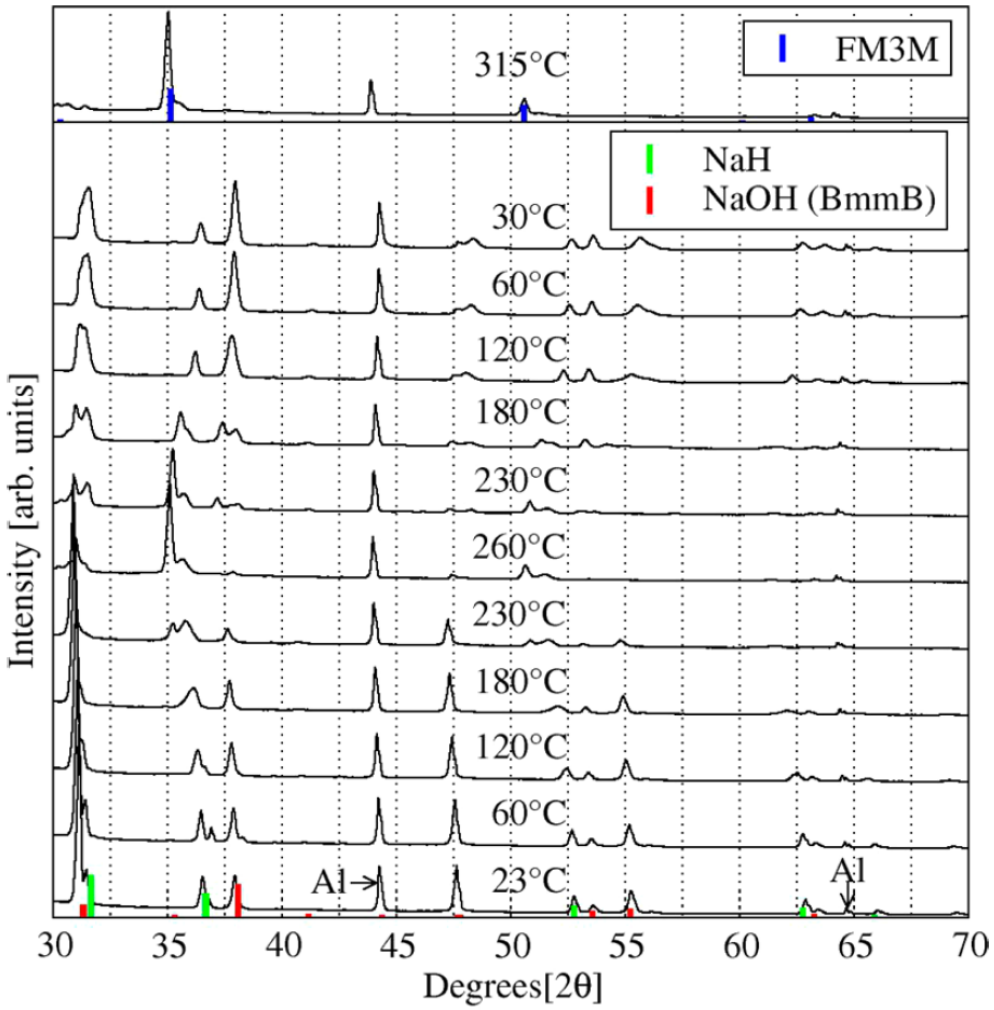

Figure 7. In situ X-ray diffraction data of the heating and cooling process for 40 mol % NaH + 60 mol % NaOH sample. The first scan is indicated at 23 °C, and the last scan is indicated at 30 °C. Vertical guidelines (dotted lines) are given to emphasize the peak shifts. The marked Al peaks were generated by the aluminum sample holder.

NaH + 60 mol % NaOH sample heated up to 260 °C. At 260 °C the sample is almost completely mixed into a single fcc phase solid solution. As the sample cools, the fcc phase solid solution is still present at 180 °C (but shifted to higher angle), but some of the solid solution has now phase separated into *Bmmb* phase NaOH and NaH. As the sample reaches room temperature, NaH and NaOH are mostly phase separated. Heating and cooling the samples during subsequent cycles showed the same repeatable behavior noted in the DSC measurements. At 315 °C (top panel in Figure 7) the sample *completely*

mixed into an fcc structure solid solution. Similar results were obtained for compositions of 90, 70, 50, and 25 mol % NaH, respectively. These results suggest necessary modifications to the phase diagram as presented in Mikheeva's work. The region of fcc β solid solutions should be extended to higher NaH concentrations at temperatures of >260 °C to accommodate hydride rich compositions that continue to form solid solutions. Further, the region where α and β solid solutions exist simultaneously shown in Mikheeva's phase diagram should possibly be extended to include higher NaH concentrations, as the X-ray diffraction data clearly show the existence of the two phases for concentrations outside the allowed region in Mikheeva's diagram. However, sluggish kinetics at lower temperature may be responsible for incomplete phase separation.

The NaH lattice parameters were extracted from the in situ X-ray diffraction data by implementing full pattern Rietveld refinement from the general structure analysis system (GSAS).[25,26] The NaH lattice expansion and unit cell volume expansion of NaH in the 40 mol % NaH + 60 mol % NaOH sample are compared to that of pure NaH in Figure 8. The

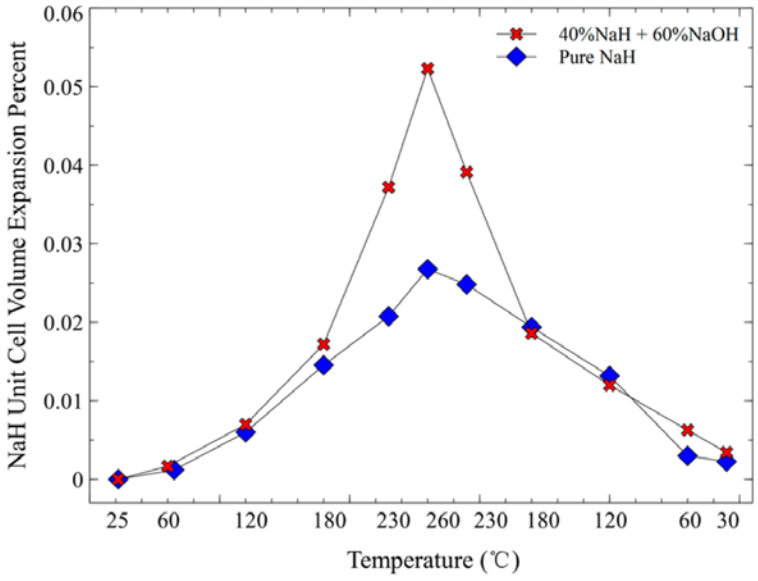

Figure 8. Cell volumes via XRD for pure NaH and 40 mol % NaH + 60 mol % NaOH mixture as a function of temperature during a heating and cooling cycle between 25 and 260 °C.

comparison shows that NaH in the 40 mol % NaH + 60 mol % NaOH sample has a much larger lattice expansion than pure NaH when heated using the same process. Also, the lattice expansion is not linear. The two-point coefficients of linear expansion, calculated using room temperature and the highest temperature point, for pure NaH and NaH in the 40 mol % NaH + 60 mol % NaOH sample are 37×10^{-6}/°C and 72×10^{-6}/°C, respectively. The massive volume expansion of the NaH in the 40 mol % NaH + 60 mol % NaOH sample is evidently due to the formation of solid solution on heating.

CONCLUSIONS

The formation of a solid solution in MH/MOH mixtures is governed by the volume difference available for H^- and OH^- anions in their parent phases of MH and MOH, respectively. Mixing occurs when volume differences are less than about 15% with lower critical temperatures for smaller volume differences. Small additions of hydroxide ion in the KH and RbH systems stabilize these hydrides, and the mixtures decompose at temperatures above the pure hydride decomposition temperature. In contrast, small hydroxide addition to NaH tends to lower the decomposition temperature of the mixture. There is no predicted solid solution in the LiH/LiOH and CsH/CsOH systems due to decomposition before mixing. When solid solution formation occurs in the NaH/NaOH system, the phase transitions in NaOH are concomitant with mixing and the high temperature structure is a single phase fcc before melting. This combination of phase transitions and mixing is fully reversible on cooling.

SUPPORTING INFORMATION

Table S1. Unit cell dimensions and space group symmetries for all structures used in this work.

Material	*a* (Å)	*b* (Å)	*c* (Å)	α	β	γ	*V* (Å^3)	Space Group Before Relaxation	Space Group After Relaxation	f.u.
H_2	20	20	20	90	90	90	-	-	-	1
LiH	8.02	8.02	8.02	90	90	90	515.35	$Fm\bar{3}m$	$Fm\bar{3}m$	32
LiOH	7.14	7.14	8.97	89.97	86.53	93.47	455.35	*P*1	*P*1	16
Li_2O	4.63	4.63	4.63	90	90	90	99.4	*P*4*mm*	*P*4*mm*	4
Na	8.41	8.41	8.41	90	90	90	594.19	$Im\bar{3}m$	$Im\bar{3}m$	16
NaH	9.64	9.64	9.64	90	90	90	896.57	$Fm\bar{3}m$	$Fm\bar{3}m$	32
NaOH	6.98	6.78	20.63	90	90	90	975.43	*Bmmb*	$Cmc2_1$	32
Na_2O	5.56	5.56	5.56	90	90	90	172.09	$Fm\bar{3}m$	$Fm\bar{3}m$	4
K	10.55	10.55	10.55	90	90	90	1175.39	$Im\bar{3}m$	$Im\bar{3}m$	16
KH	11.37	11.37	11.37	90	90	90	1471.19	$Fm\bar{3}m$	$Fm\bar{3}m$	32
KOH	8.01	7.98	21.33	90	90	90	1362.97	*Bmmb*	*P*1	32
Rb	11.33	11.33	11.33	90	90	90	1453.86	$Im\bar{3}m$	$Im\bar{3}m$	16
RbH	12.07	12.07	12.07	90	90	90	1759.35	$Fm\bar{3}m$	$Fm\bar{3}m$	32
RbOH	8.42	8.46	22.08	90	90.08	90	1571.43	*Bmmb*	*Pc*	32
Cs	12.28	12.28	12.28	90	90	90	1851.64	$Im\bar{3}m$	$Im\bar{3}m$	16
CsH	12.85	12.85	12.85	90	90	90	2120.39	$Fm\bar{3}m$	$Fm\bar{3}m$	32
$Li_{32}H_{31}OH$	8.06	8.06	8.06	90.3	90.3	90.3	523.02	*P*1	*R*3*m*	32
$Na_{32}H_{31}OH$	9.66	9.66	9.66	90.3	90.3	90.3	901.11	*P*1	*P*1	1
$Na_{32}H_{30}(OH)_2$	9.67	9.67	9.67	90.61	90.61	90.61	904.8	*P*1	*P*1	1
$Na_{32}H_{29}(OH)_3$	9.72	9.68	9.68	91	91	91	909.67	*P*1	*P*1	1
$Na_{32}H_{28}(OH)_4$	9.71	9.69	9.71	90.25	91.6	90.25	913.87	*P*1	*P*1	1
$Na_{32}H_{27}(OH)_5$	9.72	9.72	9.72	91.54	91.54	91.54	919.5	*P*1	*P*1	1
$Na_{32}H_{26}(OH)_6$	9.65	9.77	9.76	90.28	90.36	92.17	919.83	*P*1	*P*1	1
$Na_{32}H_{25}(OH)_7$	9.69	9.76	9.78	90.43	91.25	92.02	923.4	*P*1	*P*1	1
$Na_{32}H_{24}(OH)_8$	9.71	9.71	9.71	92.34	92.34	92.34	931.31	*P*1	*P*1	1
$Na_{32}H_{23}(OH)_9$	9.72	9.75	9.82	91.27	91.49	92.84	928.46	*P*1	*P*1	1
$Na_{32}H_{22}(OH)_{10}$	9.87	9.73	9.71	94.3	92.87	89.78	928.06	*P*1	*P*1	1
$Na_{32}H_{21}(OH)_{11}$	9.77	9.76	9.81	91.9	92.41	92.71	932	*P*1	*P*1	1
$Na_{32}H_{20}(OH)_{12}$	9.78	9.87	9.72	94.99	90.47	92.7	933.87	*P*1	*P*1	1
$Na_{32}H_{19}(OH)_{13}$	9.76	9.83	9.84	92.77	91.89	93.53	939.43	*P*1	*P*1	1
$K_{32}H_{31}OH$	11.38	11.38	11.38	90.27	90.27	90.27	1472.88	*P*1	*R*3*m*	1
$K_{32}H_{30}(OH)_2$	11.38	11.38	11.38	90.55	90.55	90.55	1474.56	*P*1	*R*3*m*	1
$K_{32}H_{28}(OH)_4$	11.41	11.37	11.41	90.21	91.44	90.21	1479.67	*P*1	*Cm*	1

$K_{32}H_{27}(OH)_5$	11.39	11.39	11.39	90.49	90.49	90.49	1479.11	*P*1	$C3_4$	1
$K_{32}H_{26}(OH)_6$	11.33	11.43	11.42	91.79	90.37	90.29	1478.24	*P*1	*P*1	1
$K_{32}H_{25}(OH)_7$	11.36	11.4	11.41	91.66	90.93	90.31	1476.77	*P*1	*P*1	1
$K_{32}H_{24}(OH)_8$	11.42	11.42	11.42	92.09	92.09	92.09	1487.08	*P*1	*P*1	1
$K_{32}H_{23}(OH)_9$	11.36	11.38	11.43	92.31	91.14	91.02	1476.85	*P*1	*P*1	1
$K_{32}H_{22}(OH)_{10}$	11.42	11.36	11.35	89.74	92.51	93.86	1466.77	*P*1	*P*1	1
$K_{32}H_{21}(OH)_{11}$	11.4	11.37	11.41	92.28	91.82	91.6	1477.31	*P*1	*P*1	1
$K_{32}H_{20}(OH)_{12}$	11.36	11.45	11.35	93.02	89.73	94.55	1468.47	*P*1	*P*1	1
$K_{32}H_{19}(OH)_{15}$	11.38	11.43	11.28	89.78	87.53	97.98	1452.06	*P*1	*P*1	1
$Rb_{32}H_{31}OH$	12.07	12.07	12.07	90.24	90.24	90.24	1757.58	*P*1	*R*3*m*	1
$Rb_{32}H_{30}(OH)_2$	12.07	12.07	12.07	90.48	90.48	90.48	1760.02	*P*1	*R*3*m*	1
$Rb_{32}H_{29}(OH)_3$	12.14	12.05	12.05	90.38	90.79	90.79	1762.75	*P*1	*Cm*	1
$Rb_{32}H_{28}(OH)_4$	12.1	12.05	12.1	90.17	91.25	90.17	1764.42	*P*1	*Cm*	1
$Rb_{32}H_{27}(OH)_5$	12.09	12.09	12.09	90.4	90.4	90.4	1765.44	*P*1	*R*3	1
$Rb_{32}H_{24}(OH)_8$	12.11	12.11	12.11	91.89	91.89	91.89	1771.55	*P*1	*P*1	1

Table S2. K-point meshes, total energies, vibrational energies and entropies for all structures.

Material	k-point	U_E (eV)	ZPE (eV)	S_{conf} (eV/K)	S_c (J/mol/K)	S_e (J/mol/K)
H_2	2x2x2	-6.80	0.27	-	130.70	130.70
LiH	2x2x2	-197.66	7.16	-	17.78	24.70
LiOH	2x2x2	-240.41	6.91	-	39.98	42.81
Li_2O	4x4x4	-57.75	0.89	-	33.88	37.90
Na	4x4x4	-20.89	0.25	-	45.04	51.00
NaH	2x2x2	-164.94	5.09	-	37.02	40.00
NaOH	2x2x2	-441.13	12.56	-	58.00	64.46
Na_2O	6x6x6	-45.66	0.49	-	68.46	73.00
K	4x4x4	-16.67	0.19	-	50.23	64.20
KH	2x2x2	-156.25	4.04	-	47.61	66.90
KOH	2x2x2	-431.45	11.98	-	70.86	79.00
Rb	2x2x2	-14.87	0.11	-	63.35	69.50
RbH	2x2x2	--- 150.16	3.49	-	61.02	-
RbOH	2x2x2	-424.17	11.52	-	119.32	84.10
Cs	2x2x2	-13.79	0.08	-	70.18	82.80

CsH	2x2x2	-147.85	3.06	-	75.00	-
$Li_{32}H_{31}OH$	2x2x2	-205.86	7.28	-	20.18	-
$Na_{32}H_{31}OH$	2x2x2	-173.35	5.25	0.00038	39.18	-
$Na_{32}H_{30}(OH)_2$	2x2x2	-181.77	5.46	0.00064	41.13	-
$Na_{32}H_{29}(OH)_3$	2x2x2	-190.20	5.65	0.00086	43.41	-
$Na_{32}H_{28}(OH)_4$	2x2x2	-198.66	5.86	0.00104	44.45	-
$Na_{32}H_{27}(OH)_5$	2x2x2	-207.01	6.05	0.00120	46.68	-
$Na_{32}H_{26}(OH)_6$	2x2x2	-215.71	6.29	0.00133	47.14	-
$Na_{32}H_{25}(OH)_7$	2x2x2	-224.27	6.50	0.00145	48.22	-
$Na_{32}H_{24}(OH)_8$	2x2x2	-232.44	6.65	0.00155	51.33	-
$Na_{32}H_{23}(OH)_9$	2x2x2	-241.33	6.97	0.00164	50.23	-
$Na_{32}H_{22}(OH)_{10}$	2x2x2	-249.98	7.22	0.00171	50.73	-
$Na_{32}H_{21}(OH)_{11}$	2x2x2	-258.43	7.47	0.00177	52.38	-
$Na_{32}H_{20}(OH)_{12}$	2x2x2	-266.99	7.70	0.00182	53.17	-
$Na_{32}H_{19}(OH)_{13}$	2x2x2	-275.55	7.89	0.00186	54.15	-
$K_{32}H_{31}OH$	2x2x2	-164.70	4.19	0.00038	1626.16	-
$K_{32}H_{30}(OH)_2$	2x2x2	-173.16	4.41	0.00064	1681.41	-
$K_{32}H_{28}(OH)_4$	2x2x2	-190.13	4.82	0.00104	1805.78	-
$K_{32}H_{27}(OH)_5$	2x2x2	-198.64	5.05	0.00120	1846.11	-
$K_{32}H_{26}(OH)_6$	2x2x2	-207.20	5.27	0.00133	1877.75	-
$K_{32}H_{25}(OH)_7$	2x2x2	-215.77	5.50	0.00145	1919.05	-
$K_{32}H_{24}(OH)_8$	2x2x2	-224.14	5.66	0.00155	1999.59	-
$K_{32}H_{23}(OH)_9$	2x2x2	-232.78	5.95	0.00164	1996.80	-
$K_{32}H_{22}(OH)_{10}$	2x2x2	-241.35	6.24	0.00171	2003.50	-
$K_{32}H_{21}(OH)_{11}$	2x2x2	-249.77	6.41	0.00177	2073.20	-
$K_{32}H_{20}(OH)_{12}$	2x2x2	-258.31	6.69	0.00182	2078.82	-
$K_{32}H_{19}(OH)_{15}$	2x2x2	-284.11	7.43	0.00191	2151.89	-
$Rb_{32}H_{31}OH$	2x2x2	-158.16	3.67	0.00038	2054.21	-
$Rb_{32}H_{30}(OH)_2$	2x2x2	-167.05	3.88	0.00064	2126.15	-
$Rb_{32}H_{29}(OH)_3$	2x2x2	-175.54	4.07	0.00086	2189.45	-
$Rb_{32}H_{28}(OH)_4$	2x2x2	-184.01	4.28	0.00104	2242.71	-
$Rb_{32}H_{27}(OH)_5$	2x2x2	-192.50	4.50	0.00120	2303.77	-
$Rb_{32}H_{24}(OH)_8$	2x2x2	-217.98	5.10	0.00155	2527.74	-

Tabel S3. The solution temperatures, decomposition temperatures and enthalpies for the NaH/NaOH system.

Material	T_c (°C)	ΔH_1 (J/g)	T_d (°C)
$Na_{32}H_{31}OH$	69	22	364
$Na_{32}H_{30}(OH)_2$	120	46	364
$Na_{32}H_{29}(OH)_3$	100	67	369
$Na_{32}H_{28}(OH)_4$	158	84	363
$Na_{32}H_{27}(OH)_5$	179	114	363
$Na_{32}H_{26}(OH)_6$	159	104	361
$Na_{32}H_{25}(OH)_7$	155	108	355
$Na_{32}H_{24}(OH)_8$	176	153	361
$Na_{32}H_{23}(OH)_9$	200	128	326
$Na_{32}H_{22}(OH)_{10}$	205	123	319
$Na_{32}H_{21}(OH)_{11}$	221	143	314
$Na_{32}H_{20}(OH)_{12}$	237	146	307
$Na_{32}H_{19}(OH)_{13}$	239	152	307

Table S4. The solution temperatures, decomposition temperatures and enthalpies for the KH/KOH system.

Material	T_c (°C)	ΔH_1 (J/g)	T_d (°C)
$K_{32}H_{31}OH$	-168	5	465
$K_{32}H_{30}(OH)_2$	-83	15	473
$K_{32}H_{28}(OH)_4$	-71	26	504
$K_{32}H_{27}(OH)_5$	-51	32	512
$K_{32}H_{26}(OH)_6$	-46	33	518
$K_{32}H_{25}(OH)_7$	-58	33	532
$K_{32}H_{24}(OH)_8$	-39	46	564
$K_{32}H_{23}(OH)_9$	-21	45	553
$K_{32}H_{22}(OH)_{10}$	16	49	541
$K_{32}H_{21}(OH)_{11}$	16	58	576
$K_{32}H_{20}(OH)_{12}$	61	64	560
$K_{32}H_{19}(OH)_{15}$	56	62	596

Table S5. The solution temperatures, decomposition temperatures and enthalpies for the Rb/RbOH system.

Material	T_c (°C)	ΔH_1 (J/g)	T_d (°C)
$Rb_{32}H_{31}OH$	-209	1.4	361
$Rb_{32}H_{30}(OH)_2$	-158	4.5	375
$Rb_{32}H_{29}(OH)_3$	-140	7.1	387
$Rb_{32}H_{28}(OH)_4$	-124	9.4	397
$Rb_{32}H_{27}(OH)_5$	-144	9.1	418
$Rb_{32}H_{24}(OH)_8$	-176	10	524

ACKNOWLEDGEMENTS

The authors gratefully acknowledge support from the U.S. Department of Energy, Basic Energy Science, through Grant DE-FG02-ER46256. T.E.-C. acknowledges partial support from Washington University's Office of Undergraduate Research. We thank David Osborn in the Center for Nanoscience for assistance in collecting the in situ XRD and DSC data. We also thank Bruce Burkeen in the University of Missouri St. Louis Research and Development Tech Shop for his work fabricating experimental equipment.

REFERENCES

(1) Bogdanović, B.; Schwickardi, M. Ti-doped $NaAlH_4$ as a Hydrogen-Storage Material Preparation by Ti-Catalyzed Hydrogenation of Aluminum Powder in Conjunction with Sodium Hydride. *Appl. Phys. A: Mater. Sci. Process*. **2000**, *72*, 221−223.

(2) Michel, K.; Ozolins, V. Native Defect Concentrations in $NaAlH_4$ and Na_3AlH_6. *J. Phys. Chem. C* **2011**, *115*, 21443−21453.

(3) Michel, K.; Ozolins, V. Vacancy Diffusion in $NaAlH_4$ and Na_3AlH_6. *J. Phys. Chem. C* **2011**, *115*, 21465−21472.

(4) Morioka, H.; Kakizaki, K.; Chung, C.; Yamada, A. Reversible Hydrogen Decomposition of $KAlH_4$. *J. Alloys Compd.* **2003**, *353*, 310−314.

(5) Sorte, E. G.; Majzoub, E. H.; Ellis-Caleo, T.; Hammann, B. A.; Wang, G.; Zhao, D.; Bowman, R. C., Jr.; Conradi, M. S. Effects of NaOH in Solid NaH: Solution/Segregation Phase Transition and Diffusion Acceleration. *J. Phys. Chem. C* **2013**, *117*, 23575−23581.

(6) Mikheeva, V.; Shkrabkina, M. Solid Solutions in NaOH-NaH and KOH-KH Systems. *Russ. J. Inorg. Chem.* **1962**, *7*, 1251−1255.

(7) Kresse, G.; Hafner, J. Ab Initio Molecular Dynamics for Liquid Metals. *Phys. Rev. B* **1993**, *47*, 558−561.

(8) Kresse, G.; Furthmüller, J. Efficient Iterative Schemes for ab Initio Total-Energy Calculations Using a Plane-Wave Basis Set. *Phys. Rev. B* **1996**, *54*, 11169−11186.

(9) Perdew, J.; Chevary, J.; Vosko, S.; Jackson, K.; Pederson, M.; Singh, D.; Fiolhais, C. Atoms, Molecules, Solids, and Surfaces: Applications of the Generalized Gradient Approximation for Exchange and Correlation. *Phys. Rev. B* **1992**, *46*, 6671−6687.

(10) Perdew, J.; Chevary, J.; Vosko, S.; Jackson, K.; Pederson, M.; Singh, D.; Fiolhais, C. Erratum: Atoms, Molecules, Solids, and Surfaces: Applications of the Generalized Gradient Approximation for Exchange and Correlation. *Phys. Rev. B* **1993**, *48*, 4978−4978.

(11) Monkhorst, H.; Pack, J. Special Points for Brillouin-Zone Integrations. *Phys. Rev. B* **1976**, *13*, 5188−5192.

(12) Kirkpatrick, S.; Gelatt, C., Jr.; Vecchi, M. Optimization by Simulated Annealing. *Science* **1983**, *220*, 671−680.

(13) Akbarzadeh, A.; Ozolin, V.; Wolverton, C. First-Principles Determination of Multicomponent Hydride Phase Diagrams: Application to the Li-Mg-N-H System. *Adv. Mater.* **2007**, *19*, 3233− 3239.

(14) Giauque, W. The Entropy of Hydrogen and the Third Law of Thermodynamics: The Free Energy and Dissociation of Hydrogen. *J. Am. Chem. Soc.* **1930**, *52*, 4816−4831.

(15) Grindy, S.; Meredig, B.; Kirklin, S.; Saal, J.; Wolverton, C. Approaching Chemical Accuracy with Density Functional Calculations: Diatomic Energy Corrections. *Phys. Rev. B* **2013**, *87*, 075150.

(16) Gurvich, L.; Bergman, G.; Gorokhov, L.; Iorish, V.; Leonidov, V.; Yungman, V. Thermodynamic Properties of Alkali Metal Hydroxides. Part 1. Lithium and Sodium Hydroxides. *J. Phys. Chem. Ref. Data* **1996**, *25*, 1211−1276.

(17) Jensen, F. Locating Transition Structures by Mode Following: A Comparison of Six Methods on the Ar_8 Lennard-Jones Potential. *J. Chem. Phys.* **1995**, *102*, 6706−6718.

(18) Kiat, J. M.; Boemare, G.; Rieu, B.; Aymes, D. Structural Evolution of LiOH: Evidence of a Solid−Solid Transformation toward Li_2O Close to the Melting Temperature. *Solid State Commun.* **1998**, *108*, 241−245.

(19) Ren, R.; Ortiz, A. L.; Markmaitree, T.; Osborn, W.; Shaw, L. L. Stability of Lithium Hydride in Argon and Air. *J. Phys. Chem. B* **2006**, *110*, 10567−10575.

(20) Haertling, C.; Hanrahan, R. J., Jr.; Smith, R. A Literature Review of Reactions and Kinetics of Lithium Hydride Hydrolysis. *J. Nucl. Mater.* **2006**, *349*, 195−233.

(21) Haertling, C. L.; Hanrahan, R. J., Jr.; Tesmer, J. R. Hydrolysis Studies of Polycrystalline Lithium Hydride. *J. Phys. Chem. C* **2007**, *111*, 1716−1724.

(22) Sifuentes, A.; Stowe, A. C.; Smyrl, N. Determination of the Role of Li_2O on the Corrosion of Lithium Hydride. *J. Alloys Compd.* **2013**, *580*, S271−S273.

(23) Yu, P.; Chua, Y. S.; Cao, H.; Xiong, Z.; Wu, G.; Chen, P. Hydrogen Storage over Alkali Metal Hydride and Alkali Metal Hydroxide Composites. *J. Energy Chem.* **2014**, *23*, 414−419.

(24) Kittel, C. *Introduction to Solid State Physics*, 5th ed.; John Wiley & Sons, Inc.: New York, **1976**.

(25) Toby, B. H. EXPGUI, a Graphical User Interface for GSAS. *J. Appl. Crystallogr.* **2001**, *34*, 210−213.

(26) Larson, A.; Von Dreele, R. *General Structure Analysis System (GSAS)*; Los Alamos National Laboratory Report LAUR; Los Alamos National Laboratory: Los Alamos, NM, **2004**; pp 86−748.

IV. Investigation of TiO_2 and Other Electrode Materials in Lithium-ion Batteries: Improving Capacity and Cycling Performance

Alyssa M. McFarlane[†], Dongxue Zhao,[†] E. H. Majzoub [*,†,‡]

[†]*Center for Nanoscience and Department of Physics and Astronomy, University of Missouri St. Louis, One University Boulevard, St. Louis, Missouri 63121, United States*

[‡]*Department of Chemistry and Biochemistry, University of Missouri St. Louis, One University Boulevard, St. Louis, Missouri 63121, United States*

Abstract

Two promising areas of research with respect to lithium ion batteries (LIB's) include (a) transition metal oxides, and (b) other high capacity Li-containing compounds that can serve as conversion reactions. Recent studies show that utilizing conversion reactions leads to greater capacities, and nano-porous carbons (NPCs) impregnated by materials such as metal oxides have yielded high reversible lithium storage capacities. A capacity of 600 mAh/g has been achieved using TiO_2 particles formed inside NPCs and lithium foil as a counter electrode. The sample was cycled at a constant current of 0.5 mA between .1 V to 4 V. Ordered mesoporous carbon-TiO_2 (OMCT65) was prepared by a basic polymerization method utilizing self-assembly and pyrolysis. Light metal hydrides are also attractive as conversion materials and may improve these results when used instead of metal oxides, as they have exhibited high lithium mobility. Ordered mesoporous carbon containing LiBH4 particles inside the pores has been synthesized using a similar method, and results are pending.

Introduction

Renewable sources of energy are in high demand for applications such as hybrid electric vehicles (HEV's). Lithium-ion batteries (LIB's) are promising, but limited by the properties of the electrode materials. Due to volume expansion and contraction during lithiation and extraction, the electrode experiences degradation, resulting in severe capacity fading, and buildup of insoluble reaction products.[1-2] This compromises the electrical contact and fascile diffusion of lithium and leads to poor cycle life. Interestingly, metal fluorides have proved favorable compounds for conversion reactions of the following type.[3]

$$M_n^+X_n + nLi^+ + ne^- <-> nLiX + M$$

The M-F bond is extremely ionic, which should theoretically allow for high lithium storage capabilities and high voltage range.[3] However, metal fluorides experience poor electrical conductivity due to their large band gap,[3] and are also limited by theoretical capacities to a few hundred mAh/g. Metal oxides have also been

investigated as potential electrode materials in order to take advantage of their multiple oxidation states.[4] Titanium Oxide nanostructures exhibit high structural stability and have recently drawn attention.[4] When incorporated into the pores of ordered mesoporous carbons (OMC's), the material's conductivity improves and ordered mesoporous carbon-TiO_2 is formed (OMCT). The OMC's provide a conductive matrix of amourphous carbon that directs and separates the TiO_2 nanostructures in addition to providing large pore volumes for lithium ion diffusion.[4] The high surface area and variable pore size of the OMC's make them a good option for electrode materials with other types of compounds to be incorporated into the pores.[5] Furthermore, the high porosity of the material allows the electrolyte to easily diffuse, which further maximizes active-particle contact with the electrolyte. The framework also helps keep the integrity of the electrode microstructure intact.[4] Some light metal hydrides in particular show very high lithium mobility.[2] Since the crystal structures of many light metal hydrides are known, first-principles studies can be conducted for investigation of possible lithium kinetics with the compounds. Phase diagrams for the conversion compounds (i) LiBH4, (ii) $LiNH_2$, and (iii) $Mg(BH_4)_2$ have been investigated by Mason and Majzoub, and show high lithium capacities. Incorporating these light metal hydrides into the pores of OMC's may allow for control of volume expansion and better electron transfer during conversion reactions, and may yield high specific capacities.

TiO_2 nanoparticles were inserted into OMC's, synthesized during the microstructure self-assembly. This is similar to the method utilized by Chang, Huang, and Doong.[4]. The material was tested against a lithium foil counter electrode. The results show promising capacities of 600 mAh/g for the electrode materials. $LiBH_4$ particles inside of OMC's were synthesized using similar methods. With light metal hydrides in place of metal oxides we may see high lithium mobility and therefore high capacity of the LIB.

Experimental

OMCT with a weight percentage of 65 % (OMCT65) was synthesized via a three-step process. The first step consisted of synthesis of a 20 wt % resol ethanolic solution. 6.1 grams of phenol 99 % reagent was added to a shenk flask containing a stir bar. The

flask was then placed in a 40 ℃ water bath until the phenol was fully melted. 1.3 grams of 20 % NaOH in H_2O was then added to the flask. The mixture was then stirred for ten minutes, and 10.5 grams of 37 % formaldehyde solution in H_2O was subsequently added. The water bath temperature was raised to 70 ℃ and allowed to sit for 80 minutes. The flask was then removed and allowed to cool to room temperature. The pH of the flask was then balanced to between 7 and 7.5 by adding 6.5 grams of 1N HCl solution. Initially, 5 grams is added and the remainder is added immediately afterwards drop-wise to ensure the desired pH level. The remaining drops must be added immediately to ensure that no undesired reaction products are produced. The solution was then placed in a 45 ℃ water bath and a vacuum pump was attached to remove excess water from the solution. The second step consisted of preparation of a 16.26 wt % $TiCl_4$ solution. In a separate shenk flask, 12.03 g $TiCl_4$ was added to 62 mL of deionized water. The mixture was then stirred at room temperature for 30 minutes. The third step consisted of synthesizing the OMCT65. 150 mL of 200-proof ethanol was measured into a separate flask and 15 g of F127 polymer was then added. The mixture was then heated to 40 ℃ to allow the polymer to dissolve. In another flask, the 20 wt % resol ethanolic solution and the 16.26 wt % $TiCl_4$ solution, synthesized in steps 1 and 2 respectively, were mixed and stirred at room temperature for one hour. The mixture was then transferred into petri dishes at an even thickness and dried in a vacuum oven at 40 ℃ for 24 hours. The dishes were then baked at 100 ℃ for 24 hours. After baking, the materials were allowed to cool to room temperature and calcinated in a tubular furnace from 600 ℃ to 1200 ℃ under N_2 at a rate of 1 ℃ per minute. Electrode slurry was prepared in an argon-filled glovebox using a solution of 0.8 wt % PVDF in DMSO. The OMCT65 powder was transferred into a weigh-boat and PVDF/DMSO solution was added drop-wise. The slurry was then spread by hand onto copper sheets and allowed to dry overnight. The sheets were then baked in a vacuum oven to 110 ℃ and allowed to cool to room temperature under vacuum. Electrochemical cells were assembled in an Argon-filled glovebox using lithium foil, copper coated electrodes, and a 1 M solution of $LiPF_6$ in a solution of (1:1, by weight) DEC:EC. A Celgard separator of 25 μm thickness was used. Prepared electrodes were assembled into appropriate configuration using in-house machined parts. Swagelock coin cells were used for airtightness. Capacity tests were carried out using a Maccor model

4300 constant current battery tester. Batteries were cycled between 0.1 V to 4 V at a constant current of 0.5 mA for 25 cycles.

Results and Discussion

A capacity of 600 mAh/g was achieved on the first charge cycle due to formation of the solid electrolyte interphase (SEI) layer. Subsequent cycles showed consistent behavior, but dropping capacity in the neighborhood of 200 mAh/g. (See Figure 1)

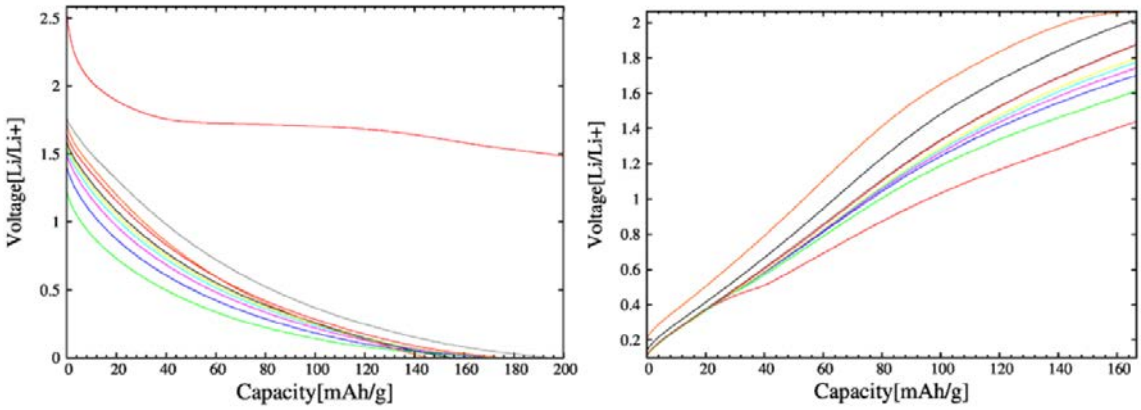

Figure 1. Cycling data for the OMCT65 electrode. The left graph shows charging, and the right graph shows discharge curves. The initial large capacity on the first cycle is attributed to the formation of the solid electrolyte interphase (SEI) layer.

We believe that the capacity of our electrodes will increase with improved electrode assembly techniques. Obtaining a proper balance of electrical conductivity and compaction in the assembled electrodes will require further study. New electrodes using OMCT65 will be synthesized using the same method previously outlined in this article. 10 wt % Carbon Black (CB) will be added to the OMCT65 powder during electrode synthesis. This has been shown to enhance electrical conductivity [(4)]. The consistency of the powder also improves and spreads onto the copper sheets more evenly with the addition of CB. We hope this will improve cyclability of the electrode. OMC's that have been infiltrated by $LiBH_4$ (OMCLBH) particles have been synthesized using a similar method as OMCT65. We will assemble LIB's with this material using the same electrode preparation method previously outlined. One electrode has currently been assembled into

a LIB and shows a stable initial voltage of 2.8 V. This cell will be cycled on the Maccor model 4300 according to the procedure previously outlined. For future electrodes, 10 wt % CB will also be added to the OMCLBH to improve conductivity and consistency. A powder electrode will also be prepared using a pellet press and OMCLBH with PVDF, as well as several other light metal hydrides. We expect that this material will exhibit good capacity and lithium storage properties.

Acknowledgements

The authors acknowledge the financial support from the NASA Missouri Space Grant Consortium, and the UMSL Department of Physics and Astronomy. Special thanks to Dr. Stephen Holmes, Dr. E.H. Majzoub, and David Peaslee.

References

[1] Yu, Z.; Zhu, S.; Li, Y.; Liu, Q.; Feng, C.; Zhang, D. Synthesis of SnO_2 nanoparticles inside mesoporous carbon via a sonochemical method for highly reversible lithium batteries. *Materials Letters*. **2011**, *65(19)*, 3072-3075.

[2] Mason, T. H.; Liu, X.; Hong, J.; Graetz, J.; Majzoub, E. H. First-Principles Study of Novel Conversion Reactions for High-Capacity Li-Ion Battery Anodes in the Li–Mg–B–N–H System. *The Journal of Physical Chemistry C*. **2011**, *115(33)*, 16681-16687.

[3] Prakash, R.; Mishra, A. K.; Roth, A.; Kübel, C.; Scherer, T.; Ghafari, M.; Hahn, H.; Fichtner, M. A ferrocene-based carbon–iron lithium fluoride nanocomposite as a stable electrode material in lithium batteries. *Journal of Materials Chemistry*. **2010**, *20(10)*, 1871-1876.

[4] Chang, P. Y.; Huang, C. H.; Doong, R. A. Ordered mesoporous carbon–TiO_2 materials for improved electrochemical performance of lithium ion battery. *Carbon*. **2012**, *50(11)*, 4259-4268.

[5] Huang, C. H.; Gu, D.; Zhao, D.; Doong, R. A. Direct synthesis of controllable microstructures of thermally stable and ordered mesoporous crystalline titanium oxides and carbide/carbon composites. *Chemistry of Materials*. **2010**, *22(5)*, 1760-1767.

SECTION

6. CONCLUSIONS

$NaAlH_4$ is a promising hydrogen storage material with high theoretical hydrogen storage capacity. The reaction properties can be changed by treating in different environments. The new S105 phase which appeared in the heat and pressure treated $NaAlH_4$, and it has lower melting and decomposition tempertures than the regular bulk material. This indicates that without catalyst, the hydrogen storage and release capbility of $NaAlH_4$ can be improved by pretreating the material.

There is a solid solution of H^- and $[OH]^-$ groups in the NaH/NaOH system which was investigated and verified by X-ray diffraction and differential scanning calorimetry, while the OH^- in NaH had been found to improve the hydrogen mobility in NaH. As evidenced in differential scanning calorimetry data, the solid solution phases in NaH/NaOH system may play a significant role in the mass transport necessary for facile hydrogen absorption and desorption in complex hydrides such as sodium alanate ($NaAlH_4$).

Nano porous carbon's nano structure can be damaged by the post ball milling treatment. On the other side, the nano porous carbon's particle size can be significantly decreased and keeping the well nano structure as well by ball milling treatment to the polymer powders before the final calcination process. Furthermore, the time lengths of ball mill treatment to polymer powders result in final nano porous carbon in different particle sizes.

Nano sized titanium dioxide crystals can be embedded into the nano porous carbon by direct synthesis and in-situ crystallization by using titanium (IV) isopropoxide titanium source rather than the toxic titanium (IV) chloride. It showed good electrochemical properties with stabilized capacity of 200 mAh/g.

A new synthesis method for making anatase titanium dioxide nano particles with very controllable particle sizes was invented. This new method has remarkable easy and efficient synthesis process and there will be much lower risk of introducing other chemical impurities to the final anatase titanium dioxide nano particles. Those anatase

titanium dioxide nano particles showed great electrochemical properties with more than 225 mAh/g reversible capacity even after several high C-rate current cycles. It is interesting that the particle sizes do affect the lithium ion diffusion kinetics and the battery capacities.

A newly developed lithium diffusion model based on the stretched exponential method was used to analyze the lithium diffusion behaviors in different nano-particle systems by fitting the relaxation portions of the galvanostatic intermittent titration technique (GITT) measurements. This model was demonstrated as a good analyzing method for lithium diffusion behavior in synthesized anatase titanium dioxides particles and the calculated lithium diffusion coefficients for those samples were in good agreement with previous work done by others. Also, by using this model, the lithium diffusion behaviors in titanium dioxide and tin dioxide were analyzed and compared, as those two systems represent intercalation and conversion reactions respectively.

For nano-structured energy storage materials, future work should be more focused on the insight principles and investigations of the materials that already have good properties. For instance, the lithium ion diffusion behaviors in anatase titanium dioxide material are affected by different nano particle sizes. More modeling and simulation work should be done in order to fully understand how the particle sizes change the lithium ion diffusion behaviors and affect other kinetics properties.

APPENDICES

APPENDIX A.

X-RAY DIFFRACTION SIMULATION CODE

The input material structure file should be in “material.txt” format in the following format (following is $NaAlH_4$ structure file as an example):

3.00000000000000 0.00000000000000 0.00000000000000 (*3 is 3 atom types*)

1.00000000000000 0.00000000000000 0.00000000000000 (*H atomic number*)
11.0000000000000 0.00000000000000 0.00000000000000 (*Na atomic number*)
13.0000000000000 0.00000000000000 0.00000000000000 (*Al atomic number*)

16.0000000000000 0.00000000000000 0.00000000000000 (*H atom numbers*)
4.00000000000000 0.00000000000000 0.00000000000000 (*Na atom numbers*)
4.00000000000000 0.00000000000000 0.00000000000000 (*Al atom numbers*)

5.02200000000000 0.00000000000000 0.00000000000000 (*Unit cell “a” length*)
5.02200000000000 0.00000000000000 0.00000000000000 (*Unit cell “b” length*)
11.3300000000000 0.00000000000000 0.00000000000000 (*Unit cell “c” length*)
90.0000000000000 0.00000000000000 0.00000000000000 (*Unit cell “α” angle*)
90.0000000000000 0.00000000000000 0.00000000000000 (*Unit cell “β” angle*)
90.0000000000000 0.00000000000000 0.00000000000000 (*Unit cell “γ” angle*)

0.26260000000000 0.59670000000000 0.04000000000000 (*H atomic positions*)
0.15330000000000 0.51260000000000 0.29000000000000
0.73740000000000 0.90330000000000 0.04000000000000
0.84670000000000 0.98740000000000 0.29000000000000
0.73740000000000 0.40330000000000 0.96000000000000
0.84670000000000 0.48740000000000 0.71000000000000
0.26260000000000 0.09670000000000 0.96000000000000
0.15330000000000 0.01260000000000 0.71000000000000
0.76260000000000 0.09670000000000 0.54000000000000
0.65330000000000 0.01260000000000 0.79000000000000

0.23740000000000 0.40330000000000 0.54000000000000
0.34670000000000 0.48740000000000 0.79000000000000
0.23740000000000 0.90330000000000 0.46000000000000
0.34670000000000 0.98740000000000 0.21000000000000
0.76260000000000 0.59670000000000 0.46000000000000
0.65330000000000 0.51260000000000 0.21000000000000

0.00000000000000 0.25000000000000 0.12500000000000 (*Na atomic positions*)
0.50000000000000 0.25000000000000 0.37500000000000
0.00000000000000 0.75000000000000 0.87500000000000
0.50000000000000 0.75000000000000 0.62500000000000

0.00000000000000 0.25000000000000 0.62500000000000 (*Al atomic positions*)
0.50000000000000 0.25000000000000 0.87500000000000
0.00000000000000 0.75000000000000 0.37500000000000
0.50000000000000 0.75000000000000 0.12500000000000

The X-ray diffraction Matlab code with detailed interpretations is showing as following:

```
%%%%%%%%%%%%%%%%%%%%%%%%%%%%%%%%%%%%%%%%%%%%%%%%%%%%%%%%%%%%%%%%%%%%%%%%%%%%%%%%
Introduction for the input "material.txt" file of materials' parameters.

%**** 1, Section 1 is for number of types of atoms of this material ,
%     for example, if you want to input NaCl, you should input "2 0 0".
%     This means there are 2 types of atoms of NaCl.

%**** 2, Section 2 is for Z values of atoms, ordered as small-->big of Z number
%     for example, if you want to input NaCl, you should input "11 0 0" and
%     "17 0 0". This means from small to big order, they are Na and Cl.

%**** 3, Section 3 is for numbers of each atom, also ordered as small-->big of
Z number
%     for example, if you want to input NaCl, you should input "4 0 0" and
%     "4 0 0". This means there are 4 Na atoms and 4 Cl atoms.

%**** 4, Secttion 4 is for is for the a,b,c,alpha,beta,and gamma for the
structure,
%     for example, if you want to input NaCl, you should input "5.5739 0
%     0","5.5739 0 0", "5.5739 0 0", "90 0 0","90 0 0", and "90 0 0".

%**** 5, Section 5 is for atoms' positions in the unit cell, also ordered as
small-->big of Z number
```

```
%     for example, if you want to input NaCl, you should input "0.5 0.5 0.5/n 0
0 0.5/n 0 0.5 0/n 0.5 0 0/n 0 0 0/n 0.5 0.5 0/n 0.5 0 0.5/n 0 0.5 0.5/n" and
%     save as "material.txt"

%**** 6, make sure you put "material.txt" file as the same folder as your
matlab's ".m" file
%%%%%%%%%%%%%%%%%%%%%%%%%%%%%%%%%%%%%%%%%%%%%%%%%%%%%%%%%%%%%%%%%%%%%%%%%%%%

% Simulate the "powder average" calculation with all possible h,k &l parameters

%%%%%%%%%%%%%%%%%%%%%%%%%%%%%%%%%%%%%%%%%%%%%%%%%%%%%%%%%%%%%%%%%%%%%%%%%%%%
% For XRD sufficient condition, Structure factor is not ZERO. I.e. F(hkl)≠ 0
% F(hkl) = ∑(n) fn exp{2πi(hxn + kyn + lzn)}
% For simple expression,

% (1) For face-centered, hkl unmixed (all odd or all even),
%     F(hkl)=4∑(n/4)fn exp{2πi(hxn + kyn + lzn)}, hkl mixed, F(hkl)=0
% (2) For body-centered, h+k+l=even, F(hkl)=2∑(n/2) fn exp{2πi(hxn + kyn + lzn)}
%     h+k+l=odd, F(hkl)=0
% (3) For hexagonal closed-packed structure,
%     h+2k=3n, l=even: F(hkl)^2 = 4xf^2,
%     h+2k=3n±1, l=odd: F(hkl)^2 = 3xf^2,
%     h+2k=3n±1, l=even: F(hkl)^2 = f^2,
%     h+2k=3n, l=odd: F(hkl)^2 = 0,

%  For example,for NaCl Sodium Chloride,face centered cubic Bravais Lattice
%  The Lattice Constant a0=5.5739 Angstrom = 5.5739 x 10^-10 meters
%  a0 = dhkl x (h^2 + k^2 + l^2)^ 0.5
%  n x lambda= 2 x d x sin θ, for caculation, we usually set n = 1
%  For X-ray (Cu) wavelength is lambda = 1.54 Angstrom = 1.54 x 10^-10 meters
%  So that the expresssion for θ is: θ = asin(lambda /2dhkl )
%  i.e.: θ = asin(lambda /2 * (a0 / ((h^2 + k^2 + l^2)^ 0.5) ) )
%  Then we can get the 2θ for hkl.

%--------------------------------------------------------------------------
% To generalize this computation, we need to back to the original basic
% spacing formulae, which related to the basic lattice parameters
% α, β, γ, a, b, c, h, k, and l
% 1/(dhkl^2) = 1 / { 1 + 2*cos(α)*cos(β)*cos(γ) - cos^2(α) - cos^2(β) -
cos^2(γ)} * { h^2*sin^2(α) / a^2 + k^2*sin^2(β) / b^2 + l^2*sin^2(γ) / c^2
% + 2*h*k*[ cos(α)*cos(β) - cos(γ) ] / ab + 2*k*l*[ cos(β)*cos(γ) - cos(α) ] /
bc + 2*l*h*[ cos(γ)*cos(α) - cos(β) ] / ac }
% We need to input the lattice parameters of the crystal, then we can get
% the desired calculation results
% For example, NaCl is face centered cubic Lattice
% a=b=c, α =β =γ =90 degrees.
% In the old code, it can be short to "a0 = dhkl x (h^2 + k^2 + l^2)^ 0.5"
% So next step is to generalize this code for Arbitrary materials.

%%%%%%%%%%%%%%%%%%%%%%%%%%%%%%%%%%%%%%%%%%%%%%%%%%%%%%%%%%%%%%%%%%%%%%%%%%%%
Read the materials' parameter
AAA=textread('material.txt'); % Get the input file of material
AAA1=AAA;
NN=AAA1(1,1);
NK=NN;% Number of atoms' types
Z=[]; % For the atoms' Z values' storage
N=[]; % For the numbers of each atom's storage
C=[]; % For the lattice contants' storage

%%%%%%%%%%%%%%%%%%%%%%%%%%%%%%%%%%%%%%%
% Get the Z-values of the atoms
for NK1=1:1:NK;
    Z(NK1)=AAA1(NK1+1,1);
```

```
end
%%%%%%%%%%%%%%%%%%%%%%%%%%%%%%%%%%%%%%

%%%%%%%%%%%%%%%%%%%%%%%%%%%%%%%%%%%%%%%%%%%%%
% Get the numbers of each kind of Atom
for NK2=1:1:NK;
    N(NK2)=AAA1(NK2+NK+1,1);
end
%%%%%%%%%%%%%%%%%%%%%%%%%%%%%%%%%%%%%%%%%%%%%

%%%%%%%%%%%%%%%%%%%%%%%%%%%%%%%%%%%%%%%%%%%%%%%%%%%%%%
% Get the lattice constants of this material
for NK3=1:1:6;
    C(NK3)=AAA1(NK3+NK*2+1,1);
end

a=C(1);  % a value
b=C(2);  % b value
c=C(3);  % c value
aa1=C(4);  % alpha value
bb1=C(5);  % beta value
cc1=C(6);  % gamma value
%%%%%%%%%%%%%%%%%%%%%%%%%%%%%%%%%%%%%%%%%%%%%%%%%%%%%%%


%%%%%%%%%%%%%%%%%%%%%%%%%%%%%%%%%%%%%%%%%%%%%%%%%%%%%%%%%%%%%%%%%%
% Get the atoms' positions of this material
NNKK=size(AAA1);
Nline=NNKK(1);
Npoline=Nline-2*NK-7; % Get the lines of positions' data

for NK4=1:1:Npoline;
    D(NK4,1)=AAA1(NK4+NK*2+7,1);
    D(NK4,2)=AAA1(NK4+NK*2+7,2);
    D(NK4,3)=AAA1(NK4+NK*2+7,3);
end

%%%%%%%%%%%%%%%%%%%%%%%%%%%%%%%%%%%%%%%%%%%%%%%%%%%%%%%%%%%%%%%%%%

%%%%%%%%%%%%%%%%%%%%%%%%%%%%%%%%%%%%%%%%%%%%%%%%%%%%%%%%%%%%%%%%%%%%%%%%%%%%%%
%%%%%%%%%%%%%%%%%%%%%%%%%%%%%%%%%%%%%%%%%%%%%%%%%%%%%%%%%%%%%%%%%%%%%%%%%%%%%%%
%%%%%%%%%

% To compute the 2θ angles value, output in unit of degrees
tho = []; % Define a NULL matrix for storage ouput angle data and h, k, l
Q = [];% Define a NULL matrix for storage ouput q-value
Q1 = [];% Define a NULL matrix for storage sorted ouput q-value

aa=aa1/180*pi; % Covert to pi unit
bb=bb1/180*pi; % Covert to pi unit
cc=cc1/180*pi; % Covert to pi unit

hm=100; %input('Input maximum value of h: '); % Input the h of the lattice
parameter.

j=1;

% Start for h k l loop
for h=0:1:hm;
   for k=0:1:hm;
    for l=0:1:hm;

    d1 = 1/(1 + 2*(cos(aa))*(cos(bb))*(cos(cc)) - (cos(aa))^2 - (cos(bb))^2 -
(cos(cc))^2 );
    d2 = h^2*(sin(aa))^2/(a^2) + k^2*(sin(bb))^2/(b^2) + l^2*(sin(cc))^2/(c^2)
+ 2*h*k*((cos(aa))*(cos(bb))-cos(cc) )/(a*b);
```

```
    d3 = 2*k*l*((cos(bb))*(cos(cc))-cos(aa))/(b*c) +
2*l*h*((cos(cc))*(cos(aa))-cos(bb))/(a*c);
    d = d1*(d2+d3);
    dhkl = (1/d)^0.5;

   lamada = 1.54; % In unit of Angstrom
    if   lamada/2/dhkl>1;  % Select the reasonable spacing satisfies Bragg's
Law

     else

   theta = asin( lamada/2/dhkl)/pi*180;

   q = 2*pi/dhkl; % Calculate the q-value

   fe = 1/(( 1+ (q/2)^2 )^2);  % Calculate the scattering factor /electron

  % fNa = 11 * fe; % scattering factor for Sodium
  % fCl = 17 * fe; % scattering factor for Chloride


%%%%%%%%%%%%%%%%%%%%%%%%%%%%%%%%%%%%%%%%%%%%%%%%%%%%%%%%%%%%%%%%%%%%%%%%%%%%%%%%
%%%%%%%%%%%%%%
 %%%%%%%%%%%%%%%%%%%%%%%% Then calculate the Fhkl's square value.% %%%%%%%%

   ppp=1; % For add the count in following loop
   Fss=0;
   Fcc=0;

WWW=[]; % Storage the Real part of type p atom
YYY=[]; % Storage the Imaginary part of type p atom

   for p=1:1:NK; % Loop from first type of atom
       f=Z(p)*fe;  % Atom's scattering factor is Z * fe
       W=[];
       Y=[];
       for pp=1:1:(N(p)); % Loop from first atom type's first atom

           x=D(ppp,1);% Each Atom x-position
           y=D(ppp,2);% Each Atom y-position
           z=D(ppp,3);% Each Atom z-position

           Fcos=f*cos(2*pi*(h*x+k*y+l*z)) ;    % Real part of type p atom
           Fsin=f*sin(2*pi*(h*x+k*y+l*z)) ;    % Imaginary part of type p atom

           W(1,pp)=Fcos;% Storage the Real part of type p atom's pp's data
           Y(1,pp)=Fsin;% Storage the Imaginary part of type p atom's pp's data

           ppp=ppp+1; % Count add up

       end

       WWW(1,p)=sum(W);% Real part of type p atom
       YYY(1,p)=sum(Y);% Imaginary part of type p atom

   end

   FhklSQ = (sum(WWW))^2 + (sum(YYY))^2; % Structure factor's square value

   % For an electron, the internsity of the scattering beam simplized to
   % following:
   Ie = 1 *  (1 + (cos(2*theta*pi/180))^2 )/2; % introduced into the
polarization coefficient.
   I = FhklSQ * Ie;  % Internsity of the unit cell


%%%%%%%%%%%%%%%%%%%%%%%%%%%%%%%%%%%%%%%%%%%%%%%%%%%%%%%%%%%%%%%%%%%%%%%%%%%%%%%%

   %Storage the data to the matrix - tho
   tho(j,1)=theta*2;
```

```
   tho(j,2)=h;
   tho(j,3)=k;
   tho(j,4)=l;
   tho(j,5)=dhkl;
   tho(j,6)=q;
   tho(j,7)=FhklSQ;
   tho(j,8)=I;

   Q(j,1)=q; % Storage the q-value into matrix Q-1
   Q(j,2)=I; % Storage the Intensity into matrix Q-2
   Q(j,3)=theta*2; % Storage the two-theta into matrix Q-3

   jcount=j; % Get the count number for the loop

   j=j+1;
     end

   end
   end
   h=h+1;
end

Q1 = sortrows(Q,1);

%%%%%%%%%%%%%%%%%%%%%%%%%%%%%%%%%%%%%%%%%%%%%%%%%%%%%%%%%%%%%%%%%%%%%%%%%%%%%%%
Then begin to bin the q-value and Intensity

Qtol=0.12;% Set the q-values' difference tolerance
U1=[]; % For the two-theta data storage
W1=[]; % For the accumulated Intensity data storage
V1=[]; % For q-value Accumulation's average value data storage
k1=1;
j1=1; % Kind
S1=size(Q1);
q1=1;


for p1=1:1:(S1(1));
    if q1+k1>(S1(1));
        break;
    else

        if abs(Q1(q1,1)-Q1(q1+k1,1))<Qtol;  % Difference's Tolenrance of q-
values
           W1(j1)=sum( Q1(q1:1:(q1+k1),2) ); % Intensity Accumulation
           V1(j1)=sum( Q1(q1:1:(q1+k1),1) )/(k1+1); % q-value Accumulation's
average value
           U1(j1,1)=Q1(q1,3);  % storage each kind of combination's smallest
two-theta value
           U1(j1,2)=Q1(q1+k1,3);  % storage each kind of combination's smallest
two-theta value
           k1=k1+1;
        else
           j1=j1+1; % New kind of combination
           W1(j1)=Q1(q1+k1,2);
           V1(j1)=Q1(q1+k1,1);
           U1(j1,1)=Q1(q1+k1,3);
           U1(j1,2)=Q1(q1+k1,3);
           q1=q1+k1;
           k1=1;
        end

    end

end

%%%%%%%%%%%%%%%%%%%%%%%%%%%%%%%%%%%%%%%%%%%%%%%%%%%%%%%%%%%%%%%%%%%%%%%%%%%%%%%
```

```
fprintf('\n\n\nThe 2 theta, h, k, and l,d-spacing, q-value, Fhkl-square,and
Intensity are as follows:\n ');
tho

%%%%%%%%%%%%%%%%%%%%%%%%%%%% Plot the binned two theta- Intensity%%%%%%%%%%%%

Su = size(U1); % Get the size of matrix for two-theta data
Sw = size(W1); % Get the size of matrix for Intensity data
Nbin = Su(1); % Get the number of binned combinations

U11=roundn(U1,-2);

PLT=[]; % Storage the plot data

for uuu=1:1:180*100;
    plotx(uuu) = uuu/100;
    PLT(uuu,1) = uuu/100;
    ploty(uuu) = 0;
    PLT(uuu,2) = 0;
end

if U11(1,1) == 0;
    xr = 2;
else
    xr=1;
end

for Nb = xr:1:Nbin; % Loop for the plot

    ploty( (U11(Nb,1)*100):1:(U11(Nb,2)*100) ) =  10000;  %W1(Nb)*90;
    PLT( (U11(Nb,1)*100):1:(U11(Nb,2)*100),2 ) = W1(Nb);

end

%%%%%%% Graph the the binned two theta- Intensity%%%%%%%%%%%%%%%%%
% Read the experiment data first
EXP=textread('experiment.txt'); % Get the input file of material
eline = size(EXP);
expline = eline(1);

for Nexp=1:1:expline;
    eplotx(Nexp,1) = EXP(Nexp,1);
    eploty(Nexp,2) = EXP(Nexp,2);
end

figure(1); clf;    % Clear figure window #1 and bring it forward
%plot(plotx,ploty,'r',EXP,'b')
plot(eplotx,eploty,'b',plotx,ploty,'r')
legend('Intensity');
xlabel('Two-Theta(Degree)');
ylabel('Intensity');
title('XRD pattern');
%%%%%%   E  N  D  %%%%%%%%%%%%%%%%%%%%%%%%%%%%%%%%%%%%%%%%%%%%%%%%%%%%%%%%%
```

APPENDIX B.

NANO POROUS CARBON DETAILED FABRICATION RECORDS

Table B1. NPC detailed fabrication records

NPC Batch	Ball Milled Before OR After	Ball Milled Time	Carbonize Time	Production Ratio Polymer→Carbon	Weight (g)	BET Surface Area: m^2/g
C17A	Not ball milled	0	2 hours	Not Measured	N/A	1010.50
C17B	Before	10 min.	2 hours	Not Measured	N/A	1209.33
C17C	Before	5 min.	2 hours	Not Measured	N/A	1457.52
C17D	After	5 min.	2 hours	Not Measured	N/A	542.18
C18A	Not ball milled	0	2 hours	20.91%	1.4161	992.63
C18B	Before	5 min.	30 min.	14.99%	0.4481	918.10
C19A	Not ball milled	0	2 hours	17.37%	1.0610	1018.80
C20A	Not ball milled	0	2 hours	26.14%	3.7769	779.00
C21	Before	5 min.	30 min.	18.17%	2.2000	647.24
C22A	Not ball milled	0	1 hour	12.90%	0.5201	1004.48
BM1 mc	Before	1 min.	30 min.	18.93%	1.0871	812.69
BM2 mc	Before	2 min.	30 min.	19.79%	1.2683	787.37
BM3 mc	Before	3 min.	30 min.	16.80%	0.9102	894.57
BM4 mc	Before	4 min.	30 min.	8.53%	0.2112	1083.00
BM5 mc	Before	5 min.	30 min.	11.49%	0.2619	995.47
JP1	Milled by pod	Milled by pod	30 min.	22.22%	2.9050	666.15
JP2	Milled by pod	Milled by pod	30 min.	21.37%	3.3856	707.63
JP3	Milled by pod	Milled by pod	1 hour	24.39%	2.7251	754.20

REFERENCES

[1] Armaroli, N.; Balzani, V. The future of energy supply: challenges and opportunities. *Angewandte Chemie International Edition*. **2007**, *46(1-2)*, 52-66.

[2] Chen, H.; Cong, T. N.; Yang, W.; Tan, C.; Li, Y.; Ding, Y. Progress in electrical energy storage system: A critical review. *Progress in Natural Science*. **2009**, *19(3)*, 291-312.

[3] McLarnon, F. R.; Cairns, E. J. Energy storage. *Annual Review of Energy*. **1989**, *14(1)*, 241-271.

[4] Dunn, B.; Kamath, H.; Tarascon, J. M. Electrical energy storage for the grid: a battery of choices. *Science*. **2011**, *334(6058)*, 928-935.

[5] Kondoh, J.; Ishii, I.; Yamaguchi, H.; Murata, A.; Otani, K.; Sakuta, K.; Niguchi, N.; Sekine, S.; Kamimoto, M. Electrical energy storage systems for energy networks. *Energy Conversion and Management*. **2000**, *41(17)*, 1863-1874.

[6] Walawalkar, R.; Apt, J.; Mancini, R. Economics of electric energy storage for energy arbitrage and regulation in New York. *Energy Policy*. **2007**, *35(4)*, 2558-2568.

[7] Weinstock, I. B. Recent advances in the US Department of Energy's energy storage technology research and development programs for hybrid electric and electric vehicles. *Journal of Power Sources*. **2002**, *110(2)*, 471-474.

[8] Hall, P. J.; Bain, E. J. Energy-storage technologies and electricity generation. *Energy Policy*. **2008**, *36(12)*, 4352-4355.

[9] Dyer, C. K. Fuel cells for portable applications. *Journal of Power Sources*. **2002**, **106(1)**, 31-34.

[10] Hadjipaschalis, I.; Poullikkas, A.; Efthimiou, V. Overview of current and future energy storage technologies for electric power applications. *Renewable and Sustainable Energy Reviews.* **2009**, *13(6)*, 1513-1522.

[11] Yüksek, Ö.; Kaygusuz, K. Small hydropower plants as a new and renewable energy source. *Energy Sources, Part B.* **2006**, *1(3)*, 279-290.

[12] Wolsink, M. Wind power and the NIMBY-myth: institutional capacity and the limited significance of public support. *Renewable Energy*. **2000**, *21(1)*, 49-64.

[13] Thounthong, P.; Chunkag, V.; Sethakul, P.; Sikkabut, S.; Pierfederici, S.; Davat, B. Energy management of fuel cell/solar cell/supercapacitor hybrid power source. *Journal of power sources*. **2011**, *196(1)*, 313-324.

[14] Energy.gov

[15] www.teslamotors.com

[16] Edwards, P. P.; Kuznetsov, V. L.; David, W. I.; Brandon, N. P. Hydrogen and fuel cells: towards a sustainable energy future. *Energy policy*. **2008**, *36(12)*, 4356-4362.

[17] www.toyota.com/FuelCell

[18] Sakintuna, B.; Lamari-Darkrim, F.; Hirscher, M. Metal hydride materials for solid hydrogen storage: a review. *International Journal of Hydrogen Energy*. **2007**, *32(9)*, 1121-1140.

[19] Schlapbach, L., & Züttel, A. Hydrogen-storage materials for mobile applications. *Nature*. **2001**, *414(6861)*, 353-358.

[20] Momirlan, M.; Veziroglu, T. N. The properties of hydrogen as fuel tomorrow in sustainable energy system for a cleaner planet. *International Journal of Hydrogen Energy*. **2005**, *30(7)*, 795-802.

[21] http://energy.gov/oe/office-electricity-delivery-and-energy-reliability

[22] http://energy.gov/eere/fuelcells/hydrogen-storage

[23] Stojić, D. L.; Marčeta, M. P.; Sovilj, S. P.; Miljanić, Š. S. Hydrogen generation from water electrolysis—possibilities of energy saving. *Journal of Power Sources*. **2003**, *118(1)*, 315-319.

[24] Zeng, K.; Zhang, D. Recent progress in alkaline water electrolysis for hydrogen production and applications. *Progress in Energy and Combustion Science*. **2010**, *36(3)*, 307-326.

[25] Ni, M.; Leung, M. K.; Leung, D. Y.; Sumathy, K. A review and recent developments in photocatalytic water-splitting using TiO_2 for hydrogen production. *Renewable and Sustainable Energy Reviews*. **2007**, *11(3)*, 401-425.

[26] Fujishima, A.; Honda, K. Electrochemical photolysis of water at a semiconductor electrode. Nature. **1972**, *(238)*, 37-8.

[27] Puga, A. V.; Forneli, A.; García, H.; Corma, A. Hydrogen Production: Production of H2 by Ethanol Photoreforming on Au/TiO_2. *Advanced Functional Materials*. **2014**, *24(2)*, 240-240.

[28] Kennedy, J.; Jones, W.; Morgan, D. J.; Bowker, M.; Lu, L.; Kiely, C. J.; Wells, P. P.; Dimitratos, N. Photocatalytic hydrogen production by reforming of methanol using Au/TiO_2, Ag/TiO_2 and $Au-Ag/TiO_2$ catalysts. *Catalysis, Structure & Reactivity*. **2015**, *1(1)*, 35-43.

[29] Fuel Cell Technologies Office Multi-Year Research, Development and Demonstration Plan, Fuel Cell Technologies Office, Office of Energy Efficiency and Renewable Energy, *U.S. Dept. of Energy* **2012**.

[30] Rosi, N. L.; Eckert, J.; Eddaoudi, M.; Vodak, D. T.; Kim, J.; O'Keeffe, M.; Yaghi, O. M. Hydrogen storage in microporous metal-organic frameworks. *Science*. **2003**, *300(5622)*, 1127-1129.

[31] Kaye, S. S.; Dailly, A.; Yaghi, O. M.; Long, J. R. Impact of preparation and handling on the hydrogen storage properties of Zn_4O (1, 4-benzenedicarboxylate) 3 (MOF-5). *Journal of the American Chemical Society*. **2007**, *129(46)*, 14176-14177.

[32] Klontzas, E.; Mavrandonakis, A.; Tylianakis, E.; Froudakis, G. E. Improving hydrogen storage capacity of MOF by functionalization of the organic linker with lithium atoms. *Nano Letters*. **2008**, *8(6)*, 1572-1576.

[33] Yang, S. J.; Kim, T.; Im, J. H.; Kim, Y. S.; Lee, K.; Jung, H.; Park, C. R. MOF-derived hierarchically porous carbon with exceptional porosity and hydrogen storage capacity. *Chemistry of Materials*. **2012**, *24(3)*, 464-470.

[34] Xu, W-C.; Takahashi, K.; Matsuo, Y.; Hattori, Y.; Kumagai, M.; Ishiyama, S.; Kaneko, K.; Iijima, K. Investigation of hydrogen storage capacity of various carbon materials. *International Journal of Hydrogen Energy*. **2007**, *32(13)*, 2504-2512.

[35] Gross, A. F.; Vajo, J. J.; Van Atta, S. L.; Olson, G. L. Enhanced hydrogen storage kinetics of $LiBH_4$ in nanoporous carbon scaffolds. *The Journal of Physical Chemistry C*. **2008**, *112(14)*, 5651-5657.

[36] Liu, X.; Peaslee, D.; Jost, C. Z.; Majzoub, E. H. Controlling the decomposition pathway of $LiBH_4$ via confinement in highly ordered nanoporous carbon. *The Journal of Physical Chemistry C*. **2010**, *114(33)*, 14036-14041.

[37] Sorte, E. G.; Majzoub, E. H.; Ellis-Caleo, T.; Hammann, B. A.; Wang, G.; Zhao, D.; Bowman, R. C. Jr.; Conradi, M. S. Effects of NaOH in Solid NaH: Solution/Segregation Phase Transition and Diffusion Acceleration. *The Journal of Physical Chemistry C*. **2013**, *117(45)*, 23575-23581.

[38] Wang, G.; Carr, C. L.; Zhao, D.; Sorte, E. G.; Ellis-Caleo, T.; Conradi, M. S.; Bowman, R. C. Jr.; Majzoub, E. H. Density Functional Theory of MH-MOH Solid Solubility (M= alkali) and Experiments in NaH-NaOH. *The Journal of Physical Chemistry C*. **2015**.

[39] Delmelle, R.; Gehrig, J. C.; Borgschulte, A.; Züttel, A. Reactivity enhancement of oxide skins in reversible Ti-doped $NaAlH_4$. *AIP Advances*. **2014**, *4(12)*, 127130.

[40] Majzoub, E. H.; Herberg, J. L.; Stumpf, R.; Spangler, S.; Maxwell, R. S. XRD and NMR investigation of Ti-compound formation in solution-doping of sodium aluminum hydrides: solubility of Ti in $NaAlH_4$ crystals grown in THF. *Journal of alloys and compounds*. **2005**, *394(1)*, 265-270.

[41] Mauron, P.; Buchter, F.; Friedrichs, O.; Remhof, A.; Bielmann, M.; Zwicky, C. N.; Züttel, A. Stability and reversibility of LiBH4. *The Journal of Physical Chemistry B*. **2008**, *112(3)*, 906-910.

[42] Kostka, J.; Lohstroh, W.; Fichtner, M.; Hahn, H. Diborane release from $LiBH_4$/silica-gel mixtures and the effect of additives. *The Journal of Physical Chemistry C*. **2007**, *111(37)*, 14026-14029.

[43] Uemura, T.; Omae, K.; Nakashima, H.; Sakurai, H.; Yamazaki, K.; Shibata, T.; Mori, K.; Kudo, M.; Kanoh, H.; Tati, M. Acute and subacute inhalation toxicity of diborane in male ICR mice. *Archives of Toxicology*. **1995**, *69(6),* 397-404.

[44] Gao, J.; Adelhelm, P.; Verkuijlen, M. H.; Rongeat, C.; Herrich, M.; van Bentum, P. J. M.; Gutfleisch, O.; Kentgens, A. PM.; de Jongh, K. P.; de Jongh, P. E. Confinement of $NaAlH_4$ in nanoporous carbon: impact on H_2 release, reversibility, and thermodynamics. *The Journal of Physical Chemistry C*. **2010**, *114(10),* 4675-4682.

[45] Stephens, R. D.; Gross, A. F.; Van Atta, S. L.; Vajo, J. J.; Pinkerton, F. E. The kinetic enhancement of hydrogen cycling in $NaAlH_4$ by melt infusion into nanoporous carbon aerogel. *Nanotechnology.* **2009**, *20(20),* 204018.

[46] Ji, L.; Zhang, X. Fabrication of porous carbon nanofibers and their application as anode materials for rechargeable lithium-ion batteries. *Nanotechnology*. **2009**, *20(15),* 155705.

[47] Zhang, F.; Wang, K. X.; Li, G. D.; Chen, J. S. Hierarchical porous carbon derived from rice straw for lithium ion batteries with high-rate performance. *Electrochemistry Communications.* **2009**, *11(1),* 130-133.

[48] Li, C.; Yin, X.; Chen, L.; Li, Q.; Wang, T. Porous carbon nanofibers derived from conducting polymer: synthesis and application in lithium-ion batteries with high-rate capability. *The Journal of Physical Chemistry C.* **2009**, *113(30),* 13438-13442.

[49] Zhang, L. L.; Zhao, X. S. Carbon-based materials as supercapacitor electrodes. *Chemical Society Reviews.* **2009**, *38(9),* 2520-2531.

[50] Frackowiak, E. Carbon materials for supercapacitor application. *Physical Chemistry Chemical Physics.* **2007**, *9(15),* 1774-1785.

[51] Stein, A.; Wang, Z.; Fierke, M. A. Functionalization of porous carbon materials with designed pore architecture. *Advanced Materials*. **2009**, *21(3),* 265-293.

[52] Huang, C. H.; Gu, D.; Zhao, D.; Doong, R. A. Direct synthesis of controllable microstructures of thermally stable and ordered mesoporous crystalline titanium oxides and carbide/carbon composites. *Chemistry of Materials*. **2010**, *22(5),* 1760-1767.

[53] Carlsson, J. M.; Scheffler, M. Structural, electronic, and chemical properties of nanoporous carbon. *Physical review letters.* **2006**, *96(4),* 046806.

[54] Meng, Y.; Gu, D.; Zhang, F.; Shi, Y.; Yang, H.; Li, Z.; Yu, C.; Tu, B.; Zhao, D. Ordered mesoporous polymers and homologous carbon frameworks: amphiphilic surfactant templating and direct transformation. *Angewandte Chemie*. **2005**, *117(43),* 7215-7221.

[55] Meng, Y.; Gu, D.; Zhang, F.; Shi, Y.; Cheng, L.; Feng, D.; Wu, Z.; Chen, Z.; Wan, Y.; Stein, A.; Zhao, D. A family of highly ordered mesoporous polymer resin and carbon structures from organic-organic self-assembly. *Chemistry of materials.* **2006**, *18(18)*, 4447-4464.

[56] Lee, J.; Han, S.; Hyeon, T. Synthesis of new nanoporous carbon materials using nanostructured silica materials as templates. *Journal of Materials Chemistry.* **2004**, *14(4)*, 478-486.

[57] Yang, C. M.; Sheu, H. S.; Chao, K. J. Templated Synthesis and Structural Study of Densely Packed Metal Nanostructures in MCM‐41 and MCM‐48. *Advanced Functional Materials.* **2002**, *12(2)*, 143-148.

[58] Huang, M. H.; Choudrey, A.; Yang, P. Ag nanowire formation within mesoporous silica. *Chemical Communications.* **2000**, *(12)*, 1063-1064.

[59] Zhu, S.; Zhou, H.; Hibino, M.; Honma, I.; Ichihara, M. Synthesis of MnO_2 nanoparticles confined in ordered mesoporous carbon using a sonochemical method. *Advanced Functional Materials.* **2005**, *15(3)*, 381-386.

[60] Jiang, H.; Yang, L.; Li, C.; Yan, C.; Lee, P. S.; Ma, J. High–rate electrochemical capacitors from highly graphitic carbon–tipped manganese oxide/mesoporous carbon/manganese oxide hybrid nanowires. *Energy & Environmental Science*. **2011**, *4(5)*, 1813-1819.

[61] Song, H. K.; Jung, Y. H.; Lee, K. H.; Dao, L. H. Electrochemical impedance spectroscopy of porous electrodes: the effect of pore size distribution. *Electrochimica Acta.* **1999**, *44(20)*, 3513-3519.

[62] Fu, R. W.; Li, Z. H.; Liang, Y. R.; Feng, L. I.; Fei, X. U.; Wu, D. C. Hierarchical porous carbons: design, preparation, and performance in energy storage. *New Carbon Materials.* **2011**, *26(3)*, 171-179.

[63] Wang, Y.; Su, F.; Lee, J. Y.; Zhao, X. S. Crystalline carbon hollow spheres, crystalline carbon-SnO2 hollow spheres, and crystalline SnO_2 hollow spheres: synthesis and performance in reversible Li-ion storage. *Chemistry of Materials.* **2006**, *18(5)*, 1347-1353.

[64] Palacín, M. R. Recent advances in rechargeable battery materials: a chemist's perspective. *Chemical Society Reviews.* **2009**, *38(9)*, 2565-2575.

[65] Gao, X. P.; Yang, H. X. Multi-electron reaction materials for high energy density batteries. *Energy & Environmental Science.* **2010**, *3(2)*, 174-189.

[66] Poizot, P.; Laruelle, S.; Grugeon, S.; Dupont, L.; Tarascon, J. M. Nano-sized transition-metal oxides as negative-electrode materials for lithium-ion batteries. *Nature.* **2000**, *407(6803)*, 496-499.

[67] Mao, O.; Turner, R. L.; Courtney, I. A.; Fredericksen, B. D.; Buckett, M. I.; Krause, L. J.; Dahn, J. R. Active/Inactive nanocomposites as anodes for Li-Ion batteries. *Electrochemical and Solid-State Letters.* **1999**, *2(1)*, 3-5.

[68] Wu, Y. P.; Rahm, E.; Holze, R. Carbon anode materials for lithium ion batteries. *Journal of Power Sources.* **2003**, *114(2),* 228-236.

[69] Brandt, K. Historical development of secondary lithium batteries. *Solid State Ionics.* **1994**, *69(3),* 173-183.

[70] Gaberscek, M.; Bele, M.; Drofenik, J.; Dominko, R.; Pejovnik, S. Improved carbon anode for lithium batteries pretreatment of carbon particles in a polyelectrolyte solution. *Electrochemical and Solid-State Letters*. **2000**, *3(4),* 171-173.

[71] Cheng, M. Y.; Hwang, C. L.; Pan, C. J.; Cheng, J. H.; Ye, Y. S.; Rick, J. F.; Hwang, B. J. Facile synthesis of SnO_2-embedded carbon nanomaterials via glucose-mediated oxidation of Sn particles. *Journal of Materials Chemistry*. **2011**, *21(29),* 10705-10710.

[72] Fischer, A. E.; Pettigrew, K. A.; Rolison, D. R.; Stroud, R. M.; Long, J. W. Incorporation of homogeneous, nanoscale MnO_2 within ultraporous carbon structures via self-limiting electroless deposition: implications for electrochemical capacitors. *Nano Letters.* **2007**, *7(2),* 281-286.

[73] Sudant, G.; Baudrin, E.; Larcher, D.; Tarascon, J. M. Electrochemical lithium reactivity with nanotextured anatase-type TiO_2. *Journal of Materials Chemistry*. **2005**, *15(12),* 1263-1269.

[74] Zachau-Christiansen, B.; West, K.; Jacobsen, T.; Atlung, S. Lithium insertion in different TiO_2 modifications. *Solid State Ionics*. **1988**, *28,* 1176-1182.

[75] Ohzuku, T.; Kodama, T.; Hirai, T. Electrochemistry of anatase titanium dioxide in lithium nonaqueous cells. *Journal of Power Sources*. **1985**, *14(1),* 153-166.

[76] Murphy, D. W.; Cava, R. J.; Zahurak, S. M.; Santoro, A. Ternary Li_xTiO_2 phases from insertion reactions. *Solid State Ionics.* **1983**, *9,* 413-417.

[77] Armstrong, G.; Armstrong, A. R.; Canales, J.; Bruce, P. G. TiO_2(B) nanotubes as negative electrodes for rechargeable lithium batteries. *Electrochemical and Solid-State Letters.* **2006**, *9(3),* A139-A143.

[78] Andreev, Y. G.; Panchmatia, P. M.; Liu, Z.; Parker, S. C.; Islam, M. S.; Bruce, P. G. The Shape of TiO_2-B Nanoparticles. *Journal of the American Chemical Society*. **2014**, *136(17),* 6306-6312.

[79] Saravanan, K.; Ananthanarayanan, K.; Balaya, P. Mesoporous TiO_2 with high packing density for superior lithium storage. *Energy & Environmental Science*. **2010**, *3(7),* 939-948.

[80] Liang, C.; Li, Z.; Dai, S. Mesoporous carbon materials: synthesis and modification. *Angewandte Chemie International Edition*. **2008**, *47(20),* 3696-3717.

[81] Huang, C. H.; Doong, R. A.; Gu, D.; Zhao, D. Dual-template synthesis of magnetically-separable hierarchically-ordered porous carbons by catalytic graphitization. *Carbon*. **2011**, *49(9),* 3055-3064.

[82] Chang, P. Y.; Huang, C. H.; Doong, R. A. Ordered mesoporous carbon–TiO_2 materials for improved electrochemical performance of lithium ion battery. *Carbon*. **2012**, *50(11)*, 4259-4268.

[83] Wang, Y.; Li, H.; He, P.; Hosono, E.; Zhou, H. Nano active materials for lithium-ion batteries. *Nanoscale*. **2010**, *2(8)*, 1294-1305.

[84] Mahshid, S.; Askari, M.; Ghamsari, M. S. Synthesis of TiO_2 nanoparticles by hydrolysis and peptization of titanium isopropoxide solution. *Journal of Materials Processing Technology*. **2007**, *189(1)*, 296-300

[85] Gribb, A. A.; Banfield, J. F. Particle size effects on transformation kinetics and phase stability in nanocrystalline TiO_2. *American Mineralogist*. **1997**, *82(7)*, 717-728.

[86] Kang, J. W.; Kim, D. H.; Mathew, V.; Lim, J. S.; Gim, J. H.; Kim, J. Particle size effect of anatase TiO_2 nanocrystals for lithium-ion batteries. *Journal of the Electrochemical Society*. **2011**, *158(2)*, A59-A62.

[87] Ivancic, T. M.; Hwang, S. J.; Bowman Jr, R. C.; Birkmire, D. S.; Jensen, C. M.; Udovic, T. J.; Conradi, M. S. Discovery of a new Al species in hydrogen reactions of $NaAlH_4$. *The Journal of Physical Chemistry Letters*. **2010**, *1(15)*, 2412-2416.

[88] Sorte, E. G.; Bowman Jr, R. C.; Majzoub, E. H.; Verkuijlen, M. H.; Udovic, T. J.; Conradi, M. S. Mobile species in $NaAlH_4$. *The Journal of Physical Chemistry C*. **2013**, *117(16)*, 8105-8113.

[89] Larson, A; Von Dreele, R. General Structure Analysis System (GSAS), *Los Alamos National Laboratory Report LAUR*. **2004**, 86-748.

[90] Mikheeva, V. I.; Shkrabkina, M. M. Solid Solutions in the NaOH-NaH and KOH-KH systems. *Russian Journal of Inorganic Chemistry*. **1962**, *7(10)*, 1251-1255.

[91] Bleif, H. J.; Dachs, H. Cystalline modifications and structural phase transitions of NaOH and NaOD. *Acta Crystallographica Section A: Crystal Physics, Diffraction, Theoretical and General Crystallography*. **1982**, *38(4)*, 470-476.

[92] Kuznetsov, V. G.; Shkrabkina, M. M. X-ray diffraction study of NaH and KH at temperatures from 20 to 400 C. *Journal of Structural Chemistry*. **1962**, *3(5)*, 532-537.

[93] Rasband, W. S. ImageJ, *U. S. National Institutes of Health*, Bethesda, Maryland, USA, http://imagej.nih.gov/ij/, **1997-2014**.

[94] Wojdyr, M. Fityk: a general-purpose peak fitting program. *Journal of Applied Crystallography*. **2010**, *43(5)*, 1126-1128.

[95] Oskam, G.; Nellore, A.; Penn, R. L.; Searson, P. C. The growth kinetics of TiO_2 nanoparticles from titanium (IV) alkoxide at high water/titanium ratio. *The Journal of Physical Chemistry B*. **2003**, *107(8)*, 1734-1738.

[96] Li, W.; Ni, C.; Lin, H.; Huang, C. P.; Shah, S. I. Size dependence of thermal stability of TiO_2 nanoparticles. *Journal of Applied Physics*. **2004**, *96(11)*, 6663-6668.

[97] Brutti, S.; Gentili, V.; Menard, H.; Scrosati, B.; Bruce, P. G. TiO_2-(B) Nanotubes as Anodes for Lithium Batteries: Origin and Mitigation of Irreversible Capacity. *Advanced Energy Materials*. **2012**, *2(3)*, 322-327.

[98] Saito, M.; Murota, Y.; Takagi, M.; Tajima, M.; Asao, T.; Inoue, H.; Tasaka, A.; Inaba, M. Improvement of the reversible capacity of TiO_2 (B) high potential negative electrode. *Journal of the Electrochemical Society*. **2011**, *159(1)*, A49-A54.

[99] Su, X.; Wu, Q.; Zhan, X.; Wu, J.; Wei, S.; Guo, Z. Advanced titania nanostructures and composites for lithium ion battery. *Journal of Materials Science*. **2012**, *47(6)*, 2519-2534.

[100] Zhang, Q. H.; Gao, L.; Sun, J. Effect of the Calcining Temperatures on the Properties of Nanocrystalline TiO_2. *Journal of Inorganic Materials (Beijing)*. **2001**, *16*, 833-838.

[101] Batzill, M.; Morales, E. H.; Diebold, U. Influence of nitrogen doping on the defect formation and surface properties of TiO_2 rutile and anatase. *Physical Review Letters*. **2006**, *96(2)*, 026103.

[102] Henderson, M. A.; Epling, W. S.; Perkins, C. L.; Peden, C. H.; Diebold, U. Interaction of molecular oxygen with the vacuum-annealed TiO_2 (110) surface: molecular and dissociative channels. *The Journal of Physical Chemistry B*. **1999**, *103(25)*, 5328-5337.

[103] http://plasma-gate.weizmann.ac.il/Grace/

[104] Ritger, P. L.; Peppas, N. A. A simple equation for description of solute release I. Fickian and non-Fickian release from non-swellable devices in the form of slabs, spheres, cylinders or discs. *Journal of Controlled Release*. **1987**, *5(1)*, 23-36.

[105] Ritger, P. L.; Peppas, N. A. A simple equation for description of solute release II. Fickian and anomalous release from swellable devices. *Journal of Controlled Release*. **1987**, *5(1)*, 37-42

[106] Wagemaker, M.; Van Well, A. A.; Kearley, G. J.; Mulder, F. M. The life and times of lithium in anatase TiO_2. *Solid State Ionics*. **2004**, *175(1)*, 191-193.

[107] Dees, D. W.; Kawauchi, S.; Abraham, D. P.; Prakash, J. Analysis of the Galvanostatic Intermittent Titration Technique (GITT) as applied to a lithium-ion porous electrode. *J. Power Sources*. **2009**, *189*, 263-268.

[108] Weppner, W.; Huggins, R. A. Determination of the Kinetic Parameters of Mixed-Conducting Electrodes and Application to the System Li_3Sb. *J. Electrochem. Soc*. **1977**, *124*, 1569-1578.

[109] Yang, H.; Bang, H. J.; Prakash, J. Evaluation of electrochemical interface area and lithium diffusion coefficient for a composite graphite anode. *J. Electrochem. Soc*. **2004**, *151*, A1247- A1250.

[110] Deiss, E. Spurious chemical diffusion coefficients of Li+ in electrode materials evaluated with GITT. *Electrochim. Acta.* **2005**, *50*, 2927-2932.

[111] Tang, K.; Yu, X.; Sun, J.; Li, H.; Huang, X. Kinetic analysis on $LiFePO_4$ thin films by CV, GITT, and EIS. *Electrochim. Acta.* **2011**, *56*, 4869-4875.

[112] http://plasma-gate.weizmann.ac.il/Grace/

[113] Ritger, P. L.; Peppas, N. A. A simple equation for description of solute release I. Fickian and non-Fickian release from non-swellable devices in the form of slabs, spheres, cylinders or discs. *J. Control. Release*. **1987**, *5*, 23-36.

[114] Ritger, P. L.; Peppas, N. A. A simple equation for description of solute release II. Fickian and anomalous release from swellable devices. *J. Control. Release*. **1987**, *5*, 37-42.

[115] Sushko, M. L.; Rosso, K. M.; Liu, J. Mechanism of Li+/electron conductivity in rutile and anatase TiO_2 nanoparticles. *J. Phys. Chem. C* **2010**, *114*, 20277-20283.

[116] Koudriachova, M. V.; Harrison, N. M.; de Leeuw, S. W. Diffusion of Li-ions in rutile. An ab initio study. *Solid State Ionics*. **2003**, *157*, 35-38.

[117] Wagemaker, M.; van de Krol, R.; Kentgens, A. P.; Van Well, A. A.; Mulder, F. M. Two phase morphology limits lithium diffusion in TiO_2 (anatase): A ^{7}Li MAS NMR study. *J. Am. Chem. Soc*. **2007**, *123*, 11454-11461.

[118] Ottaviani, M.; Panero, S.; Morzilli, S.; Scrosati, B.; Lazzari, M. The electrochromic characteristics of titanium oxide thin film electrodes. *Solid State Ionics*. **1986**, *20*, 197-202.

[119] Kanamura, K.; Yuasa, K.; Takehara, Z. Diffusion of lithium in the TiO_2 cathode of a lithium battery. *J. Power Sources*. **1987**, *20*, 127-134.

[120] Wagemaker, M.; Borghols, W. J.; van Eck, E. R.; Kentgens, A. P.; Kearley, G. J.; Mulder, F. M. The Influence of Size on Phase Morphology and Li-Ion Mobility in Nanosized Lithiated Anatase TiO_2. *Chem. Eur. J.* **2007**, *13*, 2023-2028.

[121] Wagemaker, M.; Van Well, A. A.; Kearley, G. J.; Mulder, F. M. The life and times of lithium in anatase TiO_2. *Solid State Ionics*. **2004**, *175*, 191-193.

[122] Courtney, I. A.; Dahn, J. R. Electrochemical and in situ X-ray diffraction studies of the reaction of lithium with tin oxide composites. *Journal of the Electrochemical Society*. **1997**, *144*, 2045-2052.

[123] Sanjines, R.; Tang, H.; Berger, H.; Gozzo, F.; Margaritondo, G.; Levy, F. Electronic structure of anatase TiO_2 oxide. *Journal of Applied Physics*. **1994**, *75*, 2945-2951.

[124] Olson, C. L.; Nelson, J.; Islam, M. S. Defect chemistry, surface structures, and lithium insertion in anatase TiO_2. *The Journal of Physical Chemistry B*. **2006**, *110*, 9995-10001.

[125] Na-Phattalung, S.; Smith, M. F.; Kim, K.; Du, M. H.; Wei, S. H.; Zhang, S. B.; Limpijumnong, S. First-principles study of native defects in anatase TiO_2. *Physical Review B*. **2006**, *73*, 125205.

[126] Luo, H.; Takata, T.; Lee, Y.; Zhao, J.; Domen, K.; Yan, Y. Photocatalytic activity enhancing for titanium dioxide by co-doping with bromine and chlorine. *Chemistry of Materials*. **2004**, *16*, 846-849.

[127] Nie, L. H.; Shi, C.; Xu, Y.; Wu, Q. H.; Zhu, A. M. Atmospheric cold plasmas for synthesizing nanocrystalline anatase TiO_2 using dielectric barrier discharges. *Plasma Processes and Polymers*. **2007**, *4*, 574-582.

[128] Sugimoto, T.; Zhou, X.; Muramatsu, A. Synthesis of uniform anatase TiO_2 nanoparticles by gel–sol method: 3. Formation process and size control. *Journal of Colloid and Interface Science*. **2003**, *259*, 43-52.

[129] Ding, Z.; Hu, X.; Yue, P. L.; Lu, G. Q.; Greenfield, P. F. Synthesis of anatase TiO_2 supported on porous solids by chemical vapor deposition. *Catalysis Today*. **2001**, *68*, 173-182.

[130] Golubović, A.; Šćepanović, M.; Kremenović, A.; Aškrabić, S.; Berec, V.; Dohčević-Mitrović, Z.; Popović, Z. V. Raman study of the variation in anatase structure of TiO_2 nanopowders due to the changes of sol–gel synthesis conditions. *Journal of Sol-Gel Science and Technology*. **2009**, *49*, 311-319.

[131] Sugimoto, T.; Zhou, X. Synthesis of Uniform Anatase TiO_2 Nanoparticles by the Gel–Sol Method: 2. Adsorption of OH^- Ions to $Ti(OH)_4$ Gel and TiO_2 Particles. *Journal of Colloid and Interface Science*. **2002**, *252*, 347-353.

[132] Li, G.; Li, L.; Boerio-Goates, J.; Woodfield, B. F. High purity anatase TiO_2 nanocrystals: near room-temperature synthesis, grain growth kinetics, and surface hydration chemistry. *Journal of the American Chemical Society*. **2005**, *127*, 8659-8666.

[133] Long, M.; Cai, W.; Chen, H.; Xu, J. Preparation, characterization and photocatalytic activity of visible light driven chlorine-doped TiO2. *Frontiers of Chemistry in China*. **2007**, *2*, 278-282.

VITA

Dongxue Zhao was born in December 1986 in Hebei Province, China and brought up in Hebei and Shanghai. He finished his Bachelor Degree in Optoelectronics and Information Engineering as “Honored Outstanding Graduate Award” awardee in University of Shanghai for Science and Technology in 2009. From 2009 to 2010, he studied Electrical Engineering as a graduate student in Illinois Institute of Technology. He transferred to University of Missouri – St. Louis in August 2010 and studied in Vision Science graduate program focused on electro-optics and biomedical imaging at College of Optometry until July 2011. He joined Dr. Eric H. Majzoub’s energy storage materials research group at the Department of Physics and Astronomy of University of Missouri – St. Louis in July 2011. In December 2012, he received his M.S. in Physics. In August, 2015, he received his Ph.D. in Physics which was jointly awarded by Missouri University of Science and Technology and the University of Missouri – St. Louis.

Dongxue won the Who’s Who Among Students in American Universities and Colleges Award and Winter Student Leadership Award of Missouri University of Science and Technology in 2013. He won the graduate research award in physics and applied math division in the graduate research fair in 2014 for “Investigation of alkali metal hydride/hydroxide solubility using in-situ X-Ray Diffraction and Differential Scanning Calorimetry”. He won the graduate research award in physics and physical chemistry division in the graduate research fair in 2015 for “Controlled Size Nano-particle Anatase TiO_2 for Increased Capacity Lithium-ion Batteries”.

In the summer of 2014, he worked as a research associate intern in the system research lab at HP labs, Hewlett-Packard Company in Palo Alto, California. During his internship, he did research work on thin film memristor devices for emerging resistive memory technology on HP’s “The Machine” Project, which is led by the discoverer of working solid state version memristor – Dr. Stanley R. Williams.

Dongxue’s hobbies include: movies, computer games, and long distance road trips.